INVESTIGATIONS INTO THE INTERACTIONS BETWEEN SULFUR AND ANODES FOR SOLID OXIDE FUEL CELLS

A Dissertation
Presented to
The Academic Faculty

by

Zhe Cheng

In Partial Fulfillment
Of the Requirements for the Degree
Doctor of Philosophy in the
School of Materials Science and Engineering

Georgia Institute of Technology
April 2008

INVESTIGATIONS INTO THE INTERACTIONS BETWEEN SULFUR AND ANODES FOR SOLID OXIDE FUEL CELLS

Approved by:

Dr. Meilin Liu, Advisor
School of Materials Science & Engineering
Georgia Institute of Technology

Dr. Robert F. Speyer
School of Materials Science & Engineering
Georgia Institute of Technology

Dr. W. Brent Carter
School of Materials Science & Engineering
Georgia Institute of Technology

Dr. Christopher Summers
School of Materials Science & Engineering
Georgia Institute of Technology

Dr. Preet Singh
School of Materials Science & Engineering
Georgia Institute of Technology

Dr. Pradeep K. Agrawal
School of Chemical & Biomolecular Engineering
Georgia Institute of Technology

Date Approved: February 28, 2008

ACKNOWLEDGEMENTS

I would like to thank my advisor, Professor Meilin Liu, for his insightful guidance, enthusiastic encouragement, unweaving support, and kindly help in the past five years, without which the study would not be possible. I would also like to thank Professor Carter, Professor Singh, Professor Speyer, Professor Summers, and Professor Agrawal for serving on my thesis reading committee and their kindly advice and support in the past years.

I would also like to thank Dr. Shaowu Zha, who used to work in Professor Liu's group as a post-doctor, for extensive hands-on training on fuel cell fabrication and testing techniques used in the study, numerous valuable suggestions, and close cooperation in the course of the study. I would like to thank my colleague - Mr. Harry Abernathy for his assistance with experimental methods and theory about Raman spectroscopy, which turned out to be the source for one of the most important contributions of this study. I would also like to thank all other co-workers for their help in many things especially the setting up of the complex equipment for multi-cell testing system.

Finally, I would like to express my gratitude to my dear wife, Shujia Mei, for her love, understanding, encouragement, and support in the process of my Ph.D. study. I would also like to thank my parents, Chunjun Cheng and Manke Liu for their love.

Funding of this research was provided by the Shell Chemical grant and the Department of Energy SECA Core Technology Program under award number: DE-FC26-04NT42219.

TABLE OF CONTENTS

LIST OF TABLES

LIST OF FIGURES

SUMMARY

While solid oxide fuel cells (SOFCs) have a potential to be the power of the future, the performances of the existing SOFCs degrade dramatically upon exposure to a trace amount of contaminants (e.g., sulfur) in available fuels. In this study, the interactions between sulfur contaminant (in the form of hydrogen sulfide, H_2S) and the anodes for SOFCs were systematically investigated in order to gain a fundamental understanding of the mechanism of sulfur poisoning and ultimately to achieve rational design of sulfur-tolerant anodes. First, the sulfur poisoning behavior of the state-of-the-art Ni-YSZ cermet anodes was characterized using electrochemical measurements performed on button cells (of different structures) under various operating conditions. It was found that both the rate and the extent of sulfur poisoning increased with H_2S concentration until saturation was reached. For a given H_2S concentration, the extent of sulfur poisoning increased as the operating temperature was reduced from 1000 to ~700 ^oC. The extent of sulfur poisoning, as measured by the relative increase in cell resistance, always decreased with the cell current density (or when the cell terminal voltage was decreased). However, conflicting trends in power output drop due to sulfur poisoning were observed under a constant current versus a constant voltage condition. The sulfur poisoning behavior for cells with different structures were essentially the same except that the long-term gradual degradation often observed in electrolyte-supported cells was much less significant for anode-supported cells.

Second, the mechanisms of interactions between sulfur and Ni-YSZ cermet anodes for SOFCs were examined using both ex situ and in situ characterization

techniques. No conventional nickel sulfides were observed on nickel surface at high temperatures in fuel atmosphere with H_2S under in situ conditions. The bulk nickel sulfides observed in the ex situ experiments were formed not during the sulfur poisoning process, but in the subsequent cooling process when the reaction between H_2S and nickel became thermodynamically favorable. Analysis of data from theoretical calculations and experiments clearly indicated that the sulfur poisoning of Ni-YSZ anode at high temperatures in ppm-level is due not to the formation of conventional nickel sulfides but to the adsorption of sulfur on nickel surfaces, which blocks the reaction sites for hydrogen adsorption and oxidation.

Third, the interaction between sulfur and new sulfur tolerant anode materials for SOFCs were studied. Thermodynamics were identified as an effective tool to predict and explain the phenomena concerning the reactivity of candidate sulfur-tolerant anode materials under anode atmosphere containing H_2S. The enhanced sulfur tolerance observed for some new sulfur tolerant anode materials such as $Gd_2Ti_{1.4}Mo_{0.6}O_7$ was attributed to the transition of the surface from metal oxides to metal sulfides (i.e., MoS_2), which enhances the catalytic activity and increases the number of reaction sites.

This study has systematically characterized the electrochemical behavior and the mechanism of sulfur poisoning of Ni-YSZ cermet anodes under SOFC operating conditions, providing useful information for the selection or rational design of new sulfur-tolerant anode materials.

For future research, it is recommended that studies on sulfur poisoning for SOFCs operated under high fuel utilization condition should be carried out to better simulate the practical conditions. In addition, for the development of new sulfur-tolerant anode

materials, the modification of the current Ni-YSZ anode based on the knowledge about the origin for the enhanced sulfur tolerance for some of the new materials were encouraged.

CHAPTER 1

INTRODUCTION

Solid oxide fuel cells (SOFCs) are electrochemical devices with solid oxide electrolytes that convert chemical energy in fuels (e.g., hydrogen or syngas) directly to electrical energy via electrochemical reactions. The major advantage of SOFCs over conventional power generation techniques based on combustion is that SOFCs have higher electrical efficiency especially in small systems (i.e., kilowatt to megawatt range). Other advantages of SOFCs include less emission of air pollutants such as NO_x and SO_x and the flexibility to use a variety of fuels from pure hydrogen to syngas and light hydrocarbons (van Gerwen, 2003).

1.1 Motivation of the Research

For practical applications of SOFCs, hydrocarbon fuels rather than pure hydrogen are the preferred fuels because they are more available and easier to transport and store based on current infrastructure (Minh and Takahashi, 1995, p. 37). However, one of the major problems with using hydrocarbon fuels in an SOFC is that they all contain considerable amounts of sulfur compounds, which, if not removed thoroughly, would severely poison the nickel-yttria stabilized zirconia (YSZ) cermet anode for an SOFC, leading to decreased cell performance or even cell failure. The removal of sulfur from hydrocarbon fuels incurs additional complexity and cost to SOFCs (Minh and Takahashi 1995, p. 38) and becomes one of the major barriers to the wide application of SOFCs.

Although the sulfur poisoning of SOFCs has been known for some time, one problem with previous studies on the sulfur poisoning process is that they were not very systematic and sometimes contradicted one another. For example, the sulfur poisoning under anode/electrolyte/ cathode full cell condition at lower temperatures (e.g., below ~900 ^{o}C) has not been systematically investigated. There are the still uncertainties about the exact influence of cell voltage or current density on the observed sulfur poisoning behavior. The similarity and difference between the sulfur poisoning behavior for SOFCs with different structures (i.e., anode-supported cell and electrolyte-supported cell) has not been studied. The long-term (i.e., over hundreds of hours) sulfur poisoning behavior is also not clear.

Another problem with previous studies on the sulfur poisoning for solid oxide fuel cells is that most of them were devoted solely to the characterization of the phenomenological electrochemical response of SOFCs to H_2S contaminants, which were limited to the observation of the changes in impedance spectra, current density (under constant potential condition), or cell voltage (under constant current condition) with respect to different H_2S concentration, temperature, and time. No study has been aimed at obtaining an in-depth understanding of the sulfur-nickel interaction and the poisoning mechanism by characterizing the changes on the anode upon exposure to H_2S-containing fuel. As a consequence, although different mechanisms such as the adsorption of sulfur species on the anode surface (Minh and Takahashi, 1995, p. 210; Primdhal and Mogensen, 1999; Matsuzaki et al., 2000; Sasaki et al., 2005) or the formation of surface sulfide (Minh and Takahashi, 1995, p. 210, Xia and Birss 2005) have been proposed as the causes for sulfur poisoning of SOFC anode, there is a continued lack of experiments

to directly prove or disprove these hypotheses, and all the proposed mechanisms remain largely speculative.

On the other hand, for the development of new sulfur-tolerant anode materials for solid oxide fuel cells, the selection of candidate sulfur-resistant anode materials in previous studies remained in an almost random, try-and-error manner, which is not very efficient. In addition, the origin for the enhanced sulfur tolerance observed for those new candidate sulfur-tolerant materials is also not known.

1.2 Research Objectives and Technical Approaches

In light of the problems stated before, three objectives had been set for this study. The first is to systematically characterize the sulfur poisoning behavior for SOFC full cells with conventional Ni-YSZ cermet anodes under various operating conditions. The second is to investigate the sulfur poisoning mechanism for SOFCs with Ni-YSZ cermet anodes by characterizing the changes on the Ni-based anode upon exposure to sulfur-containing fuels. The third is to develop new, sulfur-tolerant anode materials for SOFCs, try to provide some guidelines about new materials selection, and reveal the fundamental mechanism for the enhanced sulfur tolerance of some of those new materials.

To achieve these objectives, the sulfur poisoning process of SOFCs with conventional Ni-YSZ cermet anodes was characterized by monitoring the changes in electrochemical responses for cells when hydrogen sulfide (H_2S) was introduced into and removed from the fuel flow under different conditions (i.e., temperature, H_2S concentration, and cell current density/voltage, etc.). The sulfur–anode interaction mechanism was investigated by characterizing the chemical and structural changes on the

Ni-YSZ composite anodes using both ex situ techniques such as scanning electron microscopy (SEM), energy dispersive X-ray spectroscopy (EDX), and X-ray diffraction (XRD) and in situ techniques such as in situ Raman microspectroscopy. Meanwhile, for the development of new sulfur-tolerant anode materials, thermodynamic analysis was carried out to predict and explain the stability of various candidate sulfur-tolerant anode materials, while the interaction mechanism for sulfur and the new sulfur-tolerant anode materials was studied by characterizing the changes to the anode using techniques such as XRD and Raman spectroscopy.

1.3 Organization of the Thesis

In the following, Chapter II will provide some background information about solid oxide fuel cells and previous studies on the interactions between sulfur and anodes for solid oxide fuel cells. Chapter III will describe the detailed experimental procedures used in this study, which include the synthesis of cell materials, the fabrication of SOFC button cell, the electrochemical characterization under various conditions, and characterization of samples using SEM, EDX, XRD, Raman, etc. Chapter IV will present the results of the study on the sulfur poisoning behavior for solid oxide fuel cells with traditional Ni-YSZ cermet anodes. The influence of various testing parameter such as temperature, sulfur concentration, cell current density/voltage, cell structure, and sulfur exposure time will be revealed. The results will be compared with previous studies and the implication to the sulfur poisoning mechanism will be discussed. Chapter V will be on the sulfur-anode interaction mechanism for SOFCs with traditional Ni-based anodes. The results from both ex situ and in situ measurements will be presented and interpreted.

The mechanism for sulfur poisoning and regeneration will also be discussed based on available theoretical and experimental data. Chapter VI will present the results of studies on the interactions between sulfur and new sulfur-tolerant anode materials for solid oxide fuel cells. It will include two parts: the first part is on using thermodynamics as a tool to explain and predict the stability for novel candidate sulfur-tolerant anode materials, while the second one is on revealing the origin for the enhanced sulfur tolerance observed for some promising candidate materials by characterizing the changes on the materials. Finally, Chapter VII will give brief conclusions from this study and provide some recommendations for future research in this field.

CHAPTER 2

BACKGROUND

2.1 Solid Oxide Fuel Cell

2.1.1 Basic Information

A fuel cell (FC) is an electrochemical device that converts chemical energy of a fuel directly to electrical energy. A fuel cell consists of three basic components - an ionic conductive electrolyte, an anode where the fuel (e.g., hydrogen) is oxidized, and a cathode where the oxidant (usually oxygen) is reduced. The anode and the cathode are separated by the electrolyte, which must be gas impermeable and conduct only ions but not electrons or holes.

A solid oxide fuel cell (SOFC) uses a solid oxide as the electrolyte, and usually operates at high temperatures (500-1000 ^{o}C). The state-of-the-art electrolyte is yttria stabilized zirconia (YSZ, with a composition of 8 mol.% Y_2O_3 - 92 mol.% ZrO_2, sometimes referred to as 8YSZ); the anode is a porous nickel-YSZ cermet; and the cathode is a porous composite that usually contains $La_{1-x}Sr_xMnO_3$ (LSM, usually x equals to ~0.15-0.20) and YSZ. Figure 1 is a schematic for a typical single SOFC using hydrogen as the fuel and oxygen as the oxidant. On the cathode, oxygen molecules are reduced to oxygen ions that go into the YSZ electrolyte:

$$0.5\ O_2 + 2e^- = O^{2-}. \qquad (2\text{-}1)$$

On the anode, the fuel molecule (hydrogen for example) is oxidized by combining with oxygen ions and release electrons:

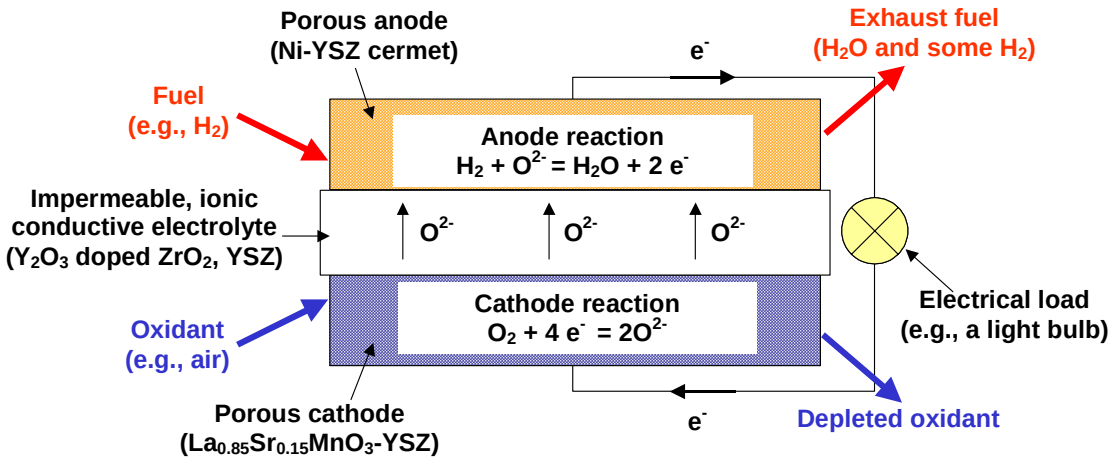

Figure 2-1 Schematic for a single solid oxide fuel cell.

$$H_2 + O^{2-} = H_2O + 2\,e^-. \tag{2-2}$$

Inside the cell, oxygen ions, e.g., O^{2-}, move through the electrolyte. Outside the cell, electrons move from the anode to the cathode through an external circuit and drive the electrical load during the process, and the conversion of chemical energy in the fuel to electrical energy is achieved. More specifically, the cathode reaction can be written as

$$0.5\,O_2 + V_O^{\bullet\bullet} + 2e = O_O^x, \tag{2-3}$$

where $V_O^{\bullet\bullet}$ represents oxygen vacancy and O_O^x represents oxygen in the electrolyte (YSZ) lattice. Accordingly, the anode reaction can be written as

$$H_2 + O_O^x = H_2O + V_O^{\bullet\bullet} + 2e. \tag{2-4}$$

The combination of Equations (2-3) and (2-4) would yield the full cell reaction of

$$2\,H_2 + O_2 = 2\,H_2O. \tag{2-5}$$

2.1.2 Thermodynamics of Solid Oxide Fuel Cells

2.1.2.1 Equilibrium Cell Potential

For SOFCs using oxygen as the oxidant and a pure oxide ion conductor (e.g., YSZ) as the electrolyte, Nernst equation predicts that when a cell is under the equilibrium condition, i.e., no net current passes through the cell and the gas on each side is uniform, a stable voltage difference, E_r, would exist across the electrolyte. Its value is given by

$$E_r = \frac{RT}{4F} \ln \frac{P_{O_2(c)}}{P_{O_2(a)}}, \tag{2-6}$$

where R is the universal gas constant of 8.314 J/mol · K, T is the absolute temperature in K, F is the Faraday constant (96485 C/mol), and $P_{O_2(c)}$ and $P_{O_2(a)}$ are the oxygen partial pressure in the cathode and anode chamber, respectively. The partial pressure of oxygen in the cathode chamber, $P_{O_2(c)}$, is usually fixed at ~0.21 for air or ~1.0 for pure oxygen. The partial pressure of oxygen in the anode chamber, $P_{O_2(a)}$, is determined by the composition of the fuel gas. For example, if H_2 is the fuel in the anode chamber, the oxygen partial pressure is determined by the equilibrium for reaction (2-5) in the anode chamber. The Gibbs free energy change for reaction (2-5) in the anode chamber is

$$\Delta G = \Delta G^\circ + RT \ln \frac{(P_{H_2O(a)} / P^\circ)^2}{(P_{H_2(a)} / P^\circ)^2 (P_{O_2(a)} / P^\circ)}, \tag{2-7}$$

where ΔG° is the standard Gibbs free energy change for reaction (2-5) and P^o is the standard pressure, i.e., one atmosphere. Under equilibrium conditions, $\Delta G = 0$, and the oxygen partial pressure in the anode chamber is

$$\frac{P_{O_2(a)}}{P^\circ} = \left(\frac{P_{H_2O}}{P_{H_2}} \right)^2 \exp\left(\frac{\Delta G^\circ}{RT} \right). \tag{2-8}$$

Therefore, the Nernst potential for the cell is

$$E_r = \frac{RT}{4F}\ln\frac{P_{O_2(c)}}{P_{O_2(a)}} = \frac{RT}{4F}\ln\frac{P_{O_2(c)}}{P^\circ\left(P_{H_2O(a)}/P_{H_2(a)}\right)^2\exp\left(\Delta G^\circ/RT\right)}$$

or

$$E_r = -\frac{\Delta G^\circ}{4F} + \frac{RT}{4F}\ln\frac{P_{O_2(c)}\left(P_{H_2(a)}\right)^2}{P^\circ\left(P_{H_2O(a)}\right)^2}$$

$$= E_r^o + \frac{RT}{4F}\ln\frac{P_{O_2(c)}\left(P_{H_2(a)}\right)^2}{P^\circ\left(P_{H_2O(a)}\right)^2}, \qquad (2\text{-}9)$$

where $E_r^o = -\frac{\Delta G^\circ}{4F}$ is the standard cell potential for reaction (2-5), written in the way that four electrons are transferred.

Alternatively, when an SOFC is under the electrochemical equilibrium condition,

$$\Delta G_{electrochem} = \Delta G_{chem} + nFE_r = 0. \qquad (2\text{-}10)$$

Therefore,

$$E_r = -\frac{\Delta G_{chem}}{nF}, \qquad (2\text{-}11)$$

where

$$\Delta G_{chem} = \Delta G^\circ + RT\ln\frac{(P_{H_2O(a)}/P^\circ)^2}{(P_{H_2(a)}/P^\circ)^2(P_{O_2(c)}/P^\circ)} \qquad (2\text{-}12)$$

for reaction (2-5). Note in this case, the partial pressure of oxygen in the *cathode* chamber $P_{O_2(c)}$ should be used in Equation (2-12) since it is for the electrochemical equilibrium between hydrogen and water in the anode chamber and oxygen in the cathode chamber (compare to Equation (2-7)). Therefore, the cell reversible potential, E_r,

is

$$E_r = -\frac{\Delta G^\circ + RT \ln \dfrac{(P_{H_2O(a)} / P^\circ)^2}{(P_{H_2(a)} / P^\circ)^2 (P_{O_2(c)} / P^\circ)}}{4F}$$

$$= -\frac{\Delta G^o}{4F} + \frac{RT}{4F} \ln \frac{P_{O_2(c)} (P_{H_2(a)})^2}{P^\circ (P_{H_2O(a)})^2},$$

which is exactly the same as Equation (2-9).

Using Equation (2-9), the equilibrium potential for a cell can be calculated if hydrogen and water partial pressure in the anode chamber and oxygen partial pressure in the cathode chamber are known. Similarly, if CO is used as the fuel, the full cell reaction for the electrochemical oxidation of CO is

$$2\ CO_{(g)} + O_{2\,(g)} = 2\ CO_{2\,(g)}. \tag{2-13}$$

The cell reversible potential is

$$E_r = -\frac{\Delta G^o}{4F} + \frac{RT}{4F} \ln \frac{P_{O_2(c)} (P_{CO(a)})^2}{P^\circ (P_{CO_2(a)})^2}$$

$$= E_r^o + \frac{RT}{4F} \ln \frac{P_{O_2(c)} (P_{CO(a)})^2}{P^\circ (P_{CO_2(a)})^2}, \tag{2-14}$$

where ΔG° is the standard Gibbs free energy change and $E_r^o = -\dfrac{\Delta G^\circ}{4F}$ is the standard cell potential for reaction (2-13), written in the way that four electrons are transferred.

Figure 2-2 shows the calculated equilibrium cell potentials, E_r, as well as standard potentials, E_r^o, versus temperature for the electrochemical oxidation of H_2 and CO. As expected from Equations (2-9) and (2-14), the equilibrium cell potential decreases with temperature. For example, a fuel with a composition of 3% H_2O/97% H_2 and an oxidant

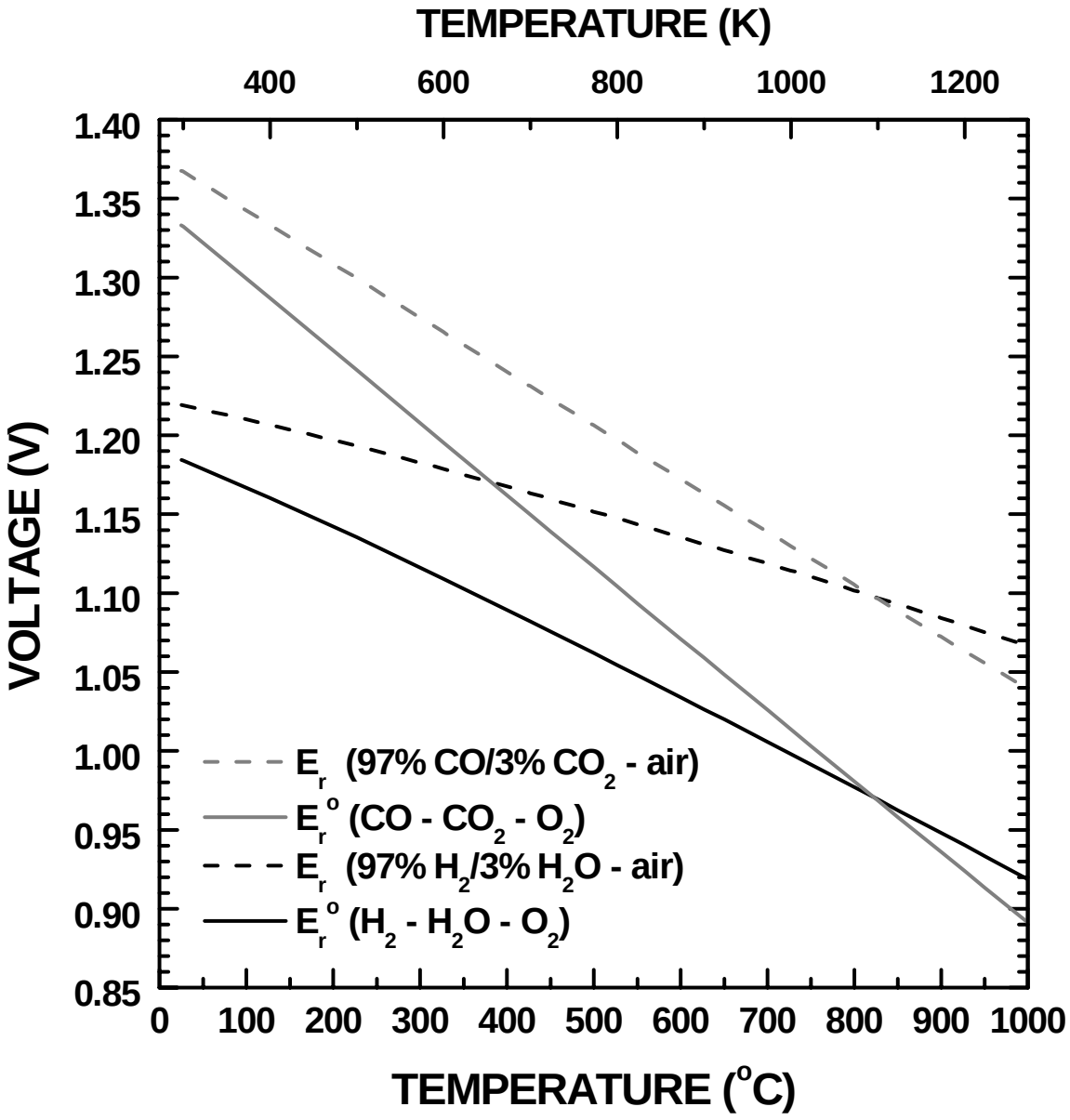

Figure 2-2 Change of standard cell voltage, E_r^o, and equilibrium cell voltage, E_r, versus temperature for the electrochemical oxidation of H_2 to produce H_2O and of CO to produce CO_2. The fuel is either 97% H_2/3% H_2O or 97% CO/3% CO_2, and the oxidant is air with 21% O_2.

of air (p_{O_2} = 0.21), the cell equilibrium potential decreases from 1.22 V at 25 ^{o}C to 1.15 V at 500 ^{o}C, 1.11 V at 750 ^{o}C, and 1.07 V at 1000 ^{o}C. The voltage difference across the electrolyte (usually ~1 V for a single cell) could drive electrical appliance, and the conversion from chemical energy in a fuel to electrical energy is achieved (Minh and Takahashi, 1995, pp. 1-18).

2.1.2.2 Efficiency of Solid Oxide Fuel Cells

- Thermodynamic efficiency

For all types of fuel cells, the maximum amount of chemical energy in the fuel that could be converted to electrical energy equals the Gibbs free energy change for the corresponding fuel oxidation reaction (i.e., reaction (2-5) or (2-13). The maximum efficiency of a fuel cell, which is also called the *thermodynamic efficiency*, ε_T^{o}, is defined by

$$\varepsilon_T^{o} = \frac{\Delta G^{o}}{\Delta H^{o}}, \tag{2-15}$$

where ΔG^{o} and ΔH^{o} are the standard Gibbs free energy change and standard enthalpy change, respectively, for the fuel oxidation reaction (i.e., reaction (2-5) or (2-13)). Note that, for simplicity, the free energy change and enthalpy change under the *standard state* are used in Equation (2-15) since the actual Gibbs free energy change would depend on fuel and oxidant compositions, which are functions of fuel utilization. For the hydrogen – oxygen pair under standard state at high temperatures (i.e., water exists as steam)

$$\Delta H^{o} = 2\Delta H_f^{o}(\mathrm{H_2O, g}) - 2\Delta H_f^{o}(\mathrm{H_2}, g) - \Delta H_f^{o}(\mathrm{O_2}, g), \tag{2-16}$$

$$\Delta G^{o} = 2\Delta G_f^{o}(\mathrm{H_2O, g}) - 2\Delta G_f^{o}(\mathrm{H_2}, g) - \Delta G_f^{o}(\mathrm{O_2}, g). \tag{2-17}$$

At 727 ^{o}C or 1000 K, from the JANAF table (Chase et al., 1985), $\Delta H_f^{\circ}(\mathrm{H_2O, g}) =$ -247.857 kJ/mol, $\Delta G_f^{\circ}(\mathrm{H_2O, g}) =$ -192.590 kJ/mol, $\Delta H_f^{\circ}(\mathrm{H_2}, g) = \Delta G_f^{\circ}(\mathrm{H_2}, g) = \Delta H_f^{\circ}(\mathrm{O_2}, g) = \Delta G_f^{\circ}(\mathrm{O_2}, g) = 0$ kJ/mol. Therefore, the thermodynamic efficiency for the electrochemical oxidation of H_2 by O_2 into gaseous H_2O at 1000 K is -192.590/-247.857 = 0.78.

Figure 2-3 shows the change in thermodynamic efficiency versus temperature for the electrochemical oxidation of H_2 and CO. (Note that the efficiency value was calculated based on the higher heating value (HHV), as water is considered as steam in the calculation.) For fuel cells using either H_2 and/or CO as the fuel, the thermodynamic efficiency is always smaller than one, and it decreases significantly with temperature. For example, for the oxidation of H_2, the thermodynamic efficiency decreases from 0.94 at 25 ^{o}C to 0.93 at 80 ^{o}C, 0.83 at 500 ^{o}C, 0.77 at 750 ^{o}C, and 0.71 at 1000 ^{o}C. The decrease in thermodynamic efficiency with temperature is due to the negative change in reaction entropy ($\Delta S < 0$) for reactions (2-5) and (2-13), which is associated with the reduction of the total number of molecules in those reactions.

For some other hydrocarbon fuels, in theory, the thermodynamic efficiency may equal one or even be greater than one. For example of the direct electrochemical oxidation of methane (CH_4), in theory, the full cell reaction would be

$$CH_4 + 2\,O_2 = CO_2 + 2\,H_2O, \qquad (2\text{-}18)$$

and $\varepsilon_T^{\circ} \approx 1$ because the change in the number of molecules is zero and $\Delta S^{\circ} \approx 0$.

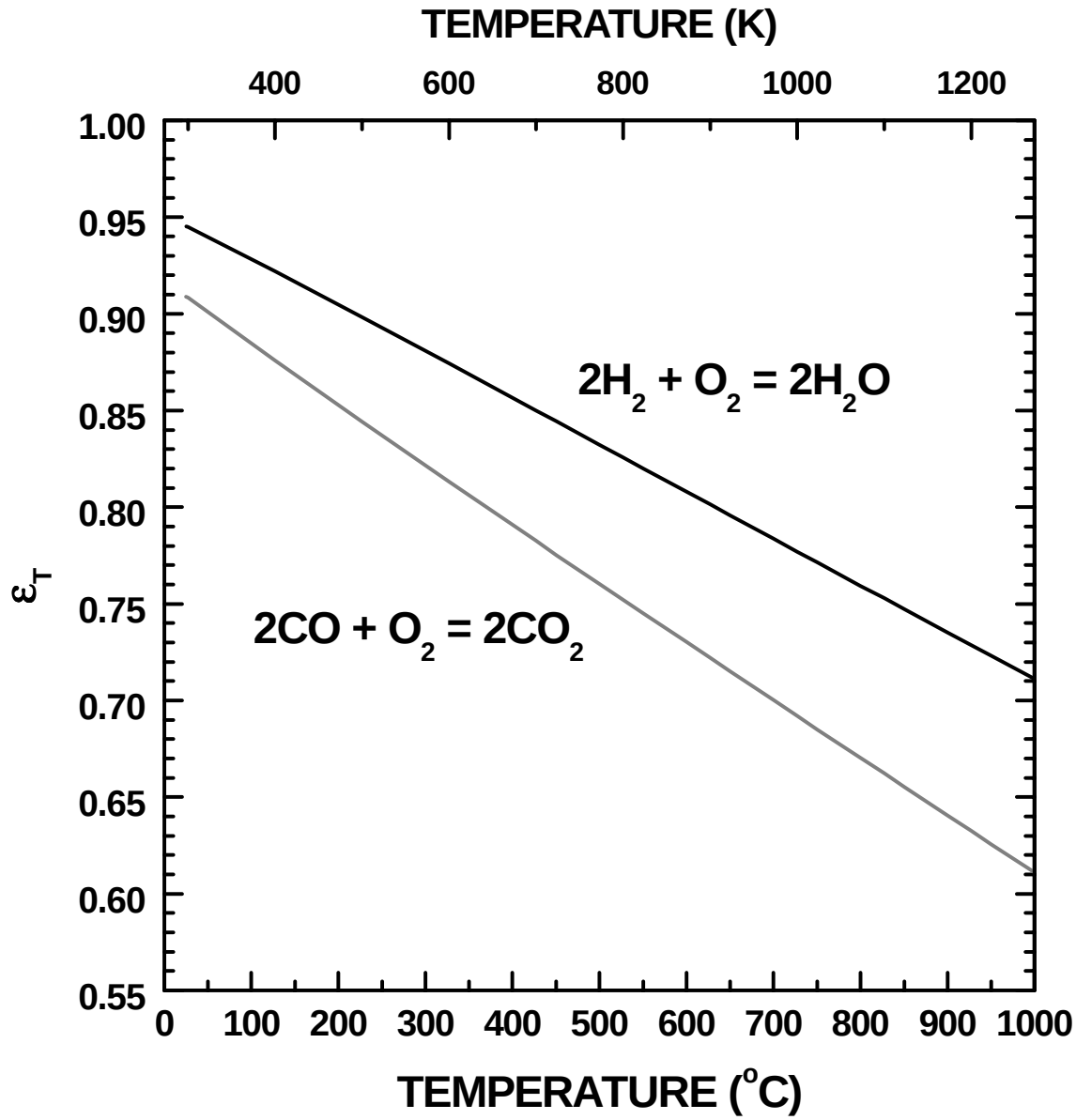

Figure 2-3 Change of thermodynamic efficiency, $\varepsilon_T^o = \Delta G^o / \Delta H^o$, versus temperature for the electrochemical oxidation of H_2 and CO. Note that the efficiency calculated based on the higher heating value (HHV) as water is considered as steam in the calculation.

Similarly, for the direct electrochemical oxidation of fuels like methanol (CH_3OH), in theory, the full cell reaction would be

$$2\ CH_3OH\ +3\ O_2\ =\ 2\ CO_2\ +\ 4\ H_2O. \qquad (2\text{-}19)$$

Because the number of molecules increases after the electrochemical oxidation, $\Delta S^o > 0$ and $\varepsilon_T^o > 1$. However, that thermodynamic efficiency can approach one or even be greater than one as in reactions like (2-18) or (2-19) only has theoretical meaning and is *not* too appealing in real world applications. This is because (i) for fuels like CH_4, the direct electrochemical reaction into CO_2 and H_2O usually will *not* happen as they are written in Equation (2-18), which is a very complex reaction involving the transfer of eight electrons. The real scenario is fuels like CH_4 will be reformed internally or externally into H_2 and CO. Therefore, the cell thermodynamic efficiency will still be determined by the value for H_2 as CO will go through the shift reaction to produce H_2. (ii) For fuels like methanol, they are produced from methane in industrial production, and the extra energy required to produce them from methane would exceed the "extra" energy that could be harvested from a greater than one thermodynamic efficiency (Rostrup-Nielsen, 2001). Nevertheless, from an efficiency point of view, the reduction of operating temperature is always desirable as more useful electrical work could be obtained at lower temperatures. Up till now, practical considerations limit the operating temperature for SOFCs to above ~700 ^oC, which corresponds to a thermodynamic (and also the highest possible) efficiency of ~0.78.

- Voltage efficiency

For practical applications, a fuel cell will *not* operate under equilibrium condition since current is required in the outside circuit. When current passes through the cell and

the outside circuit, cell voltage will always be lower than the reversible potential due to the finite cell internal resistance. The drop in cell voltage under a closed circuit condition leads to further decrease in cell efficiency and is defined as *voltage efficiency*, ε_V, by the following relationship:

$$\varepsilon_V = \frac{E}{E_r}, \tag{2-20}$$

where E is the cell terminal voltage during operation (i.e., under a closed circuit condition). The energy efficiency for a fuel cell would further be modulated by this value. In practical operations, the closed circuit voltage for an SOFC is usually above ~0.7 V. Higher cell voltage will increase voltage efficiency, but the power output decreases at the same time.

- Fuel cell system efficiency

For a solid oxide fuel cell system, the electrical efficiency would decrease further due to other factors such as fuel utilization, fuel reforming and cleaning, of which the efficiency is labeled as ε_r, and the loss in power conditioning (i.e., converting DC to AC power), of which the efficiency is labeled as ε_{pc}. The total electrical efficiency for the fuel cell system would be the product of all these terms listed above.

Considering a SOFC system running at 750 ^{o}C, for a conservative estimation, the fuel reforming efficiency $\varepsilon_r = 0.80$, the thermodynamic efficiency $\varepsilon_T^{o} = 0.77$, the voltage efficiency $\varepsilon_V = 0.75$ (assuming average OCV of 1.0 V and cell terminal voltage of 0.75 V), a power conditioning efficiency $\varepsilon_{pc} = 0.90$, and neglecting other factors such as current efficiency and heat efficiency (i.e., assuming the heat generated by IR is

sufficient to maintain cell temperature), the DC electrical efficiency for a SOFC system would be

$$\varepsilon_{sys\_DC} = \varepsilon_r \cdot \varepsilon_T^{o} \cdot \varepsilon_V . \tag{2-21}$$

$$= 0.80 \times 0.77 \times 0.75 = 46\%,$$

and the AC electrical efficiency would be

$$\varepsilon_{sys\_AC} = \varepsilon_r \cdot \varepsilon_T^{o} \cdot \varepsilon_V \cdot \varepsilon_{pc} . \tag{2-22}$$

$$= 0.80 \times 0.77 \times 0.75 \times 0.90 = 42\%,$$

both of which would be much higher than the value for small-scale reciprocal engine powered generators (lower than ~30%, van Gerwen, 2003), and are close to the efficiency reported for all SECA industrial teams in their phase I demonstration unit (Surdoval, 2007).

2.1.3 Kinetics for Solid Oxide Fuel Cells

In the discussion before about voltage efficiency, it was mentioned that cell voltage under a close circuit condition would always be lower than the open circuit voltage, which, for a pure ionic conductor, is equal to the reversible potential, E_r. The difference between the cell operating voltage, E, and the reversible voltage is called polarization,

$$\eta = E_r - E \ . \tag{2-23}$$

The votal voltage loss for a single cell can be divided into three parts: the one across the electrolyte, the anode, and the cathode, i.e.,

$$\eta = \eta_{electrolyte} + \eta_a + \eta_c . \tag{2-24}$$

The voltage loss over the electrolyte is an ohmic loss whereas that across an electrode can be further divided into the charge transfer (also called activation) polarization (η_{ct}), and mass transfer (also called concentration) polarization (η_{mt}). Therefore, we have

$$\eta = \eta_{\Omega} + (\eta_{ct,a} + \eta_{mt,a}) + (\eta_{ct,c} + \eta_{mt,c}) . \tag{2-25}$$

Figure 2-4(a) shows a typical current-voltage relationship for a solid oxide fuel cell showing different types of polarizations.

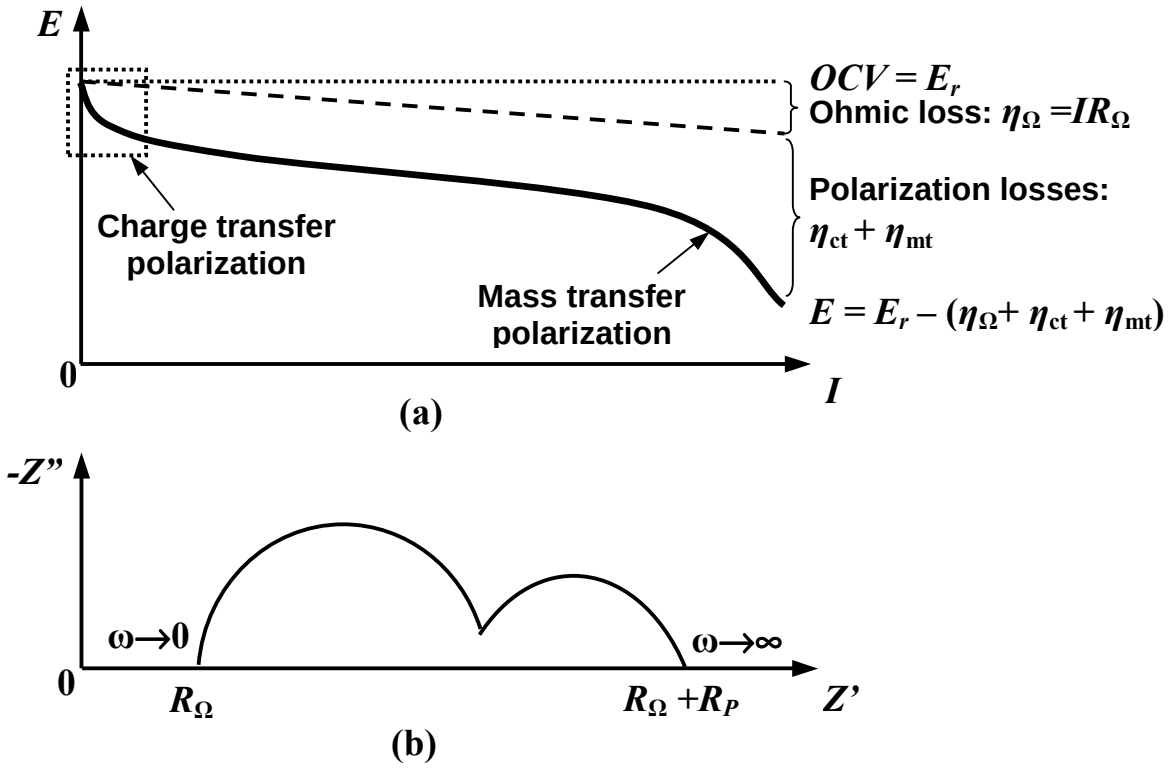

Figure 2-4 (a) Plot of a typical current-voltage relationship for a solid oxide fuel cell, showing three types of losses, (b) an impedance spectrum for a solid oxide fuel cell showing ohmic and polarization losses.

- Ohmic loss

Among the three types of losses, the ohmic loss, η_Ω, is the simplest and can be calculated using the Ohm's law:

$$\eta_\Omega = IR_\Omega , \tag{2-26}$$

where I is the cell current and R_Ω is the cell ohmic resistance, which include the ionic resistance of the electrolyte and the electronic resistance from the electrodes. In the impedance spectrum for a single cell as shown in Figure 2-4(b), the ohmic resistance can be readily determined from the high frequency intercept of the spectrum with the real axis.

- Charge transfer polarization

Charge transfer polarization or overpotential is the extra potential (i.e., the difference between equilibrium potential and the actual potential) necessary to reduce the energy barrier for an electrochemical reaction so that the reaction proceeds at a desired rate (i.e., at certain current density). Usually, when the mass transfer effect is negligible, charge transfer polarization is related to current density through the Bulter-Volmer equation:

$$j = j_0 \left[\exp\left(\frac{\alpha F \eta_{ct}}{RT} \right) - \exp\left(-\frac{(1-\alpha) F \eta_{ct}}{RT} \right) \right], \tag{2-27}$$

where α is the charge transfer coefficient, j_0 is the exchange current density, F is the Faraday constant (96485 C/mol) (Minh and Takahashi, 1995, p. 22) Although activation polarization always exists, it usually manifests when the cell voltage is close to open cell voltage, as shown in the low current region in the plot in Figure 2-4(a).

- Mass transfer polarization

When the rate of transferring reactants to or products away from the reaction sites is slower than the rate of the charge transfer processes, the entire electrochemical reaction will run into mass transfer limitation. For an electrode process with sufficiently fast charge transfer process, the mass transfer polarization (or overpotential) can be approximated by:

$$\eta_{mt} = \frac{RT}{zF} \ln\left(1 - \frac{j}{j_L}\right), \tag{2-28}$$

where z is the number of electrons transferred in a reaction, j_L is the limiting current density. Mass transfer usually plays a greater role at higher cell current density, especially when the fuel utilization is high or the electrode porosity is low. It manifests in the way that current does not increase (or increase as fast as before) when cell voltage decrease further towards short circuit condition, as shown in the high current region in the plot in Figure 2-4(a). In impedance spectroscopy, mass transfer contributions usually shows up in the lower frequency range. For more detailed information about electrochemical kinetics, please see Bard and Faulkner (2001).

2.1.4 Materials for Solid Oxide Fuel Cells

As stated in section 2.1.1, the state-of-the-art electrolyte material for SOFCs is yttria stabilized zirconia (YSZ), and the typical composition is $(ZrO_2)_{0.92}(Y_2O_3)_{0.08}$ or 8YSZ At high temperatures, 8YSZ has a cubic fluorite structure with zirconium and yttrium occupying the FCC sites and oxygen occupying the tetrahedral sites, as shown in Figure 2-5. The ionic conductivity for YSZ varies with dopant concentration and increases with increasing temperature. The maximum ionic conductivity is obtained with

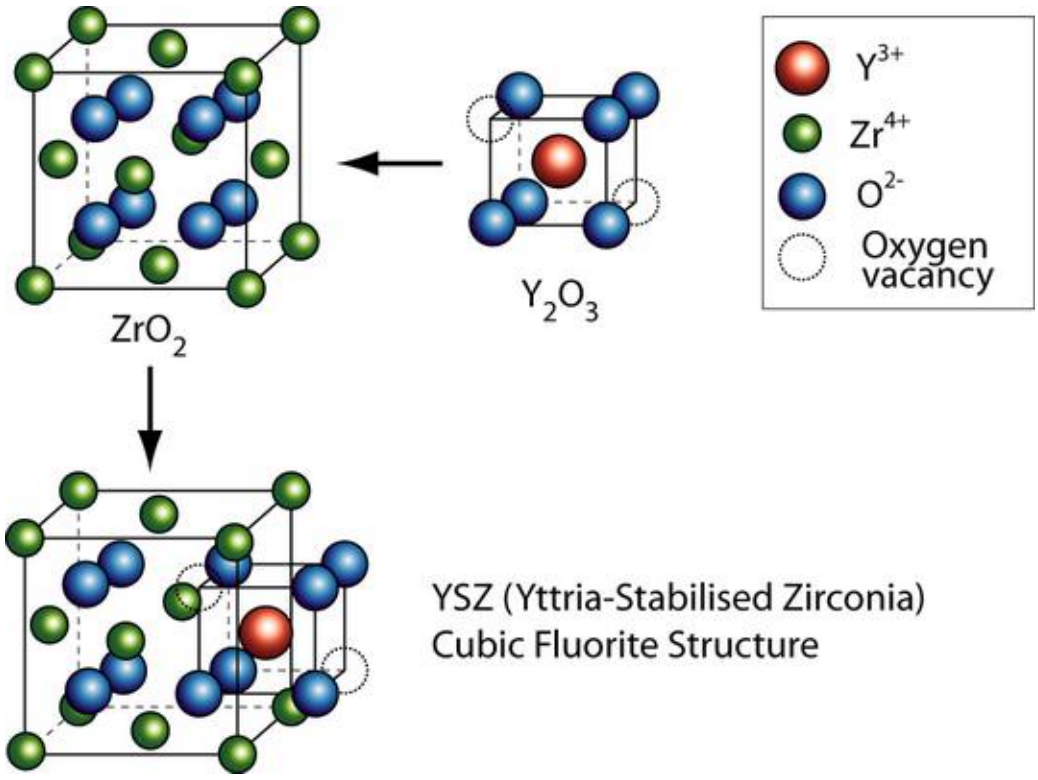

Figure 2-5 Crystal structure for cubic ZrO_2, Y_2O_3, and Y_2O_3-stabilized ZrO_2, from http://www.doitpoms.ac.uk/tlplib/fuel-cells/printall.php.

~8 mol% Y_2O_3 doping (Minh and Takahashi, 1995, p. 69; Ishihara et al., 2003, p. 90).

The active cathode material for solid oxide fuel cell is usually $La_{1-x}Sr_xMnO_3$ (LSM) or $La_{1-x}Sr_xCo_yFe_{1-y}O_3$ (LSCF). They have an ABO_3 perovskite structure, with La or Sr occupying the A-site and Mn (or Co and Fe for LSCF) occupying the B-site, as shown in Figure 2-6. The anode material for solid oxide fuel cell is usually a porous Ni-YSZ cermet with a Ni : YSZ volume ratio from ~40 : 60 to 60 : 40 and a porosity of above ~30%. Such cermets meet all of the requirements for the anode: the interconnecting Ni network acts as a good catalyst for the electrochemical oxidation of hydrogen and provides a excellent conduction path for electrons released from the electrochemical oxidation of hydrogen; the interconnecting YSZ network provides a path

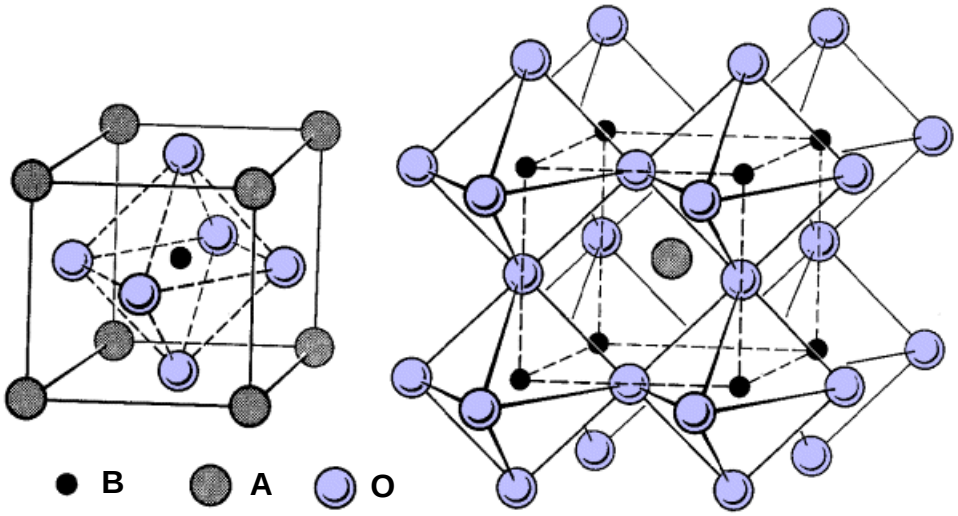

Figure 2-6 Structure for ABO_3 perovskite structured cathode materials for solid oxide fuel cells, from http://super.gsnu.ac.kr/lecture/inorganic/perovskite.html with modification.

for the oxygen ions from the electrolyte and also acts as a constraint for the growth and coalescence of nickel particles so that the fine nickel network could be maintained after long-term operation at elevated temperatures. Table 2-1 summarizes the typical physical properties such as melting point, density, electrical conductivity at 800 ^{o}C, and the coefficient of thermal expansion (CTE) for the 8YSZ electrolyte, $La_{0.85}Sr_{0.15}MnO_3$ cathode, and a cermet anode with a composition of 30 vol.%Ni-70vol.% YSZ.

In addition to cell materials listed above, some other materials are necessary to SOFCs from a system point of view. For example, when cells are placed together in series as in a solid oxide fuel cell stack, bipolar plates that connect the anode of one cell to the cathode of another have to be placed between two adjacent cells. These bipolar plates are also called interconnects. On one side of an interconnect plate, it is exposed to the fuel gas; while on the other side, it is exposed to the oxidant. The interconnect has to maintain long-term stability in bulk composition, structure, as well as electronic

Table 2-1 Physical properties of cell electrolyte, cathode, and anode materials for solid oxide fuel cells.

Property	$(ZrO_2)_{0.92}(Y_2O_3)_{0.08}$	$La_{0.85}Sr_{0.15}MnO_3$	30 vol.% Ni-70 vol.% YSZ
T_m (°C)	2680 [a]	1880 for $LaMnO_3$ [a]	1453 for Ni [a]
ρ (g/cm^3)	5.90 [a]	6.57 for $LaMnO_3$ [a]	6.87 [a]
σ_{800} (S/cm)	0.05 [b]	150 [a]	500 [a]
CTE (10^{-6} K^{-1})	10.8 [a]	11.2-12.2 [c]	12.5 [a]

Notes:

T_m	Melting point
ρ	Density
σ_{800}	Electrical conductivity at 800 °C
CTE	Coefficient of thermal expansion
[a]	Minh and Takahashi (1995), p. 75, 122, 129, and 149
[b]	Ishihara et al. (2003), p. 90
[c]	Yokokawa and Horita (2003), p. 125

conductivity electronic conductivity and gas impermeability, which raises extremely high requirements for the interconnect material. Initially, the interconnect materials were perovskite structured $LaCrO_3$–based oxides, for which the processing temperature was usually above ~1600 °C. Later, as the operating temperature of solid oxide fuel cell decreased due to the reduction of electrolyte thickness, the interconnect material are gradually replaced by iron and/or nickel based alloys (see Minh and Takahashi, 1995, p. 165; Anderson, and Tietz, 2003). Similarly, sealing materials are also critical to solid oxide fuel cell stacks, especially to those with a planar architecture. But like interconnects, they are of less importance to the study of the sulfur-anode interactions for solid oxide fuel cells and will be not discussed here.

2.1.5 Structure and Fabrication of Solid Oxide Fuel Cells

As illustrated in Figure 2-1, any single solid oxide fuel cell has three layers: the electrolyte and the anode and the cathode on each side of the electrolyte. For practical applications, solid oxide fuel cells have different structures, and each them has its own advantages and disadvantages. In addition, the fabrication methods differ considerably from one structure to another. These will be briefly summarized in this section.

2.1.5.1 Solid Oxide Fuel Cell Structure

- Planar versus tubular solid oxide fuel cells

Currently, there are two basic types of solid oxide fuel cells in terms of the entire cell structure: one is planar and the other is tubular. For planar SOFCs, each cell is made into a flat disk or a square or rectangular plate. The cells are put in series and separated and connected by the interconnect plates, as shown in Figure 2-7. For tubular SOFCs, usually the cathode is made into a long-tube with a porous wall. Outside the cathode tube are the electrolyte and then the anode. Cells are also connected through interconnects, as shown in Figure 2-8. Table 2-2 compares the planar and the tubular structures in terms of the ease of fabrication, cost, and cell power density, etc. Clearly, each structure has its own advantage and disadvantage. Earlier studies in SOFCs were focused on high temperature tubular SOFC systems, and from the late 1990s, accompanied with the reduction of electrolyte thickness in the planar SOFC technology, the development of planar SOFC system has drawn great interest due to its apparent advantages in power density and the ease of fabrication.

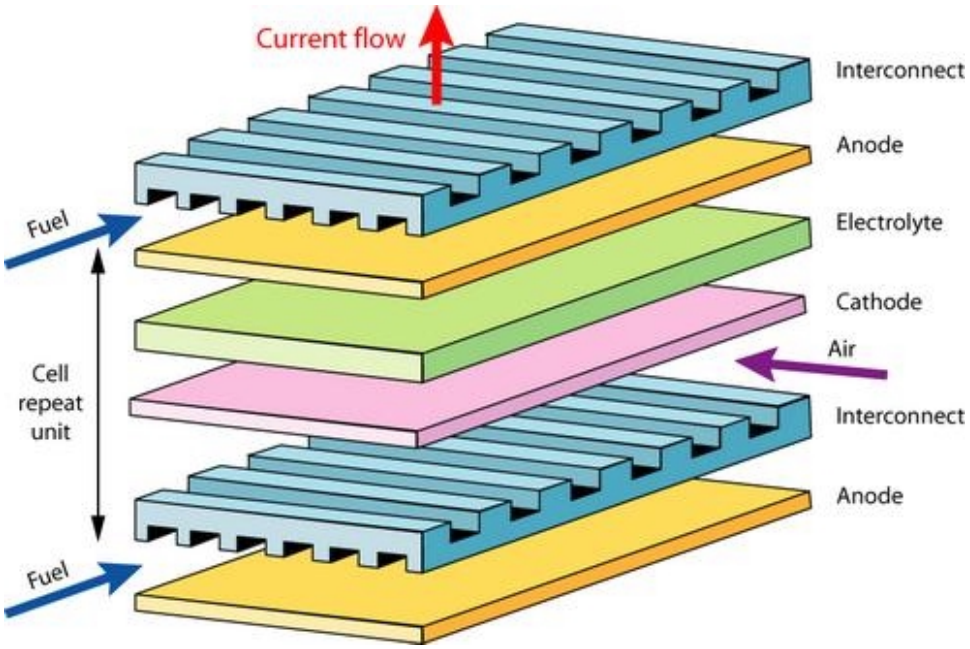

Figure 2-7 Schematic for a planar SOFC design, from http://www.doitpoms.ac.uk/tlplib/fuel-cells/high_temp_sofc.php

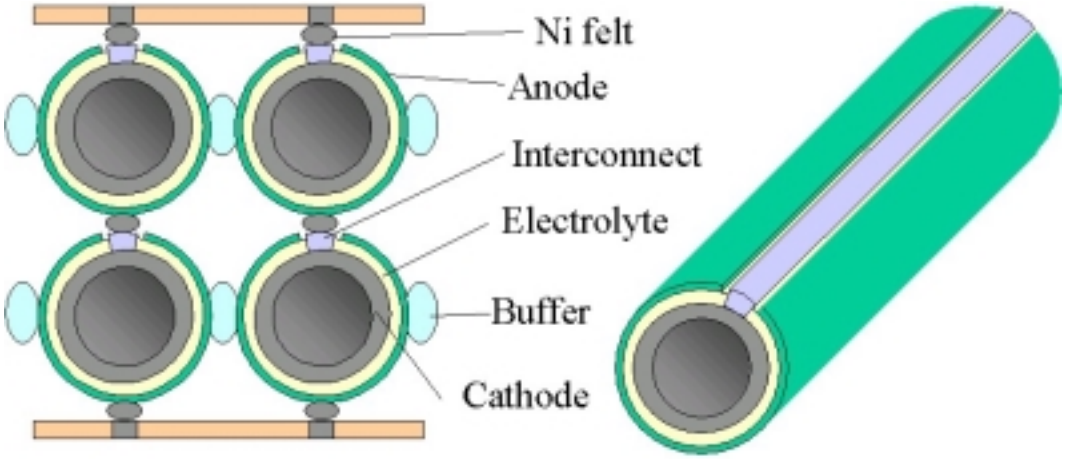

Figure 2-8 Schematic for a planar SOFC design, from Koyama at http://www.aki.che.tohoku.ac.jp/~koyama/html/research/SOFC.html.

Table 2-2 Comparison of planar and tubular structure for solid oxide fuel cells (Minh and Takahashi, 1995, p. 233; Kendall et al., 2003)

	Planar	Tubular
Power per unit area	Higher	Lower
Power per unit volume	Higher	Lower
Ease of fabrication	Easier	Difficult
Cost of fabrication	Higher	Lower
Ease of sealing	Difficult	Easy
Long-term stability	Fair	Excellent
Thermocycling stability	Fair	Good

- Electrolyte-supported versus electrode-supported solid oxide fuel cells

In terms of the relative thickness for each cell component layer (i.e., electrode versus electrolyte), there are electrolyte-supported SOFCs and electrode-supported SOFCs, as illustrated in Figure 2-9. In terms of processing technique, electrode-supported cells are more demanding compared with electrolyte-supported cells. However, electrode-supported structures are now more widely applied. For example, for the tubular structure, Siemens adopts the cathode-supported structure, and for the planar structure, most industrial teams adopt the anode-supported structure. The main advantage of the electrode-supported structure is that it provides thinner electrolyte and

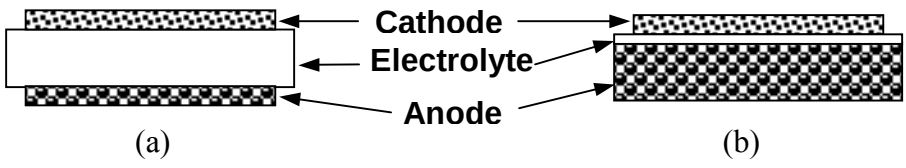

Figure 2-9 Schematic for the cross-section of (a) an electrolyte-supported SOFC and (b) an anode supported SOFC.

thus lower electrolyte ohmic resistance, which enables the operation of solid oxide fuel cells at lower temperatures, especially for the anode-supported planar structure (Minh and Takahashi, 1995, p. 233; Kendall et al., 2003).

2.1.5.2 Solid Oxide Fuel Cell Fabrication

The fabrication process for solid oxide fuel cells depends on the cell structure. For planar SOFCs, cells are made from traditional ceramic processing techniques including tape casting, screen printing, and heat treatments. For the example of a planar SOFC single cell with the anode-supported structure and the LSM cathode, the thick anode layer containing NiO, YSZ, and pore formers was tape casted. Then the electrolyte layer was casted over the anode tape, and the anode/electrolyte bilayer was co-sintered in air at temperatures up to 1400 ^{o}C. After that, a cathode paste containing LSM (and sometimes YSZ also) was screen printed onto the electrolyte side of the sintered bilayer, and the entire cell was heat treated again at temperatures up to 1250 ^{o}C to fire the cathode. For cells with the LSCF cathode, a layer of gadolinia doped ceria (GDC) was applied onto the YSZ electrolyte surface and sintered at 1300 ^{o}C before the LSCF cathode was screen printed and heat treated at temperatures up to 1100 ^{o}C.

For tubular SOFCs, the processing technique is more complicated. In Siemens, the cathode support tube was first made from traditional ceramic processing. After that, the electrolyte layer and the NiO-YSZ anode layer were made by advanced techniques such as electrochemical deposition (Minh and Takahashi, 1995, p. 233).

2.2 Sulfur Poisoning of Solid Oxide Fuel Cells

2.2.1 Hydrocarbon Fuels and Sulfur Contaminants

One of the unique advantages of SOFCs over other types of fuel cells is the fuel flexibility. SOFCs have the potential of direct utilization of hydrocarbon fuels. Compared with pure hydrogen, hydrocarbon fuels have higher energy density and are readily available and easier to transport and store based on current infrastructure. To use them, hydrocarbon fuels are reformed externally or internally into CO and H_2 on catalysts such as nickel (Minh and Takahashi, 1995, p. 37). However, one problem with all hydrocarbon fuels is that they all contain contaminants such as sulfur compounds. For example, sulfur concentration in pipeline natural gas is usually several ppm by volume (Dicks, 1996) while sulfur concentration in liquid fuels such as gasoline, jet propellant (*i.e.*, kerosene) and diesel could be as high as ~100-1000 ppm by volume (Minh et al., 1999). The sulfur compounds would transform into gaseous hydrogen sulfide (H_2S) in the reforming process and readily poison the nickel-based anode for SOFCs, leading to dramatic reduction in cell performance and operational life.

2.2.2 Previous Investigations on Sulfur Poisoning of Ni-based Anodes

This section will summarize previous studies on sulfur poisoning of Ni-based anodes under SOFC operating conditions.

- Feduska and Isenberg (1983)

The earliest report on sulfur poisoning of SOFC anodes was by Feduska and Isenberg who studied the effect of H_2S on the performance of a 7-cell stack at 1000 ^{o}C. As shown in Figure 2-10, the SOFC stack was operated for 800 h on a gas mixture of a

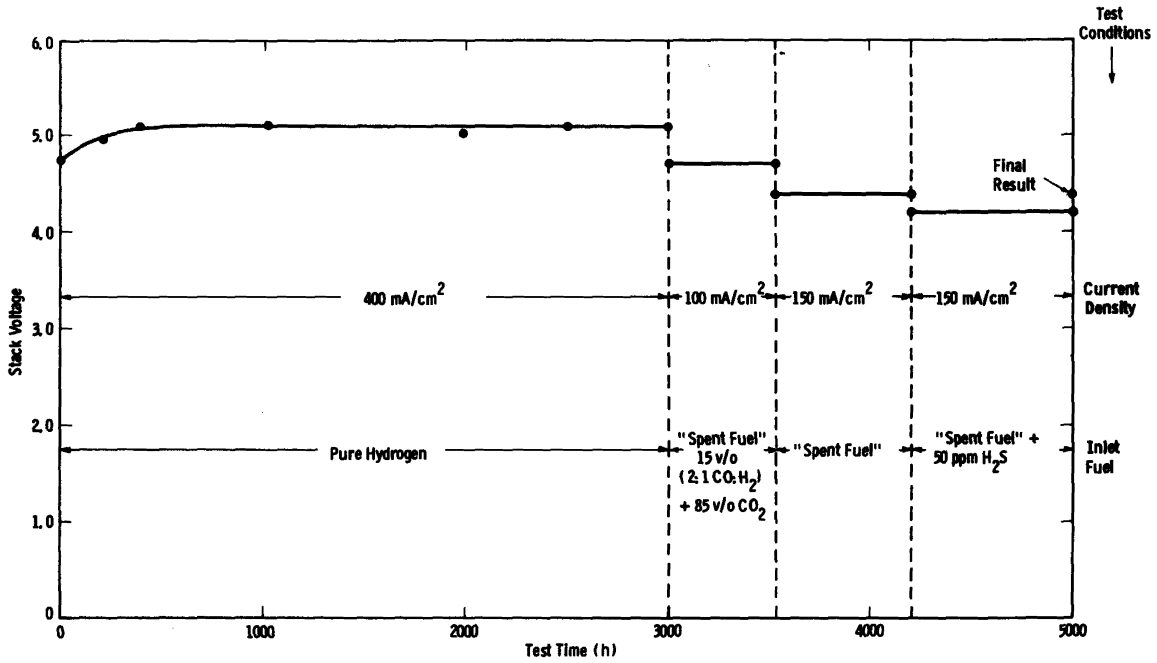

Figure 2-10 Voltage versus time for a 7-cell SOFC stack tested at 1000 ^{o}C under constant current condition in different fuels without and with 50 ppm H_2S, from Feduska and Isenberg (1983).

5%H_2/10% CO/85% CO_2 containing 50 ppm H_2S at a constant current density of 150 mA/cm^2. The authors claimed that the only effect caused by the sulfur impurity was an immediate loss of ~5% in operating cell voltage, and the cell voltage recovered to the original level when the H_2S was removed from the fuel stream. From Figure 2-10, it appeared that both the sulfur poisoning and recovery processes reached steady state instantaneously when 50 ppm H_2S was introduced and removed from the fuel stream. The authors also predicted the critical sulfur concentration, above which sulfide would start to form at different cell voltage, and used those values as the maximum sulfur concentration that can be tolerated by the Ni-YSZ anode.

- Singhal et al. (1986)

Singhal et al. (1986) found that at 1000 ^{o}C with a current density 250 mA/cm^2, after 10 ppm H_2S was introduced into the fuel stream, the performance for their SOFC dropped first quickly from ~0.61 V to 0.54 V almost instantaneously and then dropped slowly from 0.54 V to 0.52 V over a period of ~80 h with the speed of degradation decreased as time went by, as shown in Figure 2-11. The cell performance fully recovered when the 10 ppm H_2S was removed from the fuel. Singhal et al. also sampled the effect of H_2S concentration, temperature, and cell current density on the observed cell voltage drop under constant current condition and the results are summarized in Table 2-3. Their results seemed to indicate that the relative drop in cell power output (or voltage in this case of constant current condition) became more severe (on a percentage base)

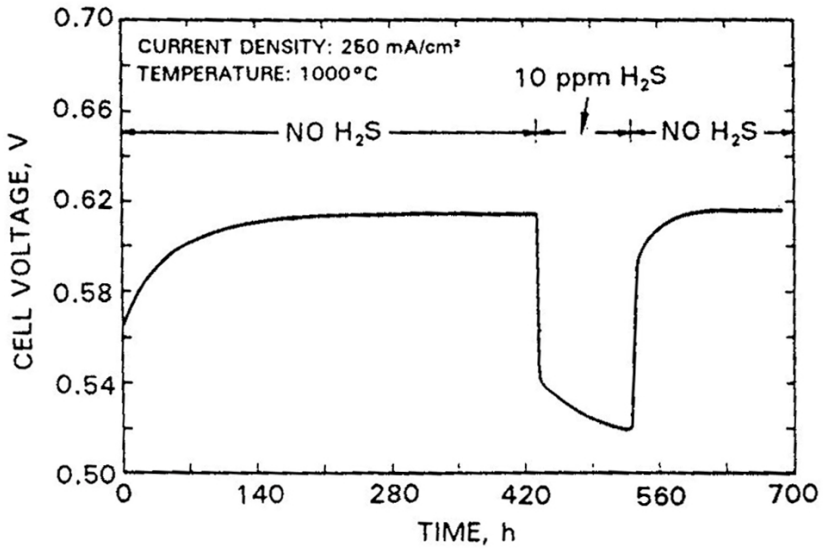

Figure 2-11 Change of cell voltage versus time for solid oxide fuel cells operated at 1000 ^{o}C when 10 ppm H_2S was introduced and later removed from the fuel stream, from Singhal et al. (1986).

Table 2-3 Cell voltage drop for an SOFC when the fuel contained different concentration of H_2S, from Singhal et al. (1986).

Temperature (^oC)	Current density (mA/cm^2)	Voltage drop in 100 h (%)	
		2 ppm H_2S	10 ppm H_2S
900	160	9.0	>22.0
1000	160	2.0	10.3
1000	250	–	15.6

with (i) increasing H_2S concentration, (ii) decreasing temperature, and (iii) increasing current density.

Similar studies on SOFC stacks at high temperatures (i.e., 900 ^oC and above) were carried out later by Stolten et al. (1997), Iritani et al. (2001), and Batawi et al. (2001). Stolten et al. (1997) reported a ~3% drop cause by 10 ppm H_2S at 950 ^oC under current density of 150 mA/cm^2 for a 40-cell stack. The degradation was fully reversible when H_2S concentration was smaller than 10 ppm. Iritani et al. (2001) reported a gradual drop (over 170 h) up to 4.3 % caused by 1 ppm H_2S under a constant current density of 200 mA/cm^2 at 900 ^oC for a 10 kW SOFC module. Only partial recovery (back to 98.5% of the original level) in 240 h was observed. Batawi et al. (2001) reported that a 5-cell stack maintained a stable power output of 130 mW/cm^2 for more than 400 h in fuels containing 100 ppm H_2S at 930 ^oC.

- Dees et al. (1989a and 1989b)

Dees et al. were the first to observe that the sulfur poisoning was due to the large increase in anode interfacial polarization resistance (R_p) instead of the change in cell ohmic resistance. As shown in Figure 2-12, Dees et al. found that the total R_p for an Ni-YSZ cermet anode/electrolyte/anode symmetrical cell in 97%H_2/3%H_2 increased from

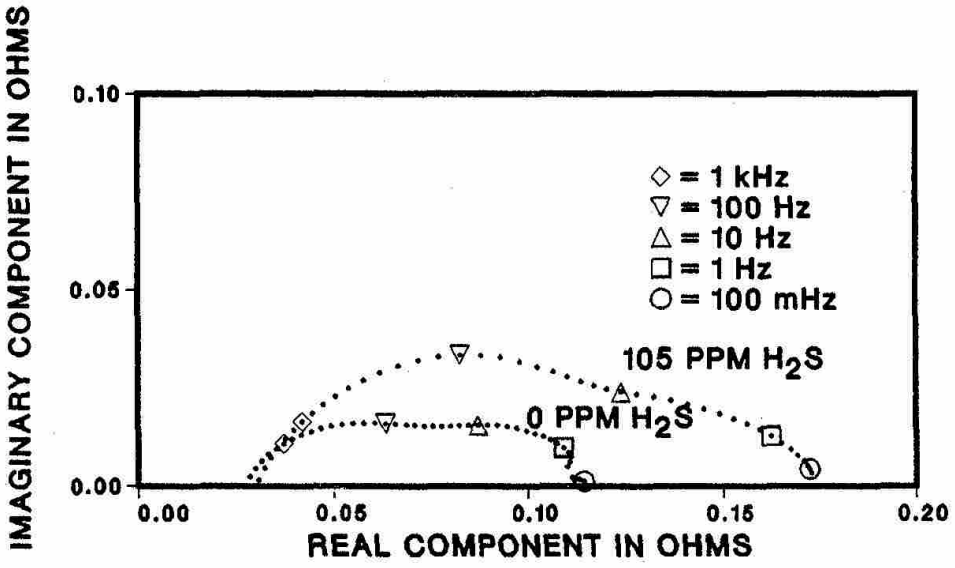

Figure 2-12 Impedance spectra for the anode/electrolyte symmetrical cell in a fuel of 97% H_2/3 % H_2O with and without 105 ppm H_2S at 1000 ^oC, from Dees et al. (1987a).

0.27 Ω cm^2 to 0.45 Ω cm^2 (~67 % increase) when 100 ppm H_2S was introduced into the fuel flow at 1000 ^oC while the bulk resistance (R_b) remained unchanged. They noted that the chief change in R_p was in the frequency range of ~1-1000 Hz. The authors observed that the post-test electrolyte was darkened and attributed that to "sulfur incorporation or oxygen depletion of the electrolyte." They also claimed "sulfur being incorporated into the electrolyte could explain why the sulfur effects were not reversible." However, neither of these arguments was supported by their experiments. It should also be noted that most researchers that followed tended to cite that "Dees et al. found the 100 ppm H_2S caused irreversible degradation to the anode", even though the authors never made this remark in their papers.

Similar observation was also made by Geyer et al. (1997) on anode symmetrical cells, who showed that the total anode polarization resistance increased 33% when 5 ppm

H_2S was introduced into the fuel of 97%H_2/3%H_2 at 950 ^oC. They also noted that the majority of the increase in anode polarization resistance occurred at the high frequency (~1 kHz) arc in the impedance spectrum, which was believed to relate to "charge transfer reaction and the ionic resistance within the cermet," while the low frequency arc of the impedance spectrum, believed to be related with mass transfer process, was not influenced by H_2S.

- Primdahl and Mogensen (1999)

Primdahl and Mogensen reported the poisoning effect (a 60% increase in anode polarization resistance) by 35 ppm H_2S was invariant to anode structure (porous Ni anode vs. Ni-YSZ cermet anode), operating temperature (850 vs. 1000 ^oC), and anodic current density (0 vs. 100 mA/cm^2), as shown in Figure 2-13, and the poisoning was fully reversible. Because the Ni-YSZ cermet anode showed the same poisoning behavior as the pure Ni anode, they proposed that "the Ni-surface is either the location of rate limiting reaction sites, or that it provides a species to the rate-limiting reaction" and the

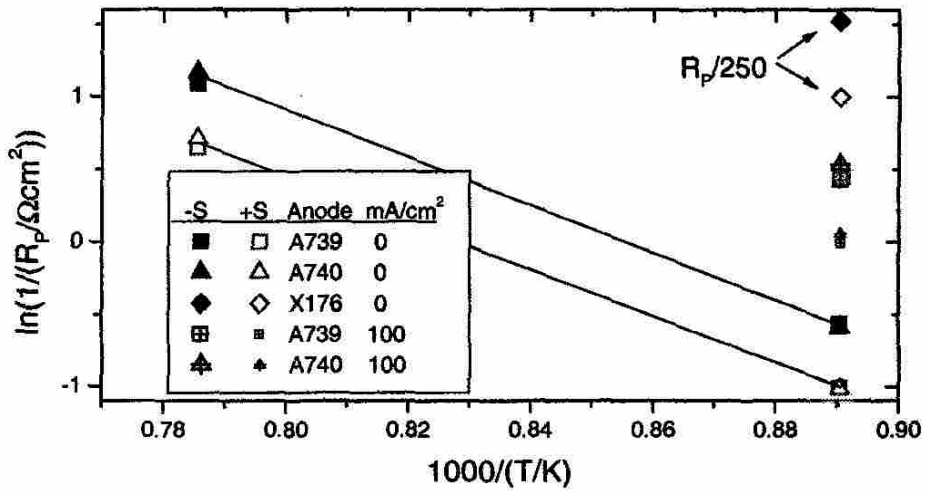

Figure 2-13 Plot of $\ln(1/R_p)$ versus inverse temperature (1/T) for different anodes under both open circuit and a constant current density of 100 mA/cm^2, from Primdahl and Mogensen (1999).

sulfur poisoning of Ni anode was because "adsorbed H_2S blocks one type or two or more types of adsorption sites on Ni, which take part in the H_2/H_2O process."

- Matsuzaki and Yasuda (2000, 2001)

Matsuzaki and Yasuda were the first to conduct a systematic study on the poisoning effect of H_2S on Ni-YSZ anode using impedance spectroscopy (IS) (see Table 2-4). Their major findings are summarized as follows. First, the critical H_2S concentration, above which the sulfur poisoning effect became significant, decreased rapidly from 2 ppm to 0.05 ppm as cell temperature decreased from 1000 ^oC to 750 ^oC. Second, the degradation became more severe (in terms of the relative increase in anode interfacial resistance) when H_2S increased up to certain concentration. Third, both the rates of poisoning and recovery increased with increasing temperature. Fourth, at lower temperatures, the recovery was much slower than poisoning, while at higher temperatures, the recovery was almost as fast as the poisoning. Fifth, the time needed for

Table 2-4 The extent and the rate of degradation caused by sulfur poisoning for Ni-YSZ cermet anode. The data are taken from Matsuzaki and Yasuda (2000 and 2001).

Temperature (^oC)	[H_2S] (ppm)	Extent of degradation (%)	Time for poisoning (10^3 sec)	Time for recovery (10^3 sec)
750	0.05	30	12	360
	0.7	115	NA	NA
900	0.5	37	NA	NA
	1	60	9	90
	8	116	NA	NA
1000	2	15	5	NA
	15	45	4	4

the influence of the sulfur impurity to saturate was independent of H_2S concentration when it was in the range of 2-15 ppm at 1000 ^oC. Finally, the degree of sulfur poisoning was not dependent on the partial pressure of S_2 but on the total sulfur content. However, it is noted that in their study, the condition was not the same as in real fuel cell testing because (i) the composition for their anode was 84 vol. % Ni - 16 vol.% YSZ, which was quite different from that of a normal anode (i.e., ~40-60 vol.% Ni); (ii) the configuration is not a full cell; (iii) their chamber for testing is quite large, which would cause delay in the response of the anode to changes in the fuel, especially when H_2S was removed. In addition, to determine the effect of partial pressure of S_2, the author changed H_2O concentration in the hope that H_2 concentration will be changed, which was not expected to be effective as the H_2 partial pressure would be fixed by fuel composition.

2.2.3 Very Recent Investigations on Sulfur Poisoning of Solid Oxide Fuel Cells

In addition to pervious studies, there have also been studies that were carried out at the same time as this study.

- Sasaki et al. (2005 and 2006)

Sasaki et al. studied the sulfur poisoning behavior for electrolyte-supported cells at high temperature and reported the cell voltage (i = 200 mA/cm^2, T= 1000 ^oC) degraded by 6.3%, 15.2% and 22.8% when H_2S concentration was 1 ppm, 3 ppm and 5 ppm, respectively. The extent of degradation caused by 5 ppm H_2S was 20%, 27% and 81% at 1000 ^oC, 900 ^oC and 850 ^oC, respectively, as shown in Figure 2-14. The degradation above ~900 ^oC was reversible when the exposure time was on the order of an hour yet the degradation below that was fatal for Ni-YSZ anode. Based on Ni-S-O phase diagram, the

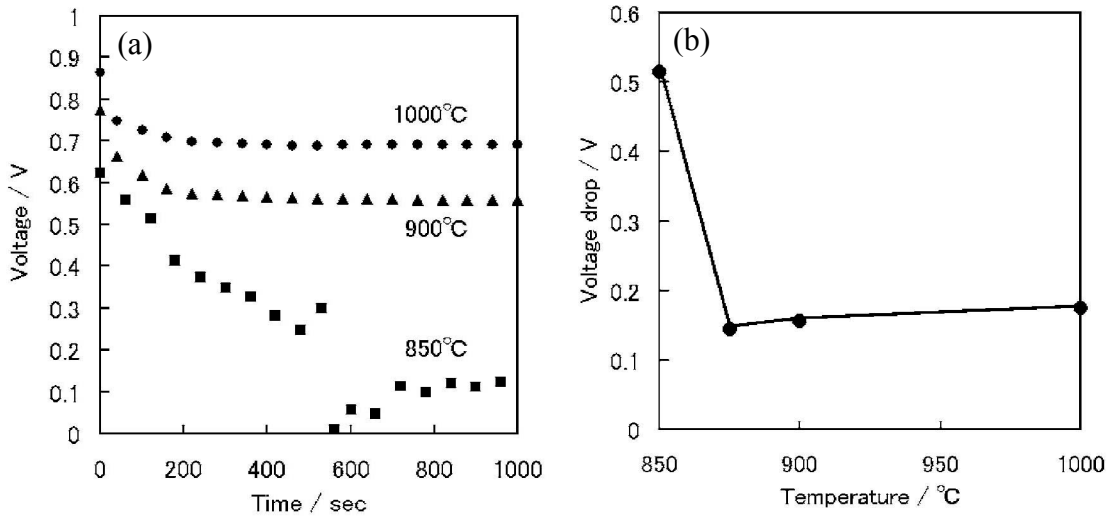

Figure 2-14 Plots of (a) change of cell voltage versus time for cells operated at 200 mA/cm^2 when 5 ppm H_2S was introduced into the H_2 fuel, and (b) change of cell voltage drop due to sulfur poisoning versus temperature, from Sasaki et al. (2006).

authors concluded that the poisoning caused by several ppm H_2S could *not* be explained by nickel sulfide formation. Instead, they proposed that the initial small voltage drop was caused by the dissociative adsorption of sulfur species around three-phase boundaries, leading to increase in anodic polarization. The failure of the cell (very large voltage drop) under higher H_2S concentration or lower temperature was expected to arise from the agglomeration of Ni particles, which was aggravated by the presence of sulfur.

- Xia and Birss (2005)

Xia and Birss studied electrolyte-supported cells and found that, upon introduction of 10 ppm H_2S at 800 ^oC, the anode polarization resistance under open circuit condition remained almost unchanged for the first two hours and then increased from ~1.6 Ω cm^2 to ~8.2 Ω cm^2 (a 400% increase) in the next 16 h. By analyzing the impedance spectra using equivalent circuit method, the authors inferred that charge transfer process was most affected by the H_2S poison. Under galvanostatic square wave

condition (300 sec at 100 mA/cm^2 then 100 sec at 400 mA/cm^2), the cell operating voltage (referred to by the author as "anode overpotential") remained stable for the first 8 cycles (3200 sec) and then decreased gradually with time. Their data also indicated that the relative cell power output drop caused by 10 ppm H_2S increased from 19% to 56% when the current density increased from 130 to 400 mA/cm^2 at 800 ^oC. The degradation appeared to be partial recoverable. Xia and Birss proposed that (i) the Ni-YSZ triple phase boundary (TPB) was partly (~80-90%) blocked by sulfur species in the poisoning process. (ii) Some Ni sites might transform to products like submonolayer Ni_3S_2, which were not blocked by sulfur, and continued to catalyze the electrochemical oxidation of H_2 without a change in reaction mechanism. (iii) That the poisoning was faster under constant current condition was attributed to either the high local current density or the "high overpotential" (lower cell operating voltage). The former was believed to either enhance the sulfur species adsorption or induce the formation of a thin layer of Ni_3S_2, while the latter could result in NiO formation, which in turn, contribute to anode deactivation. (iv) The recoverable part of the degradation was due to the adsorption of sulfur species on the surface, which can be displaced when H_2S was discontinued. The non-recoverable degradation was due to the formation of a thin (submonolayer to several monolayer) Ni-S compound (e.g., Ni_3S_2) at some locations within the anode.

- Waldbillig et al. (2005)

Waldbillig et al. examined the sulfur poisoning behavior for anode-supported cells at 750 ^oC and found (i) the extent of power output degradation increased with increasing H_2S concentration in the range from 0.1 to 5 ppm; (ii) the extent of degradation increased with decreasing temperature. One thing that was confusing in their

study was, as shown in Figure 2-15, although the authors observed that relative cell power output (or voltage) in their case was greater when cell current density was higher, the relative increase in cell resistance was lower when the cell current density was higher. In addition, the rate of recovery was observed to be faster at higher current density, which was not explained and hard to understand. In addition, the authors claimed that they could not identify any sulfur using energy dispersive X-ray spectroscopy (EDX) in either scanning electron microscopy (SEM) or transmission electron microscopy (TEM).

- Noponen et al. (2006)

Noponen et al. studied the effect of trace amount of organic sulfur compounds on three types of anode-supported cells. The cell performance fluctuate significantly in the presence of only ~6-10 ppm tetrahydro-thiophene (THT), which was attributed to the poisoning of the reforming catalyst, leading to uneven temperature distribution in the cell.

- Trembly et al. (2006)

Trembly et al. studied the sulfur poisoning on electrolyte-supported cells with Ni and GDC cermet anode. Their results showed that the cell voltage dropped instantaneously ~10% from ~0.74 V to 0.68 V when 207 ppm H_2S was introduced into the fuel mixture of 34.8% H_2/35.7 % N_2/40% CO. After that, the cell performance degraded from 0.68 V to 0.65 V for another ~450 h when the degradation seemed to saturate. They then examined the post-test anode using SEM and EDX, and identified not only morphology change but also a significant amount of sulfur, as shown in Figure 2-15. Using X-ray photoelectron spectroscopy (XPS), the authors determined that there was a 5-7% loss in the anode Ni content and a 1-2% gain in sulfur on the anode surface while Ce and Gd remained unchanged, as shown in Figure 2-16. Based on these

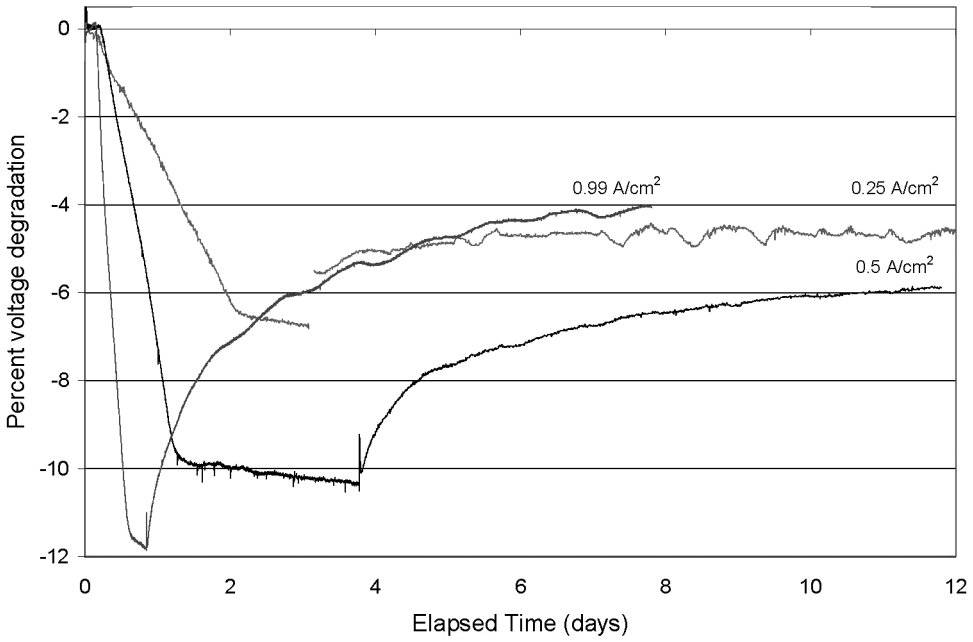

(a)

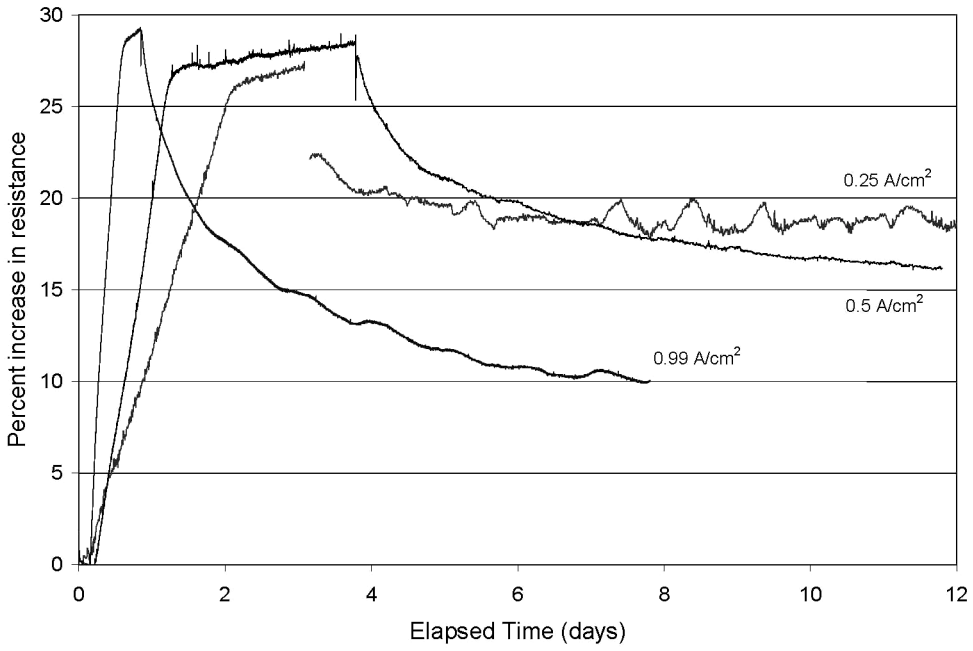

(b)

Figure 2-15 Plots of (a) change of cell voltage versus time and (b) calculated cell resistance versus time for anode-supported cells operated at 750 $_{o}$C with different current density when 1 ppm H_2S was introduced into the hydrogen fuel, from Waldbillig et al. (2005).

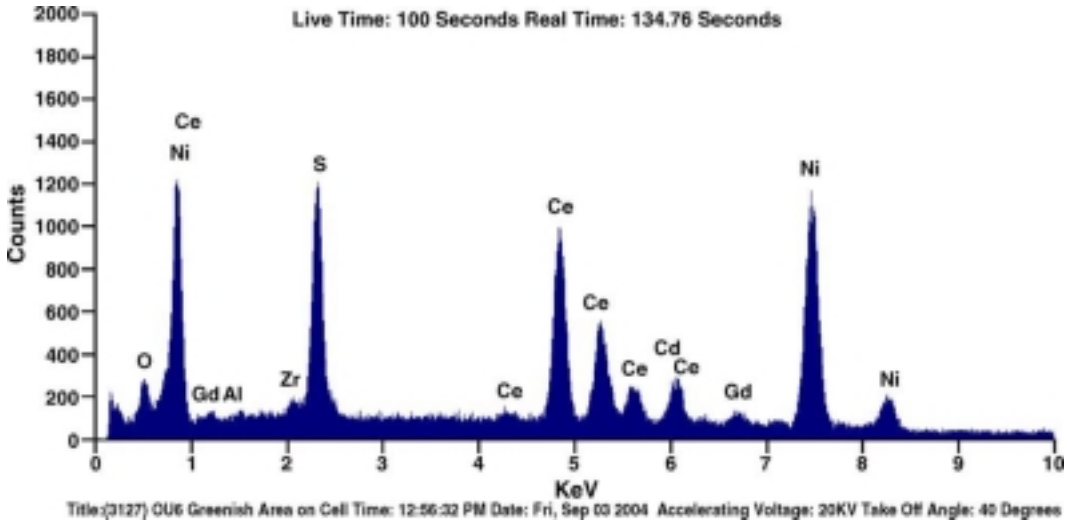

Figure 2-16 EDX pattern of the Ni-GDC anode after 570 h of operation at 850 ^{o}C in a fuel of 207 ppm H_2S/34.8% H_2/35.7 % N_2/40% CO, from Trembly et al. (2006).

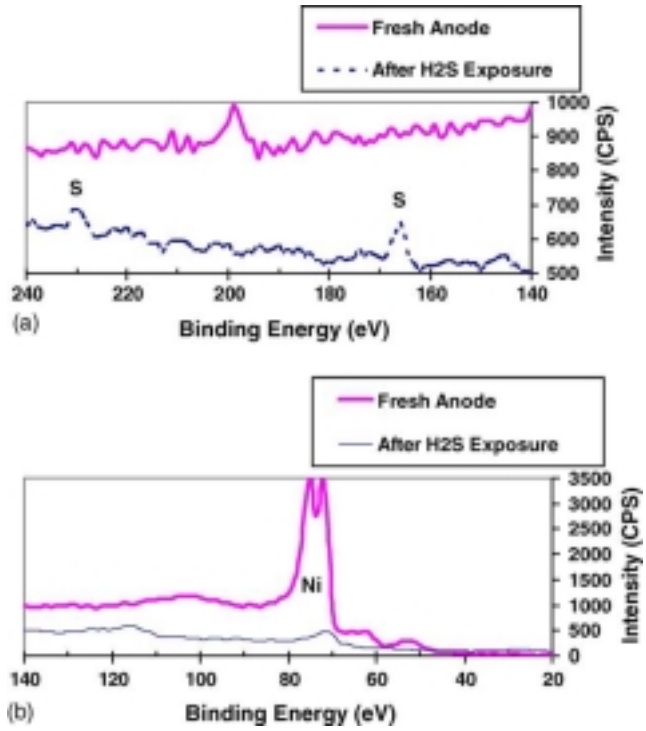

Figure 2-17 XPS analysis for the Ni-GDC anode before and after testing in a fuel of 207 ppm H_2S/34.8% H_2/35.7 % N_2/40% CO at 850 ^{o}C for 570 h, from Trembly et al. (2006).

observations, the authors claimed that the mechanism for degraded cell performance in H_2S-containing fuel is the possible formation of sulfur compounds such as NiS, and the authors claimed that Ni-GDC cermet is a good candidate anode for SOFCs operating on syngas containing H_2S based on their observation due to their claim that GDC will enhance performance and did not show signs of reaction with H_2S.

2.3 Sulfur-Tolerant Anodes for Solid Oxide Fuel Cells

Because of the severe poisoning effect of small amount of sulfur contaminants, one major requirement for current SOFCs is to reduce the sulfur concentration to below ~0.1 ppm (Minh and Takahashi, 1995, p. 38; Dicks, 1996). For large-scale fuel processing, hydrodesulfurization (HDS) is currently the preferred method to remove sulfur contaminants. The fuel, natural gas for example, is mixed with a small quantity of hydrogen and passed over a hot bed of catalyst (usually cobalt and molybdenum oxides supported on alumina) (Dicks, 1996). Organic sulfur compounds such as diethyl sulfide ($(C_2H_5)_2S$) are converted to H_2S and hydrocarbon:

$$(C_2H_5)_2S + 2H_2 \rightarrow 2C_2H_6 + H_2S \qquad (2\text{-}29)$$

H_2S is then removed by reaction on a ZnO catalyst:

$$H_2S + ZnO \rightarrow ZnS + H_2O \qquad (2\text{-}30)$$

The removal of sulfur adds complexity and cost to the already complex SOFC systems. It also decrease the energy efficiency of SOFCs since the temperature for most desulfurization process is between 350 and 400 ^oC (Dicks, 1996) while both gasification and SOFCs are operated at higher temperatures (~700-1000 ^oC), as a result, the sulfur removal process may also decrease the system efficiency since the hot gas from the

gasification process (if gasoline or coal is used as fuel) must be cooled for efficient desulfurization and then reheated to the SOFC temperature (Mukundan et al., 2004).

On the other hand, the development of new sulfur-resistant anode materials for SOFCs has attracted much attention in recent years. Such studies are important because (i) they may lead to the elimination of a separate desulfurization unit and thus reduce the system complexity and cost, and (ii) the reduction of fuel cell operating temperature has raised the requirement for desulfurization. For example, as shown by the study of Matsuzaki and Yasuda (2000, 2001), at 1000 ^{o}C, the anode can operate in fuels with H_2S concentration up to 1 ppm without observable degradation. However, when the temperature dropped to 750 ^{o}C, only 0.05 ppm of H_2S will readily poison the Ni-based anode, and ultra-deep desulfurization must be carried out to clean the fuel.

In this section, previous studies on sulfur-tolerant anode materials will be briefly summarized. The majority of the works were focused on new anode materials that could utilize fuels containing high concentrations (~5%-100%) of H_2S; a few were devoted to study of anode that can tolerate H_2S with concentration in the ppm range. In most of these studies, the electrolyte was ~200-400 μm thick YSZ pellet due to its excellent stability and the cathode materials were Pt or LSM. Pt (or other noble metal) layer were usually applied to the anode as current collector due to the insufficient electrical conductivity of those materials.

- Pujare et al. (1987)

Pujare et al. first studied an SOFC that utilized almost pure (99.5%) H_2S as the fuel. The anode was a thiospinel $CuFe_2S_4$. The measured peak power density was 2.5 mW/cm^2 at 900 ^{o}C. Later, Pujare et al. (1989) studied several other sulfide materials

as candidate anodes. They found that the relative activity (based on exchange current density) was $NiFe_2S_4 > WS_2 > CuCo_2S_4 > CuFe_2S_4 \approx NiCo_2S_4 > CuNi_2S_4$. However, the obtained power density for all cells studied was too low (smaller than 5 mW/cm^2 at 800-900 ^oC) for practical use.

- Yates and Winnick (1999)

Yates and Winnick (1999) studied CoS_2, WS_2 and $LiCoO_2$ as anode materials for SOFC that runs on 25% H_2S. The cell with CoS_2 anode gave a peak power density of 20 mW/cm^2 at 800 ^oC, but the stability was poor due to the phase change from CoS_2 to $CoS_{1.035}$. The cell with WS_2 anode gave a peak power density of ~16 mW/cm^2 at 820 ^oC and demonstrated stability for ~18 h. For the cell with anode based on $LiCoO_2$, the peak power density was 90 mW/cm^2 (412 mW/cm^2 for the cell with 40 μm thick electrolyte). However, the stability was of a concern for all those materials. In addition, the author mentioned the data were after correction of bulk resistance, but no comparison of the data before and after the correction was made.

- Wang et al. (2001)

Wang et al. (2001) investigated the conductivity and stability for several perovskite materials (i.e., $La_{0.9}Sr_{0.1}Ga_{0.8}Cr_{0.2}O_3$, $LaCr_{0.9}Ti_{0.1}O_3$, $Y_{0.9}Ca_{0.1}FeO_3$, and $SrCo_{0.8}Fe_{0.2}O_3$) as electrodes in H_2S-containing fuels. However none of them appear promising due to the low electrical conductivity (all below 0.1 S cm^{-1}) and their high reactivity with H_2S.

- Kim et al. (2001)

Kim et al. (2001) reported that a cell with a copper-ceria (CeO_2) cermet anode maintained a current of 140 mA/cm^2 at 700 ^oC under constant voltage of 0.5 V for ~100 h

in 5 % n-decane containing 100 ppm H_2S. The cell current dropped ~50 % when 5000 ppm H_2S was introduced into the fuel of 50% n-decane at 700 ^oC. He et al. (2005) of the same group reported that a similar cell maintained a stable power density of ~300 mW/cm^2 under constant voltage of 0.65 V for 300 h in 90%H_2/10%H_2O with 50-450 ppm H_2S at 800 ^oC. The performance only started to drop 13% when the H_2S concentration was increased to 600 ppm; it dropped 73 % when the H_2S concentration was further increased to 900 ppm. The authors believed that it was the ceria that played the catalytic role in the Cu-ceria cermet anode. Analysis of the Ce-O-S phase diagram indicated that ceria would transform to Ce_2O_2S when H_2S concentration was above ~450 ppm, which was exactly the observed threshold concentration for H_2S.

- Chuang and co-workers

A group of Canadian researchers led by Chuang (Liu et al., 2001; He et al., 2002; Liu et al., 2003; Wei et al., 2004) also investigated H_2S-O_2 SOFC. They started from Pt anode, and observed a maximum power density of 15 mW/cm^2 at 800 ^oC. The Pt anode detached from the electrolyte over time in H_2S stream under polarization conditions, which was believed to be caused by the reversible formation of PtS (Liu et al., 2001). He et al. (2002) introduced a TiO_2 intermediate layer between the Pt anode and the YSZ electrolyte. The stability was increased but the performance was only 2 mW/cm^2. Later, Liu et al. (2003) studied MoS_2, Fe-Mo sulfide, Co-Mo sulfide and Ni-Mo sulfide. At 800 ^oC, the highest power density (110 mW/cm^2) was observed for a Co-Mo sulfide/Ag composite anode. Wei et al. (2004) reported a power density (at 850 ^oC) as high as 220 mW/cm^2 for a cell with a 90%Ni-Mo sulfide/5%Ag/5%YSZ composite anode. However, the long-term stability for these cells with Ag in anode was not demonstrated. The

problem of silver migration and thermal, chemical stability of the sulfides were not discussed in their studies. The reported power density data were also questionable because the authors did not specify the details for the measurement of I-V curve under so-called "IR compensated mode."

- Recent studies

Very recent studies on sulfur-tolerant anode materials include those on complex oxides. For example, Mukundan et al. (2004) studied the sulfur tolerance of $La_{0.8}Sr_{0.2}Cr_{0.8}Mn_{0.2}O_3$ and $La_{0.4}Sr_{0.6}TiO_3$ as anode materials for SOFC. For $La_{0.8}Sr_{0.2}Cr_{0.8}Mn_{0.2}O_3$ anode, the additional anode overpotential (i = 300 mA/cm^2) caused by 100 ppm and 1000 ppm H_2S was only 0.03 V and ~0.15 V, respectively. For $La_{0.4}Sr_{0.6}TiO_3$, the extra anode overpotential caused by 1000 ppm H_2S was negligible. In addition, for the cell with $La_{0.4}Sr_{0.6}TiO_3$ anode, the peak power density in fuels with 5000 ppm H_2S (200 mW/cm^2) was even higher than that in similar fuel but without H_2S (175 mW/cm^2). In contrast, Marina et al. (2004) who studied sulfur tolerance for a $La_{0.35}Sr_{0.65}TiO_3/Ce_{0.5}La_{0.5}O_{1.75}$ mixture anode found that, when ~1000 ppm H_2S was introduced into the fuel at 850 ^oC, the cell current dropped ~60% (from 360 mA/cm^2 to 140 mA/cm^2) and ~30 % (from 660 mA/cm^2 to 560 mA/cm^2) when the cell voltage was 0.7V and 0.3 V, respectively. The current dropped ~9% (from 450 mA/cm^2 to 400 mA/cm^2) when 280 ppm H_2S was introduced into the fuel. The stability of the cell in H_2S was acceptable and the degradation caused by H_2S up to ~1000 ppm was reversible.

In our group, Aguilar et al. (2004a and 2004b) reported SOFCs with $La_{0.7}Sr_{0.3}VO_3$ anode, which gave a peak power density (T = 950 ^oC) as high as ~105 mW/cm^2 and 80 mW/cm^2 in humidified 5%H_2S/95%H_2 and 5%H_2S/95%N_2, respectively. The cell

current increased from ~80 mA/cm^2 to ~220 mA/cm^2 (a 175% increase) when 5% H_2S was introduced to humidified H_2 (U = 0.44 V, T = 1000 ^oC. The reason for this enhanced behavior in H_2S was attributed to the removal of insulation phase ($Sr_3V_2O_8$) at the anode/electrolyte interface and the formation of more active sulfide phases (SrS) even though no such phases were identified in the experiments.

Kurokawa et al. (2007) adopted the infiltration technique to introduced nano-sized ceria coating into the conventional Ni-YSZ anode, and observed that cover of the anode by nano-sized ceria could avoid the catastrophic failure for the Ni-YSZ anode, as shown in Figure 2-18. However, the comparison was questionable as the cell performance was quite different for cells with and without anode infiltration with ceria: the initial voltage was 0.78 V for cells with infiltration, while it was only 0.45 for cells without infiltration, indicating the contribution of the anode resistance to the total cell resistance was very different before sulfur poisoning.

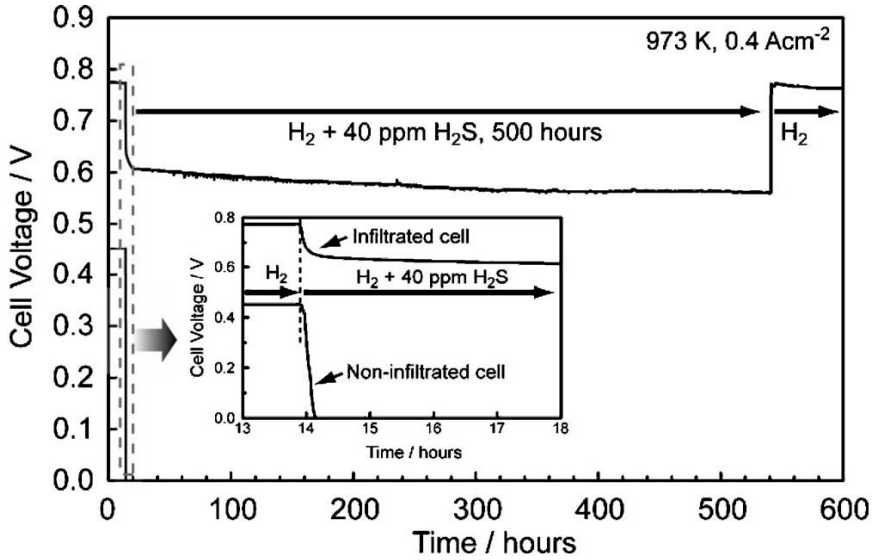

Figure 2-18 Comparison of the sulfur poisoning behavior under constant current density of 0.4 A/cm^2 when 40 ppm H_2S was introduced into the fuel stream for Ni-YSZ cermet anode without and with coating of infiltrated ceria, from Kurokawa et al. (2007).

CHAPTER 3

EXPERIMENTAL PROCEDURES

In this chapter, the experimental procedures used in this study will be described. It will include three areas. The first is one investigating the sulfur poisoning behavior of solid oxide fuel cells (SOFC) with conventional Ni-YSZ cermet anodes, which will cover the procedures and self-designed setups for SOFC materials synthesis, button cell fabrication and assembly, and testing under various conditions in fuels containing H_2S poison. The second is on investigating the mechanism of interactions between sulfur and Ni-YSZ cermet anodes, which will include the procedure and setups for sample preparation, ex situ and in situ characterizations. The last one will be on exploring new sulfur-tolerant anode materials for solid oxide fuel cells, which will include procedures for materials synthesis, fuel cell fabrication, and characterizations.

3.1 Investigation of the Sulfur Poisoning Behavior of Ni-YSZ Cermet Anodes

In this section, the experimental procedures for systematically investigating the sulfur poisoning behavior for solid oxide fuel cells with traditional Ni-YSZ cermet anodes are described. It will include (i) the synthesis of cell component materials (e.g., electrolyte, anode, and cathode), (ii) the fabrication of both electrolyte-supported and anode-supported solid oxide fuel cell button cells, (iii) button cell assembling and testing under various conditions in fuels containing sulfur contaminants.

3.1.1 Synthesis of Materials for Solid Oxide Fuel Cells with Ni-YSZ Anodes

3.1.1.1 YSZ Electrolyte Materials

Three kinds of YSZ electrolyte materials were used in this study: one was named GNP YSZ and was made in the lab; the other two were commercial powders and were purchased from vendors. The synthesis procedure and/or characteristics for these YSZ powders are described below.

- GNP YSZ

The GNP YSZ was prepared in the lab through the glycine nitrate process (GNP). Figure 3-1 illustrates a flow chart for the synthesis of GNP YSZ. Basically, the nitrate precursors, $ZrO(NO_3)_2$ for ZrO_2 and $Y(NO_3)_3$ for Y_2O_3, were dissolved in water together with glycine (H_2NCH_3COOH) to make a clear aqueous solution. The molar ratio of NO_3^- to glycine can be varied, and for YSZ, it was chosen to be 1 : 1. The mixed solution was divided into small quantities in a large beaker and intensively heated on a hot plate turned on at maximum power output. After the solution turned into a highly viscous sol, it would self-ignite and burst into a flame that spread through the sol. After the reaction finished, a foam-like powder product with an extremely low-packing density would be obtained. The obtained product was collected into porcelain cups and heat treated in air to remove any residual carbon. The GNP process has the advantage that the product powder usually has high surface area, uniform size, and an extremely low packing density. Electrolyte powders prepared through the GNP process was used in the co- pressing process developed in the lab, which would be described in detail later in

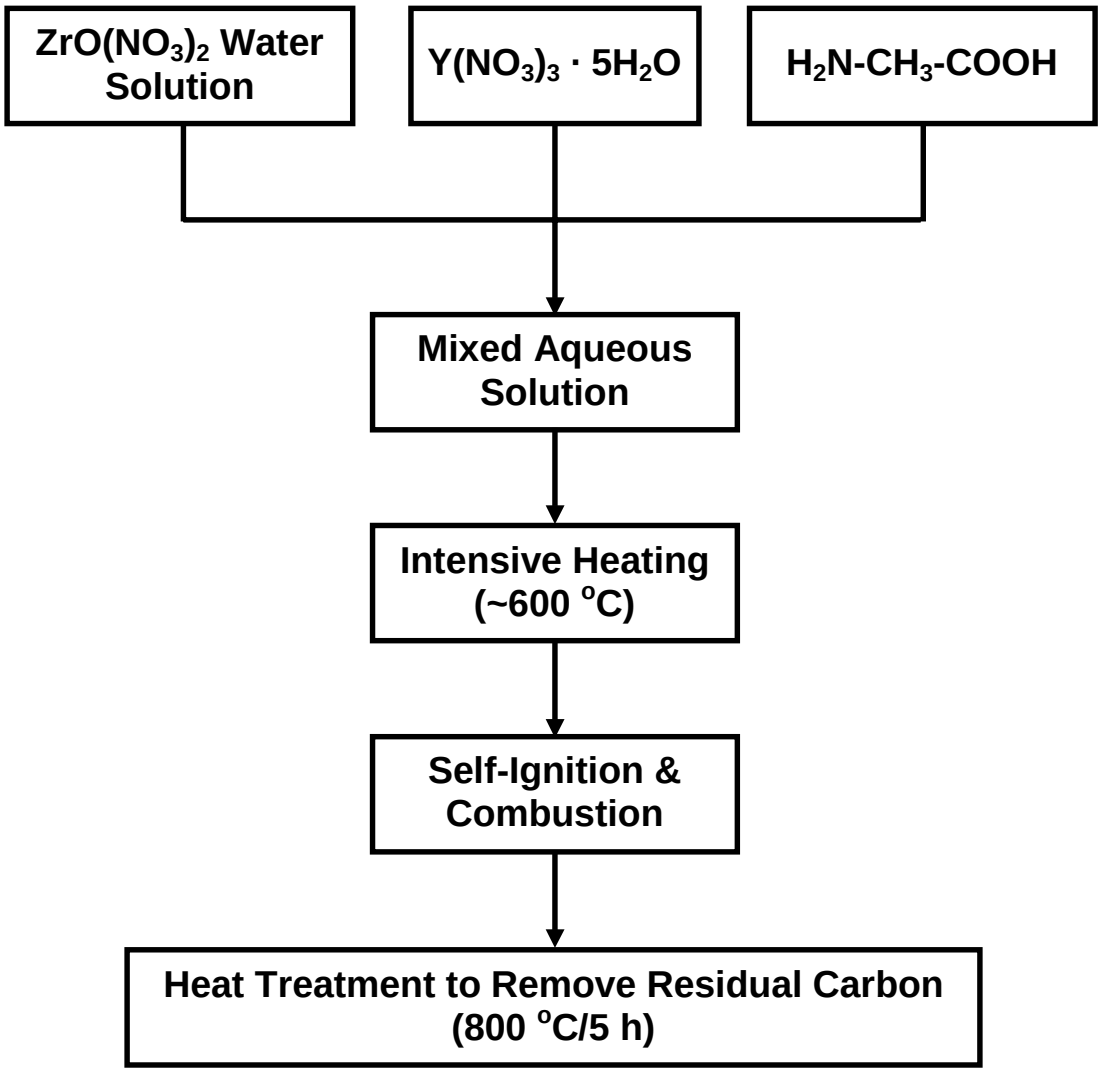

Figure 3-1 Flow chart for the synthesis of YSZ via the glycine nitrate process (GNP) in the lab.

section 3.1.2.2. The following is a step-by-step procedure for the synthesis of GNP YSZ in the lab:

1) 60.78 g 35 wt% $ZrO(NO_3)_2$ solution in water (~35 wt% $ZrO(NO_3)_2$ in dilute nitric acid, 99+%, Aldrich, # 39182-4) was measured with a balance and added to a 500 ml plastic bottle. (The expected amount of $ZrO(NO_3)_2$ was 0.092 mole.)
2) 5.84 g (0.016 mole) $Y(NO_3)_3 \cdot 5H_2O$ (99.9%, Aldrich, #23795-7) was measured and added to the 500 ml plastic bottle.
3) 250 ml deionized (DI) water was added to the 500 ml plastic bottle.
4) 17.42 g (0.232 mole) H_2NCH_3COOH (98%, Aldrich, #G6201) was added to the 500 ml plastic bottle.
5) The solution was mixed thoroughly until a clear colorless solution was obtained.
6) 60 ml mixed solution (i.e., ~1/5 of the total solution) was measured using a measuring column.
7) The 60 ml solution was poured into a 2000 ml glass beaker. The beaker must be cool (i.e., at room temperature), otherwise it will crack when the solution was poured in. This was especially important when the same beaker was to be used again in consecutive processing.
8) The outside of the beaker was wiped dry. Then, it was placed onto a hot plate turned on at maximum power output. The opening of beaker was covered with a stainless steel mesh. The hot plate surface temperature was ~600 ^oC (as the hot plate showed faint red color). Intensive heating using high temperature was important for the GNP process as lower temperature may not induce adequate

reaction and the product would have lower surface area and higher packing density.

9) During the intensive heating, the solution boiled and lost water gradually. As the solution became very concentrated and viscous, a small flame burst out from the concentrated sol, and the reacted sol expanded upward quickly into foam-like structures with the color changed from white to black or gray. The reaction zone spread through the entire concentrated sol in the beaker in a few seconds, and then the reaction finished. The total time from placing the beaker on the hot plate to when the reaction finished was ~15 min.
10) The beaker was removed from the hot plate and air cooled to room temperature.
11) The foam-like reaction product inside the beaker was collected into another 250 ml glass beaker and the top of the beaker was sealed with plastic film (Parafilm®, Pechiney Plastic Packaging). Then, the beaker was shook in the hand and some large blocks would break into smaller, loose powder compacts.
12) The powder compacts were then collected into porcelain cups and heat treated at 800 ^{o}C in air for 5 h in a box furnace (Paragon) with heating and cooling rates of 5 ^{o}C/min.

- Tosoh TZ-8Y YSZ

Tosoh TZ-8Y YSZ are spray-dried, granulated 8 mol % Y_2O_3 doped ZrO_2 (i.e., $(ZrO_2)_{0.92}(Y_2O_3)_{0.08}$) powders purchased from Tosoh Corporation (Tokyo, Japan). The powder has an average granulate size of ~20 μm. This powder was used to prepare YSZ electrolyte discs by dry pressing, as will be described in detail later in section 3.1.2.1. According to the vendor (http://www.tosoh.com/Products/bs+basic2_grades.htm), the

density of the powder is 5.9 g/cm^3, the specific surface area is 16±3 m^2/g, corresponding to an average grain size of ~0.06 μm. The electrical conductivity at 800 ^{o}C is 0.05 S/cm.

- Daiichi HSY-8 YSZ

Daiichi HSY-8 YSZ are fine 8 mol % Y_2O_3 doped ZrO_2 powders from Daiichi Kigenso Kagaku Kogyo Co., Ltd. This powder was used to form Ni-YSZ cermet anode in either electrolyte-supported or anode-supported SOFC button cells. According to the vendor, the density of the powder is 5.9 g/cm^3, the specific surface area is 6.8 m^2/g (corresponding to an average grain size of ~0.15 μm), and the primary particle size is ~0.2 μm. Readers may refer to the following link for more production information: http://www.dkkk.co.jp/english/products_e/detail3/hsy8.html.

3.1.1.2 Ni-YSZ Cermet Anode Materials

The materials for the porous Ni-YSZ cermet anode used in this study were either synthesized in the lab or purchased from vendors. The precursor for Ni was usually GNP NiO, and the precursor for YSZ was usually commercial Daiichi HSY-8 YSZ. The synthesis of GNP NiO was similar to that for GNP YSZ with the exception that the NO_3^- to glycine molar ratio was 2 : 1. The combustion reaction was more violent, and it produced a highly porous foam-like gray to green powder compact in only ~1-2 seconds. Note that only ~60 ml of solution was fired each time in a 2000 ml beaker. The obtained powder was also collected into porcelain cups and heat treated at 850 ^{o}C in air for 5 h in a box furnace (Paragon) with heating and cooling rates of 5 ^{o}C/min. The heat treatment was to remove any residual carbon and oxidize any metallic nickel phase that might be present since the flame in the GNP process could be reducing when the precursor solution

was fuel-rich (i.e., with extra glycine). The obtained GNP NiO were then mixed with Daiichi HSY-8 YSZ to prepare the Ni-YSZ cermet anode. Later, after the cell was fabricated and assembled, the NiO-YSZ composite was reduced back to Ni-YSZ at high temperatures, which will be described in detail later in section 3.1.4.1.

3.1.1.3 $La_{0.85}Sr_{0.15}MnO_3$-YSZ Cathode Materials

The materials for SOFC cathode in this study are commercial or GNP $La_{0.85}Sr_{0.15}MnO_3$ (LSM85) and commercial Daiichi HSY-8 YSZ. The synthesis of GNP $La_{0.85}Sr_{0.15}MnO_3$ was also similar to that for GNP YSZ except that (i) the Mn precursor was manganese (2+) acetate hydrate ($Mn(CH_3COO)_2 \cdot 4H_2O$) instead of manganese (2+) nitrate, and (ii) the NO_3^- to glycine molar ratio was 2 : 1. Note that only ~60 ml of solution was fired each time in a 2000 ml beaker. Towards the end of the solvent removal in the GNP process for LSM85, some white foam appeared at the bottom of the beaker. Then, suddenly, a black fume burst out from the rather concentrated sol, and no apparent flame was observed. The powders were collected into porcelain cups and heat treated at 800 ^oC in air for 5 h in Paragon furnace with heating and cooling rates of 5 ^oC/min to remove any residual carbon.

Table 3-1 summarizes the amounts of raw materials used and the molar ratio for raw materials for the preparation of $(ZrO_2)_{0.92}(Y_2O_3)_{0.08}$, NiO, and $La_{0.85}Sr_{0.15}MnO_3$ powders through the glycine nitrate process (GNP).

Table 3-1 The amounts of raw materials used and the molar ratio for raw materials for the preparation of $(ZrO_2)_{0.92}(Y_2O_3)_{0.08}$, NiO, and $La_{0.85}Sr_{0.15}MnO_3$ powders through the glycine nitrate process (GNP).

Material	Raw materials	Weight (g)	Moles (mole)	Molar ratio
$(ZrO_2)_{0.92}(Y_2O_3)_{0.08}$	Zirconium oxynitrate solution in water (35 wt % $ZrO(NO_3)_2$ solution in water with dilute nitric acid added, 99+%, Aldrich, #39182-4)	60.78	0.092	Zr : Y : NO_3^- : Glycine = 0.92 : 0.16 : 2.32 : 2.32 *
	Yttrium nitrate hydrate ($Y(NO_3)_3 \cdot 5H_2O$, 99.9%, Aldrich, #23795-7)	5.84	0.016	
	Glycine (H_2N-CH_3-COOH, 98%, Aldrich, #G6201)	17.42	0.232	
	Deionized H_2O	250		
NiO	Nickel nitrate hydrate ($Ni(NiO_3)_2 \cdot 6H_2O$, Ni 19.8% min, Alfa Aesar, #12222)	29.06	0.100	Ni : NO_3^- : Glycine = 1 : 2 : 1
	Glycine (H_2N-CH_3-COOH, 98%, Aldrich, #G6201)	7.51	0.100	
	Deionized H_2O	250		
$La_{0.85}Sr_{0.15}MnO_3$	Lanthanum nitrate hydrate ($La(NO_3)_3 \cdot xH_2O$, 99.3%, Aldrich, #23855-4, weight yield of La_2O_3 was determined to be 0.37659 on 08/02/2006)	36.77	0.085	La : Sr : Mn : NO_3^-: Glycine = 0.85 : 0.15 : 1 : 0.5
	Strontium nitrate ($Sr(NO_3)_2$, 99.0%, Alfa Aesar, #12232)	3.18	0.015	
	Manganese acetate tetrahydrate ($Mn(CH_3COO)_2$-$4H_2O$, 99+%, Aldrich, #221007)	24.51	0.100	
	Glycine (H_2N-CH_3-COOH, 98%, Aldrich, #G6201)	10.70	0.143	
	Deionized H_2O	250		

Notes:

* The amount of NO_3^- in the solution that comes from HNO_3 added to stabilize the $ZrO(NO_3)_2$ solution was not included in the calculation of the molar ratio.

3.1.2 Fabrication of Solid Oxide Fuel Cell Button Cells

Both electrolyte-supported and anode-supported SOFC button cells were fabricated and tested for sulfur poisoning behavior in this study, and the typical procedures for their fabrication will be described in this section.

3.1.2.1Fabrication of Electrolyte-Supported SOFC Button Cells

- Preparation of YSZ electrolyte discs

For electrolyte-supported button cells, the electrolyte disc should be as thin as possible. As stated in Chapter II, large area electrolyte discs could be prepared by tape casting, while small area electrolyte discs could be prepared by dry pressing. In this study, dry pressing was used to prepare the green body for the electrolyte disc. After sintering, YSZ electrolyte discs with a diameter of ~9 mm and a thickness as low as ~250 μm could be obtained. The following is a step-by-step description of the procedure for the preparation of YSZ electrolyte discs in the lab.

1) 0.1 g granulated Tosoh TZ-8Y YSZ was measured using a balance and loaded into a Φ13 mm cylindrical die with the lower pressing block in place. The die body was shaken so that the powder distributed rather uniformly inside the die.
2) The pressing column was inserted into the die and it was gently pressed against the powder and rotated both clockwise and counterclockwise using hand. This was to level the powder compact. Care was taken to uniformly spread the granulated powder inside the die so that the top surface would be parallel with the bottom surface. Then, the pressing column was gently removed from the die. (If the pressing column was removed too fast, a vacuum will be created inside the die

chamber, which would first lift the powder compact and then cause it to fall suddenly and break into pieces.)

3) Then the upper pressing block and the pressing column were placed into the die consecutively (see Figure 3-2 for a cross-section view of the die showing different parts and the powder compact). The die was put onto a uniaxial die press and cold-pressed with a force of ~0.8 ton (or ~60 MPa). If the pressure were too high (e.g., greater than 1.0 ton or ~75 MPa), the pellet would break into pieces when it was released from the die. In some cases, pellets tend stick to the surface of the upper or lower pressing block after pressing. When that happened, 3M Scotch® Magic™ tape could be applied to the surface facing the powder compact of the upper and lower pressing blocks, and the problem of sticking would usually be solved.

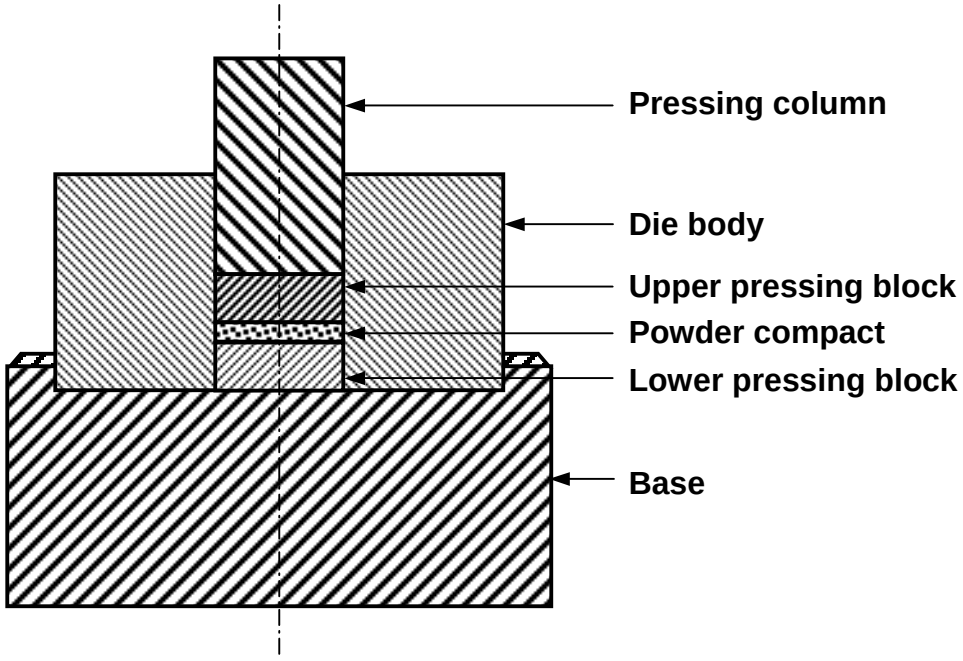

Figure 3-2 Cross-section view of the cylindrical die used in the study.

4) The green YSZ disc was released from the die and put on an alumina boat. A sintered YSZ disc with a diameter of 9 mm and a thickness of ~0.5 mm was placed on the top of the green YSZ disc, which would prevent the bending of the pellet during subsequent sintering.
5) The green YSZ discs were sintered at 1550 ^{o}C for 5 h in stagnant air to in the hot zone of a tube furnace (Lindberg) with a heating and cooling rates of 5 ^{o}C/min.

After the electrolyte discs were sintered, they had a relative density of >95%. Anode and cathode would be prepared in subsequent steps, which will be described in the following sections.

- Preparation of the Ni-YSZ anode

To prepare the anode, an anode paste was made first. Usually, 7.4 g GNP NiO, 2.6 g Daiichi HSY-8 YSZ, together with 10 g organic screen printing vehicle (V-006, Heraeus), 10 g acetone, and 30 g 3 mm-diameter YSZ grinding media were added to a 30 ml plastic bottle. The target Ni : YSZ volume ratio after the reduction of NiO was 60 : 40. The bottle was placed on a roller mill and mixed and ground for ~24 h. Then, the YSZ discs were put on paper towels and a square of 5 × 5 mm^2 was masked on the disc using plastic tapes (Scotch® Magic™, 3M), and the anode paste was applied onto the disc using a paintbrush. Figure 3-3 is a schematic for the setup of brush painting of electrodes. After one layer was painted, the button cell was dried in a drying oven set at ~100 ^{o}C. Depending on the concentration of the paste, different number of layers was applied until the desired thickness (usually ~30- 50 μm) was achieved. The electrolyte discs with painted anodes were heat treated at 1450 ^{o}C for 2 h in a tube furnace (Lindberg) with heating and cooling rates of

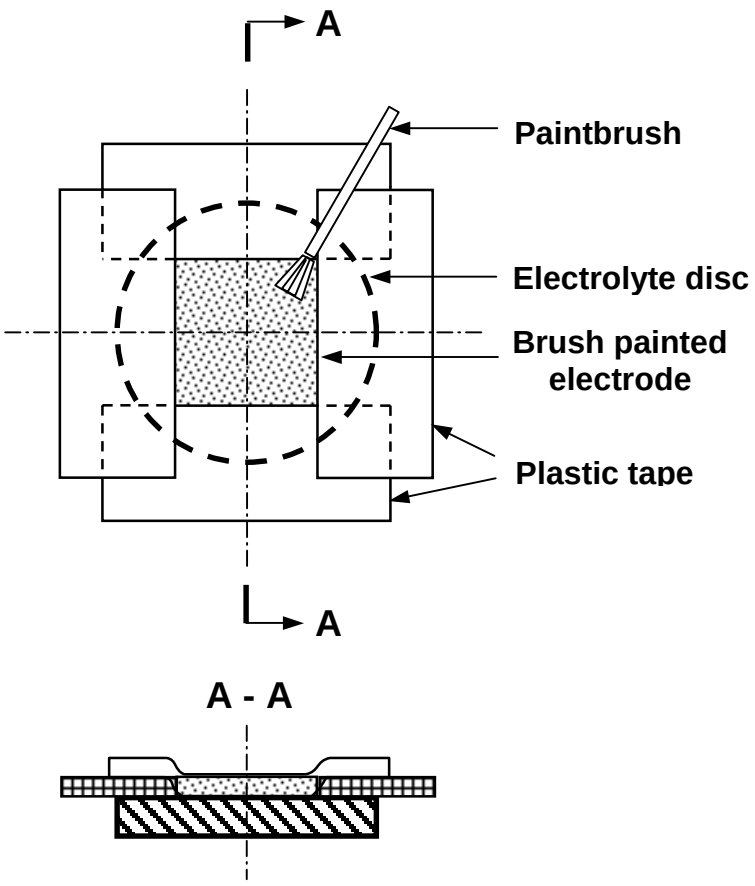

Figure 3-3 Schematic for the masking of the button cell in brush printing of electrodes using plastic tapes to form the mask.

3 ^{o}C/min. The reduction of the NiO-YSZ to Ni-YSZ was later carried out at high temperatures, and the details would be described later in section 3.1.4.1.

- Preparation of LSM-based cathode

After the anode was heat treated, the cathode was finally prepared. Two cathode pastes were prepared first to make the LSM-based cathode. The first one contained both $La_{0.85}Sr_{0.15}MnO_3$ (LSM85) and YSZ. To make it, 6.5 g $La_{0.85}Sr_{0.15}MnO_3$ (LSM85, Rhodia) and 3.5 g Daiichi HSY-8 YSZ, together with 10 g organics as screen printing vehicle (V-006, Heraeus), 10 g acetone, and 30 g 3 mm-diameter YSZ grinding media were added to a 30 ml plastic bottle. The second one contained $La_{0.85}Sr_{0.15}MnO_3$ and no

YSZ, and it was made by mixing 10 g $La_{0.85}Sr_{0.15}MnO_3$ (LSM85, Rhodia) together with 10 g organic screen printing vehicle (V-006, Heraeus), 10 g acetone, and 30 g 3 mm-diameter YSZ grinding media in a 30 ml plastic bottle. Both these pastes were roller milled for 24 h and were ready to use.

To apply the cathode, electrolyte discs with fired anodes were put onto a paper towel with the anode side facing down. Similar to the brush printing of the anode, a square of 5 × 5 mm^2 was masked on each electrolyte disc using plastic tapes (Scotch® Magic™, 3M). Then a layer of 65 wt% LSM85-3 5wt% YSZ paste was brush painted onto the YSZ electrolyte and dried at ~100 ^oC. Then a layer of pure LSM85 paste was painted over the LSM85-YSZ layer and dried again. After that, the cell with the green cathode was heat treated at 1200 ^oC in stagnant air for 2 h in a tube furnace with heating and cooling rates of 3 ^oC/min. Figure 3-4 illustrates the entire procedure for the fabrication of electrolyte-supported SOFC button cells in this study.

3.1.2.2 Fabrication of Anode-Supported SOFC Button Cells

For some trial experiments, the anode-supported cells used were completely fabricated in the lab using a unique technique. In this section, the procedure to fabricate such anode-supported SOFC button cells would be described in detail. The description is of the procedure is important because it represents the typical processing of anode-supported cells in the lab and is unique for its simplicity. The technique, which was developed by Dr. Changrong Xia in the lab (Xia and Liu, 2001a and 2001b), involves co-pressing an anode/electrolyte bilayer with a thin electrolyte followed by co- sintering of the bilayer in air. The following is a detailed description of the procedure for fabricating

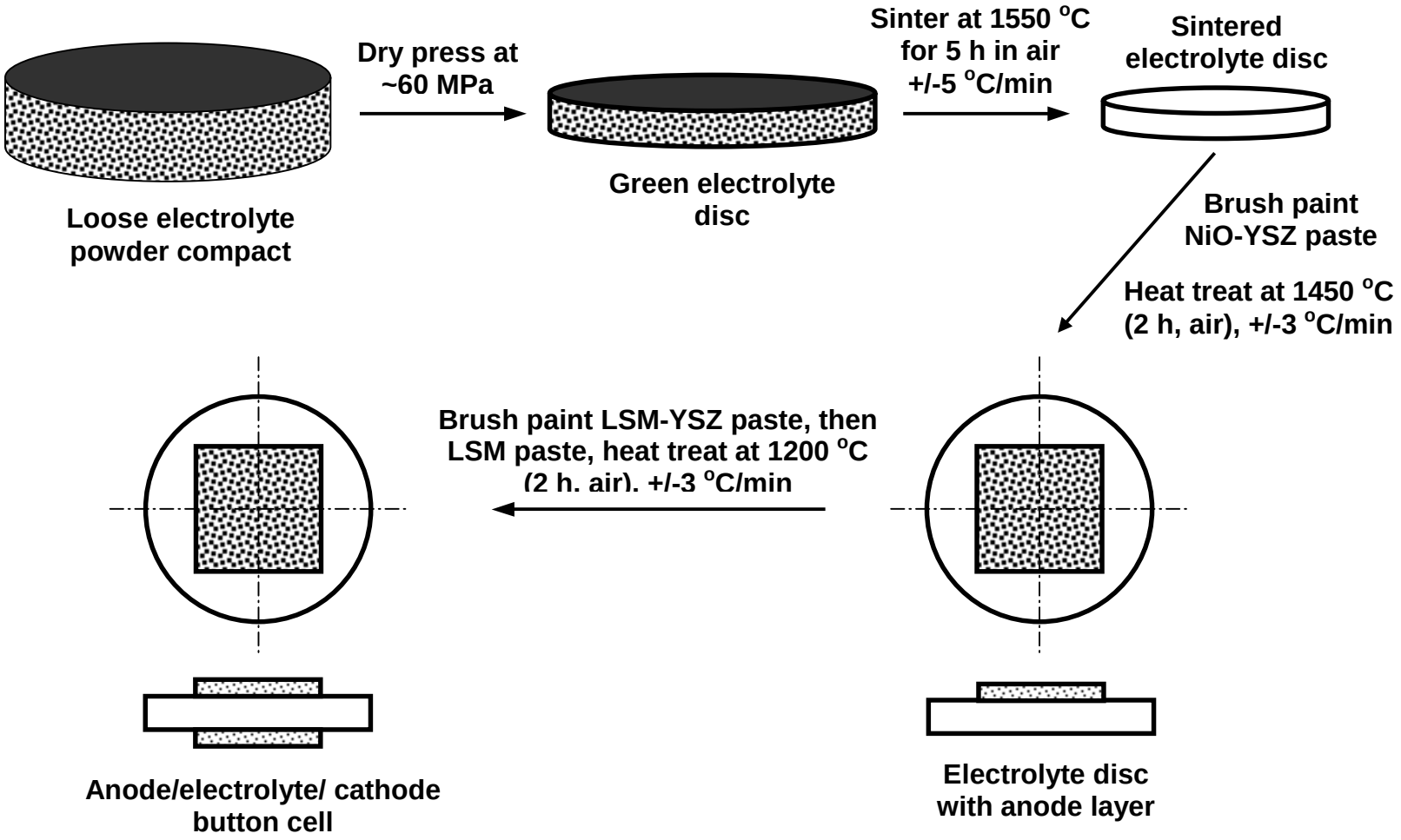

Figure 3-4 Schematic for the preparation of the electrolyte-supported cells in the lab.

fabricating anode-supported cells with YSZ as the electrolyte and a target Ni : YSZ volume ratio (after the reduction of NiO to Ni) of 55 : 45. If the target Ni : YSZ volume ratio in the anode or the porosity changes, the relative amount of raw materials should be changed to adapt to that.

- Preparation of NiO-YSZ mixture

To prepare SOFC button cells using the co-pressing method, the first step is to make a NiO-YSZ mixture for the anode, and the following is a step-by-step procedure for making a mixture with a target Ni : YSZ volume ratio (after NiO reduction) of 55 : 45.

1) 1.4 g GNP NiO and 0.6 g Daiichi HSY-8 YSZ together with 0.15 g rice starch were weighed separately using a balance. As stated, the relative amounts of GNP NiO, YSZ, and starch could be changed to achieve different target Ni : YSZ volume ratio and porosity in the anode.
2) The 0.15 g rice starch was first ground by hand using an agate mortar and a pestle for ~5 min since the particle size of the rice starch was quite large (~20-50 μm).
3) The 1.4 g GNP NiO and 0.6 g Daiichi YSZ were added to the mortar containing ground rice starch. ~2-3 ml ethanol was added gradually using a wash bottle to the mortar. When all the powder mixture was immersed by ethanol, the suspension was ground continuously by hand for ~15 min until ethanol gradually evaporized.
4) When the powder mixture was dry, ~2 ml ethanol was added again to it and ground for another ~15 min until the mixture was dry.
5) Repeat step 4) once.

6) When the powder mixture was completely dry, 2 drops (~0.2 g) of a 5 wt% polyvinyl alcohol (PVA) solution in water was added to the powder mixture, and the mixture was ground thoroughly until it broke into sub-millimeter particles that flowed easily, which usually took ~10-15 min. Note that the PVA solution must be added when alcohol evaporated completely as the PVA solution was found to react with liquid alcohol and yield a soft, rubber-like white product, which did not help making granulates for dry pressing.
7) The ground mixture was dried in air for ~10 min and was ready to use.

- Co-pressing and co-sintering of the anode/electrolyte bilayer

The co-pressing and co-sintering technique developed in the lab is capable to prepare anode/electrolyte bilayers with electrolyte thickness as low as ~10 μm and a diameter of up to ~25 mm (in green state). It involves no suspension-based processing techniques such as tape casting, which makes it highly transferable and repeatable. The following is a step-by-step description of the co-pressing and co-sintering procedure used to prepare anode/electrolyte bilayers with YSZ electrolytes.

1) 0.15 g NiO-YSZ-starch powder mixture with a target Ni : YSZ volume ratio of 55 : 45 was loaded into a 10 mm diameter die with the lower pressing block and the base in place (see Figure 3-2 for the structure and the terminology of a die).
2) The powder mixture was spread smoothly by tapping on the side of the die body and/or shuffling it around.
3) The surface of the powder compact was made flat by inserting the long pressing column into the die and twisting it while pressing it against the powder compact.

4) After that, the pressing column was gently pulled out from the die body. Care was taken to avoid pulling the pressing column too fast since it would create a vacuum inside the die chamber and cause the powder compact to move upward suddenly and then fall down and break due to the sadden loss of vacuum when the pressing column was completely removed from the die.
5) The upper pressing block was placed into the die with the smooth side facing down. The long pressing column was inserted again into the die body. The entire die was placed on a die press and pressed with a force of ~0.5 ton (~60 MPa).
6) The die was removed from the die press and held upside down. The base of the die was removed. Then, the lower pressing block was also removed.
7) Approximately 8 mg (~30 micron thick after sintering) GNP YSZ powder was poured into the vacancy left by the lower pressing block. The surface of the YSZ powder compact was made as uniform and flat as possible using a spatula.
8) The lower pressing push block was placed back with the smooth side facing the GNP YSZ powder. It was pressed against the powder compact while being twisted by hand.
9) The based for the die was attached, and the die was held normally and placed on the die press.
10) The die was pressed again with a force of ~2 (or 3) ton for ~10 sec. The corresponding pressure was ~250 MPa (or 375 MPa for 3 ton).
11) The sample was released from the die, and the surface of the YSZ should look uniform and very flat.

12) The co-pressed sample was placed on NiO powder compacts held in an alumina boat. The samples were sintered in a box furnace (Carbolite) at 1425 ^{o}C for 5 h with a heating rate of 5 ^{o}C/min and a cooling rate of 3 ^{o}C/min.

The limitation with the co-pressing and co-sintering process is that the control of both anode porosity and the flatness of the bilayer at the same time can be difficult as both anode porosity and shrinkage are controlled by the amount of pore former added to the NiO-YSZ mixture, while the electrolyte shrinkage is fixed by the GNP YSZ powder used. Therefore, higher anode porosity was usually accompanied by large anode shrinkage, which usually led to severe bending of the cell.

- Preparation of LSM-based cathode

The preparation of LSM-based cathode for anode-supported cells was the same as that in the preparation of electrolyte-supported cells described in section 3.1.2.1, and would not be repeated here. Figure 3-5 is a schematic that illustrates the entire procedure for the fabrication of anode-supported SOFC button cells with YSZ electrolytes using the co-pressing and co-sintering technique.

In addition to anode-supported cells made by co-pressing and co-sintering, other anode-supported SOFC button cells had been used in this study. One type of them was based on anode/electrolyte bilayers provided by a commercial supplier and a LSM based cathode processed in the lab (labeled thereafter as “Commercial cell with GT LSM cathode” cells) in the same way as that described before. The diameter of commercial cells was ~9 mm.

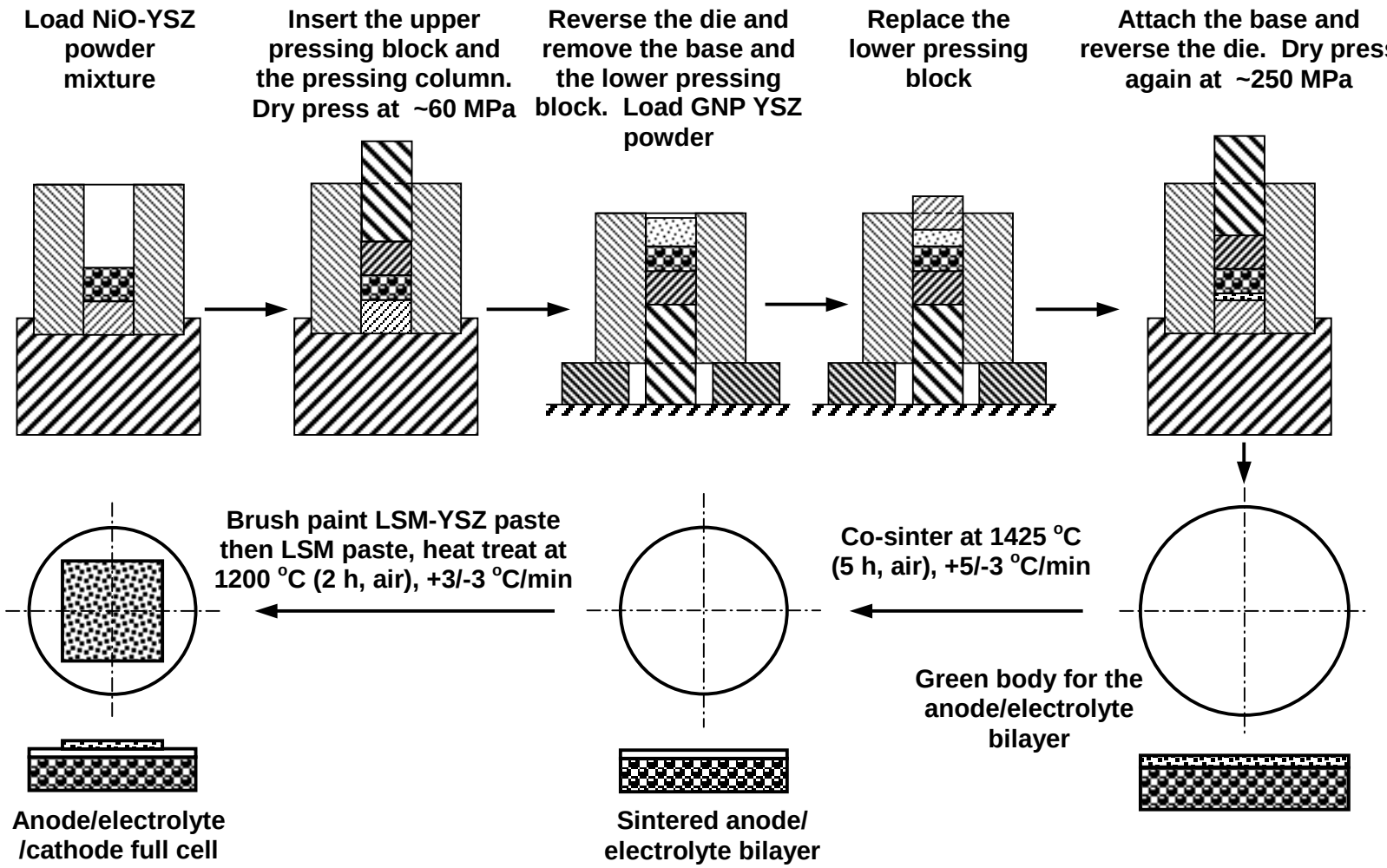

Figure 3-5 Schematic for the procedure to prepare anode-supported SOFC button cells with YSZ electrolytes using the co-pressing and co-sintering technique.

3.1.3 Assembling and Sealing of SOFC Button Cells

For both electrolyte-supported and anode-supported button cells, the cell was sealed onto a cell assembly support tube. To enhance cathode side current collection, before sealing, a metal paste, usually a fritless Pt paste (CL11-5100, Heraeus), was brush painted onto the cathode surface followed by heat treatment at 900 ^{o}C for 0.5 h with heating and cooling rates of 3 ^{o}C/min in a box furnace (Paragon).

After that, the cell was assembled onto a cell assembly, which consisted of a 12 inch long, 0.375 inch O.D. 0.25 inch I.D. alumina tube as a support tube, a 16 inch long 0.125 inch O.D. and 0.0625 inch I.D. alumina tube as fuel delivery tube, a Swagelok® stainless steel T-shaped connector with all three outlets that fit 0.375 inch O.D. tubes (catalog No. SS-600-3). One end of the T-shaped connector was connected with a Swagelok® stainless steel bored through reducer that connects the 0.375-inch fitting to a fitting for 0.125 inch O.D. tubing (catalog No. SS-200-R-6BT). The front and back ferrules for all connections between ceramic tubes and Swagelok® fitting were changed from stainless steel to plastic (Teflon® PTFE) to avoiding cracking of the alumina tubes during tightening of the fittings. The outlet for the assembly was connected with a ~1 inch long, 0.375 inch O.D. stainless steel tube. The end of the 1-inch stainless steel tube was ground flat and smoothened, and the opening was as large as the tube I.D. This was to make sure that water did not get held up at the end of the tube due to surface tension.

To seal the SOFC button cell onto the cell assembly, a 0.375-inch O.D. and ~1 mm thick round ceramic disk with four large holes (diameter ~0.125 inch) was cut from a 4- bore alumina tube. The surface was ground flat using abrasive papers. Then, nickel mesh (100 mesh, Alfa Aesar, #44128) was put onto the ceramic disk and thin Pt wires

(0.1 mm diameter, annealed, Alfa Aesar, #10289) was used to fix the nickel mesh to the porous alumina disk and provide lead wire from the nickel mesh. The surface of the nickel mesh with Pt wires was squeezed flat. Ceramic sealant (either Ceramabond® 552VFG, Aremco, or Acoustic FC-6, Flexbar) was applied to the top of the 0.375-inch O.D. alumina tube. Then, the porous alumina disk with nickel mesh was placed on the top end of the 0.375-inch O.D. alumina tube with the nickel mesh facing up, and the sealant would bond the disk to the end of the tube. After the sealant dried partially, the cell was put on top of the alumina disk with the anode side facing the nickel mesh fixed onto the alumina disk. Sealant was applied to the edge of the cell while the cell was pressed against the alumina tube gently. Care was taken to cover all crevices between the cell and the alumina support disk. After the sealant dried, a small piece of Pt mesh (100 mesh, Alfa Aesar, #10282) already contain some fritless Pt paste (CL11-5100, Heraeus) was placed on top of the cathode side Pt layer. The Pt mesh/wire was secured using the ceramic sealant. The assembled cell was then air dried at room temperature for ~24 h. Figure 3-6 shows a schematic of the cell assembly and related components, while Figure 3-7 shows images of the components in the cell assembly.

3.1.4 Electrochemical Characterization of the Sulfur Poisoning for Solid Oxide Fuel Cells

The electrochemical characterization procedures for electrolyte-supported and anode-supported cells were slightly different, as they serve different purpose in this study. For electrolyte-supported cells, the primary goal was to establish the basic sulfur poisoning behavior (e.g., the influences of temperature, H_2S concentration, and current

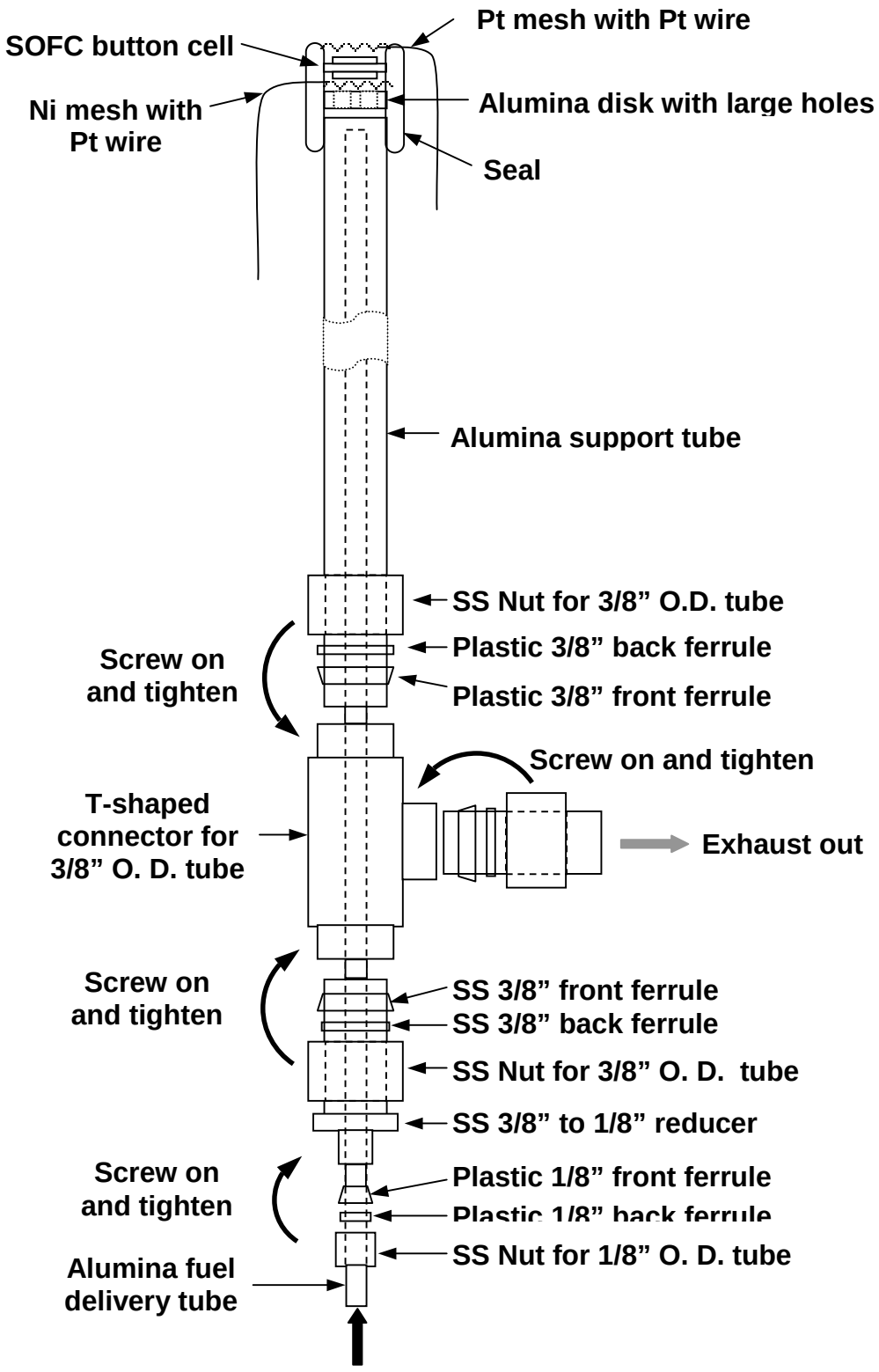

Figure 3-6 Schematic for the cell assembly and related components.

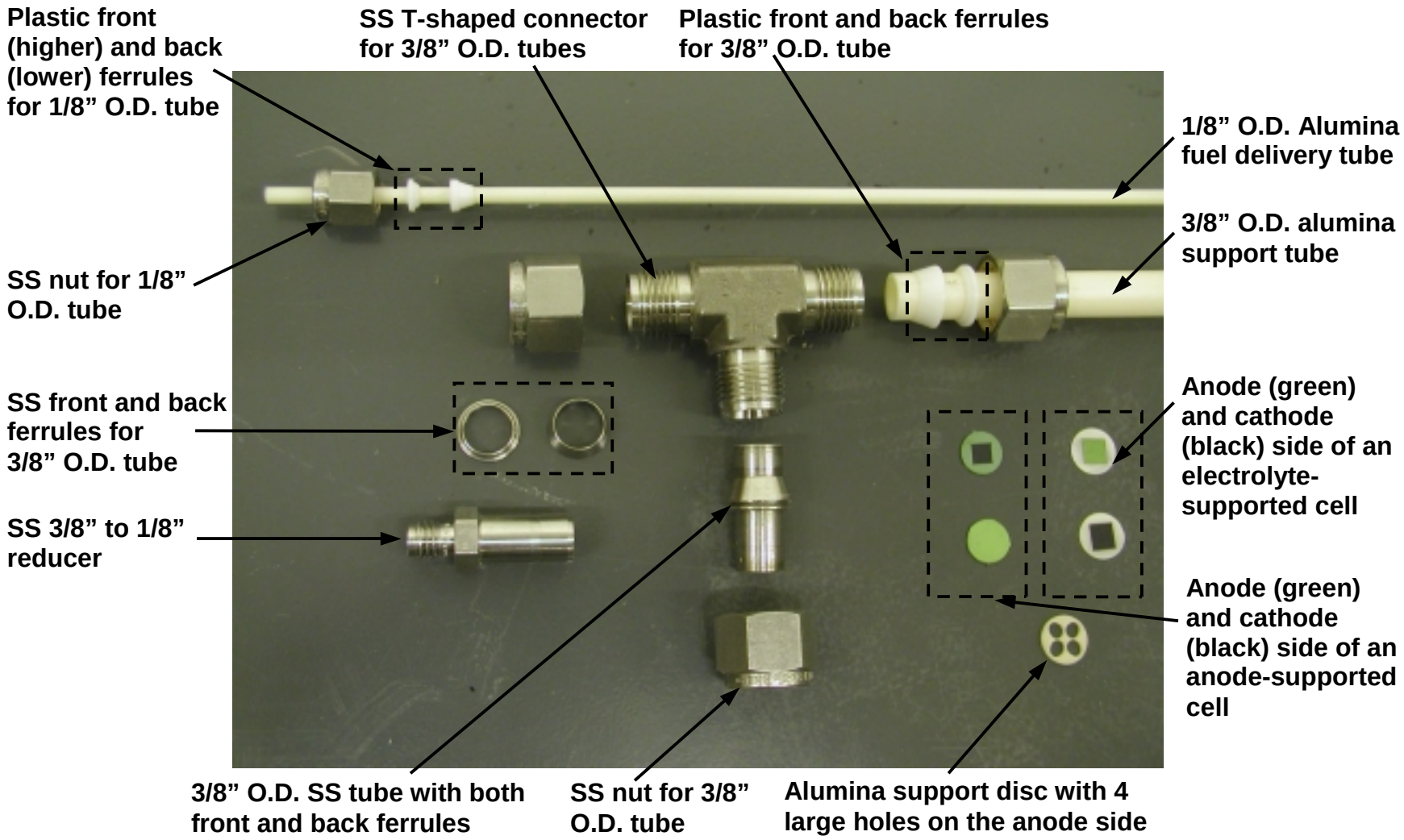

Figure 3-7 Pictures of components and button cells in the cell assembly.

density/voltage, etc.) as the electrochemical response of electrolyte-supported cells to sulfur poison is faster. For anode-supported cells, the primary goal was (i) to evaluate if the sulfur poisoning behavior for anode-supported cells was similar to that of electrolyte-supported cells, and (ii) evaluate the long-term influence of H_2S on state-of-the-art cells as they offer higher cell power output and are closer to real world scenario. Therefore, in the following, the procedure for characterization for both types of cells will be described.

3.1.4.1 Electrochemical Testing for Electrolyte-Supported Cells

For electrolyte-supported cells, after the SOFC button cell was sealed on the cell assembly, the cell assembly was inserted into the furnace and heated up in ambient air to high temperature (usually 900 ^oC). During the heating up process, no fuel was provided to the anode side. Then at 900 ^oC, the anode chamber was purged with humidified N_2 usually at a flow rate of ~10 cc/min for more than 5 min. Then H_2 with a flow rate of 10 cc/min was introduced into the fuel flow to the anode, and the anode fuel composition became ~50 vol.% H_2/1.5% H_2O/48.5% N_2. The open circuit voltage (OCV) during the anode reduction process was recorded, and it would stabilize in ~1 h. After the cell stayed at OCV for more than 5 h at ~900 ^oC, the electrochemical testing was started.

This study showed that that hydrogen fuel can only be introduced into the anode side when the cell temperature was sufficiently high (e.g., >~500 ^oC). If high concentration of hydrogen (e.g., 50 vol. % H_2) was introduced from room temperature up to ~100-200 ^oC, the anode reduction would finish at temperature below ~400 ^oC, which would yield an electrically insulating anode with very low cell performance and a low OCV (usually ~0.85 V).

To carry out electrochemical testing, the electrolyte-supported cell was first run under constant voltage condition (usually at 0.7 V) at 900 ^{o}C for ~100 h during which the cell performance (current in this case) increased dramatically (2-3 times for electrolyte-supported cells.) Then, the cell performance would stabilize and the sulfur poisoning experiment would be carried out.

To monitor the sulfur poisoning experiment, the cell was run under either constant voltage (potentiostatic) condition in which the cell terminal voltage was controlled at a fixed value and the change in cell current was monitored continuously, or under constant current (galvanostatic) condition in which the cell current was fixed and the change in cell voltage was monitored. The equipment used to control the constant voltage or constant current condition while monitoring the change in cell performance is called a potentiostat/galvanostat. The control was achieved through a personal computer using the CorrWare® software (Scribner Associates). In some cases, impedance responses of fuel cells under open circuit condition and/or DC bias were also measured in the frequency range from 100 kHz to 0.01 Hz. This was achieved using an EG&G lock-in amplifier connected with the EG&G 273A potentiostat/galvanostat, which were controlled through a PC by the PowerSine® software (Princeton Applied Research).

The sulfur poisoning process was monitored under various operating conditions including cell temperature, cell current and voltage, H_2S concentration, and operating time. To control H_2S concentration, for example, 100 ppm H_2S, pure H_2 and humidified N_2, each flowing at 10 ml/min were mixed and passed through the cell anode chamber (nominal fuel composition is 50% H_2/1.5% H_2O/48.5% N_2). Then the fuel with 100 ppm H_2S was obtained by replacing the pure H_2 flow with a certified gas mixture of 100 ppm

H_2S in H_2 (Airgas) at the same flow rate, and the nominal fuel composition became 50 ppm H_2S/50% H_2/1.5% H_2O/48.5% N_2. Note that (i) in this thesis, H_2S concentration usually refers to pH_2S/pH_2 ratio. Therefore, a fuel mixture of 50 ppm H_2S/50% H_2/1.5% H_2O/48.5% N_2 would correspond to a pH_2S/pH_2 ratio of 100 ppm. (ii) The H_2S containing mixture (e.g., 100ppm H_2S/H_2 gas mixture from Airgas) was not passed through water bubbler because H_2S could dissolve in water, which would delay the observed response of the cell. For fuels with low concentration of H_2S such as 0.2-10 ppm H_2S, the H_2S concentration was controlled by mixing pure H_2 and certified mixture gas of 10 ppm H_2S in H_2 (Airgas) using two mass flow controllers (Omega Engineering Inc.). The total flow rate was also 20 ml/min. The gas line volume from the H_2S valve to the anode surface was as little as ~6 ml. Such small idle volume has two benefits: (i) the H_2S gas can reach the anode quickly, and (ii) a very short time is needed to sweep away residual H_2S when the fuel was switched back to clean H_2. Figure 3-8 is a schematic for the setup for testing electrolyte-supported cells.

3.1.4.2 Electrochemical Testing for Anode-Supported Cells

As stated, one of the primary goals to test anode-supported cells was to evaluate the long-term effect of sulfur poison on state-of-the-art cells. To achieve this goal effectively, a multi-cell testing system was designed and installed in the lab. In the following, the multi-channel testing system as well as the procedure for the long-term multi-cell testing would be briefly described.

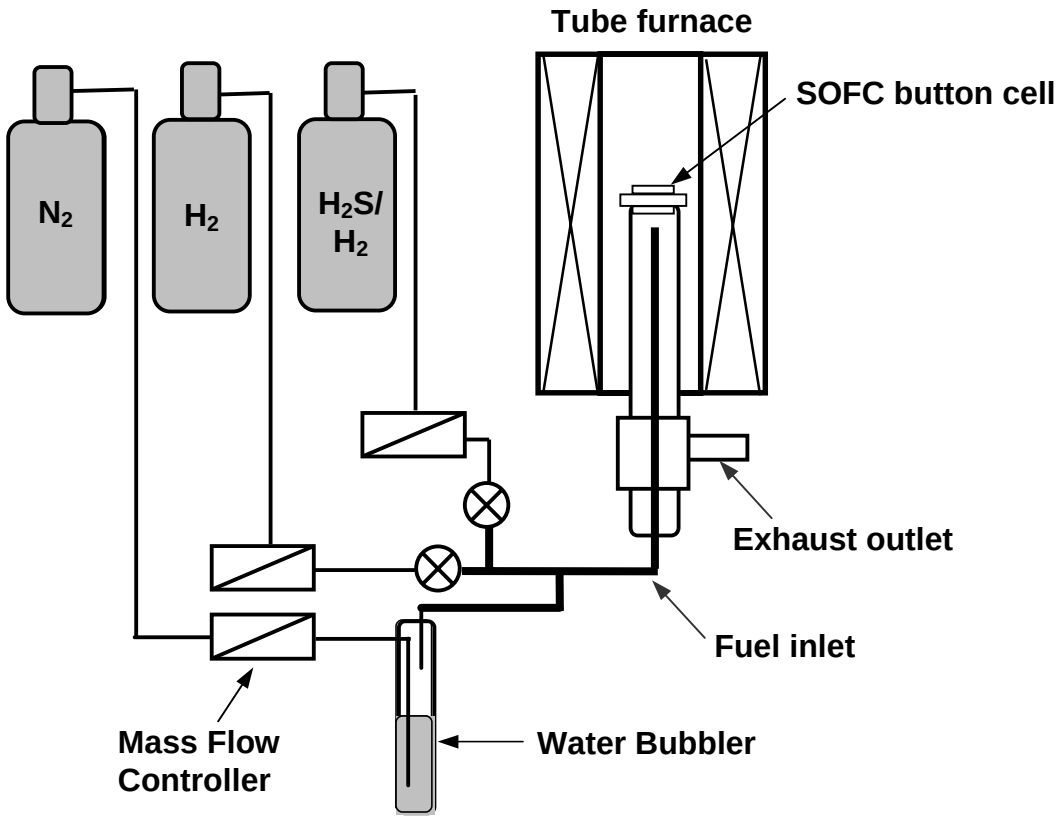

Figure 3-8 Schematic for the setup to test electrolyte-supported SOFC button cells in H_2S-containing fuels, adopted from Zha, Cheng, and Liu (2007) with modification.

- Multi-cell testing system

Figure 3-9 shows pictures of the multi-cell testing system built in the lab. It basically consists of four parts: (i) a large furnace with large inside diameter, (ii) a gas distribution system, (iii) a multi-channel potentiostat interfaced with a computer, and (iv) a supporting system. It is capable of testing up to 12 button cells simultaneously at a single temperature, delivering up to 4 different gas mixtures with 4 different concentrations of H_2S simultaneously. For button cells with thicker electrolyte, it is also capable of accommodating cell replacement during the test.

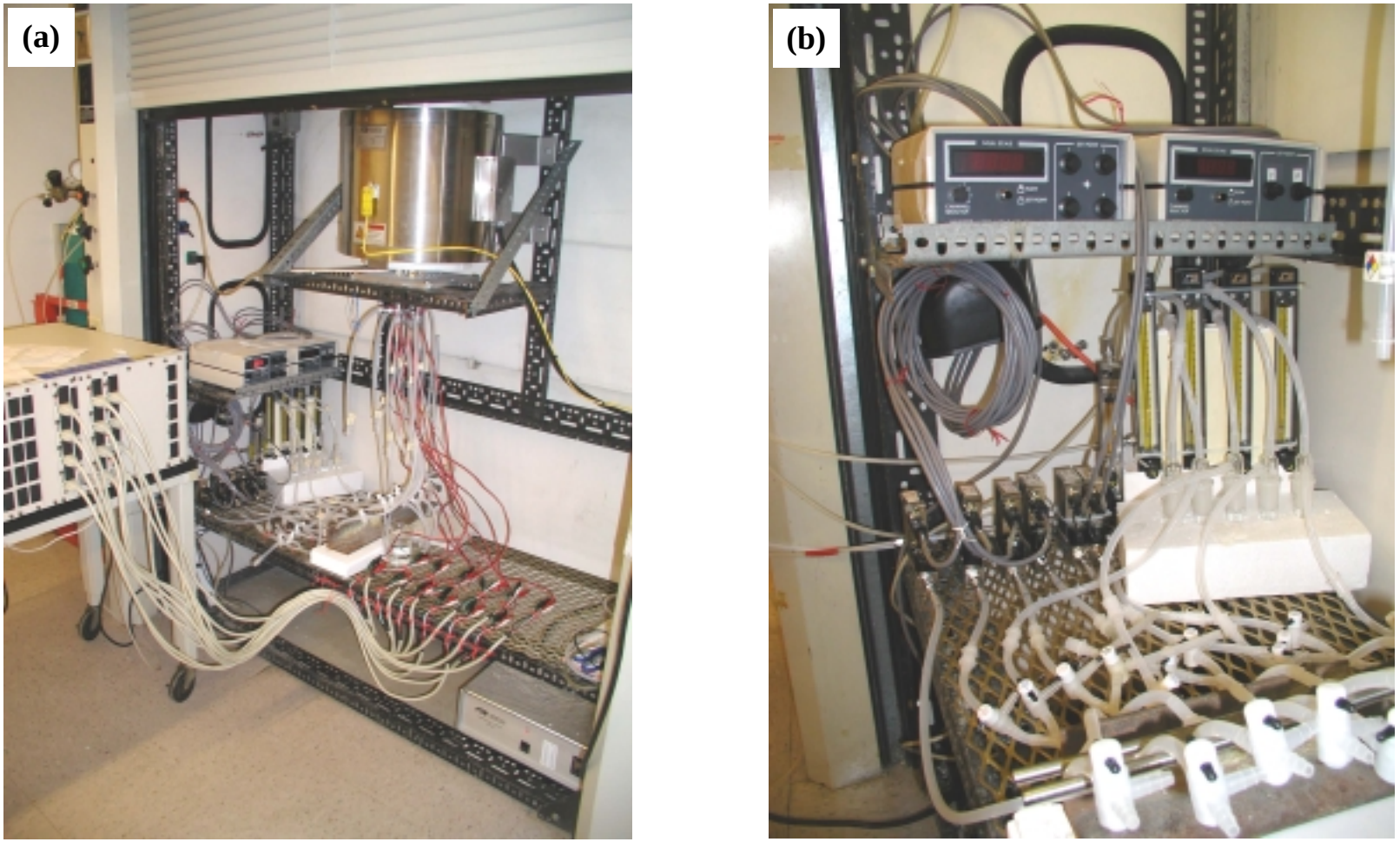

Figure 3-9 Pictures of (a) the multi-cell testing system and (b) the gas distribution system.

The furnace used was a customized single-zone tube furnace (Series 3110, Applied Testing System) with an outside diameter of 16 inch, an inside diameter of 7 inch, a length of 14 inch, and a heating zone of 10 inch. It has a temperature rating of 1200 ^{o}C and a power rating of 3450 W/15 A at 230 VAC, single phase 60 Hz. The thermocouple was type K. It was controlled by a Series 900-TC16 single set point controller.

Based on considerations of test ability and cost limits, a 4-channel fuel distribution system was designed. Each channel would provide a fuel mixture with H_2S concentration of 0, 1, 5, and 10 ppm, respectively. Fuel mixtures from each channel can then be divided into multiple cells, as required. Figure 3-10 shows the schematic for the design of the fuel distribution system, which included four cylinders: one for pure H_2, one for pure N_2 (as gas for purging the cell before introducing fuel and for carrying water vapor), one for 10 ppm H_2S balanced by H_2, and one for 1 ppm H_2S balanced by H_2. According to the design, 10 ppm and 1 ppm H_2S/H_2 will be obtained directly from the cylinders while 5 ppm H_2S/H_2 will be obtained by mixing 10 ppm H_2S/H_2 and pure H_2.

To achieve control on the different fuel mixtures, the system includes seven mass flow controllers (MFC) and four rotameters. For each type of fuel mixture, nitrogen from the cylinder will be connected to a rotameter to control the flow rate. The nitrogen from the rotameter will then be passed through a water bubbler to bring water vapor. The H_2S/H_2 fuel flow rate will be controlled by MFCs. In the case of 5 ppm H_2S/H_2, it will be obtained by mixing 10 ppmH_2S/H_2 and pure H_2 using two MFCs. In the system, there are three-way valves, which allowed the operator to purge the gas line before introducing a specific gas into the system; there are also Y-shaped connectors, which allowed mixing

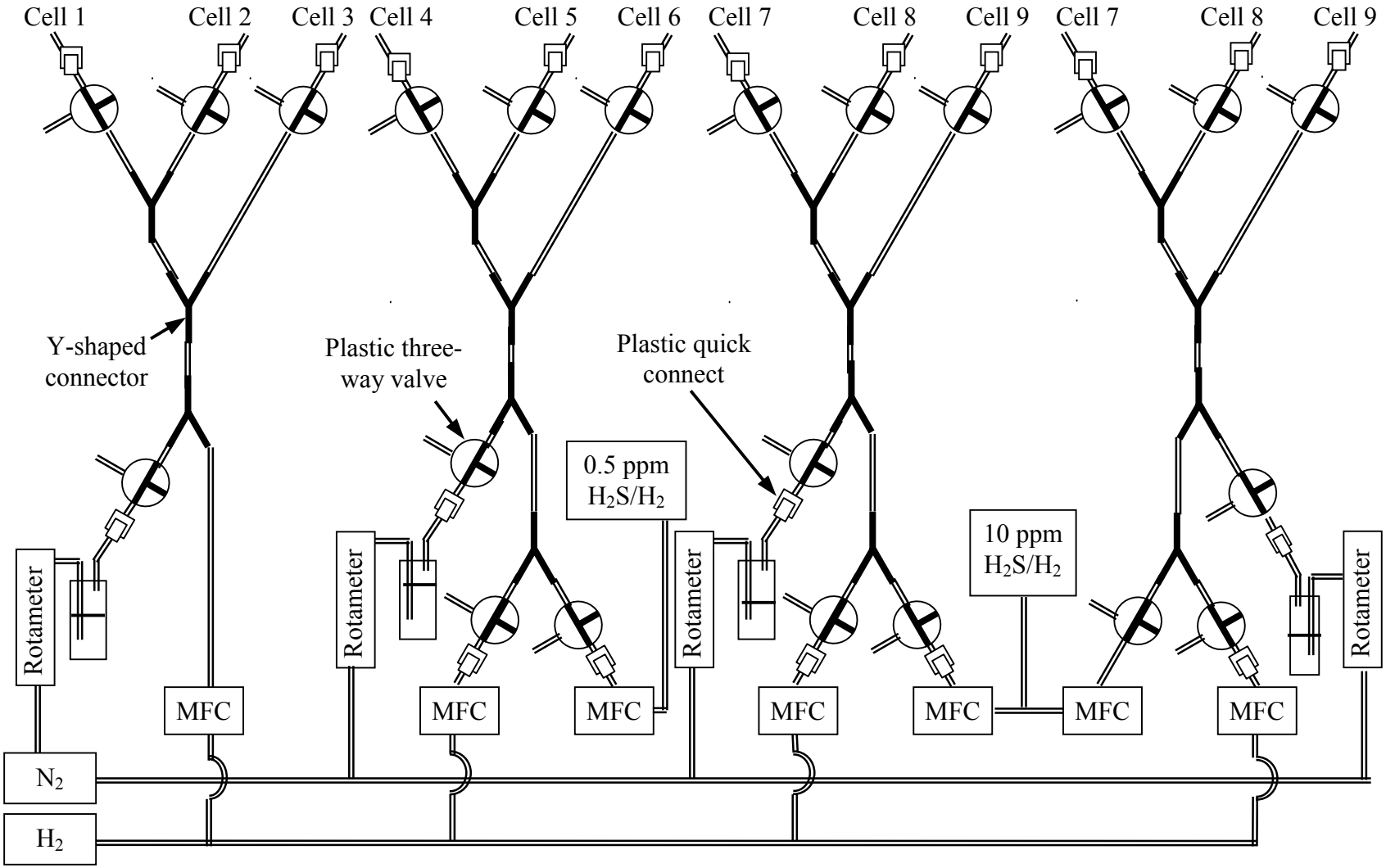

Figure 3-10 Schematic for the gas distribution system that provided four fuels with H_2S concentration of 0, 1, 5, and 10 ppm.

of different gases and division of fuel mixture. The plastic quick connects allow the establishment or disruption of gas connection easily. The tubes connecting the cell inlet with quick disconnects are silicone rubber tubing with inside diameter (I.D.) of 3/32 inch, all other tubing connecting the three-way valves, the Y-shaped connectors and the quick connects are silicone rubber tubing with I.D. of 0.25 inch. It is noted that the design in Figure 3-10 is only for certain combination of fuel mixtures required. The system can be modified to adapt to changes in the fuel composition, and the details would not be discussed here.

The multi-channel potentiostat was a 12-channel potentiostat (MSTAT8000) purchased from Arbin Instruments. The support system supports the furnace and the cells since cells would be tested under vertical position. The design of the supporting plate and accessories for the cells in the system will be given in Appendix A, and will not be described here.

- Procedure for long-term multi-cell testing

After SOFC button cells were sealed on the cell assembly, 12 of them were inserted into the multi-cell testing furnace and heated up in ambient air to 93 ^{o}C at 1 ^{o}C/min and held at 93 ^{o}C for ~1 h. Then, they were heated up in air at 1 ^{o}C/min to 260 ^{o}C and held for another 4 h for the sealant to cure. Finally, they were heated up at 1 ^{o}C/min to 750 ^{o}C also with stagnant air on the anode side. After staying at 750 ^{o}C for some time (usually ~16-24 h), the anode chamber was purged with humidified N_2 (~10 cc/min for each cell) for more than 5 min. Then H_2 (also with a flow rate of ~10 cc/min for each cell) was introduced into the gas flow to the anode chamber to reduce NiO to Ni, and the anode fuel composition became ~50 vol.% H_2/1.5% H_2O/48.5% N_2. The open circuit

voltage (OCV) during the anode reduction process was recorded at 750 ^{o}C. After the cell stayed at OCV for more than 12 h at ~750 ^{o}C, electrochemical testing was started. To avoid oxidant starvation, pure oxygen was also blown into the furnace from the top.

The electrochemical testing of anode-supported cells were similar to those for electrolyte-supported cells. The cells were running at constant current density (usually at 200 and 400 mA/cm^2) until the cell voltage increased and then stabilized. After that, different concentrations of H_2S were introduced into the fuel stream, and the cell performance (i.e., voltage) was be monitored continuously.

3.2 Investigation of the Mechanism of Interactions between Sulfur and Ni-YSZ Cermet Anodes

In this section, the experimental procedures for systematically investigating the sulfur poisoning mechanism for solid oxide fuel cells with traditional Ni-based anodes will be described, which will include characterizing the changes on the anode surface before and after the exposure to H_2S containing fuels under both ex situ and in situ conditions. Because it was found out that the relative increase in cell resistance was always greater when cell voltage was closer to open voltage condition (see later in section 4.1.4), pure chemical exposure was carried out to simulate the sulfur poisoning condition. The focus of the study was to investigate whether sulfur poisoning of the nickel-based anode was due to the formation of conventional multiplayer nickel sulfides, as suggested in the literature (Minh and Takahashi, 1995)

3.2.1 Preparation of Ni-YSZ Composite Sample with Polished Surface

The majority of samples used in the mechanism study were dense composite pellets with 40 vol. % Ni and 60 vol. % YSZ. Ni powder (-300 mesh, Alfa Aesar) was first mixed with Daiichi HSY-8 YSZ (containing 8 mol% Y_2O_3, 0.2-0.3 μm, Daiichi) for 1 h using a mortar and a pestle. The mixed powder was pressed into pellets in a 13-mm-diameter die at a pressure of 150 MPa. The pressed pellets were covered with Ni foils and sintered at 1375 ^oC for 5 h in 4% H_2/96% Ar with a heating and cooling rate of 5 ^oC/min. The sintered pellets were ground successively with SiC abrasive paper (P500, P800, and P1200, Struers) and polished with 1 μm α-alumina (Struers) suspension in water.

Compared with the cermet anode with micron-scale Ni and YSZ grains that are very difficult to distinguish under an optical microscope or an scanning electron microscopy (SEM), the dense composite samples with large sizes of Ni and YSZ grains allow easy characterizations of the individual Ni and YSZ phases as well as the boundaries between them using spatially-resolving techniques such as Raman microspectroscopy, SEM, and energy dispersive X-ray spectroscopy (EDX) elemental mapping. The problem of the signals from different phases (e.g., nickel sulfide and YSZ) overlapping one another would also be minimized compared with the conventional porous Ni-YSZ cermet, for which the signal (e.g., Raman) from YSZ grains is often overwhelmingly strong, burying the changes in the spectra from the Ni grains.

3.2.2 Ex Situ Characterizations

For ex situ experiments, the polished Ni-YSZ composite samples were put in an alumina boat, sealed in an alumina tube furnace, and heated up to a high temperature (e.g., 800 ^{o}C) in a fuel with a nominal composition of 50 ppm H_2S/50% H_2/1.5% H_2O/48.5% N_2. After the samples were held at that temperature for a predetermined period of time, they were cooled down with the furnace in the same fuel. The time required for the furnace to cool from 800 ^{o}C to room temperature was ~5 h and the average rate of cooling was ~3 ^{o}C/min. After that, the sample was examined at room temperature using Raman microspectroscopy (Renishaw 2000, 514 nm laser, 40 mW), XRD (PW1800 X-ray diffractometor, Philips Analytical, Cu-K_α line), SEM (S800, Hitachi, 10 kV), and EDX (3600-0398, Kevex X-ray).

3.2.3 In Situ Raman Microspectroscopy

Figure 3-11 shows a schematic for the in situ Raman setup in the lab. The in situ Raman experiment was carried out in a customized Raman cell with a quartz window (HVC-DRP-1, Harrick Scientific). An Ni-YSZ composite pellet with a polished surface was mounted onto the sample stage of the Raman cell using a gold paste (C5755A, Heraeus), which was then cured by heating up the Raman cell in open air to ~250 ^{o}C. (The sample temperature was calibrated using a type-K thermal couple connected to an Omega HH506R digital thermometer as well as high purity metal melt standards such as tin (T_m = 232 ^{o}C, TA Instruments) and zinc (T_m = 420^{o}C, TA instruments).) Then the Raman cell was sealed with a quartz window and purged with nitrogen. After that, the

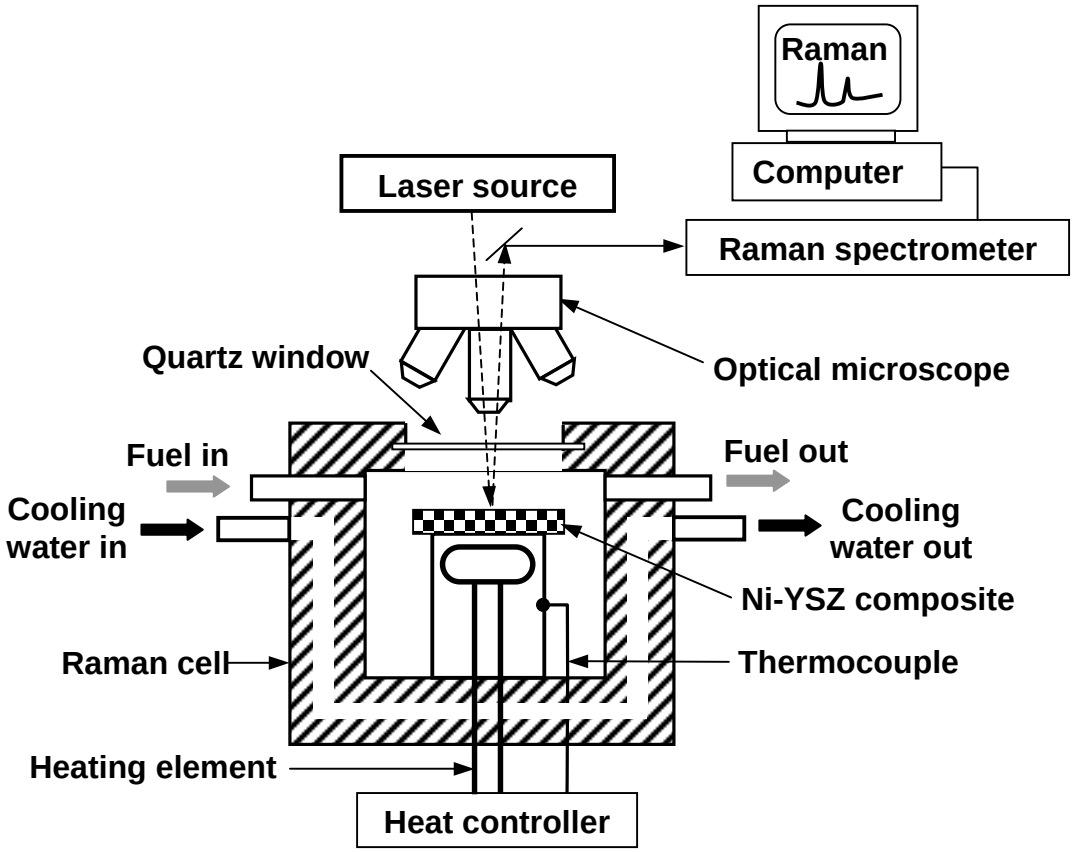

Figure 3-11 Schematic for the in situ Raman microspectroscopy setup in the lab.

nitrogen gas was replaced by a sulfur-free fuel (usually 50% H_2/1.5% H_2O/48.5% N_2), and the cell was heated up to the measuring temperature (e.g., ~570 ^oC). At that temperature, Raman spectra as well as optical images showing surface morphology were recorded before and after a trace amount of H_2S (pH_2S/pH_2 = 100 ppm) was introduced into the Raman cell. In addition, the Raman cell was also cooled at different rates in a fuel with or without H_2S to monitor the changes in the surface species and the morphology of the sample.

3.3 Exploration of New Sulfur-Tolerant Anodes for Solid Oxide Fuel Cells

3.3.1 Materials Synthesis, Stability Test, and Phase Identification for Candidate Materials

Stability Analysis

Some of the samples used in the stability analysis were obtained from commercial suppliers. For example, ZrC (99.5%) and WC (99.6%) were from Alfa Aesar, TiN (99%) was from Aldrich, and WS_2 (99.8%) was from Cerac Inc. The rest were synthesized in the authors' lab. Table 3-2 lists the precursors and preparation methods used for the syntheses. Of the precursors, La_2O_3 and $SrCO_3$ were first calcinated in air at 800 ^oC and 300 ^oC, respectively, for 2 h to remove the adsorbed moisture. All complex oxides were synthesized using a solid-state reaction method. The raw materials were mixed, ground for 1 h, dry pressed into pellets at 70 MPa, and heat-treated at high temperature. For some complex oxides like $SrVO_3$, grinding and calcination were repeated until complete reaction and uniform composition were achieved, as confirmed by X-ray diffraction (XRD, PW1800 X-ray diffractometor, Philips Analytical). The radiation source was Cu-

Table 3-2 Starting materials and preparation methods for samples synthesized in this study for candidate materials stability analysis.

Sample	Starting materials	Preparation method and final heat treatment condition
β-SiC	Phenolic resin (775D69, Georgia Pacific) tetraethoxysilane (TEOS, Alfa Aesar)	Solution based processing 1475 (4h, Ar)
$LaTiO_3$	La_2O_3 (Aldrich, 99.9%) Ti_2O_3 (Alfa Aesar, 99.8%)	Solid-state reaction 1450 (5h, 4%H_2/96%Ar), carbon covered
$LaVO_3$	La_2O_3 (Aldrich, 99.9%) V_2O_5 (Aldrich, 99.6%)	Solid-state reaction 1450 (5h, 4%H_2/96%Ar)
$SrTiO_3$	$SrCO_3$ (Aldrich, 99.9%) rutile-TiO_2 (Alfa Aesar, 99.9%)	Solid-state reaction 1300 (2h, Air)
$SrVO_3$	$SrCO_3$ (Aldrich, 99.9%) V_2O_5 (Aldrich, 99.6%)	Solid-state reaction 1450 (5h+5h, 4%H_2/96%Ar)

K_α lines. The SiC powder was synthesized using a solution-based process (Cheng et al., 2003). To investigate the stability of materials under solid oxide fuel cell anode atmosphere that contained H_2S, powders of representative materials were exposed to fuels containing H_2S at high temperature (usually 950 ^oC) for 2-5 days. The nominal composition (by volume) of the fuels was usually 10% H_2S/3% H_2O/87% H_2.

3.3.2 Fuel Cell Testing and Characterizations for Cells with New Sulfur-Tolerant Anode Materials

Fuel cell testing in H_2S-containing fuels was carried out for some promising materials. Those materials such as $Gd_2Ti_{2-x}Mo_xO_7$ were made through solid-state reactions from the corresponding simple oxides (i.e., Gd_2O_3, TiO_2, and MoO_3). The oxides were mixed and pressed into pellets followed by heat treatment at 1300 ^oC for up to 14 h in a moisturized fuel mixture of 1% H_2/3% H_2O/96% Ar.

For electrochemical characterization, YSZ electrolyte discs were prepared in the same way as that described in section 3.1.2.1. Anode paste was prepared from the corresponding candidate anode materials (e.g., $Gd_2Ti_{1.4}Mo_{0.6}O_7$) and organic screen printing vehicle (V-006, Heraeus). For electrolyte-supported full cell, the anode and cathode (e.g., $La_{0.75}Sr_{0.25}Cr_{0.5}Mn_{0.5}O_3$) pastes were brush painted on each side of the YSZ electrolyte. The active cell area was 0.25 cm^2. The electrolyte disc with the painted anode and cathode were heat treated at 1300 ^oC in a fuel mixture of 4% H_2 /3% H_2O/93% Ar with a heating and a cooling rate of 3 ^oC/min. For anode/electrolyte/anode symmetrical cell, the anode paste was painted on both sides of the YSZ electrolyte discs. Then, the cell was heat treated in a fuel mixture of 4% H_2/96%Ar at 1300 ^oC for 2 h also

with a heating and a cooling rate of 3 ^{o}C/min. After that, for full cells, the assembly process was similar to that described in section 3.1.3 except that Pt gauzes (52 mesh, Alfa Aesar) and wires were used as current collector and lead wires, respectively and the sealant used were Autostic FC-6 from Flexbar. For anode symmetrical cells, the cell with Pt current collectors on both sides was sandwiched between two alumina discs and fixed using a ceramic sealant (Ceramabond® 571, Aremco).

For electrochemical testing, the assembled cell (full cell or symmetrical cell) was heated up to elevated temperature in H_2 fuel at 1 ^{o}C/min. Then, the electrochemical measurements (i.e., impedance spectroscopy and current-voltage measurement) were carried out in clean H_2 fuel at the designated temperature. After that, H_2S was introduced into the fuel stream, and the change in electrochemical response was measured. The samples before and after testing in H_2S-containing fuel were characterized by XRD and Raman spectroscopy.

CHAPTER 4

SULFUR POISONING BEHAVIOR OF Ni-YSZ CERMET ANODES

In this chapter, the results for the investigation of the sulfur poisoning behavior for solid oxide fuel cells with traditional Ni-YSZ cermet anodes will be described. The focus will be on (i) revealing the influence of various testing parameters on the observed sulfur poisoning behavior, (ii) comparing the sulfur poisoning behavior for electrolyte-supported cells and anode-supported cells, and (iii) characterizing the long-term poisoning behavior for anode-supported solid oxide fuel cells. The results will be compared with previous studies, and their implications will be discussed.

4.1 Results

4.1.1 Fuel Cell Performance and Stability in Clean H_2 Fuel

To characterize sulfur poison behavior of an anode in an SOFC, reasonably stable cell performance in clean hydrogen fuel is necessary. Figure 4-1 shows the initial cell current densities as a function of time for a typical electrolyte-supported button cell fabricated in the lab and operated at a constant cell voltage of 0.6 V in a fuel composed of 50% H_2/1.5% H_2O/48.5% N_2. The cell current density increased from 120 mA/cm^2 to 370 mA/cm^2 during the first 82 h running at 0.6 V at 900 ^oC before the cell performance reached steady state. When the cell temperature was decreased to 800 ^oC, the cell maintained a constant power output (or current density) for another 120 h. The initial increase in cell performance with time was typical for SOFC button cells with LSM based cathode and was attributed to cathode conditioning or activation, as observed also

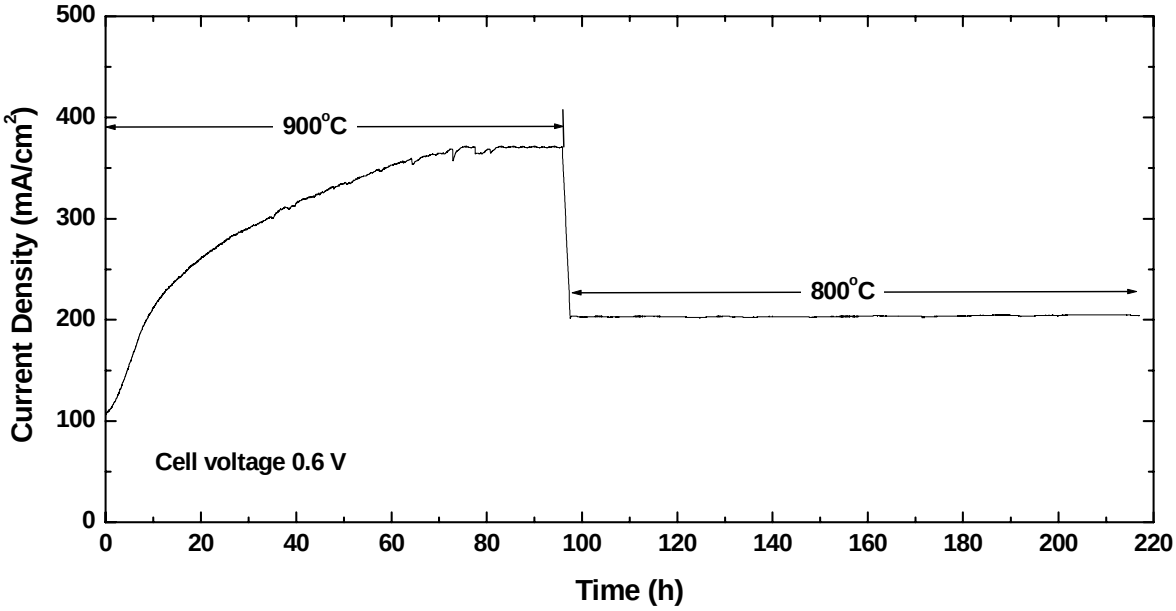

Figure 4-1 Plot of current density versus time for a SOFC button cell operated at a constant cell voltage of 0.6 V for 9 days, adopted from Zha, Cheng, and Liu (2007) with modifications.

by many researchers during the initial period of cell operation (Jiang et al., 1999; Jogensen and Mogensen, 2001; Lee et al., 2003; Simner et al., 2005). It was also found that a lower cell current density led to a longer time of operation for the cell performance to reach a steady state. As a result, electrolyte-supported button cells tested in this study were usually stabilized at a cell voltage of 0.7 V at 900 ^{o}C for >90 hours before H_2S contaminant was introduced.

Figure 4-2 shows a plot of cell voltage and power density versus current density for an electrolyte-supported SOFC button cell fabricated in our lab after the cell performance was stabilized. The maximum power density was 293, 180, and 61 mW/cm^2 when the cell temperature was 900, 800, and 700 ^{o}C, respectively. The cell performance was moderate, considering that the electrolyte-supported cell had an electrolyte of ~0.25 mm thick. The fuel cell fabrication and testing conditions were kept as identical as

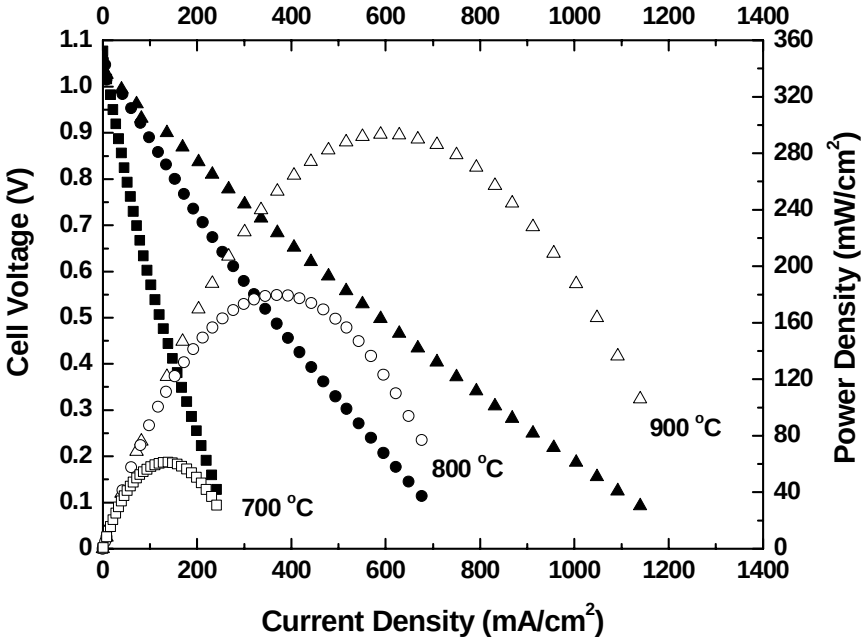

Figure 4-2 Cell voltage and power density as a function of current density for an electrolyte-supported SOFC button cell with running on H_2-N_2 fuel, adopted from Zha, Cheng, and Liu (2007) with modifications.

possible during this study to obtain repeatable performance.

For anode-supported cells with LSM cathode, the conditioning stage was similar but the extent of performance increase was even more dramatic. The I-V curve at 750 °C after the cell performance stabilized is shown in Figure 4-3. (The I-V curve was only measured at 750 °C because it was intended to simulate real fuel cell stack condition.) The maximum power density was ~280 mW/cm^2, which was almost three times of those for electrolyte-supported cells at a similar temperature.

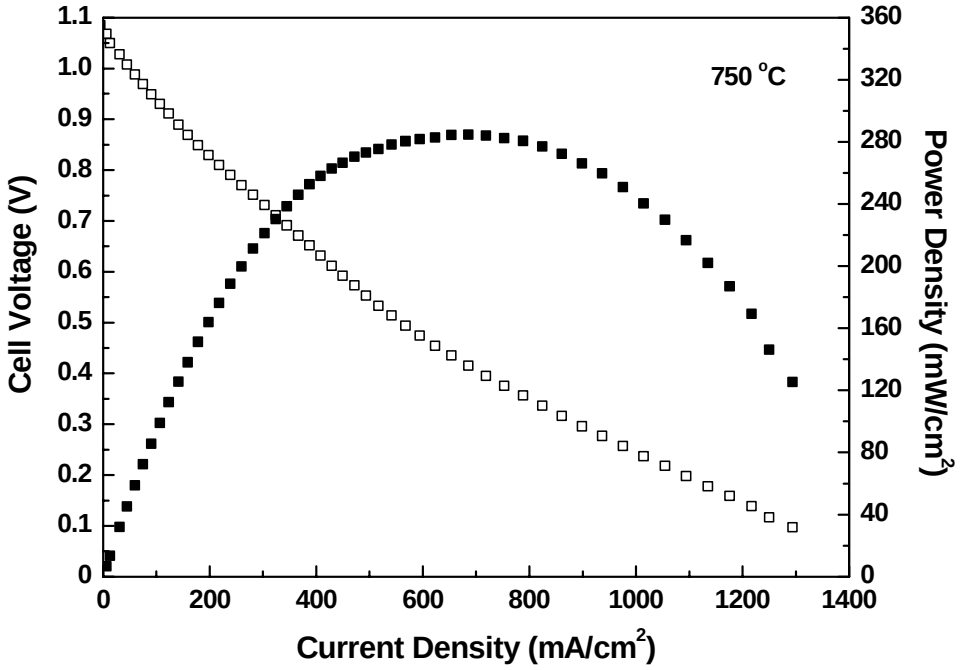

Figure 4-3 Cell voltage and power density as a function of current density for an anode-supported SOFC button cell with LSM-based cathode running on H_2-N_2 fuel.

4.1.2 Typical Sulfur Poisoning and Regeneration Behaviors for Electrolyte-Supported SOFC Button Cells

Figure 4-4 shows the typical sulfur poisoning and recovery behavior for an electrolyte-supported button cell with a nickel-YSZ cermet anode upon exposure to a fuel containing 100 ppm H_2S (i.e., pH_2S/pH_2 = 100 ppm = 10^{-4}) under a constant cell voltage of 0.6 V at 800 °C. As shown in the plot, the cell current density dropped from 252 mA/cm^2 to 214 mA/cm^2 in only ~1 h, and the majority of that drop, i.e., from 248 to 214 mA/cm^2, actually happened in only ~60 sec. Later, when H_2S was removed from the fuel stream, cell current first recovered quickly and then slowly. (The downward spike at ~145 h was due to fluctuation in flow rate upon the gas switch.) The recovery was not complete, and the cell performance stabilized at ~96% of the initial value after 50 h of

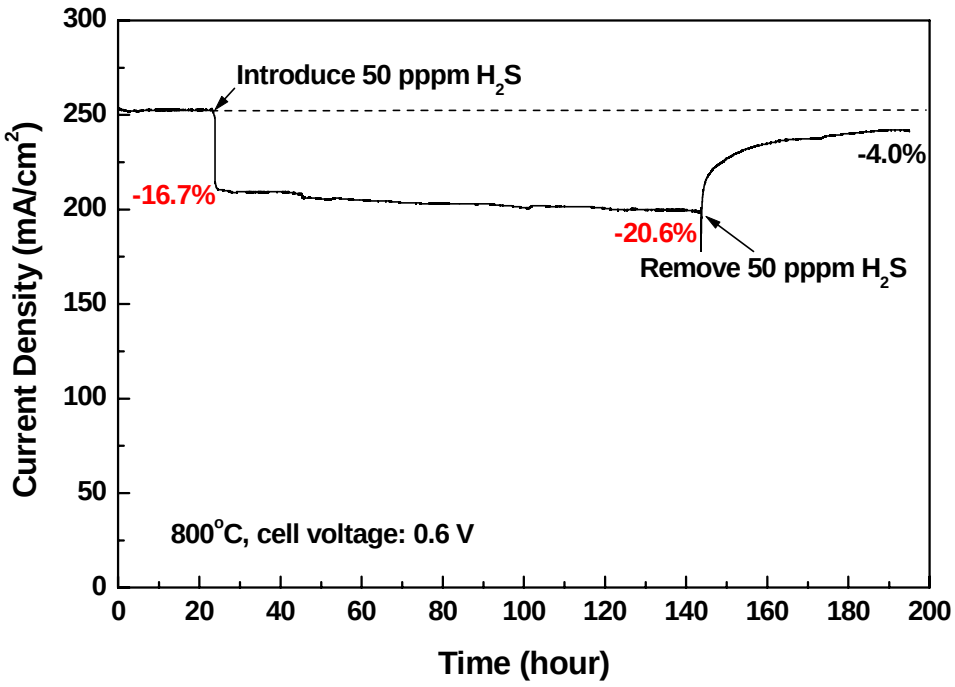

Figure 4-4 Cell current density versus time for an electrolyte-supported SOFC button cell operated with constant potential of 0.6 V at 800 °C when 50 ppm H_2S was introduced into and removed from the fuel of 50% H_2/1.5% H_2O/48.5% N_2, adopted from Zha, Cheng, and Liu (2007) with modifications.

regeneration. In Figure 4-4, after the initial 16.7% quick poisoning that lasted for less than 1 h, there also appeared to be a second stage, slower but continuous performance drop (up to -4%) in the next 120 hours, which seemed to correspond to the permanent damage to the cell.

4.1.3 Influence of H_2S Concentration and Temperature on the Sulfur Poisoning Behavior

4.1.3.1 Measurements of Cell Power Output

The influences of H_2S concentration and temperature on the observed sulfur poisoning behavior were systematically investigated over a wide range of H_2S concentration and temperature that were related to real fuel cell operation condition. It

was found that when H_2S concentration decreased from 100 ppm to 2 ppm, the observed sulfur poisoning behavior basically remained the same: the cell power output (or current in this case) still dropped first quickly and then gradually over time, as shown in Figure 4-5. Compared to the poisoning effect of 100 ppm H_2S, the extent of power output drop caused by 2 ppm H_2S was smaller with an initial degradation of 12.7% and the recovery process was faster and more complete: the cell performance stabilized to ~99% of the initial value.

Figure 4-6 shows plots of the measured relative cell power output drop, ΔP_r, due to sulfur poisoning versus H_2S concentration (pH_2S/pH_2) at temperatures from 700 to 900 ^oC. All data were collected based on the change in cell current after H_2S was

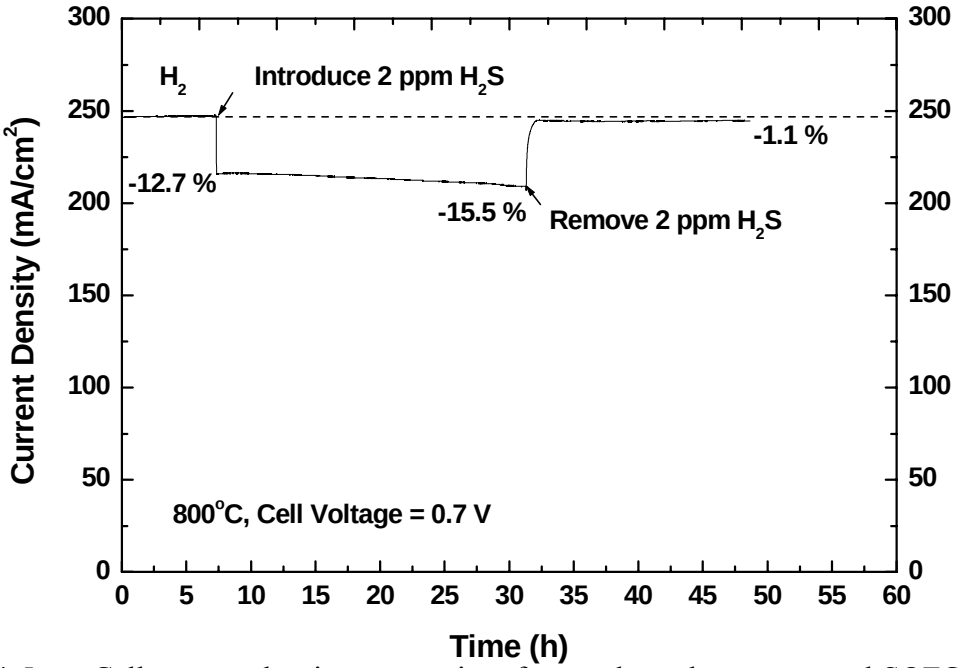

Figure 4-5 Cell current density versus time for an electrolyte-supported SOFC button cell operated with constant potential of 0.6 V at 800 ^oC when 50 ppm H_2S was introduced into and removed from the fuel of 50% H_2/1.5% H_2O/48.5% N_2, adopted from Zha, Cheng, and Liu (2007) with modifications.

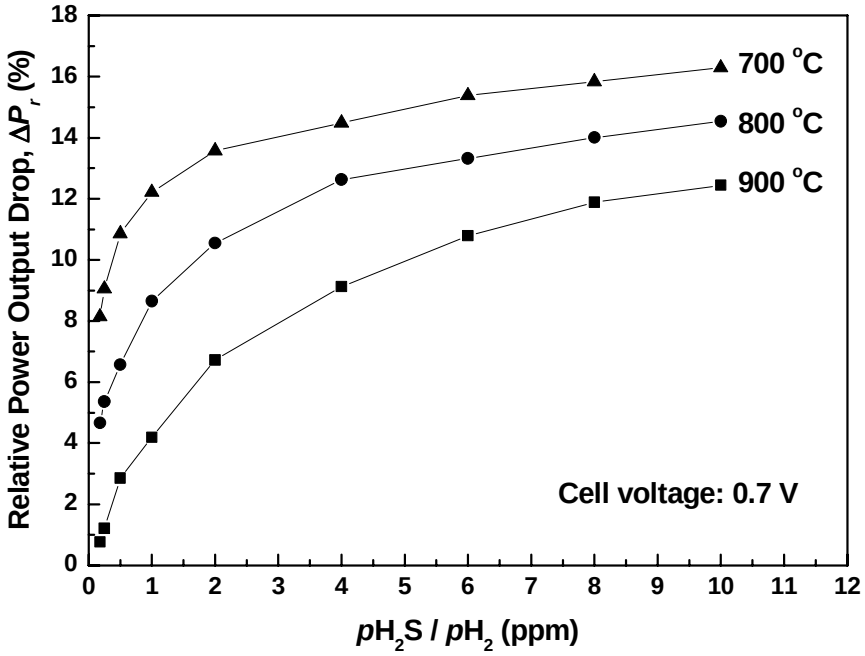

Figure 4-6 Relative cell power output drop versus pH_2S/pH_2 for an electrolyte-supported button cell operated with constant voltage of 0.7 V at 700, 800, and 900 oC, respectively, adopted from Zha, Cheng, and Liu (2007) with modifications.

introduced for 5 min (i.e., just after the quick poisoning stage as shown in Figures 4-4 and 4-5) for cells operated at constant voltage of 0.7 V. The fuel cell performance showed degradation even when pH_2S/pH_2 was as low as 0.18 ppm at all three temperatures. At a given temperature, the extent of sulfur poisoning increased first quickly and then slowly when H_2S concentration increased in the fuel. For a given H_2S concentration (e.g., pH_2S/pH_2 = 1 ppm), the measured relative cell power output drop was greater at lower temperature.

However, it was found that, as the cell temperature decreased further from 700 °C to 600 °C, the trend in relative cell power output drop with respect to H_2S concentration and temperature changed again. As shown in Figure 4-7, in the range of 600-700 °C, the increase in relative cell power output drop due to the increase in H_2S concentration

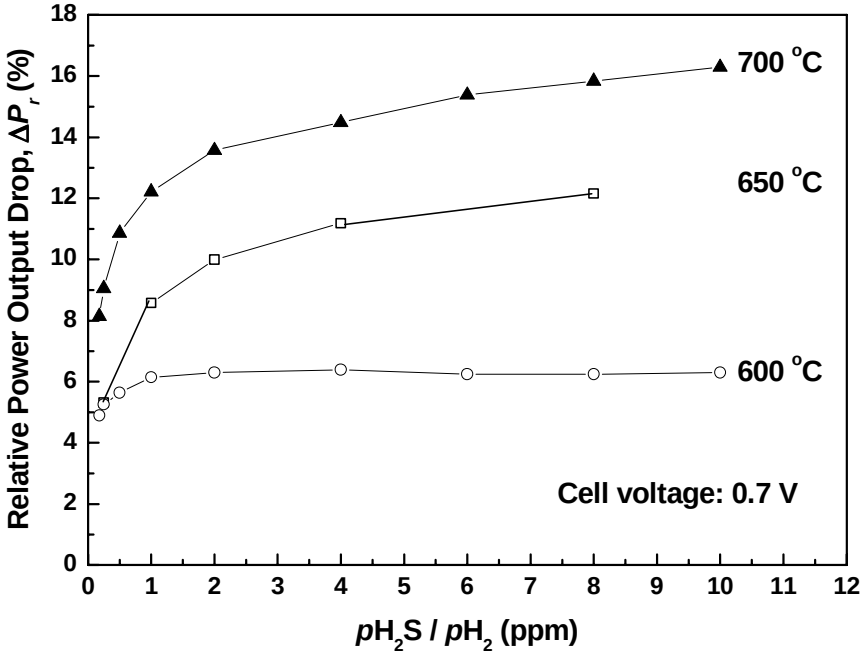

Figure 4-7 Relative cell power output drop versus $p\mathrm{H_2S}/p\mathrm{H_2}$ for an electrolyte-supported button cell operated with constant voltage of 0.7 V at 600, 650, and 700 °C, respectively.

became much less significant in the range of $p\mathrm{H_2S}/p\mathrm{H_2}$ =1 ppm and above. For example, at 600 °C, the relative cell power output drop seemed saturated at $p\mathrm{H_2S}/p\mathrm{H_2}$ of ~1 ppm, and further increase in H_2S concentration did not lead to further degradation. In addition, in the temperature range of 600-700 °C, as the temperature decreased, the relative cell power output drop did not increase in the rang of 700-900 °C, but decreased, as shown in Figure 4-7. The difference in the observed sulfur poisoning behavior in different temperature ranges will be discussed in detail later.

4.1.3.2 Measurements of Impedance Spectra

Figure 4-8(a) show some typical impedance spectra for an electrolyte-supported full cell under open circuit conditions when the anode was exposed to a fuel containing 0

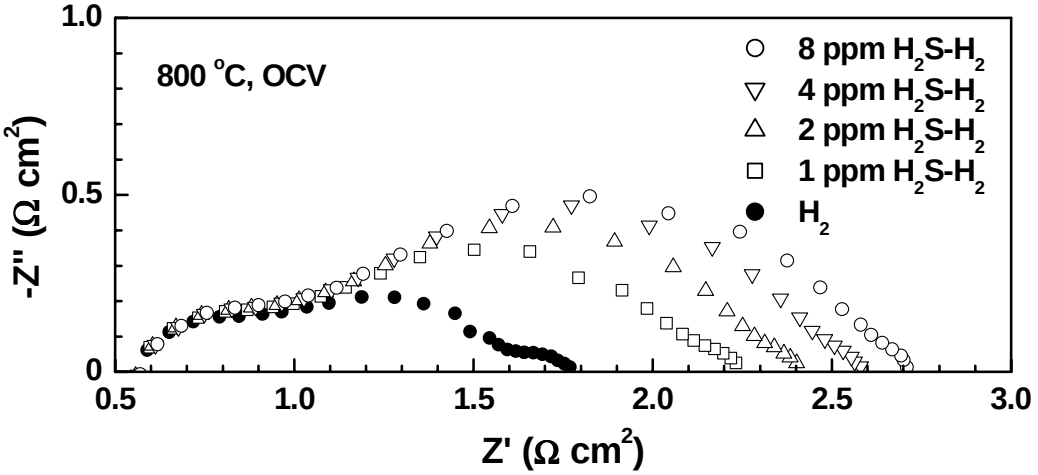

(a)

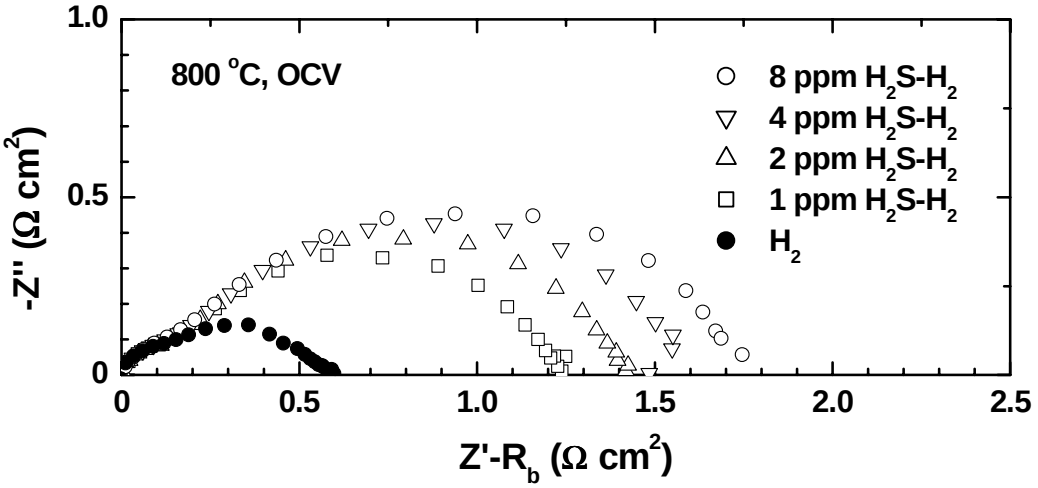

(b)

Figure 4-8 (a) Typical impedance spectra for the full cell (measured using a 2-electrode configuration), and (b) impedance spectra of the anode/electrolyte interface (measured using a 3-electrode configuration) under open circuit condition for an electrolyte-supported button cell operated 800 ^{o}C in fuels with 0, 1, 2, 4, and 8 ppm H_2S, adopted from Zha, Cheng, and Liu (2007) with modifications.

to 8 ppm H_2S at 800 ^oC. Clearly, the ohmic resistance (or bulk resistance) of the cell remained constant, but the changes in cell interfacial resistance were dramatic: the interfacial resistance increased from 1.22 Ωcm^2 to 1.68 Ωcm^2 (a 38% increase) when the fuel was switched from clean H_2 to H_2 containing only 1 ppm H_2S (pH_2S/pH_2 = 1 ppm). The relative increase in cell total interfacial resistance increased with H_2S concentration, which was consistent with the results shown in Figure 4-6. Further experiment using a reference electrode on the cathode side helped to isolate the change in the impedance spectrum for the anode/electrolyte interface, as shown in Figure 4-7(b). Unlike the observed cell power output that showed performance drop only in the range of 5-20% (as in Figure 4-16), the anode interfacial resistance increased by 100% from 0.6 Ωcm^2 to 1.24 Ωcm^2 when pH_2S/pH_2 = 1 ppm and by almost 200% to 1.74 Ωcm^2 when pH_2S/pH_2 = 8 ppm, revealing the real severity of the sulfur poisoning effect.

Figure 4-9 shows the impedance spectra of the cell before and after sulfur poisoning by 1 ppm H_2S at different temperatures in the range of 750–900 ^oC. The relative increase in total cell resistance varied from 10% at 900 ^oC, to 27% at 850 ^oC, and to 39% at 800 ^oC, also consistent with the data in Figure 4-6. However, as the temperature decreased further, the relative increase in cell total resistance due to sulfur poisoning by the same concentration of H_2S started to drop (e.g., 30% at 750 ^oC). Figure 4-10 shows that change in impedance spectra for a full cell at 600 ^oC, when the anode was subject to different concentrations of H_2S. Unlike the result at 800 ^oC (Figure 4-8(a)), the relative increase in cell resistance did not increase much as H_2S concentration increased from 1 to 8 ppm. The reason for the changed trend will be discussed later.

(a)

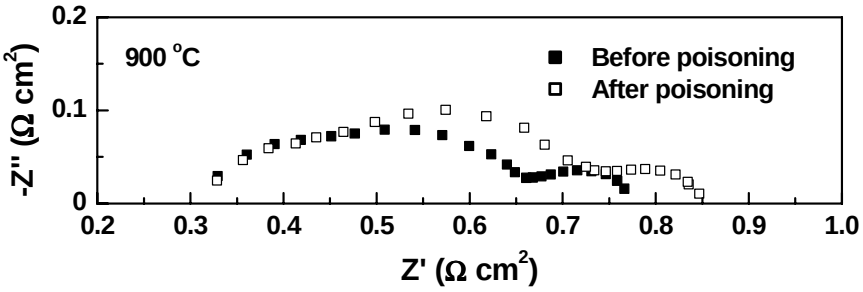

(b)

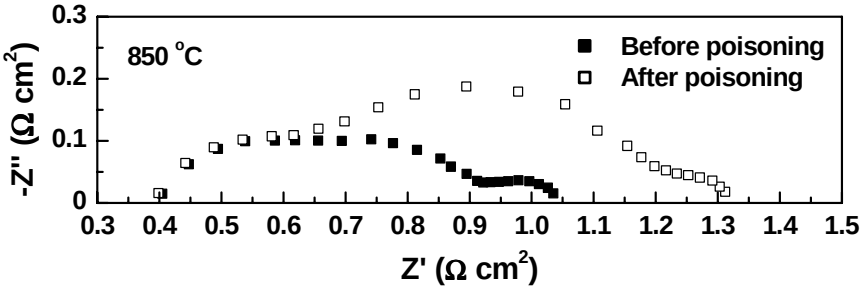

(c)

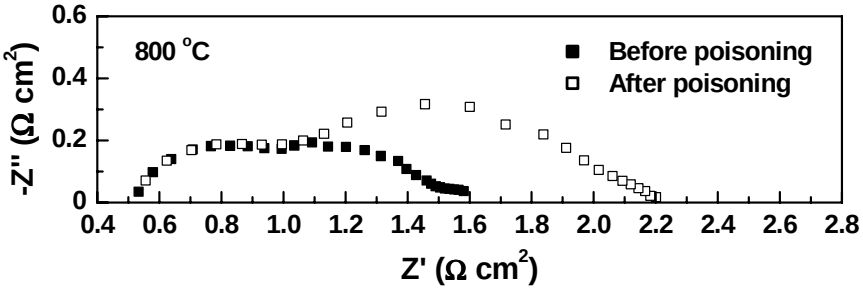

(d)

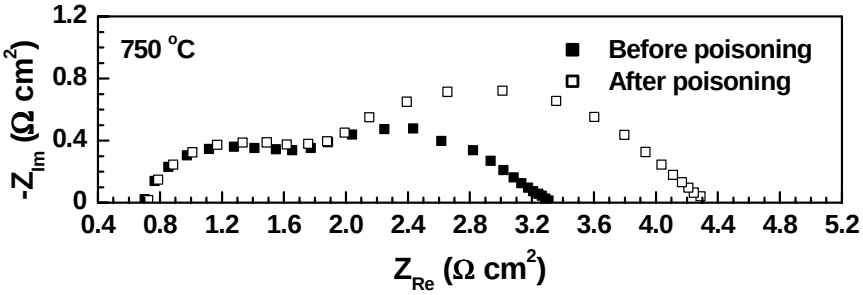

Figure 4-9 Typical impedance spectra (measured using a 2-electrode configuration) for an electrolyte-supported button cell before and after 1 ppm H_2S was introduced into the fuel stream at (a) 900 °C, (b) 850 °C, (c) 800 °C, and (d) 750 °C.

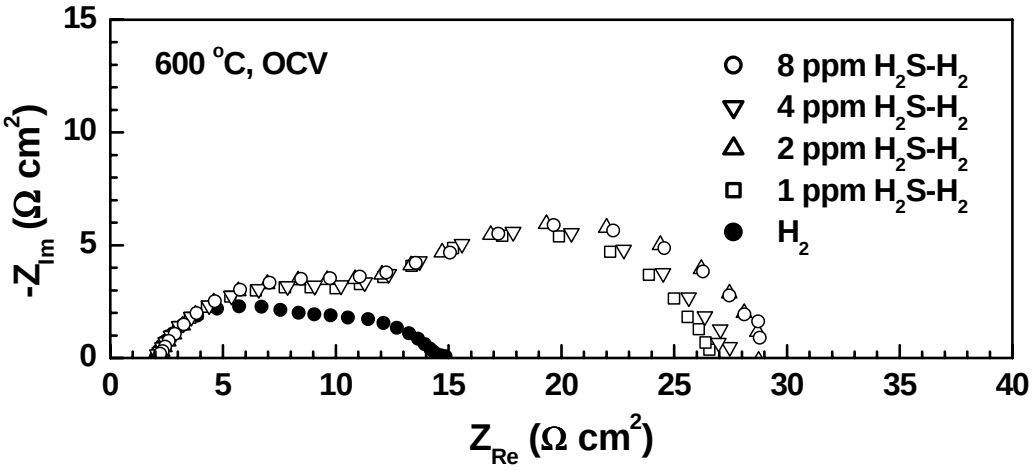

Figure 4-10 Typical impedance spectra (measured using a 2-electrode configuration) for an electrolyte-supported button cell under open circuit condition operated 600 °C in fuels with 0, 1, 2, 4, and 8 ppm H_2S.

4.1.4 Influence of Cell voltage and Current density on the Sulfur Poisoning Behavior

In addition to the phenomena that are fairly straightforward to characterize as shown before (i.e., influence of H_2S concentration and temperature), an apparent contradiction regarding the exact influence of cell voltage or current density on the observed sulfur poisoning behavior was found in this study. As stated, fuel cells could run either under constant voltage (potentiostatic) conditions, or under constant current (galvanostatic) conditions. An apparent contradiction came in when the sulfur poisoning behaviors observed under these two conditions were put together and compared. The following section will present the results of the study on the influence of cell current density and voltage on the observed sulfur poisoning behavior, and the resolution of the apparent contradiction.

4.1.4.1 A Contradiction in the Relative Cell Power Output Drop under Constant Current and Constant Voltage conditions

Figure 4-11(a) shows the measured relative drops in cell power output versus H_2S concentration for a cell was tested under constant current densities of 241 and 409 mA/cm^2, respectively. The measured relative power output drop values were smaller than those reported by Xia and Birss (2005) and by Sasaki et al. (2005 and 2006) but it was in line with the study by Trembly et al. (2006) at a similar temperature. (Xia and Birss (2005) reported that 10 ppm H_2S caused a cell voltage drop of 19.5% and 56.4% when the current density was 130 and 400 mA/cm^2, respectively, at 800 ^oC; Sasaki et al. (2005 and 2006) reported cell failure (i.e., 100% voltage drop) for a cell operated at a constant current density of 200 mA/cm^2 at 850 ^oC when it was exposed to 5 ppm H_2S.) Nevertheless, the observed trend is consistent with results reported by other groups (Singhal et al., 1986; Xia and Birss, 2005; Waldbillig et al., 2005): the measured relative drop in cell power output caused by sulfur poisoning was always *greater* when more current was drawn from the cell for all concentrations of H_2S tested.

In contrast, Figure 4-11(b) shows plots of measured relative drops in power output as a function of pH_2S/pH_2 when the cell was tested under a constant cell voltage of 0.535 V and 0.7 V, respectively. Contrary to the trend obtained under constant current conditions but consistent with that reported by Sprenkle et al. (2007), the measured relative drop in cell power output caused by sulfur poisoning was always *smaller* as the cell terminal voltage was reduced from 0.7 to 0.535 V (the corresponding cell current density before sulfur poisoning was 432 mA/cm^2 for 0.535 V and 260 mA/cm^2 for 0.7 V).

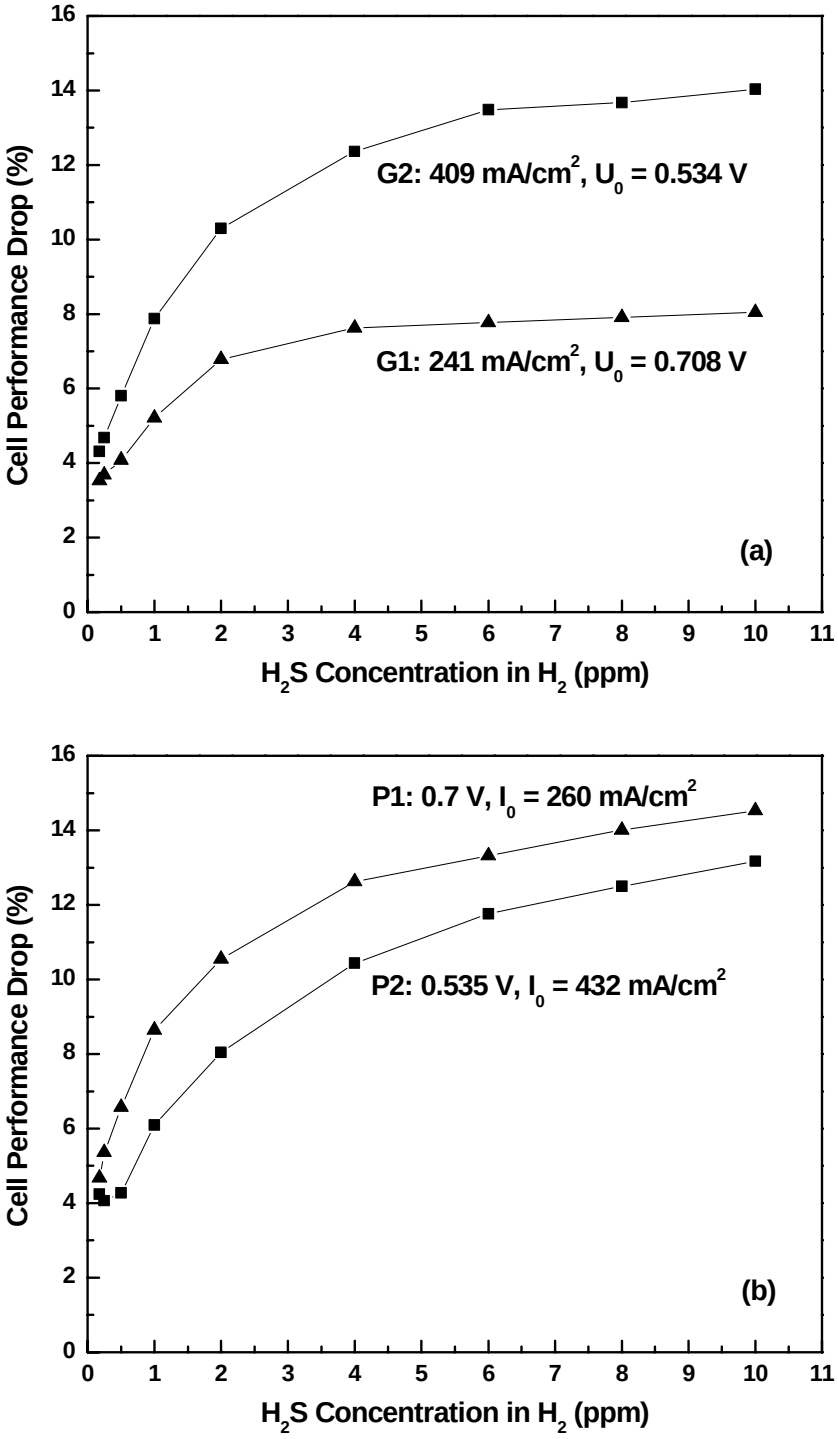

Figure 4-11 Measured relative cell power output drop versus $p\mathrm{H_2S}/p\mathrm{H_2}$ for cells operated under galvanostatic (a) and potentiostatic (b) conditions at 800 ^{o}C, from Cheng, Zha, and Liu (2007).

Now there appeared to be a contradiction: on one hand under the constant current condition, the measured relative drop in cell power output was always *greater* when more current was drawn from the cell, while on the other hand under the constant voltage condition, the relative drop in power output was always *smaller* when more current was drawn from the cell.

4.1.4.2 Resolution of the Apparent Contradiction

The resolution of the above contradiction is important because it is related to the interpretation of the sulfur poisoning and regeneration mechanism. It is also important for practical applications: the industrial teams would like to know whether a solid oxide fuel cell should be operated at lower cell voltage with higher current density or at higher voltage with lower current density to alleviate the sulfur poisoning process.

To solve this contradiction, it is realized that when a cell was poisoned by sulfur contaminants, the cell internal resistance increased. However, the contradiction was observed when comparing the measured relative cell power output drop (ΔP_r = Δ(Cell terminal voltage × Cell current), which was only an indirect representation of the change in cell due to sulfur poisoning. Therefore, the logical solution would be to compare the relative cell resistance increase, which could be obtained by either impedance measurements or by equivalent circuit analysis. In the following, the results from equivalent circuit analysis will be presented first, then the results from impedance measurement will be presented to provide verification of the circuit analysis.

- Equivalent circuit analysis

  For sulfur poisoning under the constant current (galvanostatic) condition, the cell

current, I, is kept constant, i.e., $I \equiv I_0$. Before switching from H_2 to H_2S-contaminated H_2, the cell terminal voltage, U_0, is given by

$$U_0 = E_0 - I_0 R_{cell\_0}, \tag{4-1}$$

in which E_0 is the open circuit voltage and R_{cell_0} is the total cell resistance before sulfur poisoning. After the cell is poisoned by H_2S, the cell total internal resistance changes from R_{cell_0} to $R_{cell\_0}+\Delta R_{cell}$, and the cell terminal voltage changes to

$$U = E_0 - I_0 (R_{cell\_0} + \Delta R_{cell}). \tag{4-2}$$

The relative decrease in cell power output, ΔP_r, is

$$\Delta P_r = \frac{I_0 (U_0 - U)}{I_0 U_0} = \frac{(E_0 - I_0 R_{cell\_0}) - [E_0 - I_0 (R_{cell\_0} + \Delta R_{cell})]}{U_0} = \frac{I_0 \Delta R_{cell}}{U_0}. \tag{4-3}$$

Consider that

$$I_0 = \frac{E_0 - U_0}{R_{cell\_0}}, \tag{4-4}$$

Equation (4-3) can be rewritten as

$$\Delta P_r = \frac{E_0 - U_0}{R_{cell\_0}} \cdot \frac{\Delta R_{cell}}{U_0} = \frac{\Delta R_{cell}}{R_{cell\_0}} \cdot \frac{E_0 - U_0}{U_0}. \tag{4-5}$$

Equation (4-5) shows that, under the constant current (galvanostatic) condition, the measured relative drop in cell power output (voltage in this case), ΔP_r, is a function of three variables: the relative increase in cell internal resistance ($\Delta R_{cell}/R_{cell\_0}$), the initial cell terminal voltage (U_0) before sulfur poisoning, and the cell open circuit voltage (E_0). From Equation (4-5), it is clear that $\Delta P_r < \Delta R_{cell}/R_{cell\_0}$ when $U_0 > 0.5\ E_0$ while $\Delta P_r > \Delta R_{cell}/R_{cell\_0}$ when $U_0 < 0.5\ E_0$. Rearrange Equation (4-5) and define $\Delta R_{cell\_r} = \Delta R_{cell} / R_{cell\_0}$, we have

$$\Delta R_{cell\_r} = \frac{\Delta R_{cell}}{R_{cell\_0}} = \Delta P_r \cdot \frac{U_0}{E_0 - U_0}. \tag{4-6}$$

Although, in this case, the trend of relative increase in cell resistance (ΔR_{cell_r}) could *not* be predicted directly based on the observed trend in relative cell performance drop (ΔP_r), the ΔR_{cell_r} values could be calculated using the E_0, U_0, and ΔP_r values measured in the experiment and the trend could be examined.

Similarly, for sulfur poisoning under the constant voltage (potentiostatic) condition, the cell terminal voltage U is kept constant, i.e., $U \equiv U_0$. Before sulfur poisoning, the current passing through the cell is given by

$$I_0 = \frac{E_0 - U_0}{R_{cell\_0}}. \tag{4-7}$$

Upon poisoning by H_2S, the cell internal resistance changes from R_{cell_0} to $R_{cell\_0} + \Delta R_{cell}$, and the cell current changes to

$$I = \frac{E_0 - U_0}{R_{cell\_0} + \Delta R_{cell}}. \tag{4-8}$$

The relative decrease in cell power output, ΔP_r, is

$$\Delta P_r = \frac{U_0(I_0 - I)}{U_0 I_0} = \frac{\dfrac{E_0 - U_0}{R_{cell\_0}} - \dfrac{E_0 - U_0}{R_{cell\_0} + \Delta R_{cell}}}{\dfrac{E_0 - U_0}{R_{cell\_0}}} = \frac{\Delta R_{cell}}{R_{cell\_0} + \Delta R_{cell}}, \tag{4-9}$$

or

$$\Delta P_r = \frac{\Delta R_{cell} / R_{cell\_0}}{1 + \Delta R_{cell} / R_{cell\_0}}. \tag{4-10}$$

Equation (4-10) shows the relative drop in cell power output (current in this case), ΔP_r, is an explicit function of the relative increase in cell internal resistance (ΔR_{cell_r} =

$\Delta R_{cell}/R_{cell\_0}$) under the potentiostatic condition, and ΔP_r will always be smaller than ΔR_{cell_r}. From Equation (4-10), the relative change in cell internal resistance, ΔR_{cell_r}, could be directly deduced from the relative change in cell performance:

$$\Delta R_{cell\_r} = \frac{\Delta R_{cell}}{R_{cell\_0}} = \frac{\Delta P_r}{1-\Delta P_r} = \frac{1}{1-\Delta P_r} - 1. \tag{4-11}$$

Equation (4-11) allows for the calculation of the relative increase in cell resistance due to sulfur poisoning (ΔR_{cell_r}) from the observed relative power output loss; it also indicates the relative increase in cell resistance (ΔR_{cell_r}) is a monotonomous function of the relative drop in cell performance, which means that ΔR_{cell_r} is smaller when ΔP_r is smaller. The second observation is important in that, based on the observation that the relative drop in cell power output is smaller when the cell current is higher (or the cell voltage is closer to short circuit condition, see Figure 4-11(b)), it can be inferred that the relative increase in cell resistance is also smaller when cell current is higher under the constant voltage (potentiostatic) condition.

Using the relationship obtained above for sulfur poisoning under constant current (galvanostatic) and constant voltage (potentiostatic) conditions, we can evaluate whether the sulfur poisoning behavior is consistent in terms of the relative increase in cell resistance under both conditions. Figure 4-12 shows plots of the relative cell resistance increase calculated from the data in Figure 4-11 using Equations (4-6) and (4-11) as a function of H_2S concentration for both galvanostatic (a) and potentiostatic (b) conditions. Clearly, there is no contradiction in this case: the relative increase in cell resistance

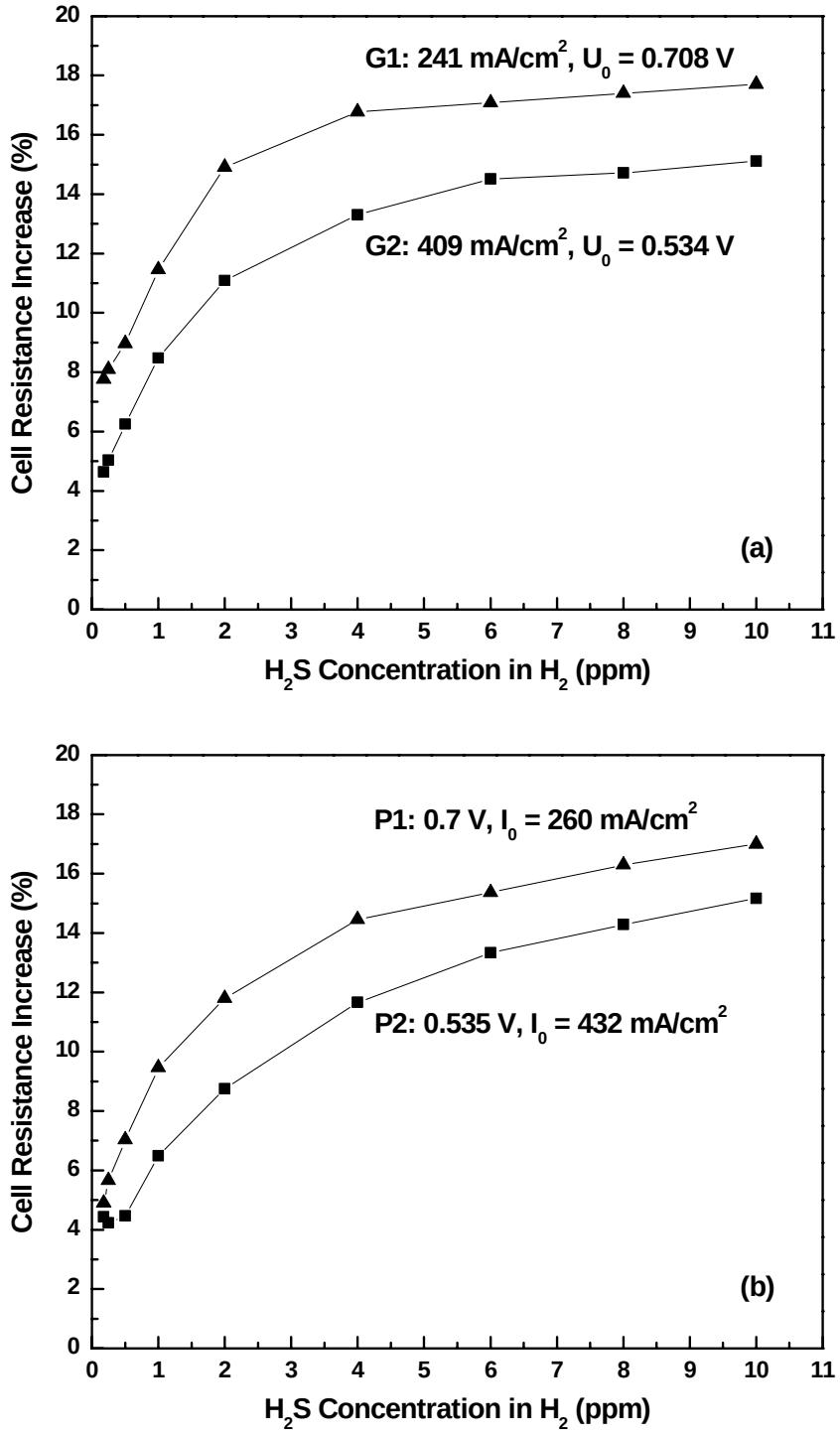

Figure 4-12 Calculated relative cell power output drop versus $p\mathrm{H_2S}/p\mathrm{H_2}$ for cells operated under galvanostatic (a) and potentiostatic (b) conditions using the data in Figure 4-11 at 800 ^{o}C, from Cheng, Zha, and Liu (2007).

(ΔR_{cell_r}) is always *smaller* when the cell current is higher or the cell terminal voltage is lower (closer to short circuit condition) no matter whether the sulfur poisoning experiment was carried out under the constant current (galvanostatic) or the constant voltage (potentiostatic) condition.

- Verification using impedance spectroscopy

To further verify the agreement obtained from the equivalent circuit analysis described above, experiments were carried out to directly measure the change in cell resistance using impedance spectroscopy before and after sulfur poisoning under both constant current (galvanostatic) and constant voltage (potentiostatic) conditions. Figures 4-13 and 4-14 show typical impedance spectra before and after sulfur poisoning under constant current and constant voltage conditions, respectively. Table 4-1 summarizes the relative losses in power output and the corresponding relative increases in cell resistance, both experimentally measured and calculated using Equations (3-6) or (3-11). Under both constant current (galvanostatic) and constant voltage (potentiostatic) conditions, the relative increase in cell internal resistance (ΔR_{cell_r}) was indeed smaller when the cell current density was higher (or when the cell terminal voltage is lower), even though the measured relative drops in cell power showed opposite trends when measured under these two conditions.

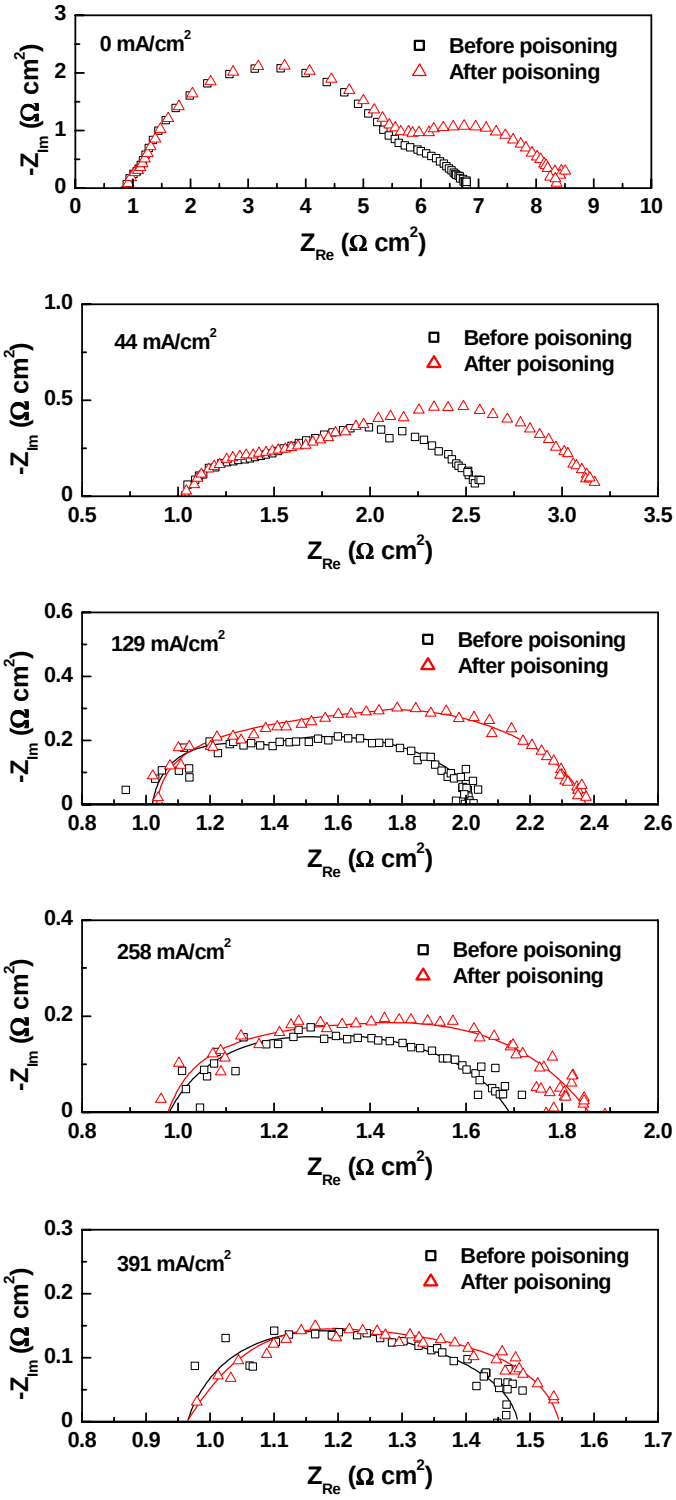

Figure 4-13 Comparison of impedance spectra for an electrolyte-supported cell operated at a constant current density of 0, 44, 129, 258, and 391 mA/cm^2 before and after 10 ppm H_2S was introduced into the fuel flow at 800 ^oC, from Cheng, Zha, and Liu (2007).

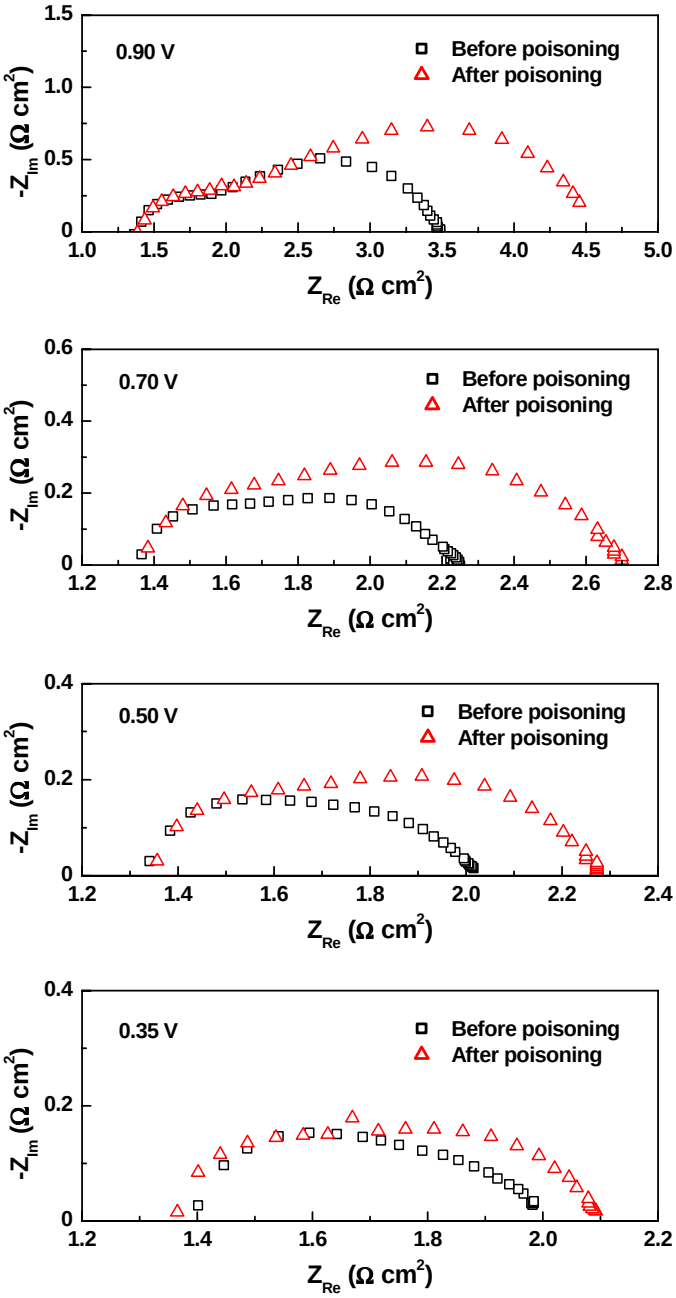

Figure 4-14 Comparison of impedance spectra for an electrolyte-supported cell operated at a constant voltage of 0.90, 0.70, 0.50, and 0.35 V before and after 10 ppm H_2S was introduced into the fuel flow at 800 ^{o}C, from Cheng, Zha, and Liu (2007).

Table 4-1 Relative performance loss, ΔP_r, relative cell resistance increase, ΔR_{cell_r}, (both calculated using Equations (4-6) and (4-11) and experimentally measured), and relative cell interfacial resistance increase, ΔR_{i_r}, for the poisoning of Ni-YSZ anode caused by 10 ppm H_2S under constant current and constant voltage conditions, from Cheng, Zha, and Liu (2007).

i (mA/cm^2)	U_0 (V)	Measured ΔP_r	Calculated ΔR_{cell_r}	Measured ΔR_{cell_r}	Measured ΔR_{i_r}
44	0.947	4.3%	29.1%	21.7%	36.2%
129	0.756	7.7%	17.6%	15.2%	26.9%
258	0.569	13.6%	15.0%	7.9%	18.2%
391	0.376	21.8%	11.6%	3.0%	8.0%
U (V)	i_0 (mA/cm^2)	Measured ΔP_r	Calculated ΔR_{cell_r}	Measured ΔR_{cell_r}	Measured ΔR_{i_r}
0.90	44	31.5%	46.0%	29.2%	50.0%
0.70	144	22.0%	28.2%	20.0%	50.0%
0.50	246	15.7%	18.7%	13.3%	38.7%
0.35	314	12.6%	14.4%	4.5%	18.5%

4.1.5 Influence of Cell Structure and Exposure Time

The sulfur poisoning behavior for anode-supported button cells were also studied. The focus were on (i) revealing the similarity and difference in the sulfur poisoning behavior between electrolyte-supported cells and anode-supported cells, and (ii) revealing the influence of exposure time especially over a period of long time (e.g., hundreds of hours or longer) on the sulfur poisoning behavior. The first problem had never been studied in the literature while the second one was of particular interest to researchers since it will determine whether a solid oxide fuel cell with the state-of-the art Ni-based anode-supported structure will survive in an H_2S-containing fuel. If there were no gradual degradation caused by sulfur over long time, then it may be possible for current SOFCs to operate in fuels containing trace amount of H_2S (e.g., 0.1 ppm) directly, which would simplify the system and drive down the cost although the cell power output would suffer somewhat. However, if there were gradual degradation caused by sulfur poisoning over long-term, deep desulfurization (e.g., below ~0.02 ppm for operation at 750 ^oC) would be necessary, which would negatively impact the prospect of wide application of SOFCs.

To achieve these goals, as stated in section 3.1.4.2, multi-cell long-term sulfur poisoning experiments were carried out using anode-supported cells in the multi-cell testing system built in our lab. The results indicated that, first, the duration of the quick poisoning depends on H_2S concentration for anode-supported cells. For example, when cells were running at a constant current density of 400 mA/cm^2, the duration of quick poisoning was ~40 h for 1 ppm H_2S, ~7 h for 5 ppm H_2S, and ~3.5 h for 10 ppm H_2S, respectively. Similarly, when cells were running at a constant current density of ~200

mA/cm^2, the duration of quick poisoning was ~9 h for 5 ppm H_2S and ~3.9 h for 10 ppm H_2S, respectively.

Second, both the relative drop in cell power output and the calculated relative increase in cell total resistance due to sulfur poisoning increased with increasing H_2S concentration. For example, for cells running at a constant current density of 400 mA/cm^2, the relative cell power output drop was 10%, 13% and 14.2% and the estimated relative cell total resistance increase was 27%, 30%, and 36% when the corresponding pH_2S/pH_2 value was 1, 5, and 10 ppm, respectively. This is consistent with the result obtained using electrolyte-supported cells, as shown earlier in sections 4.1.3.

Third, the relative drop in cell power output due to sulfur poisoning was always *greater* while the calculated relative increase in cell total resistance was always *smaller* when the cell current density was higher under the constant current (galvanostatic) condition. This is can be seen from the following examples: the relative cell power output drop due to 10 ppm H_2S measured under galvanostatic condition was 11% and 14% when the cell current density was 200 and 400 mA/cm^2, respectively, while the calculated relative cell resistance increase was 37% and 36%, respectively. This is also consistent with the study using electrolyte-supported cells, as shown in section 4.1.4.

Fourth, the extent of poisoning was significant even when the H_2S concentration was only 1 ppm: the fuel cell power output dropped 10% and the cell total resistance increased 27%, which indicated the relative increase in anode interfacial resistance could be much higher. This was consistent with results obtained using electrolyte-supported cells, as shown in Figure 4-11(a).

Fifth, long-term degradation for anode-supported SOFC button cells in fuels containing 1 ppm H_2S was not much more significant than that in the H_2S-free fuel and the regeneration of the anode-supported cells poisoned was almost complete considering the fact that cell performance recovered almost to the level before H_2S poisoning.

4.2 Discussion

- A quick poisoning process

As shown in Figures 4-4 and 4-5 for electrolyte-supported cells, the sulfur poisoning was rather quick: the bulk of the performance drop finished in only ~60 sec for electrolyte-supported cells. For anode-supported cells, the time required for the quick poisoning stage to finish was considerably longer, as stated in section 4.1.5, which is not surprising as the amount of nickel in the anode for an anode-supported cell was much larger compared to that in an electrolyte-supported cell: the thickness for anode-supported cell is usually ~500 μm or ~20 times of that for the anode in an electrolyte-supported cell.

No induction time was observed in this study for both electrolyte-supported and anode-supported cells: and the cell performance dropped as soon as H_2S was introduced into the fuel stream, which was different from the result by Xia and Birss (2005) who observed that their cell started to degrade after 10 ppm H_2S had been introduced into the fuel flow for ~1-2 h. Comparison of results with literature (e.g., Feduska and Isenberg, 1983; Singhal et al., 1986; Sasaki et al. 2005 and 2006) also indicated that generally, there is no induction period for the sulfur poisoning of the Ni-based anode. The most likely reason that Xia and Birss observed induction time was that, in their study, the H_2S

(10 ppm)-containing fuel was passed through a water bubbler to bring moisture, which would consume most of the H_2S in the fuel initially as H_2S dissolved in the water. Only after water was saturated when the actual H_2S concentration in the fuel delivered to the anode started to match the designated value.

The observed poisoning behavior was similar to that reported by Waldbillig et al. (2005) and Trembly et al. (2006) in terms of the rate and the extent of cell power output drop, but it was different from that reported by Sasaki et al. (2005 and 2006). Although Sasaki et al. used a very similar testing condition (i.e., 20 ppm H_2S at 800 and 850 ^oC under a constant cell current of 200 mA/cm^2), the degradation seen on their cells was much more severe and faster (i.e., 75% degradation in ~1000 sec). In addition, there was also a third stage of sulfur poisoning in Sasaki's study, in which the performance degradation accelerated again after ~1000 sec at cell voltage of ~0.18 V and failed quickly at ~1500 sec even in pure H_2 fuel with only 20 ppm H_2S. Considering that the cell performances are comparable with each other (250 mA/cm^2 at 0.6 V for Sasaki'e cell versus 0.7 V at 200 mA/cm^2 for cells in this study), the large difference must come from the difference in contribution of the anode to the entire cell resistance. It is likely that in Sasaki's experiment, the anode was not very good and became the limiting factor to the entire cell performance. As a result, poisoning of the anode led to drastic drop in cell total power output into very low cell voltage range (i.e., <0.3 V), which incurred oxidation of the Ni anode and drive the current to zero. This was explanation was also reasonable as such behavior was *not* observed not only in this study but also in most other researchers' studies (see Singhal et al., 1986; Xia and Birss, 2005; Waldbillig et al. 2005).

- Influence of H_2S concentration

The concentration of H_2S, in particular, the pH_2S/pH_2 ratio, would influence the sulfur poisoning behavior in several ways. First, it would influence the rate of poisoning or the time required for the quick poisoning stage to saturate, as higher concentration of H_2S would take less time to cover the active sites on the anode. This is especially true for anode-supported cells. To better illustrate this point, Figure 4-15 shows an enlargement of the quick poisoning stage for different concentrations of H_2S (1, 5, and 10 ppm) in a multi-cell testing. The time scale for the quick poisoning to reach stabilization was ~40, 7, and 3.5 h. (The upward trend for the cell performance after the quick poisoning was

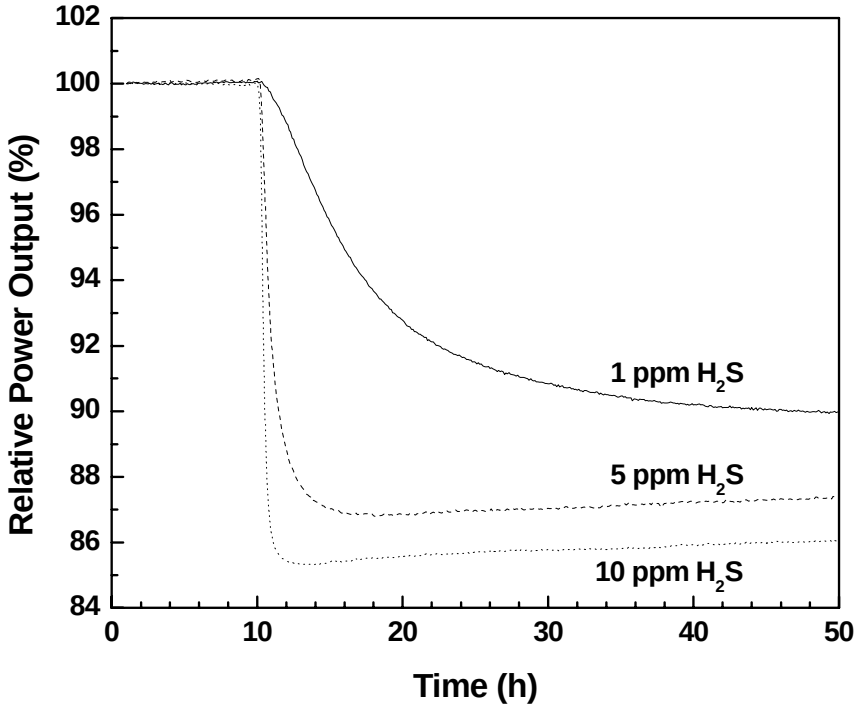

Figure 4-15 Relative power output versus time during the sulfur poisoning process for anode supported cells subject to fuel mixtures with H_2S concentration of 1, 5, and 10 ppm.

believed to be related to cell conditioning.) That the quick poisoning has a clear dependence on H_2S concentration indicates that even though sulfur poisoning was quick, it was still an accumulative process, in which sulfur species gradually accumulate on the anode surface, and induce performance degradation.

Similar observations regarding the dependence of rate for sulfur poisoning on H_2S concentration could be made from some recent studies by other groups. Table 4-2 compares the time for the quick poisoning stage in different studies. What is interesting is that the time for the quick poisoning stage was roughly inversely proportional to the H_2S concentration in all three studies. It is also noted that the time for the quick poisoning stage from different studies was in very good agreement with each other, which might be a coincidence as a result of similar flow rate for unit area.

However, the dependence of rate of poisoning on H_2S concentration is not very obvious for electrolyte-supported cells. As shown earlier in Figures 4-4 and 4-5, the performance degradation always reached the steady state within hundreds of seconds no matter whether the H_2S concentration was 100 ppm or 2 ppm. This was because the amount of active anode material in an electrolyte-supported cell was much less compared with anode-supported cells, and the anode would quickly reach a steady-state coverage

Table 4-2 Time in hour for the quick poisoning stage obtained from different studies.

	pH_2S/pH_2 (ppm)	0.1	1	5	10
Time for quick poisoning (h)	This study (200 mA/cm^2)	/	40	7	3.5
	Waldbillig et al. (2005)	200	30	8	/
	Sprenkle et a. (2007)	120	20	/	2

by sulfur species. This could also explain the claim by Matsuzaki and Yasuda (2000) that said "the time needed for the influence of the sulfide impurity to saturate was almost independent of the sulfide (H_2S) concentration," as the authors also used cells with an anode thickness of only ~25 μm.

The second influence of H_2S concentration on the sulfur poisoning behavior is on the relative cell performance drop. In the temperature range of 700-900 ^oC, the relative cell performance drop increased with increasing H_2S concentration in certain H_2S range of ~0.1 to 10 ppm, which could be seen from Figures 4-6, 4-7, and 4-11 for electrolyte supported cells. However, as cell temperature decreased to 600 ^oC range, the influence of H_2S concentration on the observed cell power output drop or cell resistance increase became less significant, especially in the range of ~1-10 ppm, as shown before in Figures 4-7 and 4-10.

The extent of cell performance degradation due to sulfur poisoning did not have linear dependence on H_2S concentration. Instead, the extent of poisoning increased first quickly in the range from zero to ~1 ppm and then gradually when the H_2S concentration increased above 1 ppm, as shown in Figures 4-6 and 4-11. This behavior was consistent with that reported by Matsuzaki and Yasuda (2000) and Sasaki et al. (2005), except that both studies only studied the trend at 1000 ^oC, while data from 700 to 900 ^oC, which was more relevant to practical fuel cell operating condition, were reported in this study.

It is interesting to note that if figures like 4-6 was re-plotted with the H_2S concentration plotted in log scale, an almost linear empirical relationship could be obtained between the measured cell performance drop and the log of H_2S concentration,

as shown in Figure 4-16. Towards the low concentration end, it seemed that if the trend lines were extrapolated, the practical limits for H_2S poisoning started to show up at

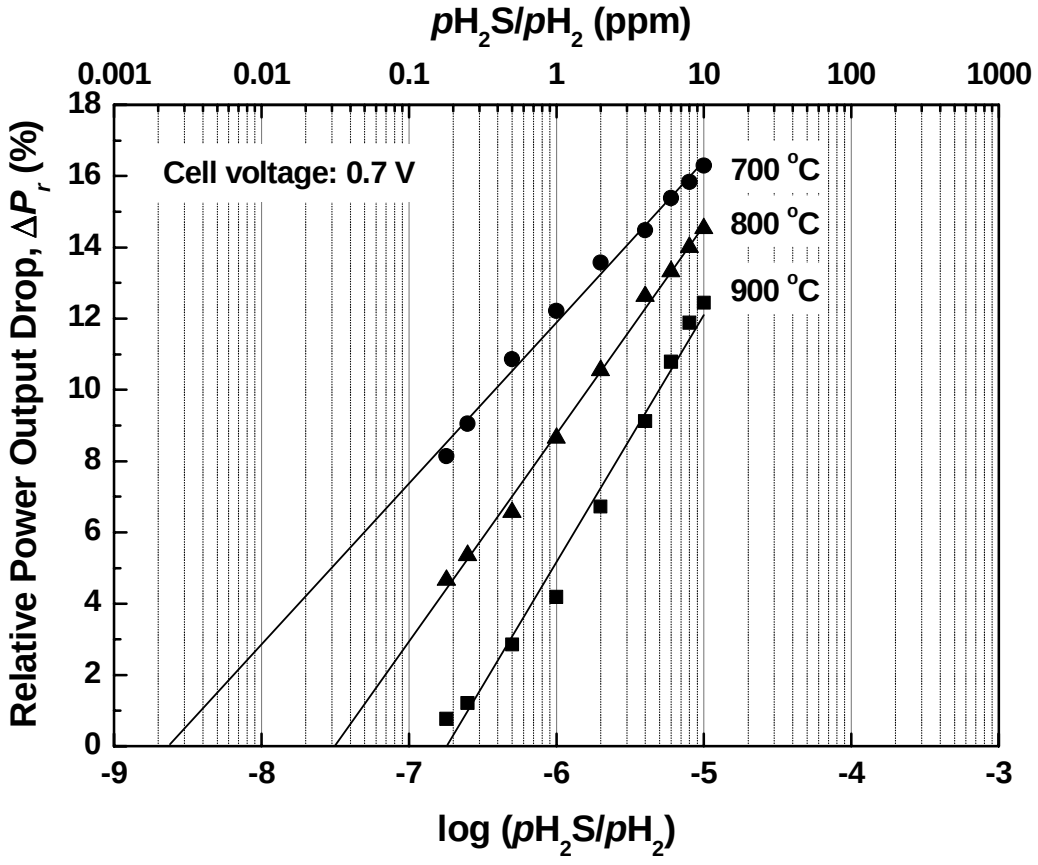

Figure 4-16 Relative power output drop due to sulfur poisoning versus log (pH_2S/pH_2) for electrolyte-supported cells tested under constant voltage of 0.7 V, plotted using the data shown in Figure 4-6.

different temperatures could be estimated. For example, according to Figure 4-16, the lower limit for pH_2S/pH_2 was estimated to be ~0.002, 0.03, and 0.2 ppm when the temperature was 700, 800, and 900 ^oC, respectively. These estimated lower limits for H_2S were in good agreement with the results determined by Mastuszaki and Yasuda using half-cells: they observed a critical H_2S concentration at which sulfur poisoning was zero was between 0.1 and 0.5 ppm at 900 ^oC, and between 0.02 and 0.05 at 750 ^oC. That

sulfur poisoning started to show up at concentration as low as 0.002 ppm (or 2 ppb) at 700 ^{o}C suggests the severity of the sulfur poisoning process, the strong affinity for sulfur on the nickel-based anode.

The limitation with the above presentation (Figure 4-16 is that it can only serve as a guidance of what the poisoning effect could be expected for electrolyte-supported cells. The actual value in relative drop in cell power output will vary due to cell architecture and operating condition such as fuel utilization. In addition, the extrapolation on the high H_2S concentration end must be careful as complication such as saturation coverage or the formation of bulk nickel sulfide would come, and complicate the trend.

- Influence of cell current density and voltage

The contradiction seen in section 4.1.4.1 regarding the sulfur poisoning behavior under constant current and constant voltage conditions was discovered by compiling and comparing the results from the literature and this study. For the results under constant current condition, both this study and studies from other groups (e.g., Singal et al., 1986; Xia and Birss, 2005; Waldbillig et al., 2005; Sprenkle et al., 2007) all found that the measured relative drop in cell power output caused by sulfur poisoning was always *greater* when more current was drawn from the cell for all concentrations of H_2S tested. However, it was found from this study and an analysis of Sprenkle's (2007) study that under constant voltage condition, the relative drop in cell power output caused by sulfur poisoning was always *smaller* when more current was drawn from the cell for all concentrations of H_2S tested.

This apparent contradiction had been successfully resolved using equivalent circuit analysis and verified using impedance spectroscopy. The results shown in Figures

4-12, 4-13, and 4-14 and Table 4-1 clearly indicate that the relative increase in total cell internal resistance is always *smaller* when the cell current density is greater or when the cell terminal voltage is lower, no matter whether the poisoning experiment was carried out under the constant current or constant voltage condition. The apparent contradiction seen for the trend in cell power output drop with respect to change in cell current density or voltage, as described in section 4.1.4.1 can be explained as follows. Under both testing conditions, the anode polarization resistance increases with the degree of sulfur poisoning. To maintain a constant cell current or terminal voltage, however, the effective resistance for the external circuit (i.e., the potentiostat/galvanostat used) has to be adjusted accordingly during the test to maintain the constant current or constant voltage condition. For example, in the galvanostatic mode, the effective external circuit resistance R_{ext} has to be *reduced* in order to maintain a constant cell current. Similarly, in the potentiostatic mode, the effective external circuit resistance R_{ext} has to be *increased* to maintain a constant cell terminal voltage. Both these effects are modulations of the original sulfur poisoning behavior, as represented by the relative increase in cell resistance, which leads to the difference in the observed drop in power output.

One last point should be noted is that, although from section 4.1.4, it seems that sulfur poisoning could be alleviated by reducing the cell terminal voltage under constant voltage condition. However, reducing the cell terminal voltage to alleviate sulfur poisoning is *not* practical from a system efficiency point of view. As stated earlier in section 2.1.2.2, when cells operate at low terminal voltage and high current density, the voltage efficiency would be lower, which means more chemical energy would be dissipated as heat, and it is *not* desirable.

- Influence of testing temperature

The influence of testing temperature in the range of 700-900 ^{o}C and above is quite clear: lower temperature leads to less extent of sulfur poisoning, as shown in Figures 4-6 and 4-9(a)-(c). This was consistent with that observed by Singhal et al. (1986), and Matsuzaki and Yasuda (2000 and 2001) using different cell structures.

However, below ~700 ^{o}C, things started to complicate again, as shown in Figures 4-7 and 4-9. The data for relative cell power output drop due to sulfur poisoning by 1-8 ppm H_2S at 600-900 ^{o}C was replotted in Figure 4-17 for easy comparison. The measured relative cell output drop did not increase further but actually decrease as temperature dropped below 700 ^{o}C to 650 and 600 ^{o}C. The reason for this is that, at lower temperature, the contribution of the anode resistance to the total resistance became

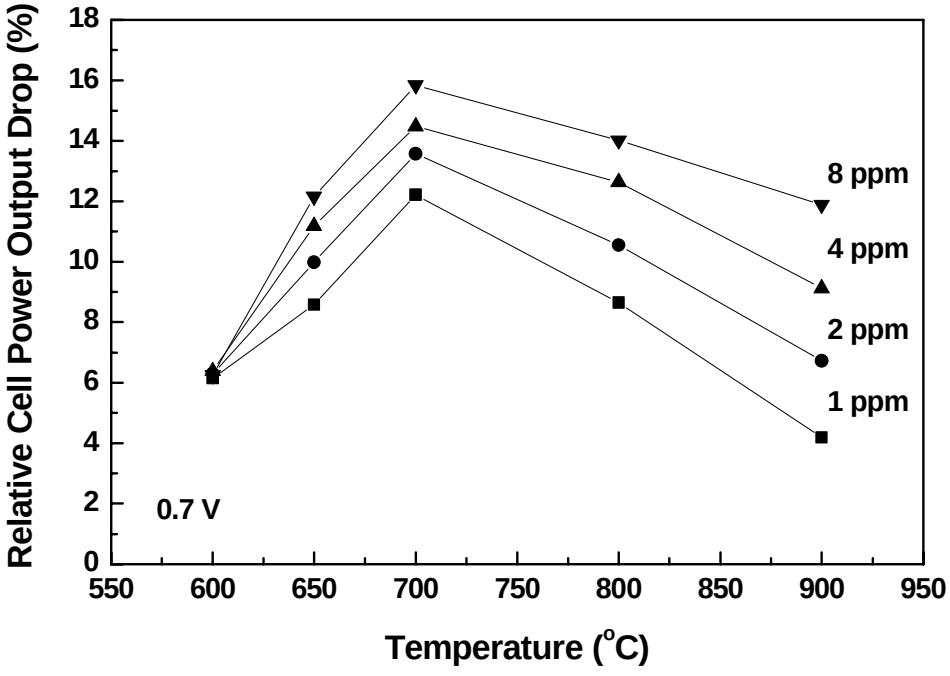

Figure 4-17 Relative cell power output drop due to sulfur poisoning versus temperature when the pH_2S/pH_2 value was 1, 2, 4, and 8 ppm, respectively.

smaller as both electrolyte and cathode resistance would increase dramatically as temperature decreased. Another complication at lower temperature is that, as discussed before, at lower temperature (e.g., 600 ^{o}C), the influence of H_2S concentration became much less significant at least in the range above ~1 ppm. The most likely reason for this is that the *saturation coverage* of the anode is probably at a concentration of ~1 ppm, which means further increase in H_2S concentration will not lead to much change in the surface coverage on the anode surface by sulfur species, and, therefore, would not change the relative power output drop much. This will be discussed further later in Chapter 5.

Nevertheless, the temperature effect on sulfur poisoning was against researchers since the lower the temperature, the cleaner the fuel has to be, which required ultra deep desulfurization. For example, at 700 ^{o}C, sulfur level has to be reduced to 2 ppb (i.e., $pH_2S/pH_2=2\times10^{-9}$) to completely avoid poisoning, which illustrates the high requirement for ultra deep desulfurization if hydrocarbon fuels are to be used in solid oxide fuel cells.

- Influence of exposure time

For electrolyte-supported cells, the poisoning was at least partially recoverable, as shown in Figures 4-4 and 4-5. This was consistent with that reported by Matsusaki and Yasuda even though they used different cell structure. In fact, complete recovery was observed when the exposure time was really short (i.e., on the scale of several minutes). Figure 4-18 shows that cell performance recovered fully after clean H_2 was flown for ~40 min for an electrolyte-supported cell poisoned for only a few minutes. These observations suggest that in a real SOFC system, a short leakage of H_2S for several minutes can be tolerated and will not cause irrecoverable damage. Such behavior was

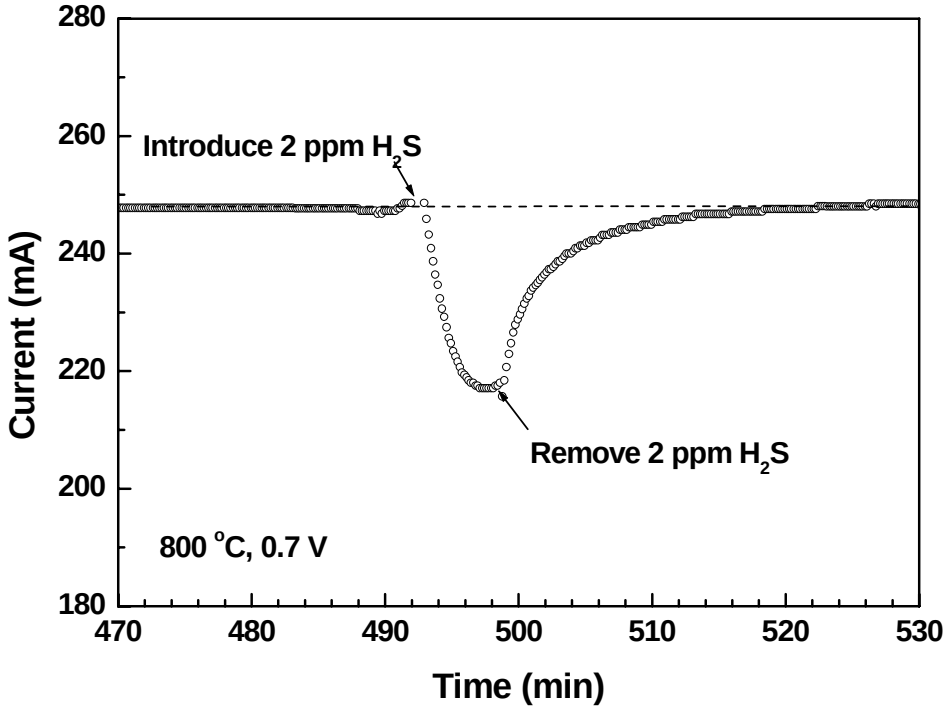

Figure 4-18 Change of cell current versus time for an electrolyte-supported cell when 2 ppm H_2S was introduced into and removed from the fuel stream in a short period of time, adopted from Zha, Cheng, and Liu (2007) with changes.

consistent with that observed by Sasaki et al. (2005) except that they used much higher temperature, which was expected to accelerate the recovery process (Matsuzaki and Yasuda, 2000).

However, as shown in Figures 4-4 and 4-5, for electrolyte-supported cells, after the quick poisoning stage, which lasted for only a few minutes, there also seemed to be a continued degradation that lasted for tens to hundreds of hours and showed no sign of saturation. Such gradual degradation also seemed to be correlated with incomplete recovery observed. Similar gradual degradation after the quick poisoning has been observed in the studies by Singhal et al. (1986) using cathode-supported cells and by Sprenkle et al. (2007) using anode-supported cell at very high current density. On the

other hand, there had been studies showing no gradual degradation at all for similar cells (Feduska and Isenberg, 1983) or a saturation of degradation after hundreds of hours (Iritani et al., 2001; Trembly et al., 2006). The nature of this observed gradual degradation was not clear, as stability test is very difficult to because of the time scale involved and the small changes involved. For practical applications, as most researchers are more concerned with the long-term behavior for state-of-the-art anode-supported cells, the results in the multi-cell long-term testing carried out in this study was of great value. There was *no* apparent slower degradation for anode-supported cells in fuels with 1 ppm H_2S for up to 1200 h, which was the longest ever reported in the literature for sulfur poisoning effect.

The possible explanations for the absence of the significant slower degradation in the long-term multi-cell testing are discussed below. First, some may argue that the total available anode was much larger in those tests compared with the tests using electrolyte-supported cells since the anode for anode-supported cells is 20-30 times thicker than that for electrolyte-supported cells. Therefore, maybe it needs longer for the gradual degradation to show up. However, considering that the testing time was on the order of 1000 h, which was also 50 times longer than that in previous studies using electrolyte-supported cells under similar condition (see Figure 4-5), this explanation was not satisfactory. However, this is still hard to believe, as those control samples did not show conditioning for that long. A third explanation is that there was *no* second stage sulfur poisoning effect for anode-supported cells at least under the conditions investigated. To completely solve this problem, even longer multi-cell testing using even higher concentration H_2S might be required and the cell performance must be stabilized before H_2S introduction.

- Influence of cell structure

The short-term sulfur poisoning behavior was consistent for all types of cell structures including electrolyte-supported full cells (Sasaki et al., 2005 and 2006; this study), anode-supported full cells (Sprenkle et al. 2007; this study), cathode supported full cells (Singhal et al., 1986), and even half cell (Dees et al., 1987; Matsuzaki et al. 2000). The only difference is about the long-term sulfur poisoning behavior. While it seems that second-stage slower degradation that lasted for hundreds of hours for thin anode was sometimes observed (Singhal et al., 1986; this study), it was not obvious for SOFCs with thick anodes, as in this study.

- Influence of testing method

The methods of electrochemical testing also have significant influence on the sulfur poisoning behavior observed and perceived. For example, in Figures 4-6, 4-7, and 4-11 or Table 4-1, the relative power output drop (ΔP_r) was not too big: at 800 ^{o}C 1 ppm H_2S only caused a power output drop of 8.8%, which seemed to be acceptable. However, that is only partial representation of the real poisoning effect, as the effect of poisoning was buried by the large bulk resistance and cathode side polarization. If the anode interfacial resistance was examined, as in Figure 4-8, the extent of poisoning was rather dramatic: at 800 ^{o}C, 1 ppm H_2S lead to a 107% increase in the anode interfacial resistance.

Another example for the influence of testing method on the observed sulfur poisoning behavior is on the testing under constant current versus constant voltage conditions. The measurements under both conditions provide useful information about sulfur poisoning: measurements under constant voltage (potentiostatic) conditions have

the advantage that the observed trend in current change is consistent with that in the actual cell resistance change. However, cell current drops as the anode is poisoned by sulfur, leading to an increase in cathode polarization resistance but a decrease in cathode overpotential, which increases the difficulty in analyzing the kinetic information. In comparison, under the constant current (galvanostatic) condition, because the cathode process can be assumed not to change much at least during the quick poisoning process, the measured increase in cell terminal potential and cell resistance could be directly regarded as the increase in anode overpotential and polarization resistance. Therefore, unless the cathodic polarization can be separated from the anodic polarization (such as when using a three-electrode configuration), constant current (galvanostatic) condition is better for both impedance and cell power output measurements.

4.3 Summary

To summarize this Chapter, the observations had been made about the sulfur poisoning behavior for solid oxide fuel cells with Ni-YSZ cermet anodes:

1) It is a very quick process.
2) Both the rate of sulfur poisoning and the extent of sulfur poisoning increase with increasing H_2S concentration until saturation was reached.
3) The extent of sulfur poisoning increased with decreasing temperature in the range of 700 – 900 ^{o}C. At temperature below ~700 oC, the observed relative sulfur poisoning effect started to decrease due to greater contribution of the electrolyte resistance and the cathode resistance.

4) The extent of sulfur poisoning, as measured by the relative increase in cell resistance increase, always decreases when cell current density increases or cell terminal voltage decreases (towards short circuit condition) even though the measured relative decrease in cell power output will show different trends when measured under the constant current versus the constant voltage condition.
5) Long-term gradual degradation due to low concentration of sulfur for anode-supported cells was not as significant as that for electrolyte-supported cells.

CHAPTER 5

THE MECHANISMS OF INTERACTIONS BETWEEN SULFUR AND Ni-YSZ CERMET ANODES

In this chapter, the investigation into the mechanism for the interactions between sulfur (in the form of H_2S) and the conventional Ni-YSZ cermet is described, focusing on probing and mapping the changes on the anode surfaces upon exposure to H_2S using both ex situ and in situ techniques. The apparent contradiction between observations from ex situ characterizations and thermodynamic considerations will be resolved by in situ experiments. Finally, the sulfur poisoning mechanism will be discussed based on available results from phenomenological electrochemical experiments and theoretical calculations.

5.1 Results

5.1.1 Characterization of the As-Prepared Ni-YSZ Composite Sample

Figure 5-1 (a) shows an optical micrograph of the polished surface of a dense Ni-YSZ composite. The bright, often isolated regions are Ni, and the gray regions are YSZ. Figure 5-1(b) shows the typical Raman spectra taken from the Ni and the YSZ regions. While the Raman spectrum for the Ni region is essentially featureless, the Raman spectrum for the YSZ region has one strong band at ~623 cm^{-1} and several weaker bands or shoulders at 288, 320, 353, 374, 488, and 697 cm^{-1}. The appearance of multiple bands for the YSZ phase indicates that the surface of the YSZ is not a perfect cubic structure but has tetragonal or monoclinic distortions (Liu, et al., 1988; Sekulic et al., 1997; Moon

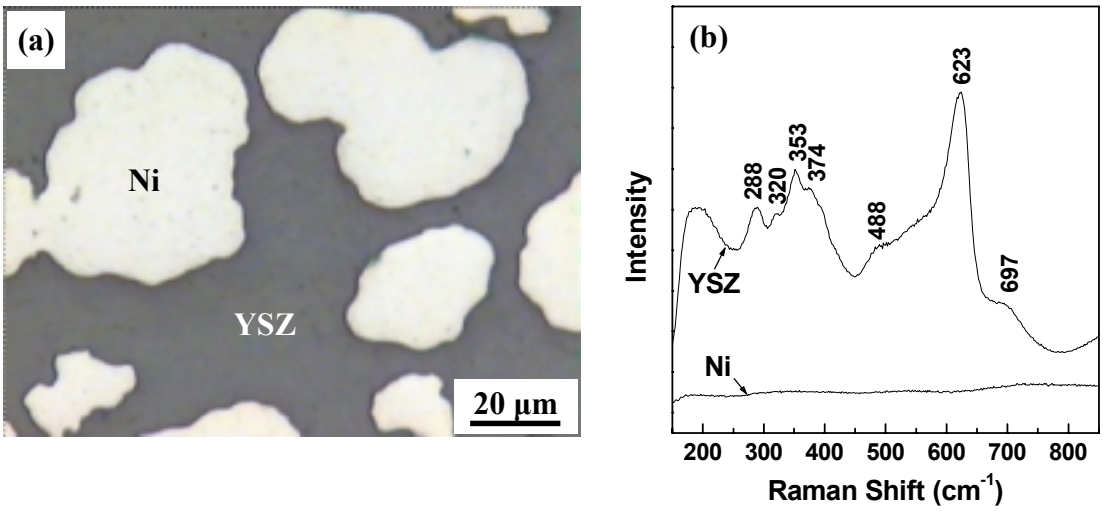

Figure 5-1 (a) An optical microscopy image and (b) the corresponding Raman spectra from the YSZ and the Ni region on a polished surface of an as-prepared Ni-YSZ composite sample, from Cheng and Liu (2007).

et al., 2001; Li et al., 2002). The Ni-YSZ composite was used to mimic the conventional porous Ni-YSZ cermet anode for an SOFC as described in section 3.2.1.

5.1.2 Ex situ Characterizations of the Ni-YSZ Composite After Exposure to H_2S-Containing Fuel

5.1.2.1 Changes in Sample Morphology

Figure 5-2 shows the optical and SEM micrographs of a nickel-YSZ composite exposed to a fuel mixture of 50 ppm H_2S/50% H_2/1.5% H_2O/48.5% N_2 for 48 h and then cooled down gradually in the furnace while being exposed to the same fuel. Surprisingly, after the exposure to fuels containing only ppm level H_2S, the appearance of the Ni surface changed dramatically. Compared to Figure 5-2(a), the color of the nickel surface changed from metallic white to brown (Figure 5-2(a)) or metallic yellow (Figure 5-2(b)). In some regions, the edges of Ni particles rose above Ni and YSZ (Figures 5-2(a) and 5-

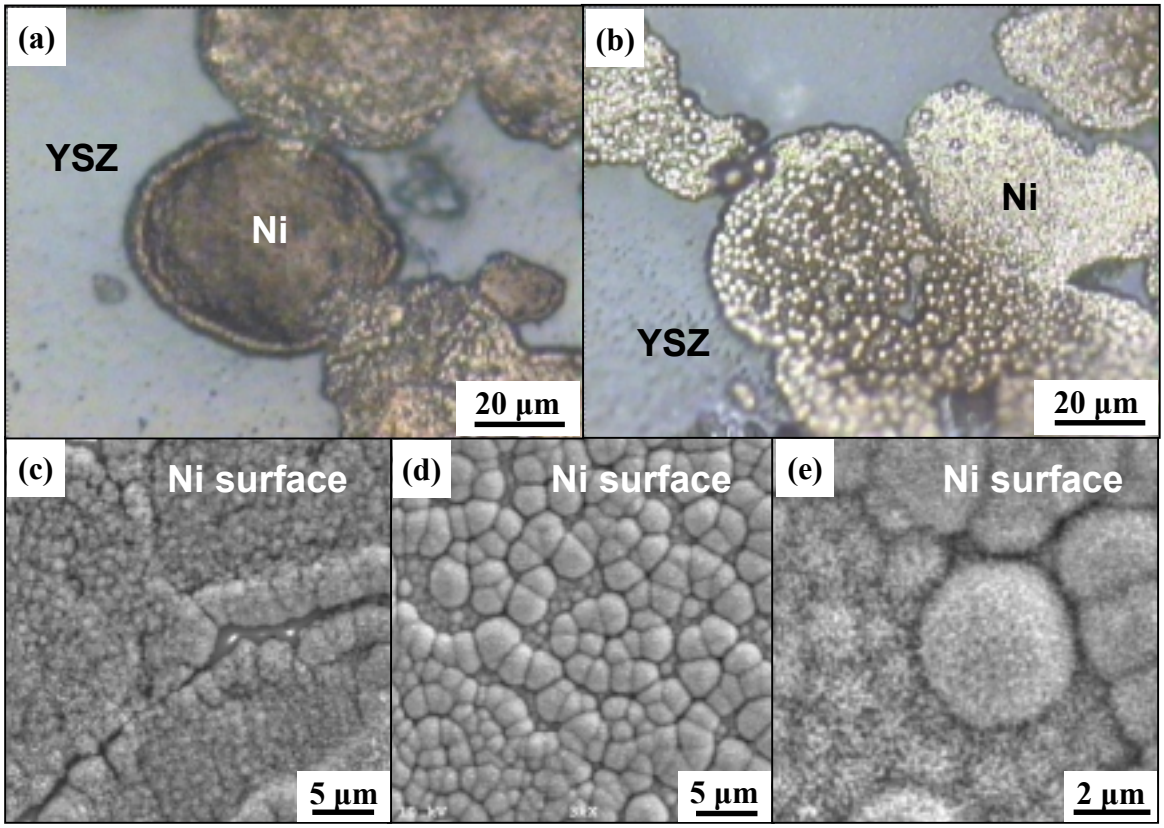

Figure 5-2 Optical microscopy (a, b) and SEM (c, d, e) images of the Ni-YSZ composite after exposure to an H_2S-containing fuel (50 ppm H_2S/1.5% H_2O/48.5% N_2/50% H_2) at 800 ^oC for 48 h, from Cheng and Liu (2007).

2(c)) while in other regions, the Ni surfaces were covered by micron-scale, sphere-like structures (Figures 5-2(b), (d), and (e)). The SEM images showed that the surfaces of the spheres and the regions in between were composed of submicron-scale, irregular-shaped particles (Figures 5-5(d) and 5-2(e)). Similar morphology change were also observed for samples that were exposed to 100 ppm H_2S at 800 ^oC for a shorter period of time, e.g., 2 h 45 min under the same heating and cooling procedure, as shown in Figure 5-3, and for samples that were exposed to 100 ppm H_2S at 600 ^oC for 18h, as shown in Figure 5-4. The dramatic morphology change of the nickel surfaces suggested that nickel reacted with H_2S to form bulk nickel sulfides.

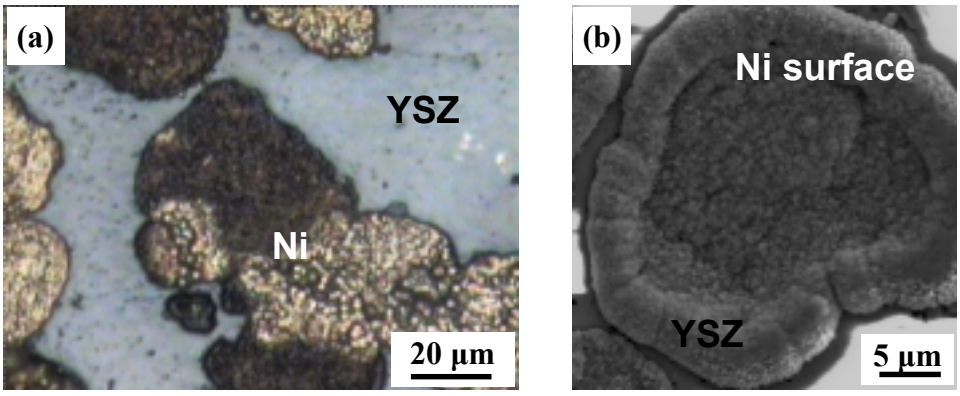

Figure 5-3 Optical microscopy (a) and SEM (b) images of the Ni-YSZ composite after exposure to an H_2S-containing fuel (50 ppm H_2S/1.5% H_2O/48.5% N_2/50% H_2) at 800 ^oC for 2 h 45 min.

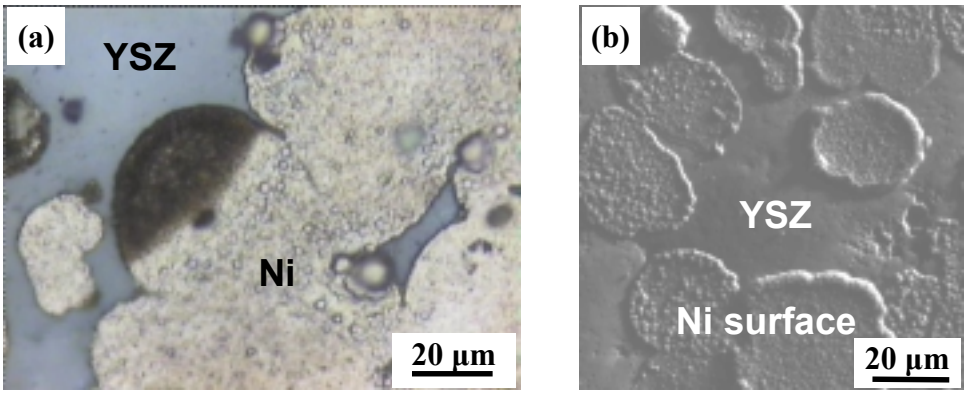

Figure 5-4 Optical microscopy (a) and SEM (b) images of the Ni-YSZ composite after exposure to an H_2S-containing fuel (50 ppm H_2S/1.5% H_2O/48.5% N_2/50% H_2) at 600 ^oC for 18 h.

5.1.2.2 Accumulation of Sulfur on the Nickel Surface

The presence of sulfur on nickel surface was confirmed using EDX. Figure 5-5 shows the low magnification SEM image and the corresponding Zr- and S-elemental maps of the Ni-YSZ composite exposed to 50 ppm H_2S/50% H_2/1.5% H_2O/48.5% N_2 at 800 ^oC for 48 h and then cooled down gradually in the furnace while being exposed to the same gas mixture. The distributions of sulfur and zirconium complement one another, indicating that sulfur selectively attacks nickel in the composite. No sulfur could be detected in the YSZ region, which was consistent with the observation that the morphology of YSZ region did not show significant change. Similar EDX-elemental maps were also obtained for samples exposed to 100 ppm for a shorter period of time (say 2 h 45 min), as shown in Figure 5-6, or at a lower temperature (600 ^oC), as shown in Figure 5-7.

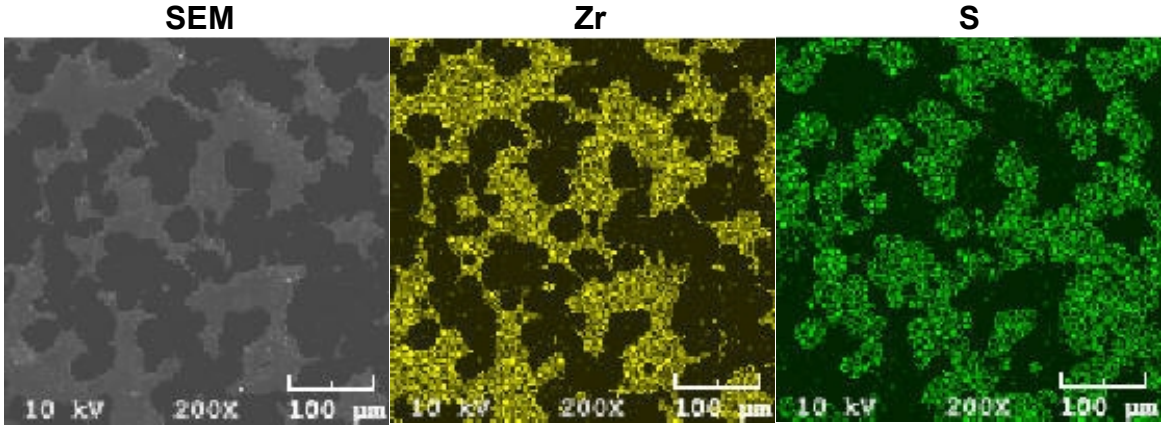

Figure 5-5 SEM image and EDX elemental maps of the Ni-YSZ composite after exposure to an H_2S-containing fuel (50 ppm H_2S/1.5% H_2O/48.5% N_2/50% H_2) at 800 ^oC for 48 h. (The full length of the scale bar is 100 μm.), from Cheng and Liu (2007).

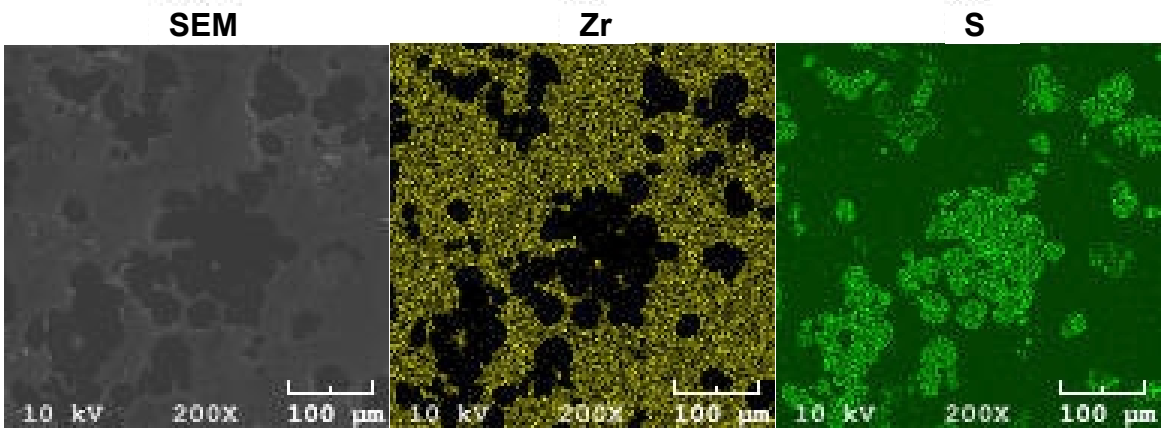

Figure 5-6 SEM image and EDX elemental maps of the Ni-YSZ composite after exposure to an H_2S-containing fuel (50 ppm H_2S/1.5% H_2O/48.5% N_2/50% H_2) at 800 ^oC for 2 h 45 min. (The full length of the scale bar is 100 µm.)

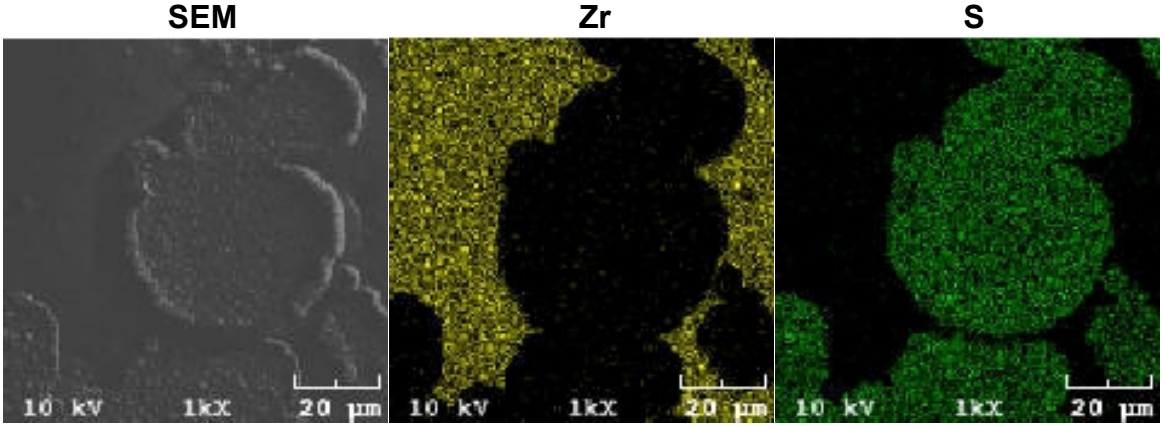

Figure 5-7 SEM image and EDX elemental maps of the Ni-YSZ composite after exposure to an H_2S-containing fuel (50 ppm H_2S/1.5% H_2O/48.5% N_2/50% H_2) at 600 ^oC for 18 h. (The full length of the scale bar is 20 µm.)

5.1.2.3 Identification of Nickel Sulfides Using Ex Situ Raman

While EDX provided useful information on the distribution of sulfur on the surface of dense Ni-YSZ composite, it has no information on the oxidation state or the phase of the sulfur species. Also, its sensitivity to surface species was limited due to the large sampling volume. To overcome this limitation, we used Raman spectroscopy to identify phases on the surface. Figures 5-8, 5-9, and 5-10 shows typical optical microscopy images and the corresponding Raman spectra taken from a sample after it was exposed to a fuel mixture of 50 ppm H_2S/50% H_2/1.5% H_2O/48.5% N_2 at 800 ^oC for 48 h (Figure 5-8) and 2 h 45 min (Figure 5-9), and at 600 ^oC for 18 h (Figure 5-10) respectively, and then cooled down gradually in the furnace while being exposed to the same fuel. Several forms of nickel sulfides had been identified. For example, in some dark brown regions on the nickel surface (Figures 5-8(c), 5-9(a), and 5-10(a)), the Raman spectrum shows a sharp band at 287 cm^{-1} and three smaller bands at ~223-226, 337, and ~378-379 cm^{-1} (Figures 4-7(b) and 4-8(b)), which correspond to Ni_3S_4. (RRUFF data base; Anthony et al. 1990; Wang et al., 2007). In some yellow regions with ball-like structures, Raman bands at 246, 300, 348, and 370 cm^{-1}, which closely match those of β-NiS (Bishop et al., 1998 and 2000; Shen et al., 2003; Wang et al. 2007) were obtained from those regions (Figures 5-9(c)-(d) and 5-10(e)-(f)). In some other yellow regions, the Raman spectrum only shows a very wide band from ~280 to ~380 cm^{-1}, which probably corresponds to certain nickel sulfides with a less well-defined structure (Figures 5-8(a)-(b) and 5-10(c)-(d)). Meanwhile, no observable changes in the surface morphology or the Raman signals were detected from the YSZ region, as shown in Figures 5-8 (f) and 5-9(f).

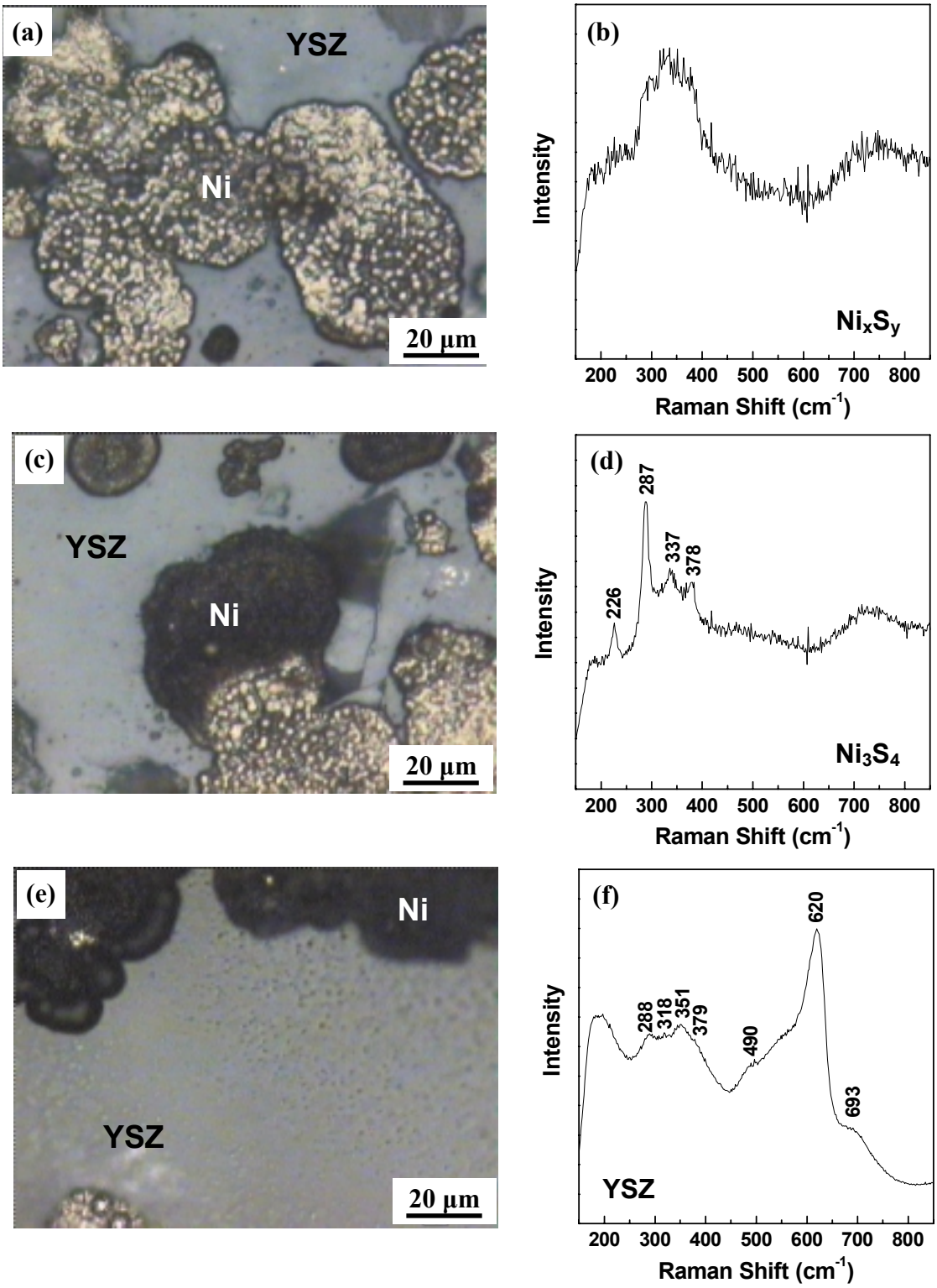

Figure 5-8 Optical microscopy images (a, c, e) and the corresponding Raman spectra (b, d, f) taken from the Ni (b, d) and YSZ (f) of the Ni-YSZ composite after exposure to an H_2S-containing fuel (50 ppm H_2S/50% H_2/1.5% H_2O/48.5% N_2) at 800 ^oC for 48 h.

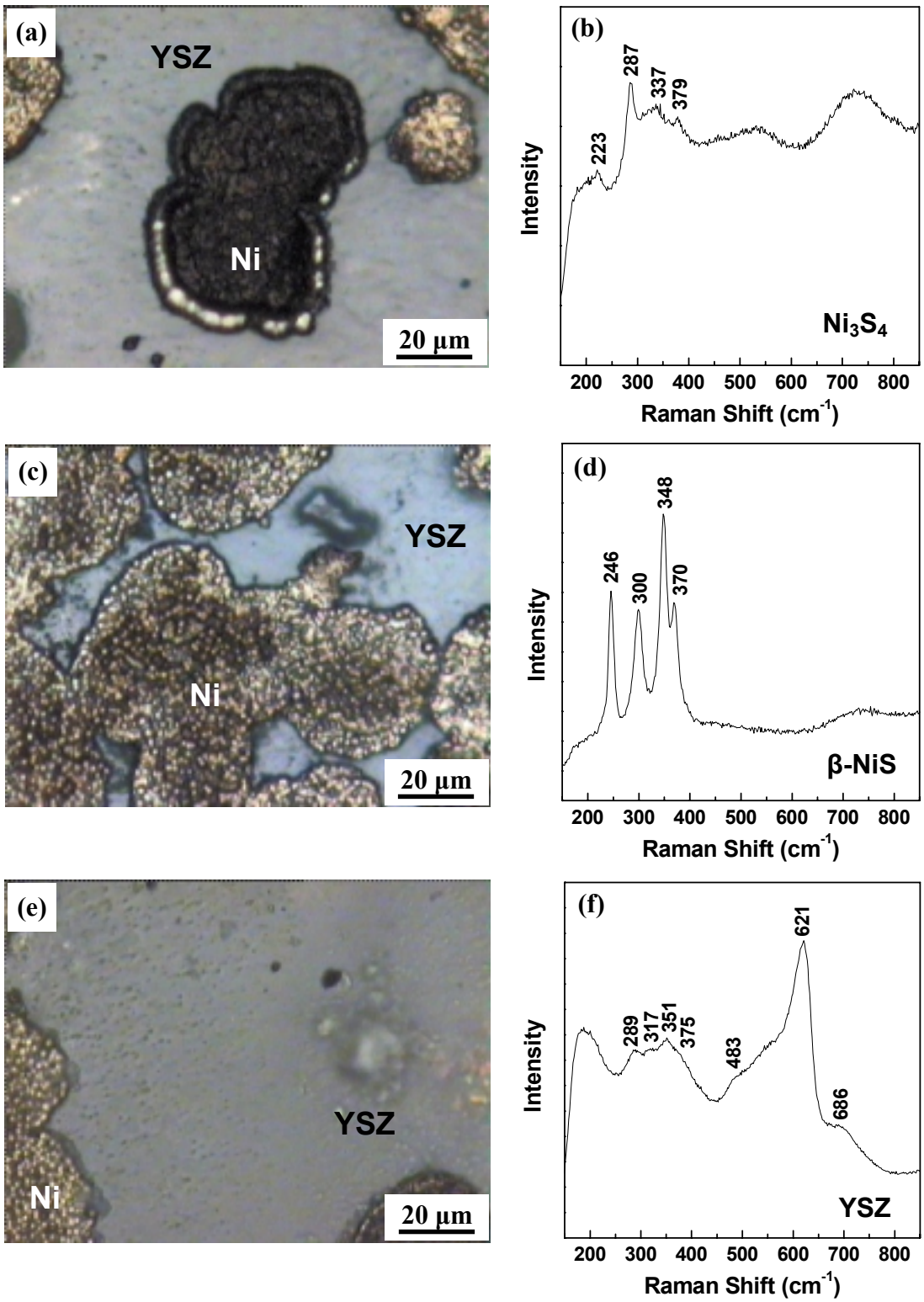

Figure 5-9 Optical microscopy images (a, c, e) and the corresponding Raman spectra (b, d, f) taken from the Ni (b, d) and YSZ (f) of the Ni-YSZ composite after exposure to an H_2S-containing fuel (50 ppm H_2S/50% H_2/1.5% H_2O/48.5% N_2) at 800 ^oC for 2 h 45 min, from Cheng and Liu (2007).

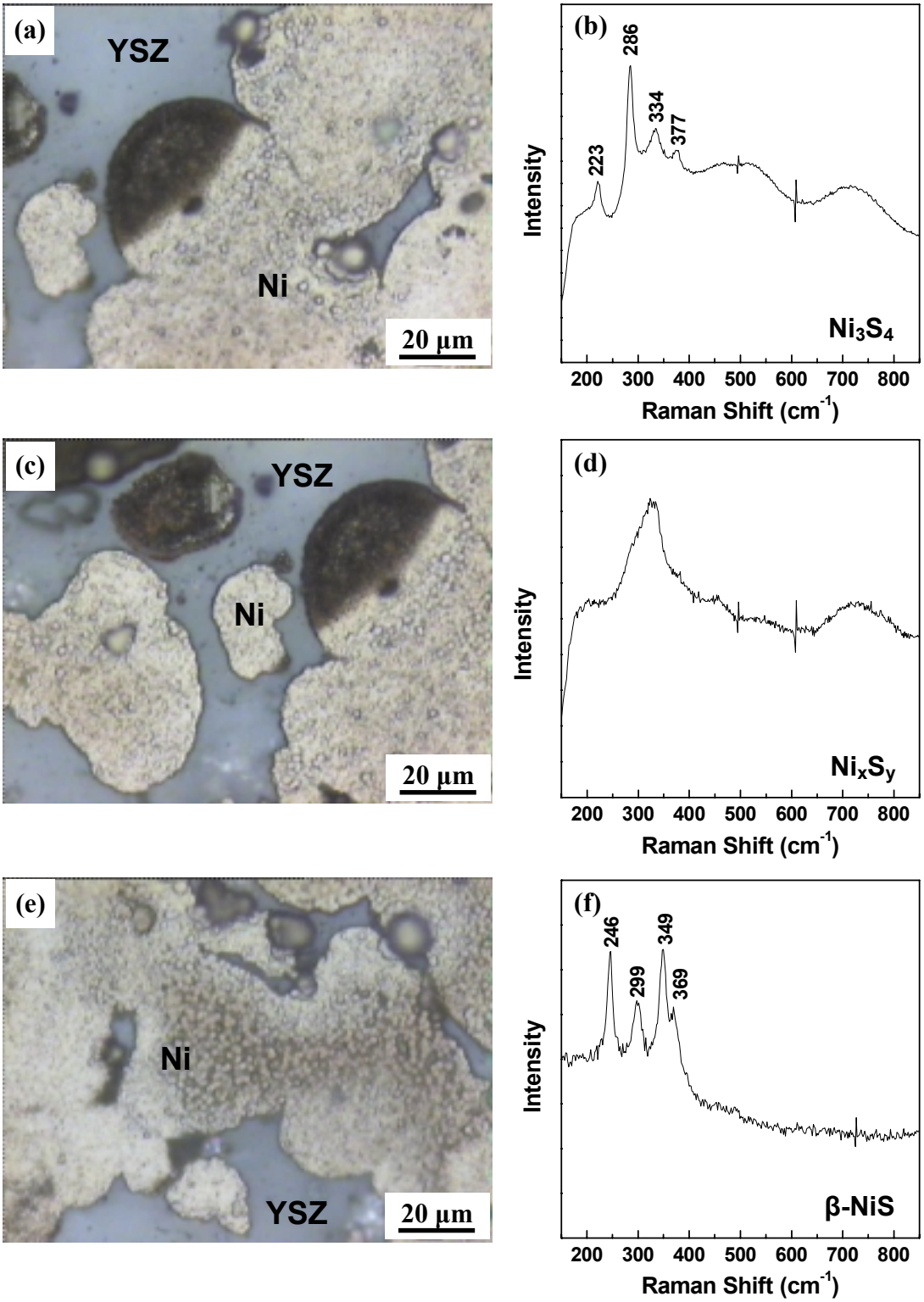

Figure 5-10 Optical microscopy images (a, c, e) and the corresponding Raman spectra (b, d, f) taken from the Ni of the Ni-YSZ composite after exposure to an H_2S-containing fuel (50 ppm H_2S/50% H_2/1.5% H_2O/48.5% N_2) at 600 ^oC for 18 h.

In addition, the identification and the mapping of the sulfur-containing phase on the Ni-YSZ composite surface could be achieved simultaneously using the Raman mapping technique with a spatial resolution of ~1 μm (Smith and Dent, 2005). For example, Figure 5-11 shows the optical micrograph, typical Raman spectra, and the corresponding Raman map taken from a 25×18 μm area (enclosed by the rectangular outline) in a sample exposed to 50 ppm H_2S/1.5% H_2O/48.5% N_2/50% H_2 at 800 ^oC for 18 h followed by annealing at 500 ^oC for 2 h in 4% H_2/3% H_2O/93% Ar. To obtain the map, Raman spectra were obtained point-by-point from the region with a step size of 1 μm. The typical Raman spectra obtained from the Ni region (darker) and the YSZ region (brighter) are shown in Figure 5-11(b). The spectrum from the Ni region corresponds to heazlewoodite phase Ni_3S_2 (Cheng et al., 2007; Wang et al., 2007), which was also confirmed using XRD as shown in Figure 5-12. (As discussed in the paper by

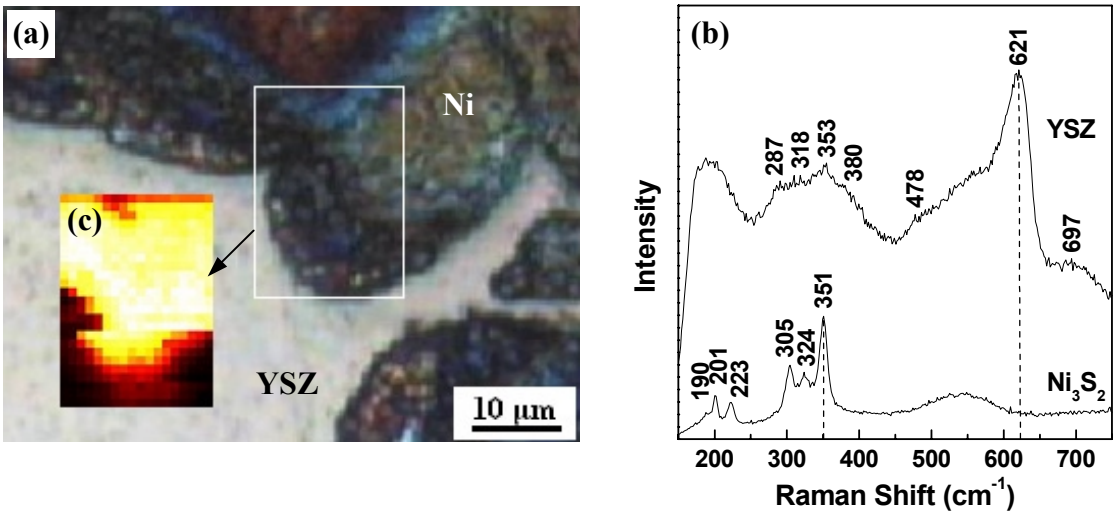

Figure 5-11 Optical microscopy image (a), typical Raman spectra taken from the Ni and YSZ regions (b), and corresponding Raman map for the circled region (c) of the Ni-YSZ composite after exposure to 50 ppm H_2S/1.5% H_2O/48.5% N_2/50% H_2 at 800 ^oC for 18 h followed by annealing at 500 ^oC for 2 h in 4% H_2/3% H_2O/93% Ar, from Cheng and Liu (2007).

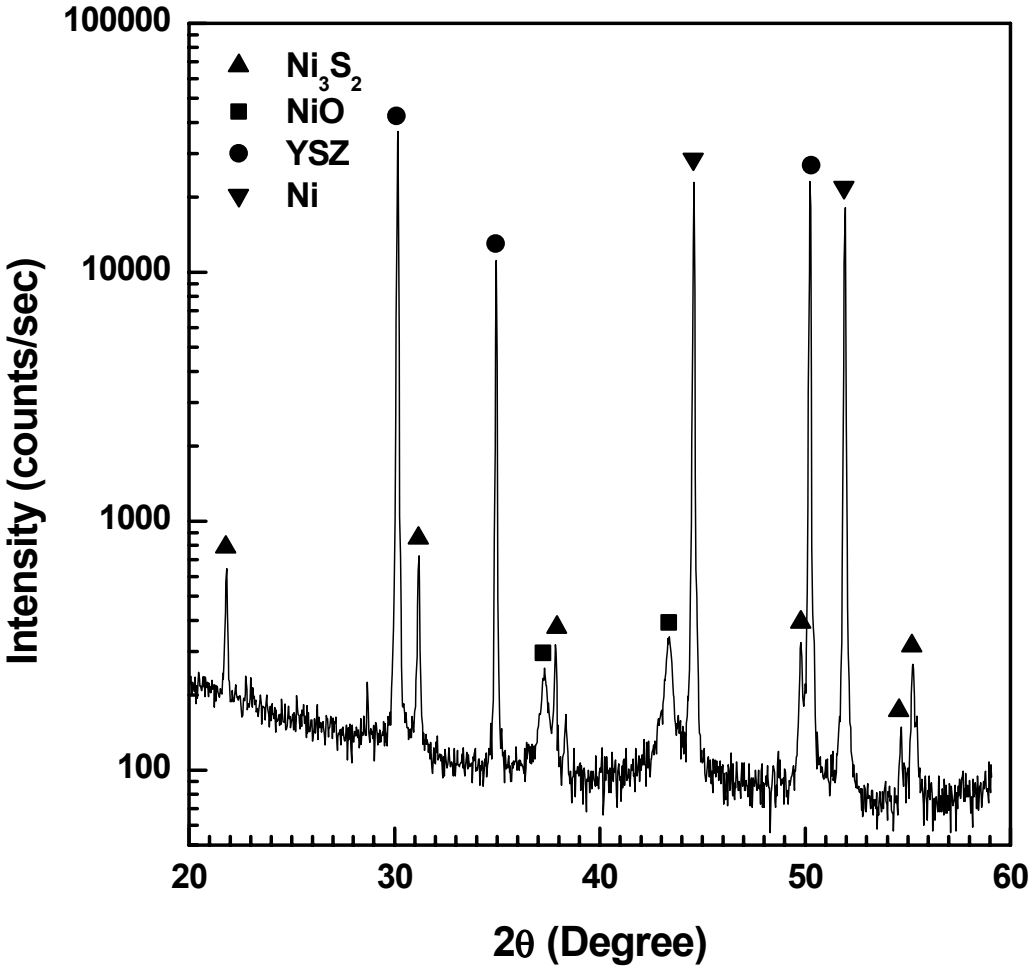

Figure 5-12 XRD pattern of the Ni-YSZ composite after exposure to 50 ppm H_2S/1.5% H_2O/48.5% N_2/50% H_2 at 800 ^oC for 18 h followed by annealing at 500 ^oC for 2 h in 4% H_2/3% H_2O/93% Ar, from Cheng and Liu (2007).

Cheng et al. (2007), previous references such as Dong et al. (2005 and 2006) and Bishop et al. (2000) and are *not* correct about the Raman spectrum for Ni_3S_2.) NiO, as indicated in the XRD pattern, must come from the slight oxidation of nickel sulfide at lower temperature due to the exposure to the air. Nevertheless, NiO has a space group of *Fm3m* (225) or O_h^5, for which $\Gamma_{vib}^{NiO,crystal} = F_{1u}^{IR}$, which is not Raman active. In fact, studies by Dietz et al. (1971) and Melendres and Xu (1984) revealed no sharp features in the 150-

400 cm^{-1} region of the Raman spectrum for NiO powders. The examination of all the spectra obtained showed that the Ni surface was uniformly covered by Ni_3S_2. Since the Raman signal for YSZ is stronger than that for Ni_3S_2, the Raman map (Figure 5-11(c)) was obtained by plotting the ratio of the signal at 351 cm^{-1} to that at 621 cm^{-1} with respect to the position on the sample surface. A large ratio (brighter part in the map) indicates Ni_3S_2, a small ratio (darker part in the map) indicates YSZ, and an intermediate ratio indicates both phases (close to the boundary between the Ni and the YSZ phases). Compared with XRD (Figure 4-12) that shows a majority of Ni and YSZ with a trace amount of Ni_3S_2, clearly Raman is much more sensitive to the phase on the surface.

5.1.3 In situ Characterization of the Ni-YSZ Composite during Exposure to H_2S-Containing Fuel using Raman Microspectroscopy

Based on the results of the ex situ experiments, it appeared that that several forms of nickel sulfides (i.e., Ni_3S_4, β-NiS, and Ni_3S_2) formed on the surface of nickel, leading to dramatic morphology change upon exposure to an H_2S-containing fuel at elevated temperature. To investigate whether this was the reason for the sulfur poisoning of the Ni-based anode for an SOFC, in situ Raman microspectroscopy was carried out to determine when the sulfides were formed and the surface morphology were changed. The focus of the study was on the Ni region because no significant change was identified on the YSZ region using the ex situ measurements.

Figure 5-13 shows optical micrograph and corresponding Raman spectra obtained from the nickel region under in situ conditions. Figures 5-13(a) and (b) are the optical

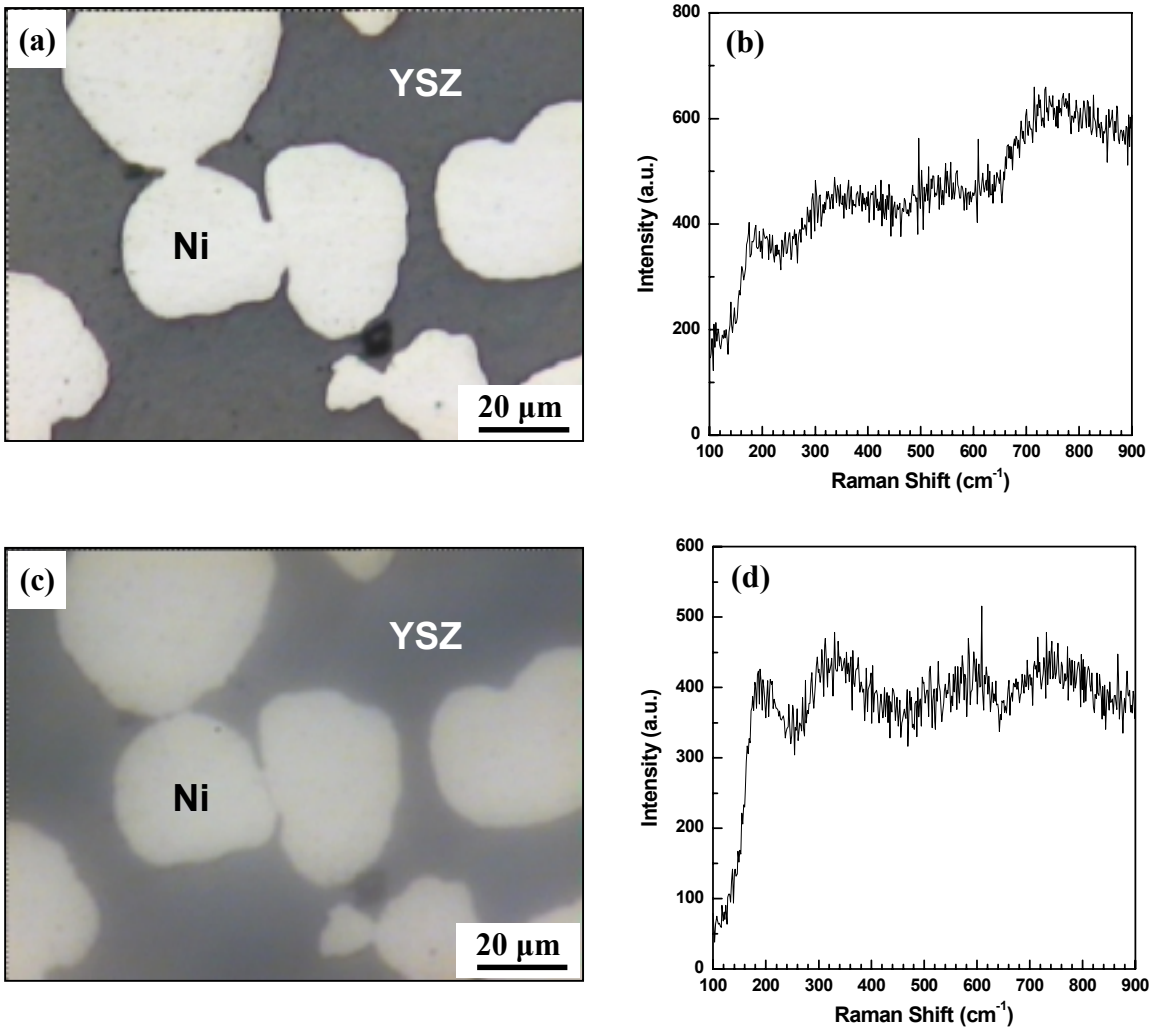

Figure 5-13 Optical microscopy images (a, c) and the corresponding Raman spectra taken from the nickel region (b, d) for the Ni-YSZ composite sample during the in situ H_2S exposure experiment: (a) and (b) are for the sample before the experiment, (c) and (d) are for the sample held at 570 ^oC in 4% H_2/96%Ar, (e) and (f) are for the sample exposing to a gas mixture (50% H_2/1.5% H_2O/48.5% N_2) containing 50 ppm H_2S for a total of 14 h, (g) and (h) are for the sample after cooling down at 5 ^oC/min to 20 ^oC in the H_2S containing fuel. (The optical image and Raman spectrum for (e)-(h) were all taken through a quartz window.)

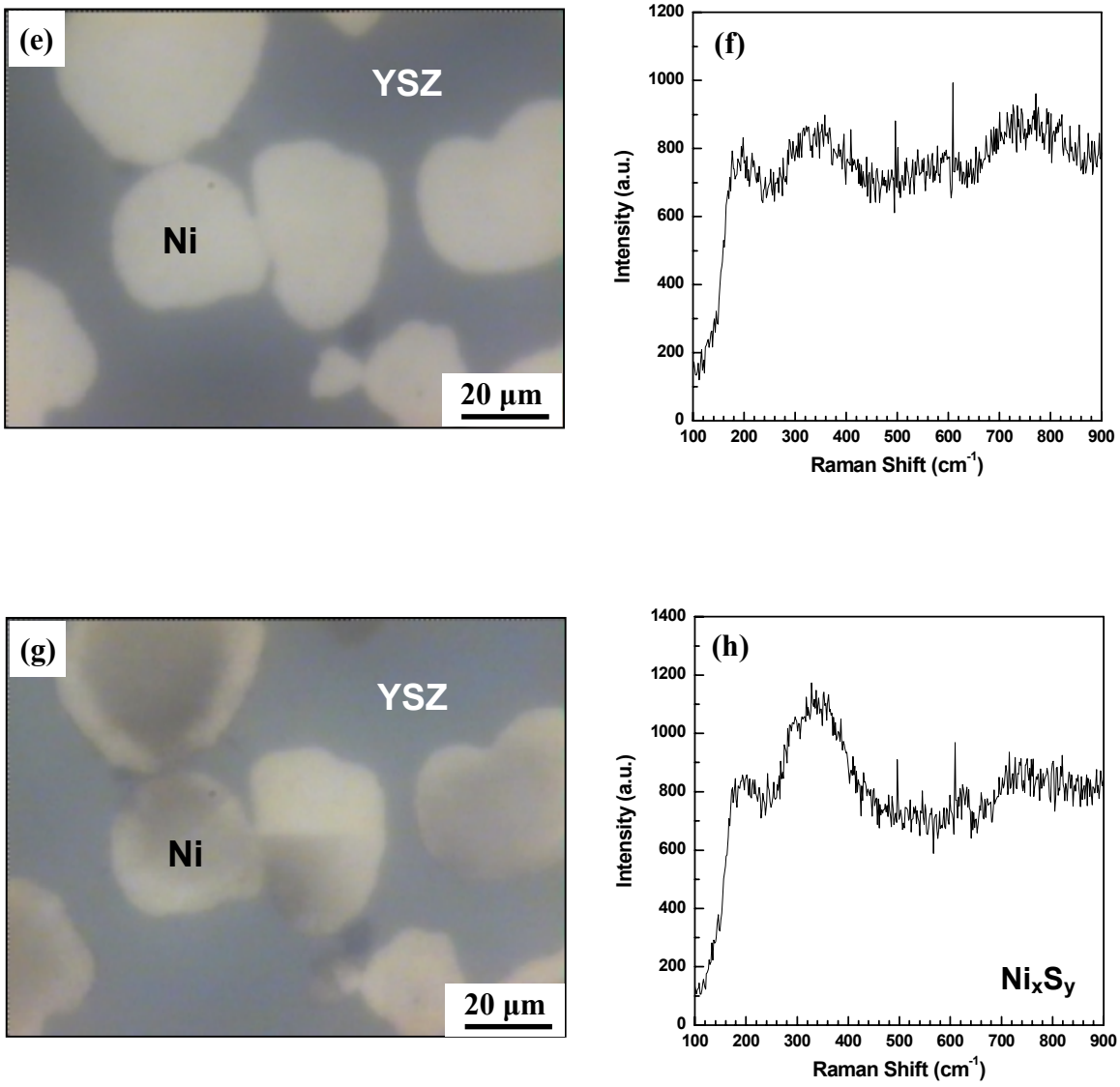

Figure 5-13 (continued)

micrograph and the Raman spectrum from the Ni region at room temperature in air. Figures 5-13(c) and (d) are for the same region at ~570 ^{o}C in a clean fuel of 50% H_2/1.5% H_2O/48.5% N_2. Then trace level of H_2S was introduced into the fuel stream (pH_2S/pH_2 = 100 ppm), and the surface morphology as well as the Raman spectrum from the nickel region was monitored continuously. However, no significant changes were observed on the nickel surface after extended period of exposure. For example, Figures 5-13(e) and (f) are for the same region after exposure to 100 ppm H_2S at ~570 ^{o}C for more than ~14 h. No dramatic morphology changes such as those shown before under the ex situ conditions were observed (see Figure 5-4 for the result of an 18 h exposure at 600 ^{o}C in a fuel with 100 ppm H_2S), and no Raman bands corresponding to conventional bulk nickel sulfides were identified. However, when the sample was cooled down at 5 ^{o}C/min, it was found that the sample surface started to change when the sample temperature dropped below ~300 ^{o}C, and when the sample was cooled to room temperature, the color in some regions on the nickel surface already changed from metallic white to light brown, which was accompanied by the evolution of a broad Raman brand in the range of ~280 to 380, as shown in Figures 5-13 (g) and (h). This in situ experiment suggested that those bulk nickel sulfides observed before under ex situ conditions were *not* formed at elevated temperatures. Instead, they were actually formed at lower temperatures in the same fuel during the cooling process.

To prove the above argument, it was reasoned that if the morphology change happed during the cooling process, change in the cooling rate might lead to changes in the obtained morphology change and corresponding Raman spectrum. To verify that, another set of in situ experiments were carried out. Figures 5-14 (a) and (b) are optical

micrographs and the corresponding Raman spectrum obtained from the Ni region for a nickel-YSZ after the sample was exposed to a fuel of 100 ppm H_2S/H_2 at 570 ^oC for 5 h and then cooled down quickly at ~70 ^oC/min to room temperature. Unlike the results from the slow cooling (e.g., 5 ^oC/min, as in Figures 5-13(g) and (h)), no significant change in sample morphology or color could be identified, and no observable Raman band could be identified.

In comparison, Figures 5-15(a) and (b) show the optical image and the corresponding Raman spectra taken from the Ni region for an Ni-YSZ composite cooled at 2.5 ^oC/min to ~500 ^oC and held at that temperature in a fuel of 50 ppm H_2S/1.5% H_2O/48.5% N_2/50% H_2 after it had been exposed to the same fuel at ~570 ^oC for 5 h. Similar to the result at 570 ^oC (see Figures 5-13(e) and (f)), no significant changes in

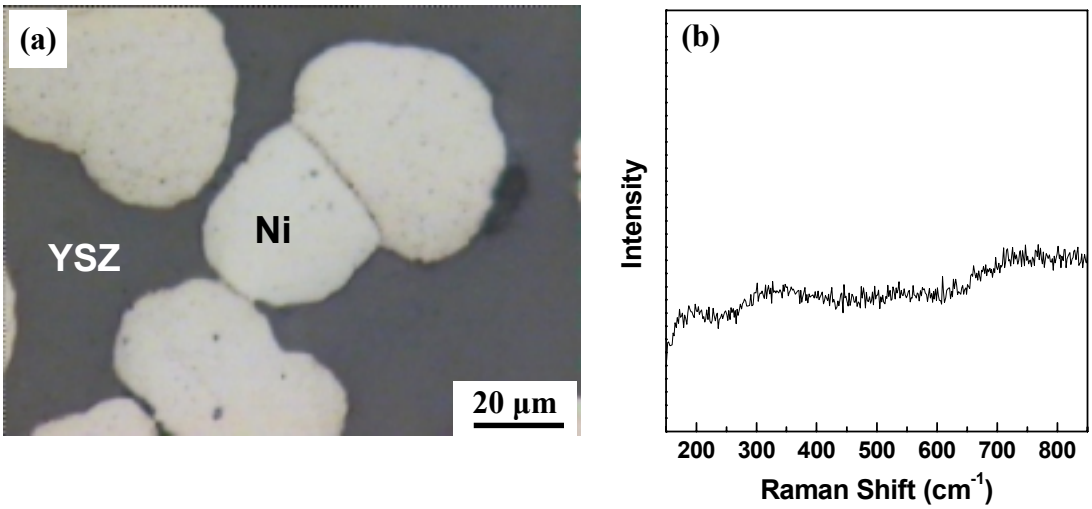

Figure 5-14 Optical microscopy image (a) and the corresponding in situ Raman spectrum (b) taken from the Ni region for a Ni-YSZ composite after it was exposed to an H_2S-containing fuel (50 ppm H_2S/1.5% H_2O/48.5% N_2/50% H_2) at 570 ^oC for 5 h and cooled to room temperature at ~70 ^oC/min, from Cheng and Liu (2007).

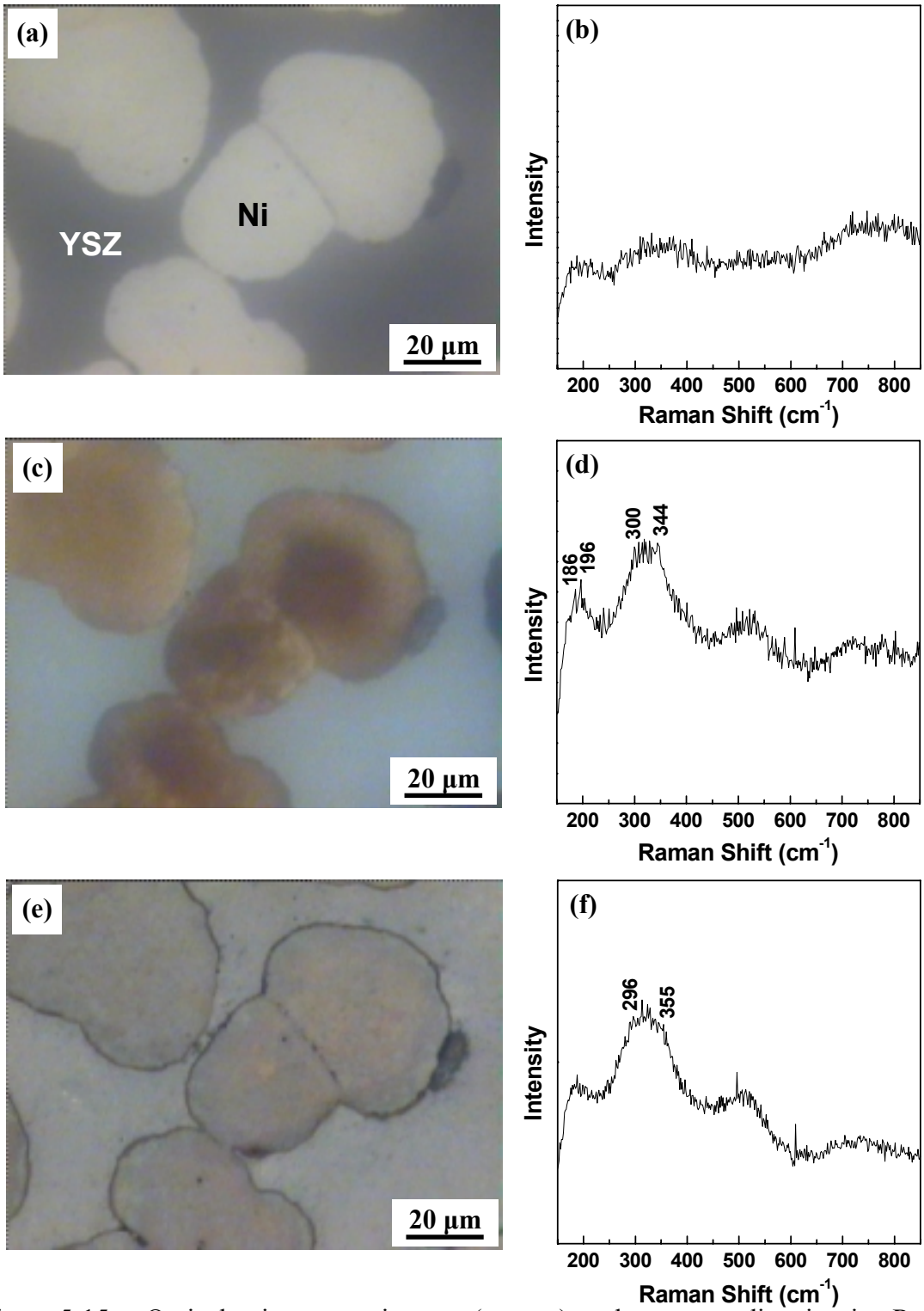

Figure 5-15 Optical microscopy images (a, c, e) and corresponding in situ Raman spectra (b, d, f) taken from the Ni region for a Ni-YSZ composite when exposed to an H_2S-containing fuel (50 ppm H_2S/1.5% H_2O/48.5% N_2/50% H_2) at 500 ^oC (a, b), and cooled at 2.5 ^oC/min to 216 ^oC (c, d) and 20 ^oC (e, f) successively, from Cheng and Liu (2007).

morphology or Raman signal corresponding to a nickel sulfide were observed on the Ni surface. However, when that sample was cooled down from 500 ^{o}C at a rate of 2.5 ^{o}C/min, the surface of Ni started to change gradually as the sample temperature dropped below ~350 ^{o}C. This time, a short-term isotherm was created at lower temperature to monitor the changes. Figures 5-15(c) and (d) show the optical image and the corresponding Raman spectrum taken from the same region after the sample was cooled at 2.5 ^{o}C/min to 216 ^{o}C and then held at 216 ^{o}C for 0.5 h. Accompanying the appearance of brown regions on the Ni surface, Raman peaks at 186, 196 cm^{-1} and a broad band in the range of ~300-344 cm^{-1} were observed (Cheng et al., 2007; Wang et al., 2007), most likely corresponding to Ni_3S_2. Continued exposure to the same fuel (pH_2S/pH_2 = 100 ppm) at 216 ^{o}C and below led to further changes in the surface morphology and the Raman spectrum (see Figures 5-15(e) and 7(f)), indicating that the sulfidation reaction was probably producing nickel sulfide phases with even higher sulfur contents (e.g., Ni_7S_6).

To investigate whether the sulfide formed at intermediate temperatures (e.g., 216 ^{o}C) would remain upon heating back to an elevated temperature, the same sample (see the description for Figures 5-14 and 4-15) was reheated inside the Raman cell after it was cooled down to room temperature at 2.5 ^{o}C/min in the fuel with pH_2S/pH_2 = 100 ppm. During the reheating process, the surface morphology changed and the Raman bands corresponding to nickel sulfides disappeared gradually. At ~500 ^{o}C, the surface of the Ni grain became non-uniform and the Raman spectrum was the same as that for pure Ni (Figures 5-16(a) and (b)). After being heated up to ~570 ^{o}C and held for another 12 h, the sample was cooled down in the same fuel at ~70 ^{o}C/min again. This time, the

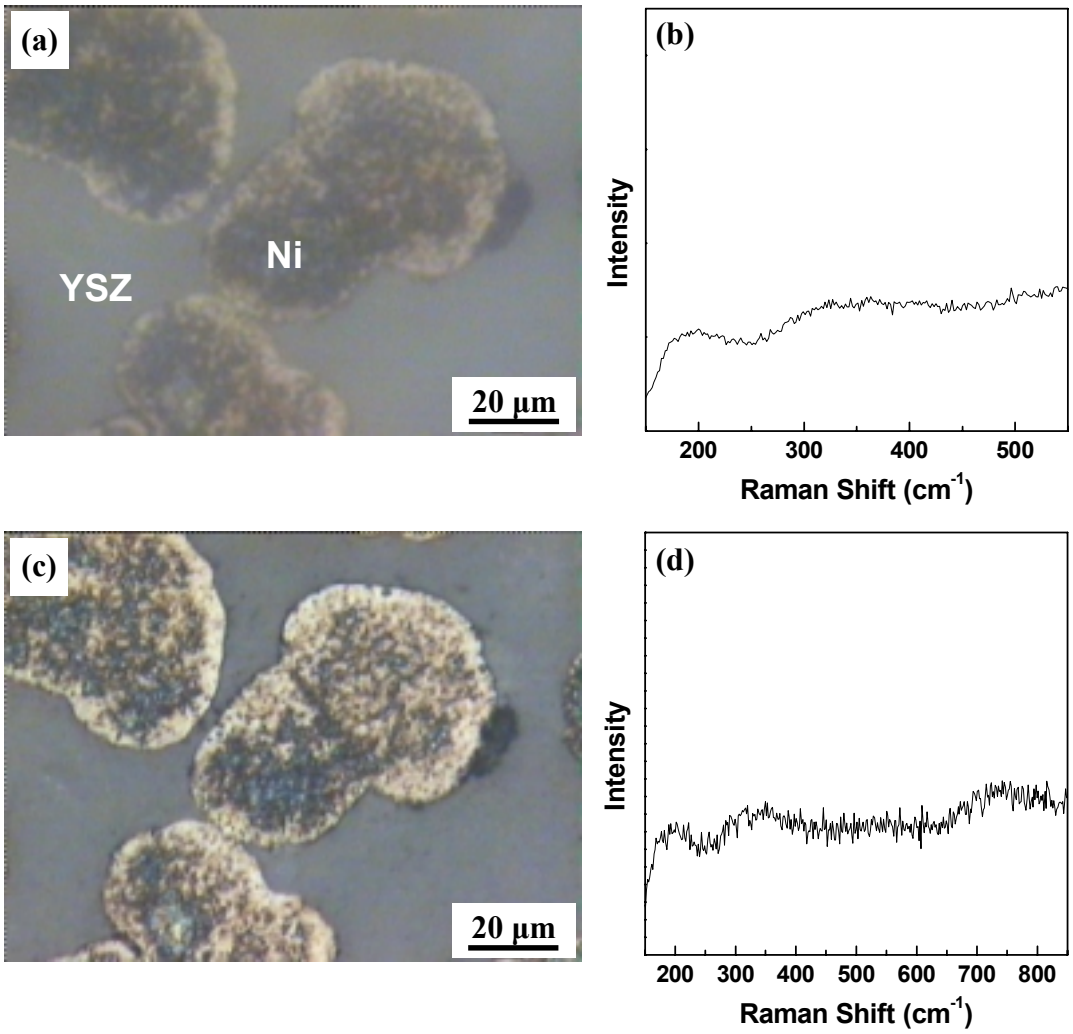

Figure 5-16 Optical microscopy images (a, c) and the corresponding in situ Raman spectra (b, d) taken from the Ni region for a Ni-YSZ composite after exposure to H_2S-containing fuel (50 ppm H_2S/1.5% H_2O/48.5% N_2/50% H_2) at 570 ^oC, followed by cooling at 2.5 ^oC/min to room temperature, reheating to ≥500 ^oC (a, b) and cooling again at ~70 ^oC/min to room temperature (c, d), from Cheng and Liu (2007).

morphology did not change further (Figure 5-16(c)) and no Raman band corresponding to sulfides could be identified (Figure 5-16(d)), which was consistent with the result shown in Figure 5-14.

Correspondingly, Figure 5-17 shows the SEM image, the Zr element map, and the EDX spectrum taken from the Ni region for the Ni-YSZ composite sample after the in situ experiment and cooled quickly at ~70 ^{o}C/min in a fuel with $p\mathrm{H_2S}/p\mathrm{H_2} = 10^{-4}$ (see the description for Figures 5-14 to 5-16). No sulfur was identified from the Ni region, indicating most, if not all, of the sulfides formed during the slow cooling decomposed by subsequent heat treatment at higher temperatures. But the morphology change was not reversible, as seen in all the pits left on the nickel surface in Figure 5-17 (b).

These in situ measurements clearly illustrated that the morphology change and the appearance of Raman band corresponding to conventional nickel sulfides actually happened at lower temperatures during the cooling process. This is actually in good agreement with the bulk phase Ni – H_2S – H_2 phase diagram. To illustrate that, another in situ experiment was carried out. According to the Ni – H_2S – H_2 phase diagram, Ni_3S_2 will form in a fuel of 100 ppm H_2S/H_2 at temperatures below ~450 ^{o}C (Rosenqvist, 1954). Therefore, the in situ experiment was carried out at ~440 ºC in a fuel mixture of 100 ppm H_2S/H_2. (Lower temperature such as in the range of ~300-400^{o}C was *not* used because (i) the reaction kinetics would be slower, and (ii) some other nickel sulfides such as Ni_7S_6 or NiS will start to form in the same fuel at lower temperatures.)

After only a few hours when 100 ppm H_2S was introduced into the fuel, Ni_3S_2 started to form on the nickel surface, and Figure 5-18 shows the optical microscopy images and corresponding Raman spectrum taken from the Ni and Ni_3S_2 surface before

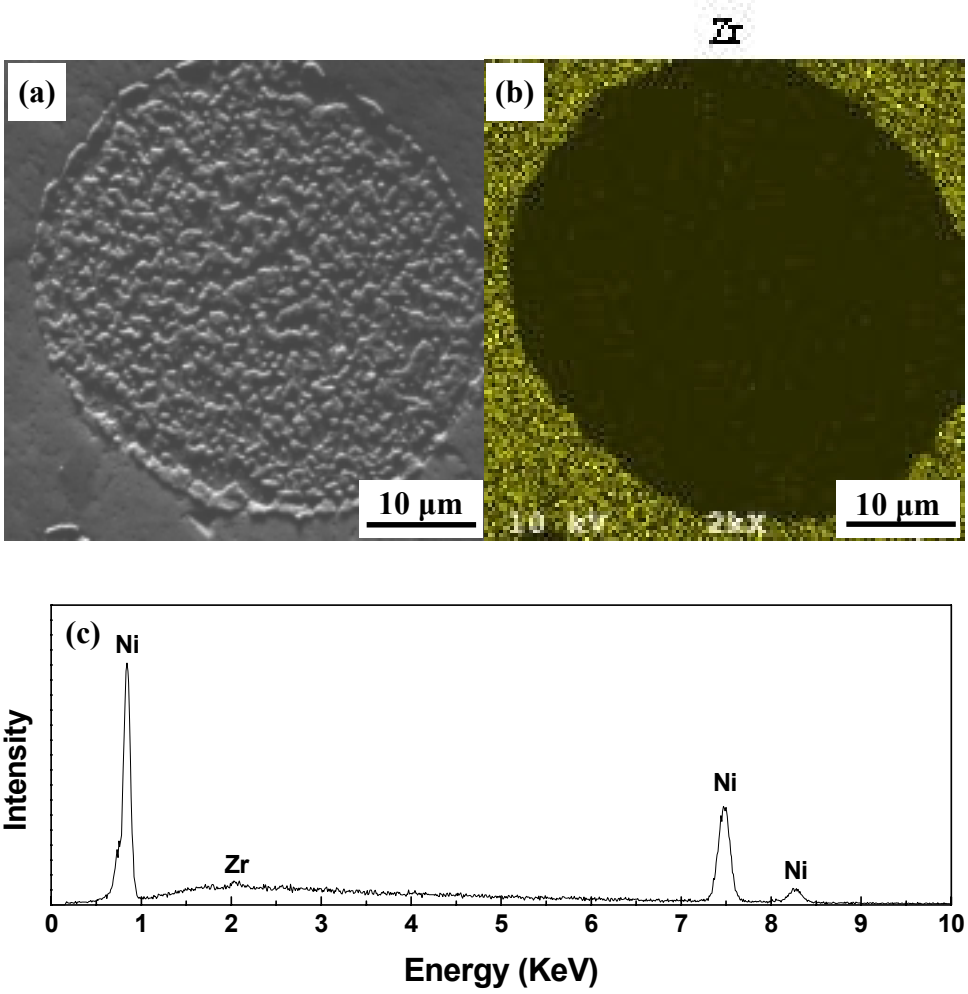

Figure 5-17 (a) An SEM image, (b) the corresponding Zr elemental map, and (c) the EDX spectrum from the Ni region of a Ni-YSZ composite after exposure to H_2S-containing fuel (50 ppm H_2S/1.5% H_2O/48.5% N_2/50% H_2) at 570 ^oC, followed by cooling at 2.5 ^oC/min to room temperature, reheating to ≥500 ^oC (a, b) and cooling again at ~70 ^oC/min to room temperature, from Cheng and Liu (2007).

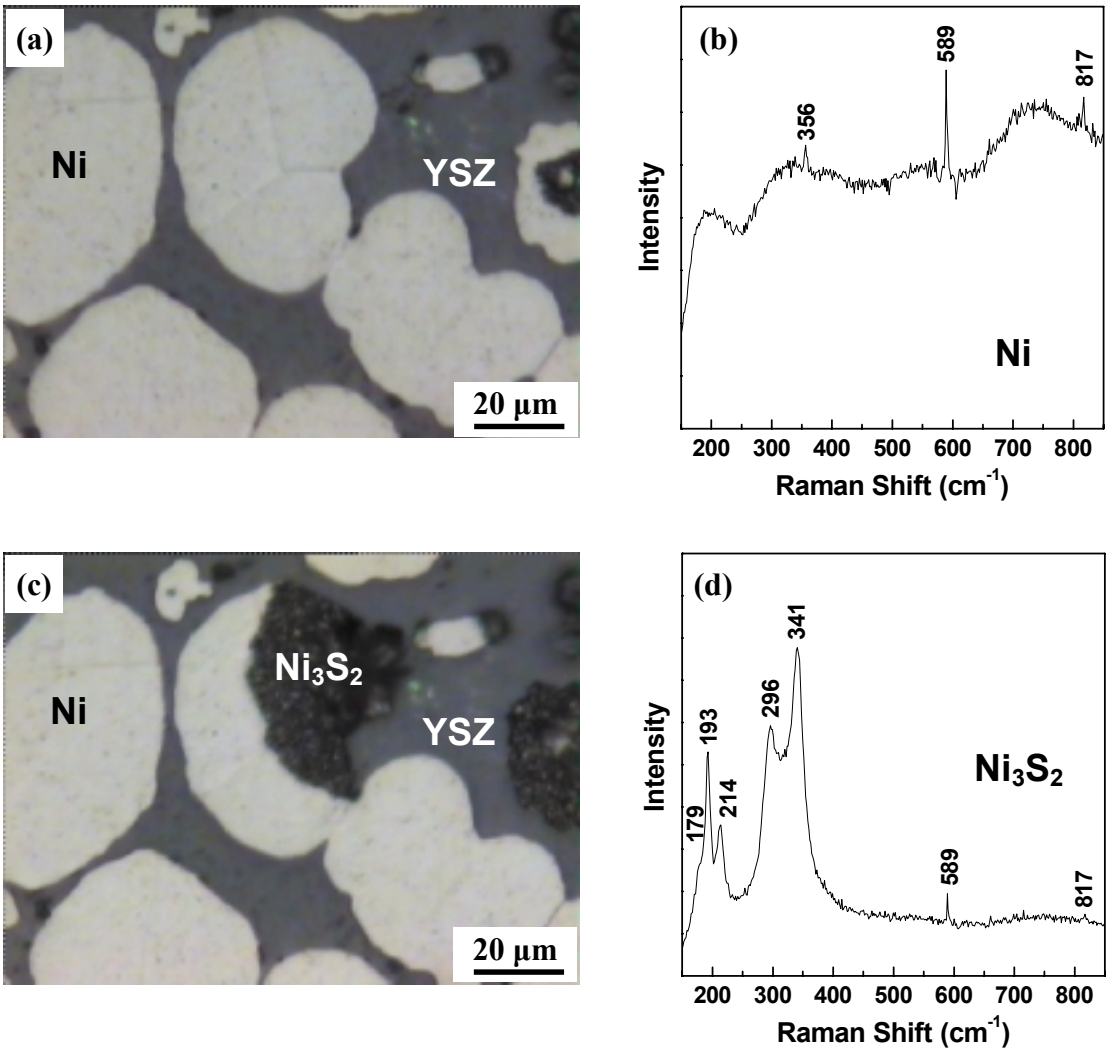

Figure 5-18 Optical microscopy images (a, c) and the corresponding Raman spectrum (b, d) obtained from the nickel region before and after the formation of Ni_3S_2 in a fuel of 100 ppm H_2S/H_2 at ~440 ^oC in the in situ Raman experiment.

and after Ni_3S_2 formation. The relative position and intensity of those Raman peaks (179, 193, 214, 296, and 341 cm^{-1}) match those obtained at room temperature (see Figure 5-11(b)) very well except that every peak shifted to a lower wavenumber: for example, the peak at 350 cm^{-1} shifted to 341 cm^{-1} as the sample temperature increased from 20°C to ~440°C, which was expected from the thermal expansion of the lattice (Wang et al., 2007). The peak at ~325 cm^{-1} in Figure 5-11(b) is not visible probably because it is buried by the two adjacent peaks. The sharp peaks at 358, 589, and 816 cm^{-1} in those spectra are due to the rotation of physically-adsorbed hydrogen (Colpa and Ketelaar, 1958).

5.2 Discussion

5.2.1 Ex situ Experiments

In the ex situ experiments described in section 5.1.2, the Ni-YSZ composites were exposed to fuels containing ppm-level H_2S (usually pH_2S/pH_2 = 100 ppm) for a certain period of time (i.e., from 2 h 45 min up to 48 h) at elevated temperatures (800 and 600 °C) and then cooled down gradually (~2-5 °C/min) in the same fuel with the furnace. Then, the samples were examined using various techniques including optical microscopy, SEM, EDX, XRD, and Raman spectroscopy. Several observations were made from those characterizations:

1) Dramatic morphology change happened to the Ni surface: various structures such as balls, ridges, and branchlike structures formed on the nickel surface while no detectable changes happened to the YSZ surface (see section 5.1.2.1).

2) Significant amount of sulfur was detected from the Ni region while no sulfur could be detected from the YSZ region using EDX, indicating H_2S exclusively attacked and attached to Ni surface and did not react with YSZ (see section 5.1.2.2).
3) Various conventional bulk nickel sulfides such as NiS, Ni_3S_4, etc. had been identified on the Ni surface of the post H_2S-exposure sample using Raman spectroscopy while no observable changes in the Raman spectrum for YSZ were detected (see section 5.1.2.3).

The results of the ex situ experiments *seem* to suggests that poisoning of the Ni-YSZ anode for solid oxide fuel cells by ppm-level H_2S is caused by the formation of conventional nickel sulfides on nickel surface. In fact, this was also the conclusion reached in several studies carried out recently using ex situ characterizations. For example, as stated in Chapter II, Trembly et al. (2006) tested electrolyte-supported cells with Ni-based anode in a fuel with pH_2S/pH_2 = 590 ppm (pH_2S = 207 ppm and pH_2 = 0.348) at 850 ^oC, and identified the presence of a significant amount of sulfur using EDX and XPS in the anode after the test in the H_2S-containing fuel (see Figures 2-15 and 2-16), and they concluded that the mechanism for sulfur poisoning includes "NiS formation." Similarly, Dong et al. (2005) also identified conventional nickel sulfides Raman bands in the composite anode after exposure to a fuel with 100 ppm H_2S at 727 ^oC for 120 h.

However, the conclusions from the ex situ experiments seem to contradict the existing thermodynamic data. According to the phase diagram constructed by Rosenqvist (1954) as well standard thermochemical data such as JANAF table (Chase et al., 1985),

bulk nickel sulfides would *not* be thermodynamically stable under the typical sulfur poisoning condition, for example, 800 ^{o}C, pH_2S/pH_2 = 1 ppm. Even under the most severe poisoning conditions such as 600 ^{o}C, pH_2S/pH_2 = 100 ppm as in this study or the 850 ^{o}C, pH_2S/pH_2 = 590 ppm as in Trembly's study, none of the bulk phase nickel sulfides would be stable. Instead, those sulfides would decompose into Ni and H_2S. Some other researchers including Xia and Birss (2005) might have also realized this and attributed only the "irreversible portion" of the sulfur poisoning to the formation of a thin ("submonolayer to several monolayers" according to them) of a Ni-S compound such as Ni_3S_2. However, this is still not satisfactory as at high temperature, kinetics would be fast and thermodynamics would become the determining factor for the bulk phase present: if a bulk phase is not stable, no matter how thin it is (down to several monolayer), it would still decompose.

Further, although nickel sulfides had been observed in those ex situ experiments such as EDX and Raman, what was observed may not be on the surface under the real fuel cell testing condition. The reason for this is that as all experiments were carried out ex situ, which means, after the samples had been exposed to H_2S-containing fuels, they had to be cooled down from elevated temperatures to room temperature and transferred from the fuel environment to be examined by all those ex situ characterization techniques. The sample surface could change during this cooling and transfer process, which might complicate the observed phenomena.

5.2.2 In situ Experiments

Therefore, to validate the argument from ex situ measurements, in situ experiments are necessary. In an in situ experiment, the changes on the anode surface at elevated temperatures in the fuel environment during the exposure to sulfur poison will be monitored directly in real time, which gives it great advantage over conventional ex situ characterization techniques. To analyze changes on the surface, there are many electron or ion-based techniques such as X-ray photoelectron spectroscopy (XPS) and Auger electron spectroscopy (AES), etc. However, all of those electron or ion-based techniques require an ultrahigh vacuum (UHV) condition, which is far from the real anode fuel environment containing not only fuel gas such as hydrogen but also significant amounts of water vapor and H_2S. Therefore, those electron-based technique could *not* fully simulate the real scenario under typical sulfur poisoning conditions, i.e., at high temperature in fuel atmosphere. On the other hand, the in situ characterization of the sample surface under conditions very close to that for real sulfur poisoning could be achieved using in situ Raman spectroscopy, which is a technique sensitive to the surface (see Appendix B for a demonstration of the sensitivity towards thin layer of sulfide down to ~30 nm at room temperature), compatible with the presence of hydrogen and water vapor, and functional at temperature up to ~600 ^{o}C in the current system.

The in situ Raman experiments described in section 5.1.3 basically included (i) characterizing the changes at elevated temperatures (i.e., ~570 ^{o}C) on Ni surface when H_2S was introduced into the Raman cell, (ii) characterizing the formation of nickel sulfides at lower temperature (~400 ^{o}C and below) during the cooling process with different cooling rates, and (iii) characterizing the reversibility of the sulfide formed in

terms of chemistry and surface structure. From the in situ experiments, the following observations could be made:

1) No Raman bands corresponding to conventional nickel sulfides (e.g., Ni_3S_2 and NiS) were observed on the Ni-YSZ composite surface at high temperatures (up to ~570 ^oC) in a fuel containing ppm-level H_2S (pH_2S/pH_2 = 100 ppm in this study). Meanwhile, no morphology change such as those observed in the ex situ experiments were observed on the nickel surface (see Figures 5-13 and 5-15).
2) Nickel sulfides (e.g., Ni_3S_2) started to form on nickel surface when the sample was held isothermally at lower temperatures (e.g., ~440 ^oC and below for 100 ppm H_2S) or when the sample was cooled slowly (e.g., at 5 ^oC/min or slower) in the H_2S-containing fuel (e.g., pH_2S/pH_2 = 100 ppm). The formation of nickel sulfides induced great morphology change on the Ni surface (see Figures 5-13, 5-15, and 5-18).
3) No sulfides could be detected on the nickel surface if the sample was cooled quickly (e.g., ~70 ^oC/min such as in a quench process) in the same fuel using Raman (see Figures 5-14, 5-16, and 5-17).
4) The nickel sulfide formed at lower temperature either isothermally or during the slow cooling process would decompose when the sample was heated up back to elevated temperatures (e.g., >500 ^oC for 100 ppm H_2S) in the same fuel. However, the morphology of nickel surface could *not* recover to the original state before sulfide formation (see Figures 5-16 and 5-17).

From the observations of in situ Raman experiments, two arguments could be made: (i) the formation of conventional nickel sulfides is *not* the reason for the sulfur

poisoning of the Ni-YSZ anode for solid oxide fuel cells, (ii) all the nickel sulfides observed in the ex situ experiments performed earlier in this study and the studies by Dong et al. (2005) and Trembly et al. (2006) actually formed at lower temperatures during the slow cooling process when H_2S reacted with Ni, which also caused the dramatic morphology change.

Both these arguments are consistent with thermodynamic considerations and are supported by experiments. For example, the first one is supported by the observation that, unlike in the ex situ experiments, no conventional bulk nickel sulfides were detected on the nickel surface even after extended exposure during the in situ experiments. The second argument is supported by the observation that slower cooling (e.g., ~2-5 ^{o}C/min) or low temperature isothermal exposure (e.g., at 440 ^{o}C or 216 ^{o}C) of the Ni-YSZ composite in the H_2S-containing fuel led to the formation of significant amounts of various nickel sulfides and dramatic changes in surface morphology (Figures 5-13, 5-15, and 5-18) whereas fast cooling (70 ^{o}C/min) from ~570 ^{o}C to 20 ^{o}C in the same fuel did not lead to detectable changes in Raman spectra (Figures 5-14 and 5-16). The second argument is also supported by the EDX characterization of the Ni-YSZ composite sample cooled at different rates in the H_2S-containing fuel. As shown in Figure 5-17, after the sample was cooled quickly in the fuel containing 100 ppm H_2S, no sulfur could be identified from the Ni region. In comparison, significant amount of sulfur is present on the nickel surface when the sample was cooled slowly with the furnace as shown in Figures 5-5 to 5-7. A third piece of evidence for the second argument is that, no observable changes in morphology, Raman signal or EDX spectrum could be identified

when the Ni-YSZ composite was cooled (quickly or slowly) in an H_2S-free fuel after it was exposed to an H_2S-containing fuel at an elevated temperature.

5.2.3 Sulfur-Anode Interaction Mechanism

- Interaction at high temperature in fuels containing ppm-level H_2S

From the discussion in previous section, the formation of conventional bulk nickel sulfides is definitely ruled out as the mechanism for sulfur poisoning of the Ni-YSZ cermet anodes for solid oxide fuel cells at high temperature in fuels with ppm level H_2S based on both in situ experiments and thermodynamic considerations. Therefore, the only reasonable mechanism left for the quick poisoning is the adsorption of sulfur on nickel surface, i.e.,

$$H_2S\ (gas) + Ni\ (solid) \rightarrow Ni\text{-}S\ (surface) + H_2, \qquad (5\text{-}1)$$

which blocks reaction sites for hydrogen adsorption, dissociation, and diffusion along surfaces, and inhibits the electrochemical reaction. Although in this experiment, the Raman band for adsorbed sulfur was not detected directly at elevated temperatures in H_2S-containing fuel, (which was believed to be a result of thermal noise at those elevated temperature), careful analysis of information in the literature and available experiments unambiguously suggest that the adsorption of sulfur on the nickel surface is the reason for the decreased cell performance in fuels containing ppm level H_2S at elevated temperatures (e.g., $>\sim 600\ ^oC$) for the following reasons.

First, thermodynamically, the adsorption of sulfur on nickel in low concentration (ppm or lower) of H_2S is an energetically favorable process (see the review by Bartholomew, Agrawal, and Katzer 1982, p. 164-169). Through both experiments

(McCarty and Wise, 1982) and theoretical calculations (Goddard et al., 1977; Marquez et al., 2006; Choi et al., 2006 and 2007; Wang and Liu, 2007), it has been established that the adsorption enthalpy for sulfur on nickel surface is ~130-160 kJ/mol (based from H_2S) in hydrogen containing ppm-level H_2S, which is ~55-85 kJ/mol greater than that for the formation enthalpy of Ni_3S_2 (i.e., 75 kJ/mol from H_2S) at the same temperature. In fact, only through adsorption can we explain the observed poisoning phenomena that occurred at extremely low H_2S concentration at high temperatures (e.g., 0.05 ppm at 750 ^oC as observed by Matsuzaki and Yasuda (2000)).

A clearer picture from an energetic point of view that covers sulfur poisoning conditions for solid oxide fuel cell is given in an updated Ni-H_2S-H_2 phase diagram constructed by Dr. Jeng-Han Wang of our group through theoretical calculation, as shown in Figure 5-19 (Wang and Liu, 2007). Like traditional phase diagram, the white region represents clean nickel surface and the yellow represents bulk Ni_3S_2 phase, which, among all conventional bulk phase nickel sulfides (i.e., Ni_3S_2, Ni_7S_6, Ni_9S_8, NiS, Ni_3S_4, and NiS_2), is the phase that requires the lowest pH_2S/pH_2 to be thermodynamically stable. The black line represents the experimentally determined phase boundary between Ni and Ni_3S_2 phase. Compared with all traditional bulk phase diagrams such as that by Rosenqvist (1954), this new phase diagram is unique in that it includes a transition region between the clean nickel and the Ni_3S_2 phase. This region in blue represents the equilibrium condition under which sulfur would only adsorb on the nickel surface and form a partial to full monolayer coverage, depending on temperature and pH_2S/pH_2 value. The black symbols represent experimentally determined chemisorption data points obtained by McCarty and Wise (1980), and the numbers to the right of each set of points

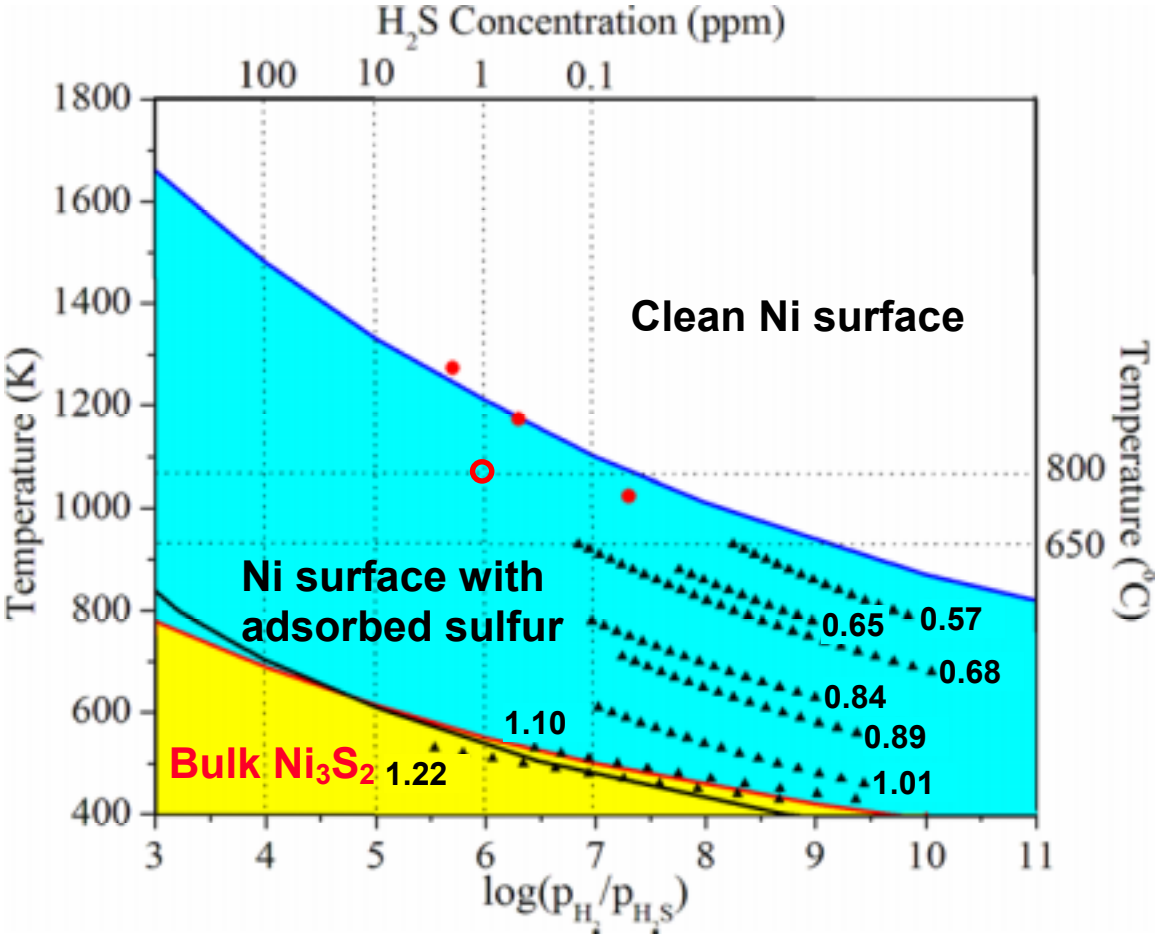

Figure 5-19 Calculated Ni-H_2S-H_2 phase diagram. The black line is from the bulk phase diagrams Rosenqvist (1954). The black symbols are experimentally determined chemisorption data points with different "area coverage" obtained by McCarty and Wise (1982). The red dots are related to the sulfur tolerance limits as determined by Matsuzaki and Yasuda (2000), adopted with change from Wang and Liu (2007).

represent the different equilibrium surface coverage ratios by sulfur on the nickel surface. The typical sulfur poisoning conditions, for example, 800 ^{o}C, pH$_2$S/pH$_2$ from 0.1 up to 100 ppm will fall right into this transition region for the sulfur adsorption on nickel in this new phase diagram, while it will simply fall into pure nickel region in any traditional phase diagram, which could not explained the observed cell poisoning behavior.

Second, kinetically, the observed rapid change in cell performance when trace amount of H_2S was introduced into the fuel stream is consistent with the mechanism of adsorption. It has been shown in Chapter IV that the majority of the performance degradation happened within ~60 sec after the introduction of H_2S into the fuel stream for electrolyte-supported cells with thin anodes. On the other hand, previous studies indicated that the adsorption of sulfur on metal catalyst such as nickel was very rapid with a sticking coefficient approaching 1 at lower surface coverage (see Bartholomew, Agrawal, and Katzer, 1982, pp. 153-158). If the poisoning process involved any bulk sulfide phase formation, it would be much slower because (i) it would need much more sulfur, and (ii) the driving force (i.e., the heat of sulfide formation) would be smaller.

Third, the relative extent of sulfur poisoning is consistent with the surface coverage for sulfur adsorption on nickel. For the example of 800 ^{o}C, 1 ppm and 8 ppm H_2S, if the experimentally determined data points for sulfur chemisorption on nickel surface (from McCarty and Wise (1982)) were extrapolated to higher temperature, the rough surface coverage for sulfur on nickel under that condition would be estimated to be ~0.6 and ~0.7, which is quite reasonable as it has been shown in Figure 4-8 that 1 ppm and 8 ppm H_2S induced a ~100% and a 200% increase in the anode/electrolyte interfacial resistance, respectively. Another example is to use the result of Matuszaki and Yasuda

(2000), who observed anode interfacial increase of ~30% when 0.05 ppm H_2S was in the fuel at 750 ^oC. The condition would corresponds to a surface coverage of smaller than ~0.5, which is in good agreement with the relative interfacial resistance increase.

Fourth, the boundary between sulfur poisoning and non-poisoning is consistent with the boundary between nickel surface with adsorbed sulfur and that without. For example, Matsuzaki and Yasuda (2000) determined that critical H_2S concentration was between 0.02 and 0.05 ppm at 750 ^oC, which is in close match with the phase diagram in Figure 5-19 for sulfur adsorption. Earlier, in section 4.2, the critical H_2S concentration at 900, 800, and 700 ^oC was determined to be ~0.2, 0.03, and 0.002 ppm, which are also in good agreement with the boundary established in the updated phase diagram.

In addition, Figure 5-19 also indicates the dependence of surface coverage by sulfur on H_2S concentration is *not* linear. Still take the example of 800 ^oC: in low H_2S concentration range, when the H_2S concentration increases from 0.03 to 0.3 ppm (i.e., over one decade), the coverage to increase from zero to ~0.5), and then from 0.3 ppm to ~100 ppm (i.e., over more than three decades), the coverage only increases from ~0.5 to ~1.0. Further increase in H_2S concentration (i.e., above 300 ppm) would not lead to much higher coverage as the surface already saturated. This also explains the observation that the extent of cell performance degradation did not change much at 600 ^oC when H_2S concentration increased from 1 to 8 ppm (see Figures 4-7 and 4-10): the surface coverage by sulfur was already above ~0.8 at 1 ppm and would not increase much even though the H_2S concentration increased further to 8 ppm.

- Interaction at intermediate temperatures in fuels with ppm-level H_2S

Other phenomena concerning the interaction of sulfur with Ni-YSZ anode under non-typical SOFC operating conditions could also be explained. First, the observation of conventional nickel sulfide formation on the Ni surface at intermediate temperatures (~200-400 ^oC) in the in situ experiments is *not* unexpected from a thermodynamics point of view. Although bulk nickel sulfides are not stable at high temperature in fuels with ppm level H_2S (e.g., 800 ^oC, pH_2S/pH_2 = 100 ppm), the equilibrium pH_2S/pH_2 ratio decreases dramatically as the temperature drops from to a lower temperature. In fact, according to the updated phase diagram in Figure 5-19, Ni_3S_2 becomes thermodynamically stable at temperatures below ~440 ^oC when $pH_2S/pH_2 = 10^{-4}$, which means that if the sample is cooled down in a fuel of 100 ppm H_2S, Ni_3S_2 will start to form when the temperature dropped below ~440 ^oC. In addition, based on the thermodynamic analysis using the data in a standard reference (JANAF Thermochemical Table, Chase et al., 1985), even the more sulfur-rich β-NiS and Ni_3S_4 phases will also become thermodynamically stable at temperature below ~250 and ~160 ^oC, respectively, when $pH_2S/pH_2 = 10^{-4}$, which could explain the appearance of β-NiS and Ni_3S_4 in the ex situ experiments (Figures 5-8 to 5-10). The observation of various sulfides on Ni surfaces is also consistent with previous investigations showing that the corrosion of Ni starts with the formation of Ni_3S_2, and the outer layer of the sulfide scale consists of more sulfur-rich phases such as Ni_7S_6 and then β-NiS (Bastow and Wood, 1975).

The dramatic morphologies such as balls and ridges observed on Ni surfaces (Figures 5-2 to 5-4) are most likely due to the swelling effect of the sulfidation of Ni: the volume expansion from Ni to Ni_3S_2 and from Ni to β-NiS (as calculated from the

information in JCPDS card) is 107% and 150%, respectively. The dramatic morphologies may also be related to the decrease in the melting point for nickel sulfide (e.g., Ni_3S_2) with the decrease in pH_2S/pH_2 ratio as indicated by the Ni-S phase diagram (Rosenqvist, 1954).

From the phase diagram in Figure 5-19, it is also clear that the bulk sulfide formed at low temperature will decompose when the sample is heated back to high temperature in the same fuel. However, as shown in Figures 5-16 and 4-17, the morphology change induced in this process is *not* reversible: the morphology would *not* recover to the original after the sulfide formed at low temperature decomposed back to Ni. This indicates that commercial SOFCs should not be cooled in fuels containing even ppm-level H_2S. Otherwise, conventional nickel sulfides could form, leading to irreversible microstructural changes, which would negatively influence the cell performance.

- Anode regeneration process

For the anode regeneration process after sulfur poisoning, from a thermodynamic point of view, reaction (5-1) will be reversed when H_2S is removed from the feed, releasing the surface-adsorbed sulfur from the surface. However, as shown in this study and the by Matsuzaki and Yasuda (2001), the recovery process is much slower compared to the poisoning process.

The observation that the extent of cell resistance increase was always smaller with higher current density or lower voltage, as shown earlier in section 4.1.4, indicates that passage of oxygen ions may accelerate the regeneration (or de-sulfurization) process through the following reaction:

$$S_{(ad)} + 2O^{2-} = SO_{2\,(g)} + 4e^{-}, \quad (5\text{-}2)$$

However, it is noted that SO_2 may exist only as a "short-lived" reaction intermediate because SO_2 would be reduced back to H_2S in the fuel environment (at least from a thermodynamic point of view). For example, for a humidified hydrogen with pH_2O/pH_2 = 3:97, the equilibrium pSO_2/pH_2S ratio would be on the order of $\sim 6\times10^{-11}$ at 1000 K for the reaction of

$$SO_2 + 3H_2 = H_2S + 2H_2O. \quad (5\text{-}3)$$

In fact, if we combine reactions (5-2) and (5-3) and rearrange the equation, we have

$$S_{(ad)} + H_{2\,(g)} = H_2S_{\,(g)}, \quad (5\text{-}4)$$

$$2O^{2-} + 2H_{2\,(g)} + = 2H_2O_{\,(g)} + 4e^{-}, \quad (5\text{-}5)$$

which are equivalent to the desorption of sulfur in H_2S/H_2 environment on the electrode (reaction (5-4)) plus the electrochemical oxidation of H_2 (reaction (5-5)).

- Interaction of sulfur with YSZ

Any interaction of sulfur with the YSZ phase is ruled out as mechanism for sulfur poisoning of SOFCs because no change could be determined through either Raman or EDX experiments. In addition, it had been shown that the adsorption of sulfur on oxides is negligible (Bartholomew, Agrawal, and Katzer, 1982, p. 157).

5.3 Summary

To summarize the study on the mechanism of interactions between sulfur and Ni-YSZ cermet anodes for solid oxide fuel cells, the following observations had been made through this study:

1) Sulfur poisoning of SOFC anodes at high temperature in fuels with ppm-level H_2S is not caused by the formation of conventional nickel sulfides as none of them had been identified in in situ experiments under conditions close to sulfur poisoning experiments.
2) The bulk nickel sulfides observed in the ex situ experiments both in this study and in other studies were formed not during the poisoning process, but the subsequent cooling process when the reaction between H_2S and nickel to form bulk sulfide became thermodynamically favorable.
3) Analysis of data from theoretical calculation and experiments clearly indicates that sulfur poisoning is due to the adsorption of sulfur on nickel surface, which blocks reaction site, leading to decreased performance.

CHAPTER 6

EXPLORATION OF NEW SULFUR-TOLERANT ANODE MATERIALS FOR SOLID OXIDE FUEL CELLS

The effective utilization of sulfur-containing fuels in solid oxide fuel cells (SOFCs) has generated great interest in the development of sulfur-resistant anode materials for SOFC. As shown in section 2.3, previous studies on sulfur-tolerant anode materials can be grouped into two categories: those for SOFCs exposed to fuels with very high concentrations (~5-100 % by volume) of H_2S (Pujare et al., 1987 and 1989; Yates and Winnick, 1999; Wang et al. 2001; Liu et al., 2003; Wei et al., 2004) and those exposed to fuels with H_2S on the ppm-range (Kim et al., 2001; Mukundan et al., 2004; Marina et al. 2004; He et al., 2005). These studies are of great importance because they may lead to the elimination of the desulfurization system in the current SOFC fuel-processing unit, which would significantly simplify the operation and reduce the cost.

This chapter will be on the investigation of the interactions between sulfur (in the form of H_2S) and new, candidate sulfur resistant anode materials. The focus is on two aspects. The first is on predicting and explaining the stability for new sulfur-tolerant anode materials since the number one requirement for a successful anode material is chemical stability, which means the candidate material should not react with fuel gases and other cell components during cell preparation and testing. This was achieved using thermodynamic analysis combined with experimental verifications. The second aspect is on investigating the possible mechanism for the enhanced sulfur tolerance for some new

candidate materials by characterizing the changes on the anode surface and link that to the observed sulfur tolerance.

6.1 Stability for Candidate Sulfur-Tolerant Anode Materials

6.1.1 Introduction

Although sulfur-resistant anode materials have been studied for some time, to date, unfortunately, the selection of sulfur-resistant anode materials seems to remain largely in a try-and-error manner: potential candidate material was fabricated as the anode in an SOFC and tested in sulfur-containing fuel. The problem with this method is that it was often found that the candidate material simply transformed into other phases upon exposure to H_2S-containing fuels and failed due to lost of the structural integrity as in the studies by Yates and Winnick (1999).

On the other hand, one effective tool to guide the selection of sulfur-resistant anode material is to analyze the thermodynamic stability of the candidate materials. Thermodynamics has been used to analyze the stability of cathode and interconnect materials for SOFCs (Yokokawa et al., 1991a and 1991b). For the study of new sulfur-tolerant anodes, this involves predicting whether the material will react with hydrogen, hydrogen sulfide, and water vapor in a typical SOFC anode environment. This method, though appearing straightforward, has never been applied to guide the search of anode in the field. It is expected to be of great use because, in real SOFCs, the porous anode is subject to high temperature ($\geq$700 ^{o}C) for years and the materials stability would most likely be determined by thermodynamics. Depending on specific requirements, the prediction of the materials stability based on thermodynamics could help to rule out a

large number materials that are destined to fail so that researchers could focus on the most promising candidates.

In this section, the results of thermodynamic analysis on the stability of several classes of candidate sulfur-resistant anode materials will be presented. The most probable reactions that would cause the failure of the candidates have been identified. For the most typical materials of each class, the predictions are compared with experimental observations. The limitations of the thermodynamic analysis will also be discussed.

6.1.2 Thermodynamic Analysis

To carry out thermodynamic analysis, the Gibbs free energy change for the reaction of interest (ΔG_r) will be calculated. If the Gibbs free energy change for an *undesirable* reaction for the candidate material is *negative* (i.e., $\Delta G_r < 0$) under a typical SOFC anode atmosphere, the candidate material can be ruled out as it *can* (i.e., based on thermodynamics) and *will* (based on kinetics) go through the undesirable reaction and lose its properties. This is because kinetics is *not* expected to be inhibiting since (i) the actual anode is a highly porous structure with the primary particle size on the order of 1 μm, and (ii) the anode material will stay at a high temperature (above ~700 ^{o}C) for tens of thousands of hours or even longer, which will give sufficient time for any slow reaction to occur significantly.

The thermochemical analysis for simple compounds is straightforward since the thermochemical data for most simple compounds involved are well documented in standard references (Chase et al., 1985; Barin, 1995). In contrast, the thermochemical

data for most ABO_3 perovskites are *not* documented, and the method for analyzing the thermodynamic stability for ABO_3 perovskites as candidate anodes for SOFC has never been studied.

To solve the problem of thermodynamic analysis for complex materials such as ABO_3 perovskites under the anode atmosphere, the idea that a perovskite could be viewed as a reaction product from the corresponding simple oxides is borrowed. For example, an $A^{2+}B^{4+}O_3$ type perovskite can be viewed (and in fact is) as the reaction product of corresponding simple oxides (i.e., $A^{2+}O$ and $B^{4+}O_2$ or $B^{4+}{}_2O_4$ from the following reaction:

$$AO + BO_2 = ABO_3, \tag{6-1}$$

or

$$AO + \frac{1}{2}B_2O_4 = ABO_3. \tag{6-2}$$

Similarly, an $A^{3+}B^{3+}O_3$ type perovskite could be viewed as the reaction product of corresponding simple oxides (i.e., $A^{3+}{}_2O_3$ and $B^{3+}{}_2O_3$) from the following reaction:

$$\frac{1}{2}A_2O_3 + \frac{1}{2}B_2O_3 = ABO_3. \tag{6-3}$$

Careful search of literature indicates that, although the standard thermochemical data (e.g., standard formation enthalpy, entropy, and Gibbs free energy versus pure elements) for most perovskites are nowhere to be found, there are very good linear relationships between the reaction enthalpy for the reactions of perovskite formation from corresponding simple oxides (i.e., reactions (6-1) to (6-3)), ΔH_r^{oxide}, and the Goldschmidt tolerance factor (t_p) for different types of perovskites (Navrotsky, 1981; Yokokawa, et al. 1989 and 1990; Cheng, Navrotsky and co-workers, 2003, 2004 and 2005). In particular,

Yokokawa et al. (1989) found that the reaction enthalpy for the formation of $A^{2+}B^{4+}O_3$ oxide from the reactions (6-1) or (6-2) could be approximated by:

$$\Delta H_r^{oxide} = 875 - 1000 t_p \text{ kJ/mol}, \tag{6-4}$$

while the reaction enthalpy for the formation of $A^{3+}B^{3+}O_3$ oxide from reaction (6-3) could be approximated by:

$$\Delta H_r^{oxide} = 630 - 720 t_p \text{ kJ/mol}. \tag{6-5}$$

Yokokawa and co-workers (1990, 1991a, and 1991b) used these empirical equations in a series of studies to analyze stability and the reactivity of perovskites with materials like yttria stabilized zirconia (YSZ) and demonstrated the applicability of these equations. Recently, similar empirical relations were also proposed by Cheng and Navrotsky (2003) who found the reaction enthalpy for reaction (6-1) or (6-2) could be approximated by:

$$\Delta H_r^{oxide} = 844.4 - 956.0 t_p \text{ kJ/mol}, \tag{6-6}$$

while the reaction enthalpy for reaction (6-3) could be approximated by:

$$\Delta H_r^{oxide} = 323.8 - 389.3 t_p \text{ kJ/mol}. \tag{6-7}$$

Careful search of literature also indicated that the entropy change for the formation of complex-structured oxide (e.g., ABO_3 perovskite) from simple oxides, ΔS_r^{oxide}, are usually very small (~0-5 J/mol K) (see Yokokawa, 1989). The contribution of the entropy change to the total free energy change ($T\Delta S_r^{oxide}$) for perovskites formation through reactions (6-1) to (6-3) was on the order of a few kJ/mol, which is usually much less than one tenth of the enthalpy change ΔH_r^{oxide}. Therefore, as a first approximation, the entropy term was omitted in the calculation of the free energy change for reactions from simple oxides to complex materials (e.g., ABO_3, see Yokokawa, 1991). Therefore,

the Gibbs free energy change for perovskites formation from simple oxide, ΔG_r^{oxide}, would approximated by:

$$\Delta G_r^{oxide} = \Delta H_r^{oxide} - T\Delta S_r^{oxide} \approx \Delta H_r^{oxide} . \quad (6\text{-}8)$$

On the other hand, when an ABO_3 perovskite is under typical anode condition in an atmosphere containing hydrogen, water vapor, and, in this case, hydrogen sulfide, it may react with those gases and form something else and lose its properties. This may involve the reactions between the gases with the individual A-site simple oxide and/or the B-site simple oxide, which would disrupt the original perovskite structure. This may also simply involve a transformation of the material as a whole. In either case, the corresponding reaction(s) would be specified, and the free energy change could be calculated to determine if it is energetically favorable or not.

Putting all the information above together, the procedure to analyze the stability for ABO_3 perovskites was as follows:

1) The Goldschmidt tolerance factor (t_p) was calculated from the following equation:

$$t_p = \frac{r_A + r_O}{\sqrt{2}(r_B + r_O)}, \quad (6\text{-}9)$$

in which r_A, r_B and r_O are the radii of A, B and oxygen ions, respectively, and Shannon's effective radii (Shannon, 1976) for A-site ions in 12-coordination state and for B-site ions in 6-coordination state should be used to calculate t_p (Navrotsky, 1981).

2) The reaction enthalpy for the formation of a perovskite from simple oxides, ΔH_r^{oxide}, is estimated from different empirical relationships for different types of perovskites. In particular, both ΔH_r^{oxide} values from Equations (6-4) and (6-6)

were calculated for $A^{2+}B^{4+}O_3$ type perovskites (i.e., reaction (6-1) or (6-2)) and both ΔH_r^{oxide} values from Equations (6-5) and (6-7) were calculated for $A^{3+}B^{3+}O_3$ type perovskites (i.e., reaction (6-3)). Unless stated otherwise, the values calculated using Equations (6-6) and (6-7) are given directly, while the values calculated using Equations (6-4) and (6-5) are listed in the bracket that follows.

3) The standard free energy of formation (versus pure elements) for a perovskite was obtained. For an $A^{2+}B^{4+}O_3$ type perovskite formed through reaction (6-1), the standard free energy of formation for it would be:

$$\Delta G_f^{ABO_3} = \Delta G_f^{AO} + \Delta G_f^{BO_2} + \Delta G_r^{oxide} \approx \Delta G_f^{AO} + \Delta G_f^{BO_2} + \Delta H_r^{oxide}. \qquad (6\text{-}10)$$

For $A^{3+}B^{3+}O_3$ type of perovskite formed through reaction (6-3), the standard free energy of formation for it would be:

$$\Delta G_f^{ABO_3} = 0.5\Delta G_f^{A_2O_3} + 0.5\Delta G_f^{B_2O_3} + \Delta G_r^{oxide}$$

$$\approx 0.5\Delta G_f^{A_2O_3} + 0.5\Delta G_f^{B_2O_3} + \Delta H_r^{oxide}. \qquad (6\text{-}11)$$

In Equations (6-10) and (6-11), the standard formation energy for A-site and B-site simple oxides were obtained from standard references (Chase et al., 1985; Barin, 1995).

4) The thermodynamic analysis for the stability of these materials in a specific atmosphere would be carried out as usual by calculating the reaction Gibbs free energy change for a specified reaction.

6.1.3 Results

6.1.3.1 Stability for Simple Compounds

- Metal Carbides

Many transition metal carbides have very high melting point and excellent electrical conductivity (Weimer, 1997). Listed in Table 6-1 are the melting point, electrical conductivity, and coefficient of thermal expansion (CTE) for some of the most common metal carbides. Some of the metal carbide materials such as Mo_2C have been reported to have good catalytic activity for various chemical reactions and, unlike metal catalyst, have the potential advantage of preventing carbon deposition (see LaMont et al., 2003 for a summary of using metal carbide as catalysts). However, the suitability of these materials as candidate sulfur-resistant anode materials for SOFCs has not been determined. Since SOFC anode is exposed to fuels containing significant amount of water vapor, one possible reaction that may lead to the failure of metal carbide anode would be:

$$M_xC_y + (y+z)\ H_2O = M_xO_z + y\ CO + (y+z)\ H_2 \qquad (6\text{-}12)$$

If the elemental metal is more stable than the corresponding metal oxides in reducing atmosphere (such as molybdenum and tungsten), the reaction would be written as:

$$M_xC_y + y\ H_2O = x\ M + y\ CO + y\ H_2 \qquad (6\text{-}13)$$

Table 6-2 lists the free energy change for the hydrolysis of some common metal carbide materials at 950 ^oC in fuels with two different CO concentrations. For most carbides except molybdenum and tungsten carbide, the hydrolysis reaction is an extremely energetically favorable process over a wide CO partial pressure range (e.g., pCO from 10^{-6} to 10^{-1}). The hydrolysis reactions become even more energetically favorable as the

Table 6-1 Melting point (T_m), electrical conductivity at 25 °C (σ_{25}) and 800 °C (σ_{800}), coefficient of thermal expansion (CTE) (25-1000 °C) for some materials investigated in this study, from Cheng et al. (2006).

Material	T_m (°C)	σ_{25} (S cm^{-1})	σ_{800} (S cm^{-1})	CTE (10^{-6}/K)
B_4C [a]	2470	1.0×10^3	1.0×10^3	4.8-5.5
Cr_3C_2 [a]	1800 [g]	1.3×10^4	4.8×10^3	11.7
Mo_2C [a]	2500	1.4×10^4	3.6×10^3	7.3
β-SiC [a]	2986 [g]	1.0	NA	3.8-5.8
TaC [a]	4000	4.6×10^4	2.5×10^4	7.1
TiC [a]	3017	5.0×10^3	2.1×10^3	8.0
WC [a]	2800 [g]	5.2×10^4	3.8×10^4	5.8
W_2C [a]	2785	1.3×10^4	5.3×10^3	6.4-8.1
ZrC [a]	3532	1.3×10^4	5.9×10^3	7.0
TiB_2 [a]	2920	1.1×10^5	4.4×10^4	4.6
ZrB_2 [a]	3050	1.0×10^5	3.7×10^4	5.9
CrN [a]	1500 [g]	1.6×10^3	NA	0.7-3.1
TiN [a]	2950	2.5×10^4	1.9×10^4	8.1-9.0
VN [a]	2177	1.7×10^4	1.6×10^4	8.1
ZrN [a]	2952	5.6×10^4	2.2×10^4	7.0
$MoSi_2$ [a]	2280	4.6×10^4	7.8×10^3	8.2
$La_{0.4}Sr_{0.6}TiO_3$ [b]	>1600	6.0×10^3	5.0×10^2	11-12
$La_{0.7}Sr_{0.3}VO_3$ [c]	>1600	7.0×10^2	1.5×10^2	9.6-11.5
$La_{0.75}Sr_{0.25}Cr_{0.5}Mn_{0.5}O_3$ [d, e]	>1600	NA	1.0	8.9-10.1
$Gd_2Ti_{1.4}Mo_{0.6}O_7$ [f]	>1500	NA	5.0	NA

Notes:
[a] from Weimer (1997), [b] from Marina et al. (2002), [c] from Cheng et al. (2005), [d] from Tao and Irvine (2004), [e] from Zha et al. (2005a), [f] from Porat et al. (1997), [g] decomposition temperature.

Table 6-2 Gibbs Free energy change (ΔG_r) for the reaction between water vapor and transition metal carbides at 950 ^{o}C. The partial pressure of H_2 and H_2O are fixed at 0.87 and 0.03, respectively, and the partial pressure of CO is 10^{-6} or 10^{-1}, from Cheng et al. (2006).

Reaction (written based on 1 mole of H_2O)	ΔG_r (pCO = 10^{-6}) in kJ/mol	ΔG_r (pCO = 10^{-1}) in kJ/mol
1/7 $B_4C_{(s)}$ + $H_2O_{(g)}$ = 2/7 $B_2O_{3\ (l)}$ + 1/7 $CO_{(g)}$ + $H_{2\ (g)}$	-106	-89
2/13 $Cr_3C_{2\ (s)}$ + $H_2O_{(g)}$ = 3/13 $Cr_2O_{3\ (s)}$ + 4/13 $CO_{(g)}$ + $H_{2\ (g)}$	-69	-33
$MoC_{(s)}$ + $H_2O_{(g)}$ = $Mo_{(s)}$ + $CO_{(g)}$ + $H_{2\ (g)}$	-116	1
$Mo_2C_{(s)}$ + $H_2O_{(g)}$ = 2 $Mo_{(s)}$ + $CO_{(g)}$ + $H_{2\ (g)}$	-86	31
1/3 $SiC_{(s,\ beta)}$ + $H_2O_{(g)}$ = 1/3 $SiO_{2\ (s,\ high\text{-}cristobalite)}$ + 1/3 $CO_{(g)}$ + $H_{2\ (g)}$	-115	-76
2/7 $TaC_{(s)}$ + $H_2O_{(g)}$ = 1/7 $Ta_2O_{5\ (s)}$ + 2/7 $CO_{(g)}$ + $H_{2\ (g)}$	-64	-31
1/3 $TiC_{(s)}$ + $H_2O_{(g)}$ = 1/3 $TiO_{2\ (s,\ rutile)}$ + 1/3 $CO_{(g)}$ + $H_{2\ (g)}$	-90	-51
$WC_{(s)}$ + $H_2O_{(g)}$ = $W_{(s)}$ + $CO_{(g)}$ + $H_{2\ (g)}$	-111	6
$W_2C_{(s)}$ + $H_2O_{(g)}$ = 2 $W_{(s)}$ + $CO_{(g)}$ + $H_{2\ (g)}$	-120	-2
1/3 $ZrC_{(s)}$ + $H_2O_{(g)}$ = 1/3 $ZrO_{2\ (s)}$ + 1/3 $CO_{(g)}$ + $H_{2\ (g)}$	-133	-94

CO concentration decreases or the water vapor concentration increases.

On the other hand, in the presence of H_2S, those carbides may also react with it to form metal sulfides such as the following reaction:

$$M_xC_y + z\ H_2S + y\ H_2O = M_xS_z + y\ CO + (z+y)\ H_2 \qquad (6\text{-}14)$$

(Of course, there could be other reactions that can be written out such as

$$M_xC_y + z\ H_2S = M_xS_z + y\ C + z\ H_2. \qquad (6\text{-}15)$$

However, at high temperature in the presence of significant amount of water vapor, solid carbon will reaction with water vapor to form CO and H_2, especially when the CO concentration was low. Therefore, reaction (6-14) was not considered in the study.) Reaction (6-14) is a complex one involving three reactants and three products. Even if it happens, the real scenario might be that the carbides are first hydrolyzed as in reaction (6-12) or (6-13), then the hydrolysis product (metal oxides or metal) reacts with H_2S to form metal sulfides as in the following reactions:

$$M_xO_z + y\ H_2S + (z\text{-}y)\ H_2 = M_xS_y + z\ H_2O \qquad (6\text{-}16)$$

or

$$x\ M + y\ H_2S = M_xS_y + y\ H_2 \qquad (6\text{-}17)$$

In terms of thermodynamics, to predict whether the product of hydrolysis (reaction (6-12) or (6-13)) or sulfidation (reaction (6-14)) will be final product, it is sufficient to evaluate the free energy change for reaction (5-16) or (5-17). If the free energy change for reaction (6-16) or (6-17) is negative, the sulfide could be the final product. If the free energy change is positive, the sulfide cannot be the final product; instead, the metal oxide or metal from hydrolysis would be the final product. Table 6-3 lists the free energy change for the sulfidation of some hydrolysis products from carbides

Table 6-3 Free energy change for the reaction between H_2S and hydrolysis products of metal carbides (i.e., oxides and metals) at 950 ^oC. The partial pressure of H_2 and H_2O were fixed at 0.87 and 0.03, respectively, from Cheng et al. (2006).

Reaction (written based on 1 mole of H_2S)	ΔG_r (in kJ/mol)	
	$p$$H_2S$= 50 ppm	$p$$H_2S$ = 0.1
0.5 $Cr_2O_{3\,(s)}$ + $H_2S_{\,(g)}$ + 0.5 $H_{2\,(g)}$ = $CrS_{\,(s)}$ + 1.5 $H_2O_{\,(g)}$	77	-0.1
0.5 $Mo_{\,(s)}$ + $H_2S_{\,(g)}$ = 0.5 $MoS_{2\,(s)}$ + $H_{2\,(g)}$	41	-36
0.5 $SiO_{2\,(s,\,cristobalite)}$ + $H_2S_{\,(g)}$ = 0.5 $SiS_{2\,(s)}$ + $H_2O_{\,(g)}$	183	105
0.5 $TiO_{2\,(s,\,rutile)}$ + $H_2S_{\,(g)}$ = 0.5 $TiS_{2\,(s,\,rutile)}$ + $H_2O_{\,(g)}$	102 [a]	39 [a]
0.5 $W_{\,(s)}$ + $H_2S_{\,(g)}$ = 0.5 $WS_{2\,(s)}$ + $H_{2\,(g)}$	50	-27
0.5 $ZrO_{2\,(s,\,monoclinic)}$ + $H_2S_{\,(g)}$ = 0.5 $ZrS_{2\,(s)}$ + $H_2O_{\,(g)}$	107	30

Note:
[a] thermochemical data at 727 ^oC instead of 950 ^oC.

in fuels with different concentration of H_2S. Except for Mo and W in fuels with high concentration of H_2S, the free energy change for all the reactions between hydrolysis products and high concentration of H_2S is positive, indicating the metal oxide or metal from the hydrolysis will be the final product. Therefore, from the above thermodynamic analysis, most metal carbides materials are ruled out as sulfur-resistant anode of SOFC not because of reaction with H_2S but because of their poor resistance to water vapor in the fuel gas.

To verify the prediction by thermodynamics, several materials including β-SiC, ZrC, and WC were exposed to a gas mixture of 10% H_2S/3% H_2O/87% H_2 at 950 ^oC for 2-5 days. The CO concentration in the fuel was ~1 ppm. Figures 6-1 to 6-3 show the comparison of the XRD patterns for β-SiC, ZrC and WC before and after the stability test. As predicted, the hydrolysis of β-SiC and ZrC were observed: β-SiC transformed to silica (high cristobalite phase) and ZrC transformed to monoclinic zirconia. For WC,

although most of the materials did not change, XRD identified trace amount of WS_2, which was confirmed by the appearance of strong Raman bands corresponding to WS_2 as shown in Figure 6-4 for the post-exposure sample.

- Metal Borides, Nitrides and Silicides

Similar to the transition metal carbides, many transition metal borides, nitrides and silicides also have high melting point, good electrical conductivity (see Table 6-1) and better oxidation resistance than metal carbides (Weimer, 1997). However, similar to transition metal carbides, thermodynamic analysis shows that hydrolysis is still a serious problem for these materials. Table 6-4 shows the free energy change for the hydrolysis of several common metal borides, nitrides, and silicides under a typical anode fuel atmosphere that contains 10% H_2S. All those hydrolysis reactions are energetically favorable. Like transition metal carbides, the reaction of these materials with H_2S could still be regarded as two steps with the first one as hydrolysis and the second as sulfidation of the corresponding hydrolysis products. Nevertheless, unless inhibited by slow kinetics (unlikely for porous structure), the hydrolysis reactions will happen and none of those materials are going to survive in typical SOFC anode atmosphere. As an experimental verification, Figure 6-5 shows the comparison of the XRD patterns of TiN powder before and after exposure to a fuel mixture of 10% H_2S/3% H_2O/87% H_2 at 950 ^oC for 2 days. Exactly as predicted from thermodynamics, TiO_2 (rutile phase) was the only solid product after the exposure. Therefore, these borides, nitrides and silicides are also ruled out as sulfur-resistant anode for SOFCs.

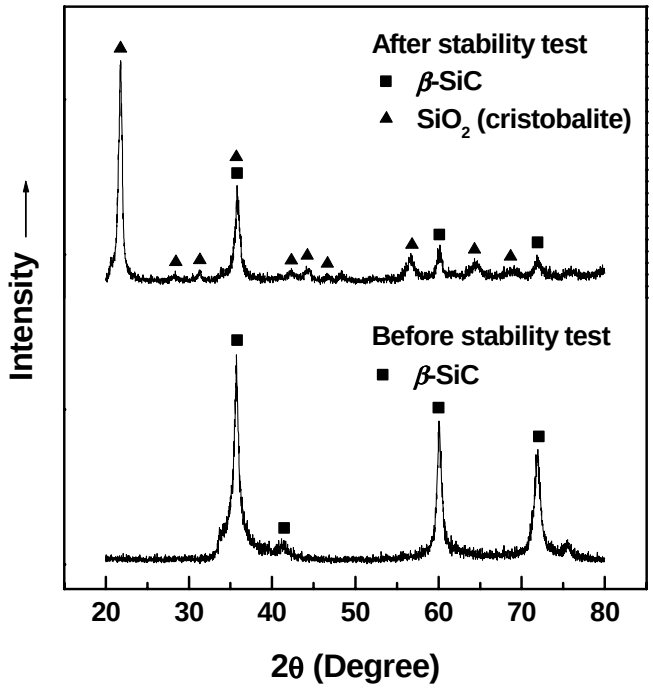

Figure 6-1 XRD patterns for the β-SiC sample before and after exposure to 10% H_2S/3% H_2O/87% H_2 at 950 ^oC for 5 days, from Cheng et al. (2006).

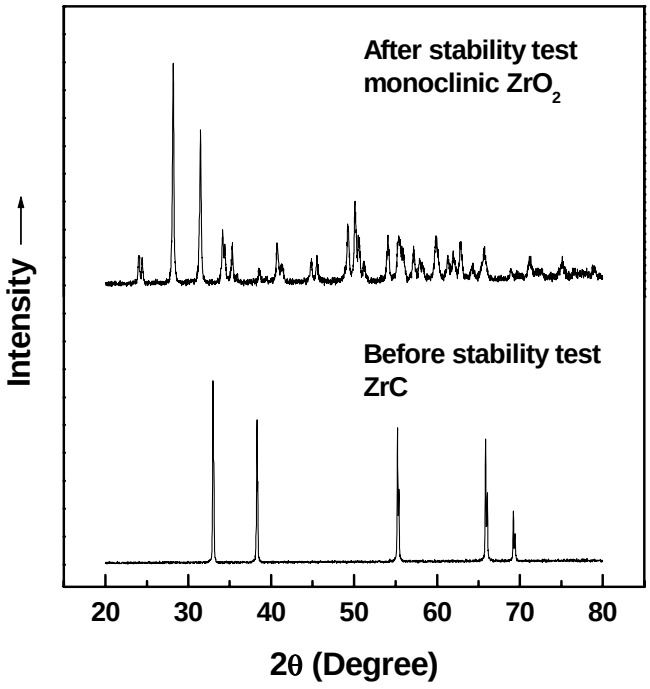

Figure 6-2 XRD patterns for the ZrC sample before and after exposure to 10% H_2S/3% H_2O/87% H_2 at 950 ^oC for 5 days, from Cheng et al. (2006).

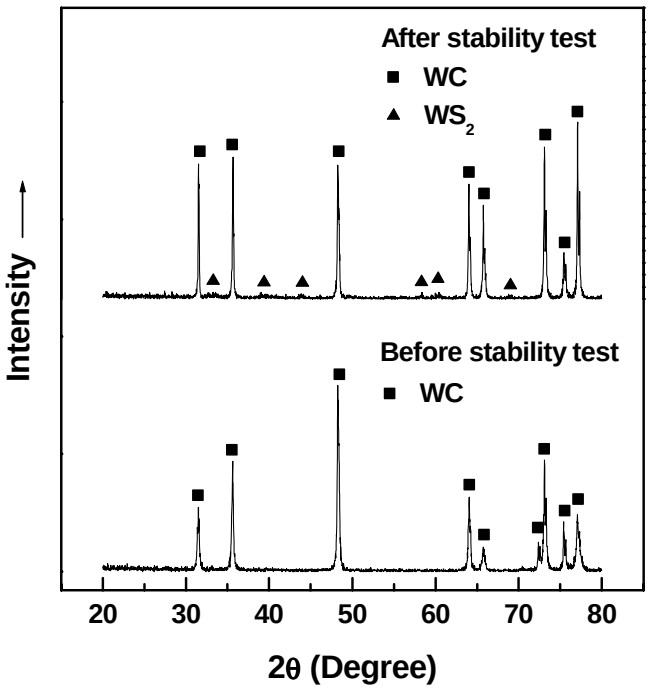

Figure 6-3 XRD patterns for the WC sample before and after exposure to 10% H_2S/3% H_2O/87% H_2 at 950 ^oC for 2 days, from Cheng et al. (2006).

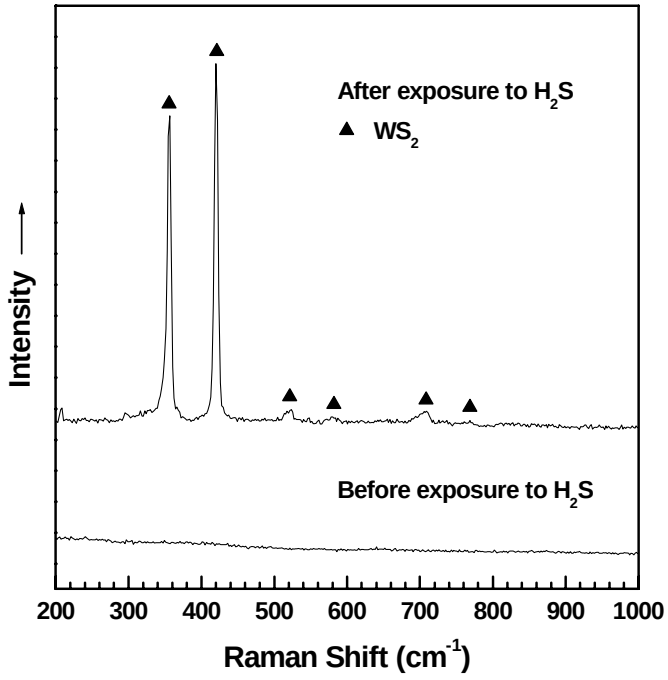

Figure 6-4 Raman spectra of the WC sample before and after exposure to 10% H_2S/3% H_2O/87% H_2 at 950 ^oC for 2 days, from Cheng et al. (2006).

Table 6-4 Free energy change for the reaction between water vapor and transition metal borides (M_xB_y), nitrides (M_xN_y) and silicide (M_xSi_y) at 950 ^oC. The partial pressure of H_2 and H_2O are fixed at 0.87 and 0.03, respectively, from Cheng et al. (2006).

Reaction (written based on 1 mole of H_2O)	ΔG_r (kJ/mol)
$0.2\ TiB_{2\ (s)} + H_2O_{\ (g)} = 0.2\ TiO_{2\ (s)} + 0.2\ B_2O_{3\ (l)} + H_{2\ (g)}$	-72
$0.2\ ZrB_{2\ (s)} + H_2O_{\ (g)} = 0.2\ ZrO_{2\ (s)} + 0.2\ B_2O_{3\ (l)} + H_{2\ (g)}$	-93
$2/3\ CrN_{\ (s)} + H_2O_{\ (g)} = 1/3\ Cr_2O_{3\ (s)} + 1/3\ N_{2\ (g)} + H_{2\ (g)}$	-88 [a]
$0.5\ TiN_{\ (s)} + H_2O_{\ (g)} = 0.5\ TiO_{2\ (s,\ rutile)} + 0.25\ N_{2\ (g)} + H_{2\ (g)}$	-71 [a]
$2/3\ VN_{\ (s)} + H_2O_{\ (g)} = 1/3\ V_2O_{3\ (s)} + 1/3\ N_{2\ (g)} + H_{2\ (g)}$	-60 [a]
$0.5\ ZrN_{\ (s)} + H_2O_{\ (g)} = 0.5\ ZrO_{2\ (s)} + 0.25\ N_{2\ (g)} + H_{2\ (g)}$	-129 [a]
$0.25\ MoSi_{2\ (s)} + H_2O_{\ (g)} = 0.25\ Mo_{\ (s)} + 0.5\ SiO_{2\ (s)} + H_{2\ (g)}$	-102

Note:
[a] partial pressure of N_2 is 10^{-6}.

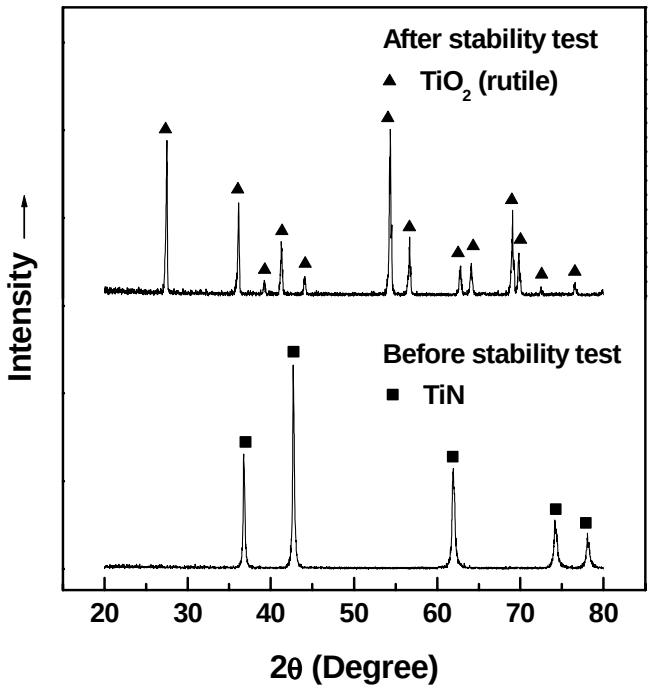

Figure 6-5 XRD patterns for the TiN sample before and after exposure to 10% H_2S/3% H_2O/87% H_2 at 950 ^oC for 2 days, from Cheng et al. (2006).

6.1.3.2 Stability for ABO_3 Perovskites

Metal oxides, especially those with the ABO_3 perovskite structure, have been studied as candidate materials for sulfur-resistant anode of SOFCs (Wang et al., 2001; Aguilar et al., 2004a and 2004b; Zha et al., 2005a; Mukundan et al., 2004; Marina et al., 2004). Some of them have a combination of desirable properties for anode including reasonable electrical conductivity and a close match of CTE with other cell components (see Table 6-1). To date, however, the determination of chemical stability (especially sulfur resistance) for these materials depends largely on experiments, i.e., the materials were exposed to H_2S containing fuels at high temperature and the phase change is analyzed afterwards (Wang et al., 2001; Zha et al., 2005a). A more efficient way is to predict their stability from the free energy change for the reaction of interest (e.g., sulfidation). In the following, the chemical stability for perovskite-structured oxides was analyzed using the method described in section 6.1.2 illustrated through several interesting candidate sulfur-tolerant anode materials. The majority of the analysis showed excellent agreement with experiments, indicating the method developed could provide useful guidance into future development of new sulfur-tolerant anode materials.

- $La_{1-x}Sr_xTiO_3$ materials

The $La_{1-x}Sr_xTiO_3$ materials have been reported as candidate sulfur-resistant anode materials in fuels with H_2S in the ~25-1000 ppm range (Mukundan et al., 2004; Marina et al., 2004). However, the chemical resistance of this material to H_2S has not been reported. In this study, the chemical stability of $LaTiO_3$ and $SrTiO_3$, the two end-members of the $La_{1-x}Sr_xTiO_3$ family, was analyzed.

For $LaTiO_3$, the B-site Ti is at +3 valence state, and can be easily oxidized (Stoklosa and Zajecki, 1996), and the oxidation of $LaTiO_3$ via the following reaction

$$2\ LaTiO_{3\ (s)} + H_2O_{\ (g)} = La_2Ti_2O_{7\ (s)} + H_{2\ (g)} \qquad (6\text{-}18)$$

is possible. To determine whether reaction (6-18) could happen thermodynamically, the tolerance factor t_p for $LaTiO_3$ was calculated from Equation (6-9) to be 0.943. Therefore, for the formation of $La^{3+}Ti^{3+}O_3$ from simple oxides

$$\frac{1}{2} La_2O_{3\ (s)} + \frac{1}{2} Ti_2O_{3\ (s)} \rightarrow LaTiO_{3\ (s)}, \qquad (6\text{-}19)$$

the enthalpy change, ΔH_r^{oxide} ($LaTiO_3$), calculated from Equation (6-7) is -43.3 kJ/mol (-49.0 kJ/mol if Equation (6-5) is used). As stated before, the entropy change for reactions like Equation (6-18) is usually very small and the entropy contribution to the free energy change ($T\Delta S_r^{oxide}$) was neglected. Therefore, the standard Gibbs formation energy of $LaTiO_3$ could be estimated:

$$\Delta G_f^{O}(LaTiO_3) \approx 0.5\,\Delta G_f^{O}(La_2O_3) + 0.5\,\Delta G_f^{O}(Ti_2O_3) + \Delta H_r^{oxide}\ (LaTiO_3) \qquad (6\text{-}20)$$

Assuming that the reaction enthalpy for reaction (6-19) is independent of temperature, then, at 950 ^{o}C, $\Delta G_f^{O}(LaTiO_3)$ = -1358.2 kJ/mol (–1363.9 kJ/mol if ΔH_r^{oxide} from Equation (6-5) is used).

On the other hand, for $La_2Ti_2O_7$, the enthalpy change for the reaction:

$$La_2O_{3\ (s)} + 2\ TiO_{2\ (s)} = La_2Ti_2O_{7\ (s)} \qquad (6\text{-}21)$$

is –206.0 kJ/mol (Helean et al., 2004). The standard Gibbs formation energy of $La_2Ti_2O_7$ would be:

$$\Delta G_f^{O}(La_2Ti_2O_7) \approx \Delta G_f^{O}(La_2O_3) + 2\,\Delta G_f^{O}(TiO_2) + \Delta H_r^{oxide}(La_2Ti_2O_7) \qquad (6\text{-}22)$$

At 950 ^{o}C, $\Delta G_f^{O}(La_2Ti_2O_7)$ = -3098.0 kJ/mol. Therefore, the change in Gibbs free energy for reaction (6-18) is given by:

$$\Delta G_r = \Delta G_f^{O}(La_2Ti_2O_7) + \Delta G_f^{O}(H_2) - 2\Delta G_f^{O}(LaTiO_3) - \Delta G_f^{O}(H_2O) + RT\ln\frac{P_{H_2}}{P_{H_2O}}. \quad (6\text{-}23)$$

At 950 ^{o}C in a fuel mixture of 10% H_2S/3% H_2O/87% H_2, ΔG_r = -167.2 kJ/mol (-155.8 kJ/mol if ΔH_r^{oxide} from Equation (6-5) is used). Therefore, reaction (6-18) is a highly energetically favorable process.

In comparison, if $LaTiO_3$ were to react with H_2S, the A-site simple oxide - La_2O_3 might transform to La_2S_3, while the B-site simple oxide Ti_2O_3 would oxidize into TiO_2, and the total reaction should be

$$2/3\ LaTiO_{3\,(s)} + H_2S_{(g)} = 1/3\ La_2S_{3\,(s)} + 2/3\ TiO_{2\,(s)} + 1/3\ H_{2\,(g)} + 2/3\ H_2O_{(g)} \quad (6\text{-}24)$$

The free energy change for the above reaction under the same condition (950 ^{o}C in a fuel of 10% H_2S/3% H_2O/87% H_2) was calculated to be ΔG_r = -23.9 kJ/mol (-20.1 kJ/mol if ΔH_r^{oxide} from Equation (6-5) is used), indicating it is also a spontaneous process. However, the hydrolysis reaction (6-18) is more likely to happen compared with the sulfidation-oxidation reaction (5-24) since (5-18) is more energetically favorable and only involves the oxidation of Ti^{3+} instead of both sulfidation (of La^{3+}) and phase separation as in the sulfidation reaction (6-24).

For the other end member - $SrTiO_3$, the standard Gibbs formation energy is available in the literature (Barin, 1995). Because both Sr^{2+} and Ti^{4+} are stable against oxidation/reduction and no transformation of TiO_2 to titanium sulfide was observed in experiment (see Figure 6-5) at 950 ^{o}C in fuels with 10% H_2S, the only possible reaction is

the sulfidation of the A-site simple oxide - SrO, and the entire sulfidation reaction for $SrTiO_3$ should be:

$$SrTiO_{3\,(s)} + H_2S_{\,(g)} = SrS_{\,(s)} + TiO_{2\,(s)} + H_2O_{\,(g)} \quad (6\text{-}25)$$

The free energy change for this reaction is given by:

$$\Delta G_r = \Delta G_f^{O}(SrS) + \Delta G_f^{O}(TiO_2) + \Delta G_f^{O}(H_2O)$$

$$- \Delta G_f^{O}(SrTiO_3) - \Delta G_f^{O}(H_2S) + RT \ln \frac{P_{H_2O}}{P_{H_2S}} \quad (6\text{-}26)$$

At 950 ^{o}C in a fuel of 10% H_2S/3% H_2O/87% H_2, ΔG_r = 33.0 kJ/mol. Therefore, the sulfidation reaction for $SrTiO_3$ under that condition cannot happen.

Finally, experiments were carried out to verify the analysis made above. Figures 6-6 and 6-7 show the XRD patterns of $LaTiO_3$ and $SrTiO_3$ before and after the exposure to a fuel mixture of 10% H_2S/3% H_2O/87% H_2 at 950 ^{o}C for 5 days. Exactly as predicted in the analysis, $LaTiO_3$ (JCPDS card No. 34-0596) was oxidized to $La_2Ti_2O_7$ (JCPDS card No. 28-0517) completely but did not form any sulfide, while $SrTiO_3$ (JCPDS card No. 35-0734) remained intact without the formation of any SrS.

- $La_{1-x}Sr_xVO_3$ materials

$La_{1-x}Sr_xVO_3$ was proposed as candidate sulfur-resistant anode material for SOFCs that utilize fuels with H_2S concentration in the 5-10 % range (Aguilar et al., 2004a and 2004b). However, the phenomena met with the stability for these materials were very interesting. In this study, the stability for the two end compositions, $LaVO_3$ and $SrVO_3$, were analyzed, and it was found that, after exposing to 10% H_2S/3% H_2O/87% H_2 at 950 ^{o}C for 5 days, the majority of $SrVO_3$ (JCPDS card No. 44-0039) transformed to SrS (JCPDS card No. 08-0489), while $LaVO_3$ did not react with H_2S but transformed partially

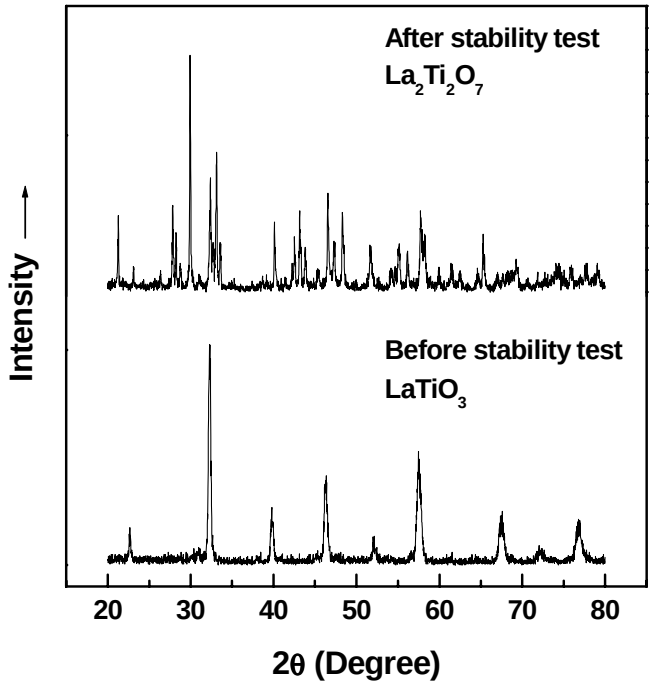

Figure 6-6 XRD patterns for the $LaTiO_3$ sample before and after exposure to 10% H_2S/3% H_2O/87% H_2 at 950 ^oC for 5 days, from Cheng et al. (2006).

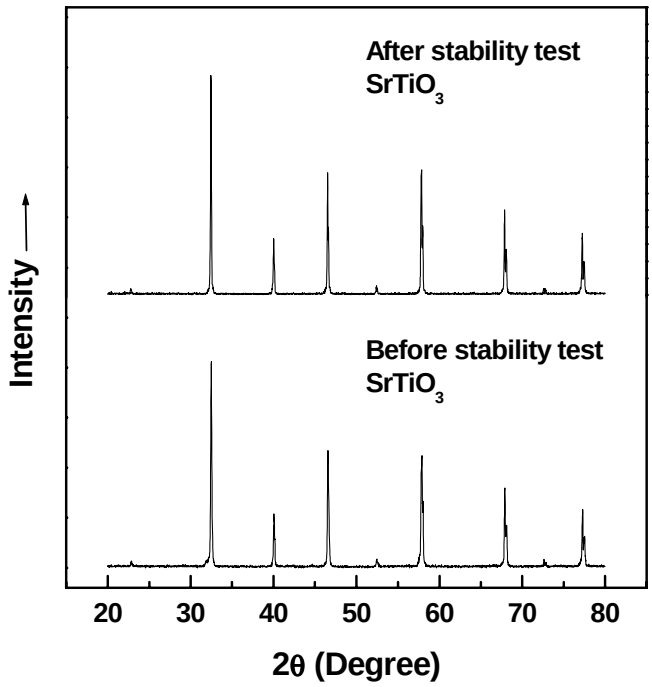

Figure 6-7 XRD patterns for the $SrTiO_3$ sample before and after exposure to 10% H_2S/3% H_2O/87% H_2 at 950 ^oC for 5 days, from Cheng et al. (2006).

from tetragonal structure (JCPDS card No. 11-0024) to orthorhombic structure (JCPDS card No. 36-0141), as shown in Figures 6-8 and 6-9.

To explain these phenomena, the tolerance factor, t_p, for $LaVO_3$ and $SrVO_3$ was calculated to be 0.957 and 1.014, respectively. Similar to $LaTiO_3$, the estimated standard Gibbs formation energy at 950 ^oC was -1226.1 kJ/mol for $LaVO_3$ and -1106.3 kJ/mol for $SrVO_3$ (-1236.3 kJ/mol and –1120.3 kJ/mol, respectively, if ΔH_r^{oxide} values from Equations (6-5) and (6-4) were used). For $SrVO_3$, upon the exposure to the H_2S-containing fuel, careful analysis indicates the possible reactions include (i) the sulfidation of the A-site SrO, and (ii) the reduction of the B-site V_2O_4, as both of them would be energetically favorable under the stability test condition. Therefore, the entire reaction for $SrVO_3$ would be:

$$SrVO_{3\,(s)} + H_2S_{\,(g)} + H_{2\,(g)} = SrS_{\,(s)} + 0.5\ V_2O_{3\,(s)} + 1.5\ H_2O_{\,(g)} \qquad (6\text{-}27)$$

The Gibbs free energy change for the above reaction at 950 ^oC in 10% H_2S/3% H_2O/87% H_2 is -29.2 kJ/mol (-15.2 kJ/mol if ΔH_r^{oxide} from Equation (6-4) is used). Therefore, the sulfidation of $SrVO_3$ in fuels containing 10% H_2S can happen (and did happen).

For $LaVO_3$, the situation is slightly more complicated. The A-site La_2O_3 could react with H_2S to form La_2S_3, while the B-site V_2O_3 is stable against sulfidation and reduction. Therefore, the entire reaction would be

$$2/3\ LaVO_{3\,(s)} + H_2S_{\,(g)} = 1/3\ La_2S_{3\,(s)} + 1/3\ V_2O_{3\,(s)} + H_2O_{\,(g)}. \qquad (6\text{-}28)$$

The Gibbs free energy change for this reaction under similar condition is very close to zero (-4.3 kJ/mol if ΔH_r^{oxide} from Equation (6-7) is used and 2.5 kJ/mol if ΔH_r^{oxide} from Equation (6-5) is used). Considering the uncertainty in the thermochemical data, it is

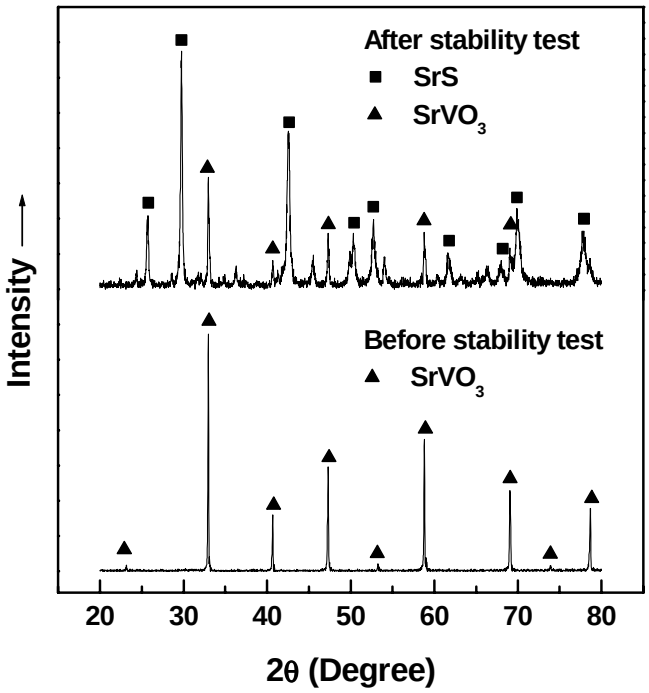

Figure 6-8 XRD patterns for the $SrVO_3$ sample before and after exposure to 10% H_2S/3% H_2O/87% H_2 at 950 ^oC for 5 days, from Cheng et al. (2006).

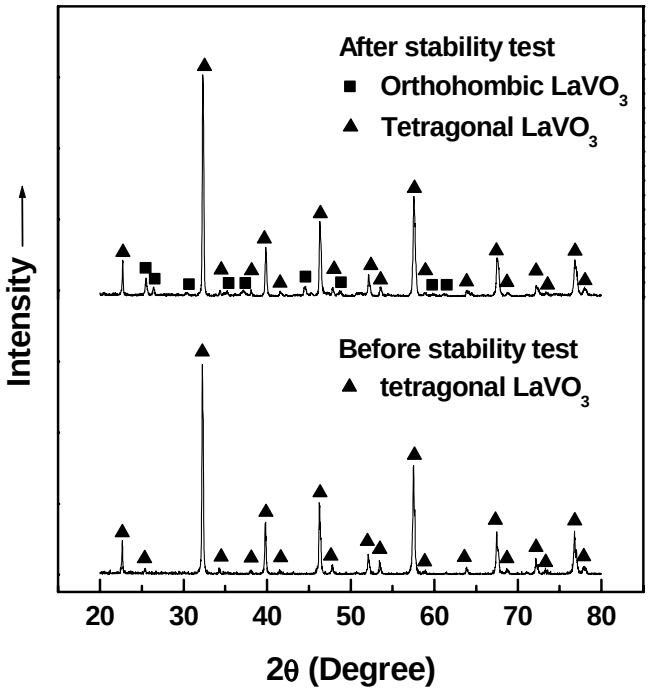

Figure 6-9 XRD patterns for the $LaVO_3$ sample before and after exposure to 10% H_2S/3% H_2O/87% H_2 at 950 ^oC for 5 days, from Cheng et al. (2006).

concluded that this material is on the border of reaction since small variation in the experimental condition (e.g., temperature or H_2S concentration) could lead to different results.

6.1.4 Discussion

The reason why metal carbides, borides, nitrides, and silicides are not resistant against hydrolysis is that the corresponding oxides (e.g., B_2O_3, SiO_2, TiO_2, Ta_2O_5, ZrO_2) are much more stable than the carbides, borides, nitrides, and silicides even in an SOFC anode atmosphere, which is considered reducing ($pO_2 \approx 10^{-18}$ to 10^{-20}). The only exceptions were W and Mo-based carbide materials: the corresponding metal phase are more stable in reducing atmosphere and the free energy change for hydrolysis is rather small as long as the CO concentration is high (i.e., on the percentage range) and the water concentration is low. Therefore, if these types of materials were to be studied, W and Mo containing should be the materials to be investigated first. However, it is noted that the low CTE and high processing temperatures of these materials (i.e., Mo and W based carbides) may pose other challenges.

The reason for the difference in stability of ABO_3 perovskite oxides can be explained from the comparison of the free energy change from simple oxides to complex oxides (i.e., ΔG_r^{oxide} for reactions (6-1) to (6-3), also called the *stabilizing factor* for ABO_3 perovskite, $\Delta G_{Stabilize}^{ABO_3}$, in this study) and the free energy change for the simple oxides to transform to other phases like sulfides (also called the *disruptive factor* for ABO_3 perovskite, $\Delta G_{Distrupt}^{ABO_3}$, in this study). For example, the stabilizing factor, $\Delta G_{Stabilize}^{ABO_3} = \Delta G_r^{oxide}$, for $SrTiO_3$ is -137.7 kJ/mol while the disruptive factor ($\Delta G_{Distrupt}^{ABO_3}$, which equals

the ΔG_r for the sulfidation of SrO to SrS) under the condition of the stability test (i.e., 950 ^{o}C, 10% H_2S/3% H_2O/ 87% H_2) is only -104.7 kJ/mol. Therefore, $\left|\Delta G_{Distruptive}^{ABO_3}\right| < \left|\Delta G_{Stabilize}^{ABO_3}\right|$, and $SrTiO_3$ will be stable.

In comparison, for $LaTiO_3$, the stabilizing factor $\Delta G_{Stabilize}^{ABO_3} = \Delta G_r^{oxide} =$ -43.3 kJ/mol (-49.0 kJ/mol if ΔH_r^{oxide} from Equation (6-5) is used) while the disruptive factor $\Delta G_{Distrupt}^{ABO_3}$ includes two contributions:

1) ΔG_r for the oxidation of B-site simple oxide 1/2 Ti_2O_3 to TiO_2 (-24.0 kJ/mol at 950 ^{o}C in 10% H_2S/87% H_2/3% H_2O)
2) ΔG_r for the combination of TiO_2 with 1/2 La_2O_3 to form 1/2 $La_2Ti_2O_7$ (-206/2 = -103.0 kJ/mol, Helean et al., 2004).

The total disruptive factor $\Delta G_{Distrupt}^{ABO_3}$ = (-24.0) + (-103) = -127 kJ/mol. Therefore, $\left|\Delta G_{Distruptive}^{ABO_3}\right| > \left|\Delta G_{Stabilize}^{ABO_3}\right|$, $LaTiO_3$ can (and did) transform to 1/2 $La_2Ti_2O_7$ under the testing condition.

Similarly, for $SrVO_3$, the stabilizing factor $\Delta G_{Stabilize}^{ABO_3} = \Delta G_r^{oxide}$ = -125.0 kJ/mol (-139.0 kJ/mol if ΔH_r^{oxide} from Equation (6-4) is used), while the disruptive factor $\Delta G_{Distrupt}^{ABO_3}$ also includes two contributions:

1) ΔG_r for the sulfidation of SrO to SrS (-104.7 kJ/mol at 950 ^{o}C in 10% H_2S/3% H_2O/ 87% H_2)
2) ΔG_r for the reduction of 1/2 V_2O_4 to 1/2 V_2O_3 (-49.5 kJ/mol at 950 ^{o}C in 10% H_2S/3% H_2O/ 87% H_2).

The combined disruptive factor is $\Delta G_{Distrupt}^{ABO_3}$ = (-104.7) + (-49.5) = -154.2 kJ/mol. Therefore, $\left|\Delta G_{Distruptive}^{ABO_3}\right| > \left|\Delta G_{Stabilize}^{ABO_3}\right|$, and $SrVO_3$ can (and did) react with the fuel with 10% H_2S and 87% H_2 at 950 ^oC.

The above discussion is also true for some other materials like doped $YFeO_3$ that had been tried as sulfur-resistant anode in previous studies (Wang et al., 2001). Both of the simple oxides of A-site ion (Y_2O_3) and B-site ion (1/2 Fe_2O_3) could be sulfidized, and ΔG_r for the sulfidation of 1/2 Fe_2O_3 alone was more negative than –100 kJ/mol at 900 ^oC in 4% H_2S/96% H_2 (assuming 0.1% H_2O). On the other hand, the material has a tolerance factor of only ~0.89, which would yield a rather small stabilizing factor (~20 kJ/mol). Therefore, the disruptive force is so large that the material will fail anyway in fuels with high concentration of H_2S, as observed in the experiment (Wang et al., 2001).

It is noted that the thermodynamic analysis made here was still limited in several ways. First, it only predicted the chemical stability of bulk materials. It did not provide any direct information about the stability of surface species (e.g., adsorbed sulfur) nor catalytic activity of the materials. This is clearly seen for the Ni-YSZ cermet anode: the equilibrium pH_2S/pH_2 ratio for bulk nickel sulfide at 950 ^oC in H_2 fuel is as high as 10^{-2}, while it has been known in Chapter III that the Ni-based anode is poisoned by H_2S in the ppm range at that temperature. Second, thermodynamic stability is a necessary but not sufficient condition for a sulfur-tolerant anode material to be successful: it must have other desired properties such as adequate electrical conductivity, high catalytic activity for fuel oxidation, as well as compatibility with other cell components such as electrolyte and interconnect. Nevertheless, the method of using thermodynamics in helping to

predict and/or explain the stability for both simple and complex candidate sulfur-tolerant anode materials has been established and could be applied to future study in the search of new, sulfur-tolerant anode materials.

6.2 Mechanism for the Sulfur Tolerance of Some Candidate SOFC Anode Materials

As stated before, although the sulfur-tolerant anode materials have been studied for some time, there have been no studies that characterized the changes on the surface of the candidate materials (especially those oxide materials) before and after exposure to H_2S containing fuel, and, as a result, the mechanism for the enhanced sulfur tolerance is still not known. In this study, some promising sulfur tolerant anode materials were prepared and the sulfur tolerance in terms of electrochemical response was demonstrated. The changes on the anode surface were characterized and the possible mechanism origin for the enhanced sulfur tolerance was presented.

6.2.1 Results

$Gd_2Ti_{2-x}Mo_xO_7$ (GTMO) was proposed as a candidate sulfur-tolerant anode materials based on previous reports on the high ionic conductivity of those materials (Kramer and Tuller, 1995; Porat et al., 1997) and the fact that it contains Mo, which is a good catalyst both as a metal and as an oxide. In this study, it was found that among the family of GTMO materials, $Gd_2Ti_{1.4}Mo_{0.6}O_7$ turned out to be a promising sulfur-tolerant anode material in terms of both chemical stability and electrochemical response to H_2S.

Figure 6-10 shows the performance for a full cell it was operated in fuels with and without high concentration (10%) of H_2S. Instead of showing large degradation as nickel

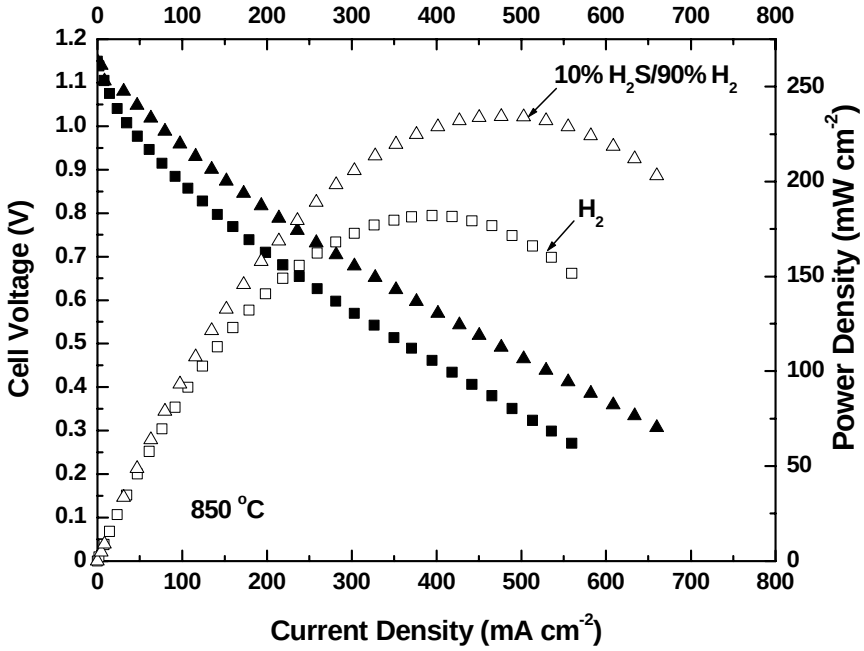

Figure 6-10 Comparison of performance for electrolyte-supported full cell with $Gd_2Ti_{1.4}Mo_{0.6}O_7$ anode in H_2 fuel without and with 10% H_2S at 850 °C.

(In fact, nickel would form bulk nickel sulfide in this case, which will melt and lead to catastrophic cell failure), the cell performance actually increased in the presence of high concentration of H_2S: the maximum power density increased from 182 mW/cm^2 to 234 mW/cm^2 at 850 °C after the introduction of 10% H_2S. Measurement of the anode/electrolyte/anode symmetrical cell under similar conditions reveals even greater changes. Figure 6-11 shows the impedance spectra for the anode/electrolyte symmetrical cell at 850 °C in H_2 fuel without and with 10% H_2S. Both the anode interfacial resistance and the bulk resistance decreased dramatically when there was H_2S present. Further study indicated that the enhanced performance in the presence of H_2S could be observed over a wide temperature range. For example, Figure 6-12 shows the change in anode interfacial conductance (i.e., the inverse of anode interfacial resistance) as determined

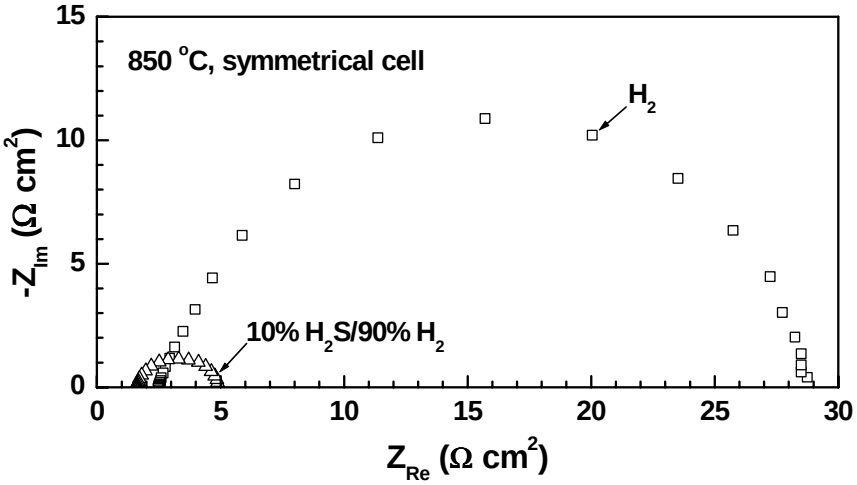

Figure 6-11 Comparison of the impedance spectrum for the $Gd_2Ti_{1.4}Mo_{0.6}O_7$ anode symmetrical cell in H_2 fuel without and with 10% H_2S at 850 °C.

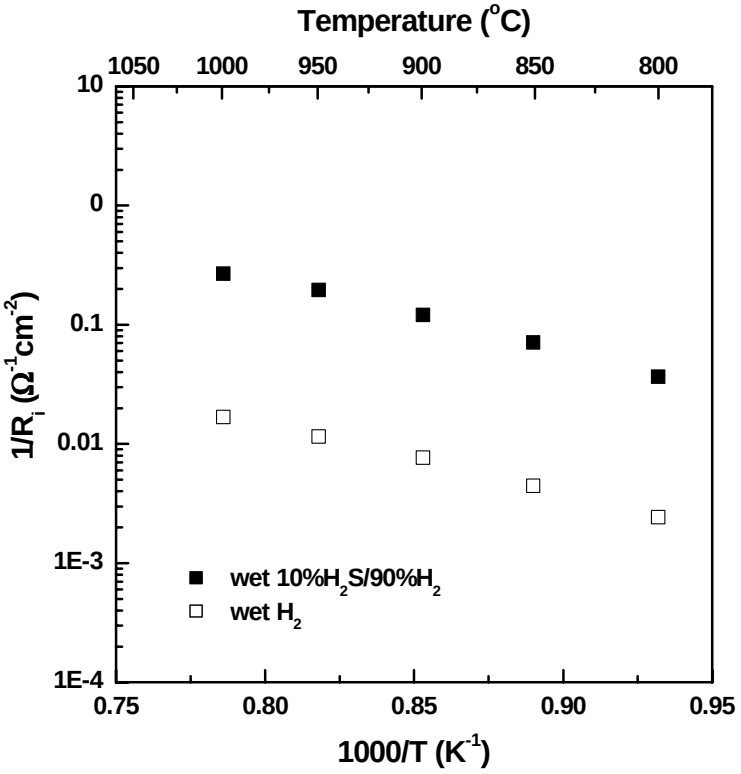

Figure 6-12 Change of anode interfacial conductance (1/Ri) versus inverse temperature for $Gd_2Ti_{1.4}Mo_{0.6}O_7$ anode symmetrical cell in H_2 fuel without and with 10% H_2S.

from anode symmetrical cell versus inverse temperature in hydrogen fuels with and without 10% H_2S. It was found that, over a temperature range from 800 to 1000 ^oC, the anode interfacial resistance almost decreased 10 times when there was 10% H_2S in the fuel, while there was no significant change in the anode activation energy: 128±4 kJ/mol in humidified H_2 versus 122±1 kJ/mol in humidified H_2 with 10% H_2S.

To understand the enhanced sulfur tolerance (or sulfur enhancement effect as opposed to sulfur poisoning effect) observed for the GTMO material, the anode before and after testing in H_2S-containing fuels was characterized. Figure 6-13 shows the XRD patterns of the anode before and after testing in humidified H_2 containing 10% H_2S at temperatures up to 950 ^oC for 5 days. Except for GTMO and YSZ, no impurity phases could be identified from the anode. However, when the sample was examined using Raman spectroscopy, which was more sensitive the surface, the changes could be identified. Figure 6-14 shows the Raman spectrum of the anode before and after electrochemical testing in fuels containing 10% H_2S. Clearly, MoS_2 was detected on the GTMO anode surface, which indicated that the surface Mo-containing phase partially transformed into MoS_2 upon exposure to H_2S containing fuel. However, the extent of reaction was limited only to a few layers as no bulk phases could be identified using XRD, indicating the ratio of MoS_2 should be quite small.

6.2.2 Discussion

The GTMO materials studied demonstrated not just sulfur tolerance but actually sulfur enhancement behavior. The sulfur tolerance for Mo (and also Nb, see Choi et al., 2007) based oxide materials comes from the transition of the very surface from metal

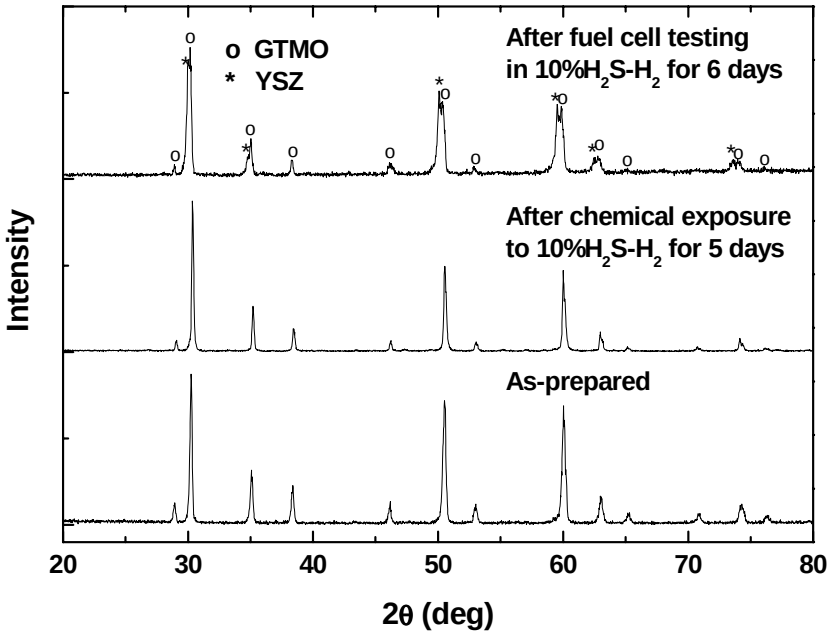

Figure 6-13 XRD pattern for the $Gd_2Ti_{1.4}Mo_{0.6}O_7$ anode before and after exposure to fuels containing 10% H_2S at elevated temperature, from Zha, Cheng, and Liu (2005a).

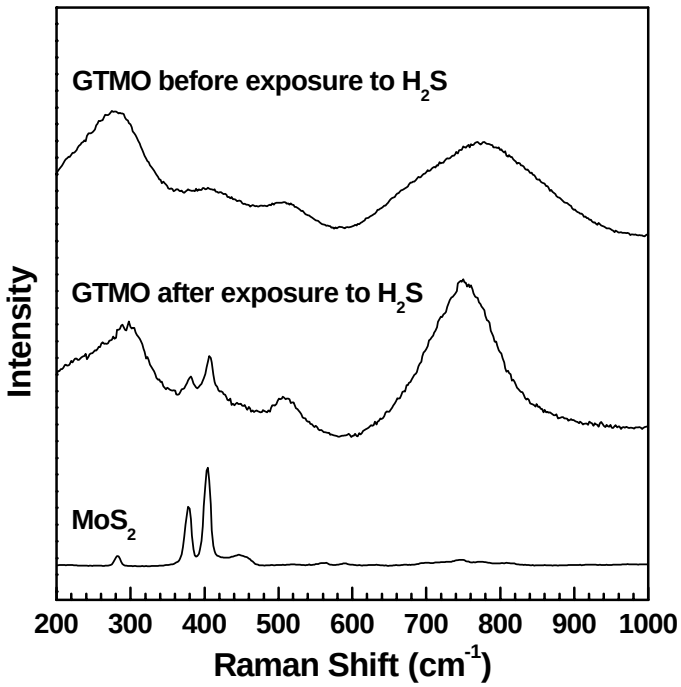

Figure 6-14 Raman spectra for the $Gd_2Ti_{1.4}Mo_{0.6}O_7$ anode before and after exposure to fuels containing 10% H_2S at elevated temperature and for the standard MoS_2 material.

oxide to metal sulfide, as has been illustrated in Figures 6-13 and 6-14. As to the fundamental reason for this sulfur tolerance behavior, although no changes had been identified using XRD, the presence of MoS_2 was unambiguously identified using Raman spectroscopy. Clearly, the amount of MoS_2 must be very small (below ~5 %) so that it is below the detection limit for XRD. On the other hand, as shown in Figure 6-12, there was no significant change in the activation energy after the introduction of H_2S. Therefore, the possible mechanism for the enhanced sulfur tolerance for GTMO material was that upon exposure to H_2S containing fuel, a very thin layer of MoS_2 formed on the anode surface. This thin layer of MoS_2 enhanced the anode electrochemical performance in two ways: first, it may provide better catalytic activity; second, it may provide more reaction sites. The first argument is reasonable as pure MoS_2 is a good catalyst in fuels with H_2S; the second one is also reasonable since the activation energy for the anode electrochemical process remained largely the same yet the anode interfacial resistance decreased by almost 10 times. Considering that MoS_2 has a melting point of 1185 ^oC, at an elevated temperature of 850 ^oC, the formed MoS_2 might better link the active sites on the oxide anodes so that more active sites on the anode would be available for the electrochemical reaction. As a result, the rate for the overall reaction increased dramatically, leading to enhanced performance in H_2S-containing fuel. This hypothesis is also consistent with the observation of a decrease in not only the anode interfacial resistance, but also in the cell bulk resistance, indicating better current collection over the anode.

The observed sulfur tolerance for GTMO material is more significant compared with some studies reported earlier, in which the cell performance was still negatively

impacted by the presence of H_2S (e.g., see the study by Kurokawa et al. (2007) in Figure 2-18). The observation is also important as it utilizes the desirable properties for Mo-based material but is not limited as pure MoS_2: Pure MoS_2 is not a satisfactory sulfur-tolerant anode material for SOFC due to its limited chemical stability in oxidizing atmosphere (for fuel cell fabrication) and its structural instability at high temperature.

6.3 Summary

To summarize this chapter, thermodynamics was successfully applied to predict and explain the phenomena concerning the stability of candidate sulfur tolerant anode materials including metal carbides, borides, nitrides, silicides, and perovskite-structured oxides in typical anode atmosphere. The enhanced sulfur tolerance observed for some new sulfur tolerant anode materials was attributed to the transition of the surface from metal oxides to metal sulfides, which enhance the catalytic activity and increase the number of reaction sites.

CHAPTER 7

CONCLUSIONS AND RECOMMENDATIONS

7.1 Conclusions

The main conclusions from this study are as follows:

1) The extent of sulfur poisoning increases with the H_2S concentration and as the operating temperature is reduced.
2) The extent of sulfur poisoning, as measured by the relative increase in cell resistance, decreases with the current density passing through the cell, independent of the mode of electrochemical testing – either under constant current or constant voltage conditions.
3) The long-term degradation due to sulfur poisoning for anode-supported cells was less significant than the self degradation of the cells.
4) The observed degradation in performance of Ni-based anodes exposed to ppm-level H_2S at high temperatures is due not to the formation of conventional sulfides but to the adsorption of sulfur on nickel surfaces.
5) The conventional nickel sulfides observed in the ex situ experiments were actually formed during the cooling process by reaction of nickel and the trace amount of H_2S in the fuel. Therefore, the cooling of SOFCs in fuels containing even ppm level H_2S should be avoided, which may complicate the interpretation of the poisoning mechanism and cause irreversible morphology changes.

6) Thermodynamics can be used effectively to guide the screening of new sulfur-tolerant anode materials and to explain many observations regarding materials reactivity with sulfur compounds.
7) The sulfur tolerance observed for some candidate anode materials (metal oxides) is due to the transformation of the surface from oxides to sulfides upon exposure to H_2S. The sulfides must be thermally, physically, and chemically stable and catalytically active.

7.2 Recommendations

For future investigation into the sulfur-anode interactions, work in the following areas is recommended:

1) Investigation of the sulfur poisoning behavior for SOFCs under high fuel utilization conditions. This is because of the button cell setup in the lab, the fuel utilization was always quite small (i.e., <10%). The poisoning behavior may be more dramatic when the cell was running under high fuel utilization condition or even fuel starvation condition.
2) Modification the current Ni-YSZ cermet anode using the knowledge about the sulfur tolerance for those candidate materials. Although several candidate sulfur tolerant anode materials have been proposed, each of them are limited and are not likely to replace the current Ni-YSZ cermet anode due to insufficient cell performance. Therefore, modification of the current nickel-YSZ anode using the knowledge about the sulfur tolerance may lead to a successful sulfur-tolerant anode for real world applications.

APPENDEX A

ENGINEERING DRAWINGS AND PICTURES FOR

THE MULTI-CELL TESTING SYSTEM

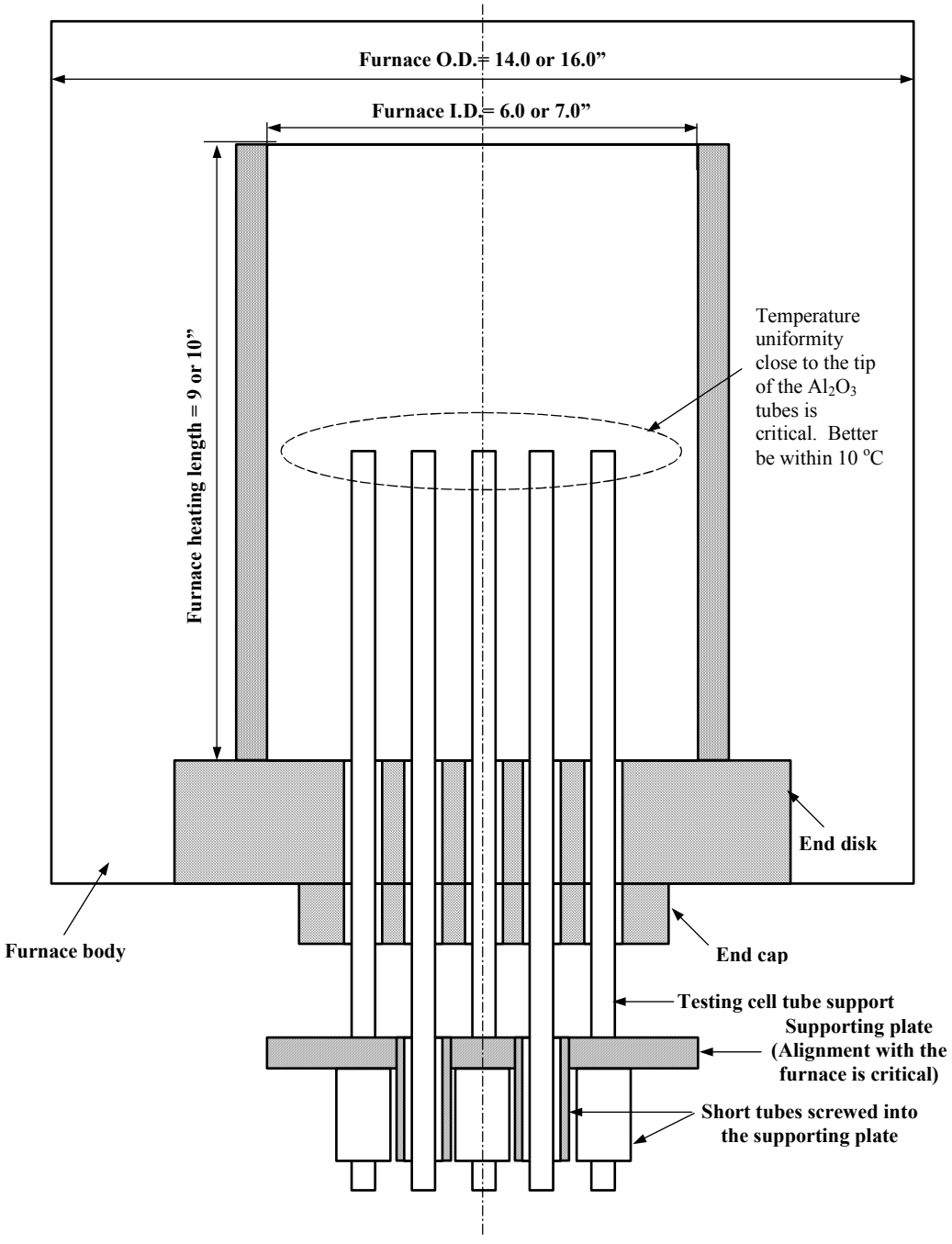

Figure A-1 Schematic for the large furnace and the supporting plate and tubes for the multi-cell testing.

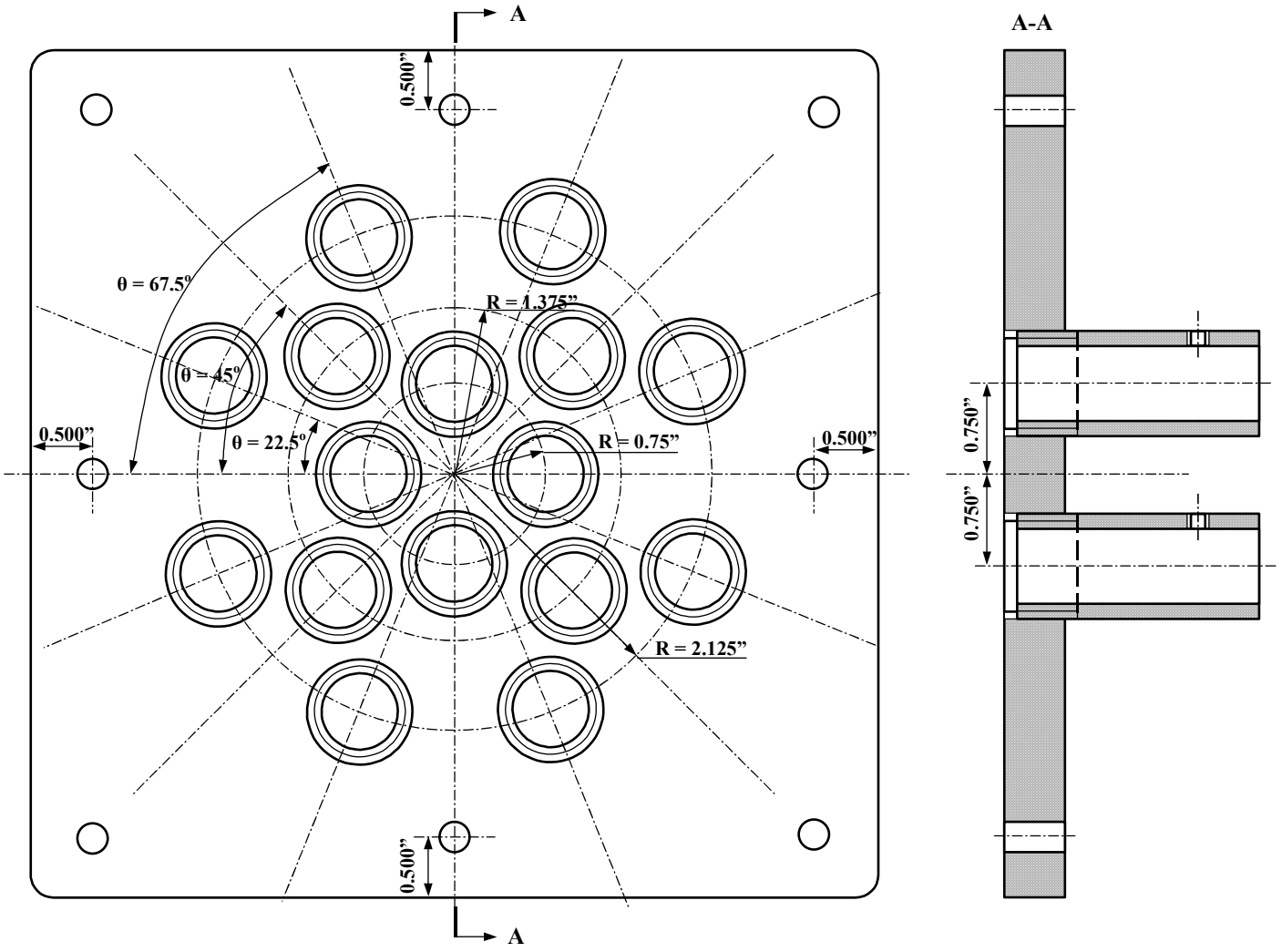

Figure A-2 Engineering drawing for the cell support plate with screw-in nipples (16 in all) in the multi-cell testing system.

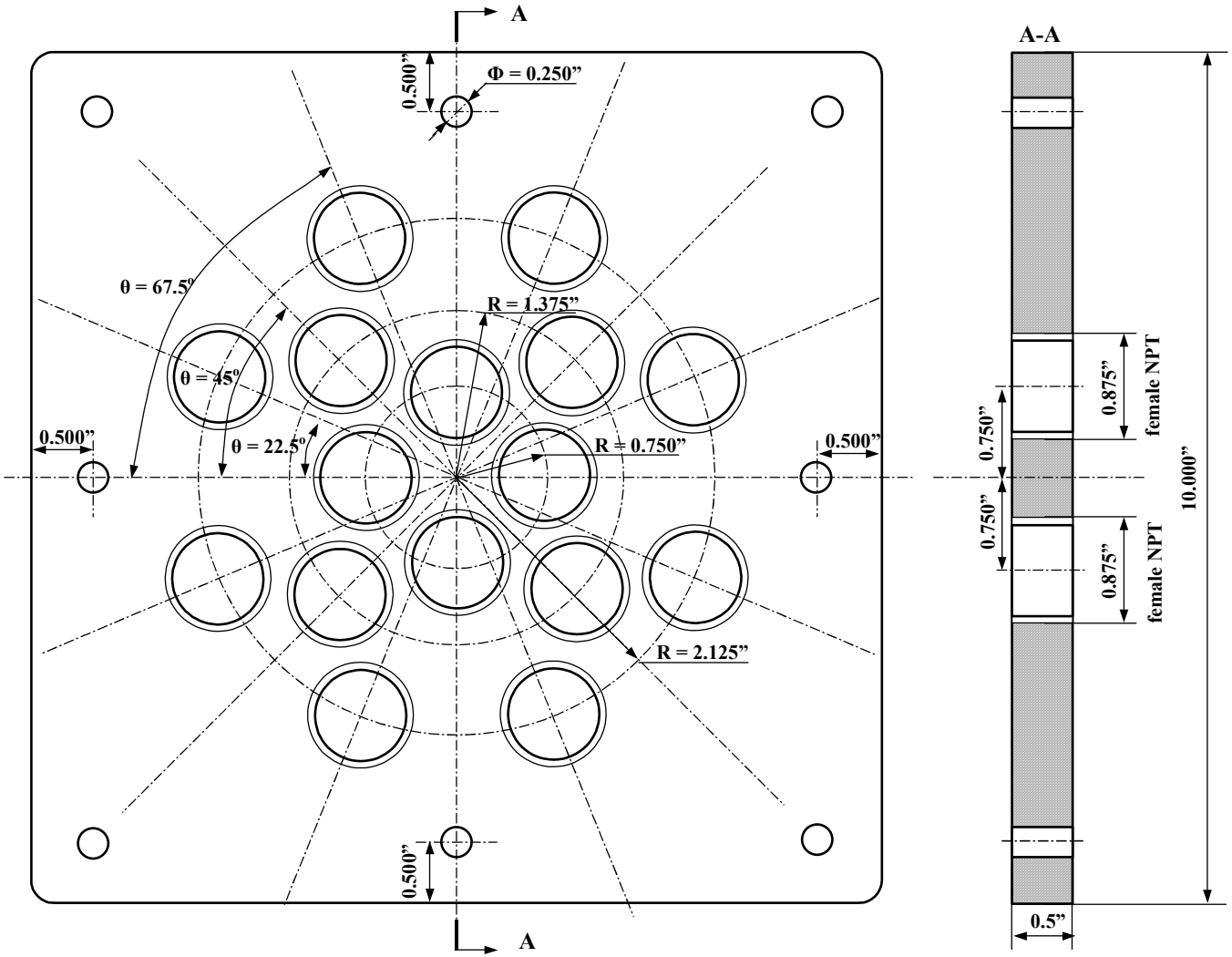

Figure A-3 Engineering drawing for the cell support plate without the screw-in nipples.

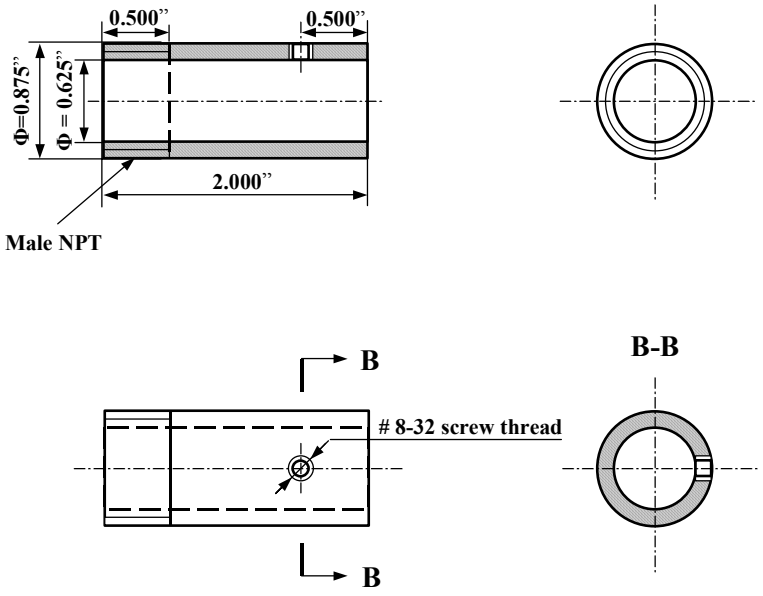

Figure A-4 Engineering drawing for the cell support plate without the screw-in nipples.

Figure A-5 Picture of the furnace and the supporting frame for the multi-cell testing system.

Figure A-6 Picture of the furnace and the supporting frame for the multi-cell testing system.

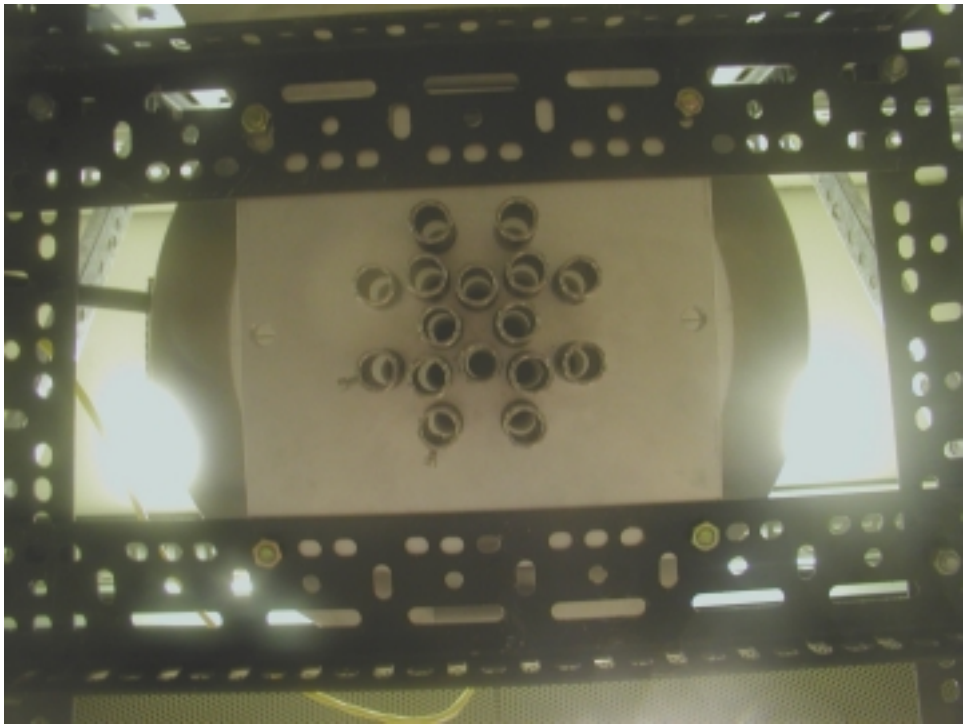

Figure A-7 Picture of the cell support plate, viewed from the bottom of the furnace.

APPENDEX B

DETECTION OF THIN FILM NICKEL SULFIDE USING RAMAN

Thin film nickel sulfides were prepared and characterized using Raman spectroscopy to establish the detection limit for Raman on bulk phase nickel sulfides.

1. Preparation and characterization of thin film nickel sulfide

Nickel metal was sputtered onto quartz and silicon wafer by Songho Choi in the Professor Meilin Liu's group. A Ni metal target with a purity of 99.99% was used. After the chamber was evacuated down to 2×10^{-6} torr, the working pressure was maintained at 2×10^{-2} torr with the introduction of Ar. The deposition was done at 80 W, and the sputtering time was 30 sec, 3 min and 9 min, respectively. The prepared samples (i.e., Ni film on quartz and silicon) were placed into alumina boats and placed inside a tube furnace and heated up to 300 ^{o}C and held for 13.5 h in a fuel mixture of 50 ppm H_2S/50% H_2/1.5% H_2O/48.5% N_2 to transform the nickel film into nickel sulfide film. Then the samples were cooled down in the same fuel and characterized using Raman spectroscopy, SEM and EDS.

2. Characterization of thin film nickel sulfides

Figure B-1 shows the SEM micrographs of surface and cross-section of the nickel sulfide films on Si wafer. The thickness of the 30 sec, 3 min and 9 min sputtered samples was approximately 30, 100, and 200 nm, respectively. The surface of the nickel sulfide film consisted of nanometer-scale particles. Figure B-2 shows the Raman spectra of the nickel sulfide thin film samples prepared on quartz substrate. For the 30 sec sputtered

sample, there was a very wide bump from 290 to 490 cm^{-1}; for the 3 min sputtered sample, the Raman peaks corresponds to β-NiS; for the 9 min sputtered sample, a broad Raman band from 290 to 380 cm^{-1} appears, corresponding to nickel sulfides with structures poorly defined.

To investigate whether there was interference from the quartz substrate, the Raman spectrum for quartz film were also obtained. It looks like that the background from quartz substrate contributed to the Raman spectra observed for the thinnest sample (i.e., 30 sec sputtered). Therefore, the background of quartz substrate is subtracted out (by monitoring the height at 489 cm^{-1}), and the result is shown in Figure B-3.

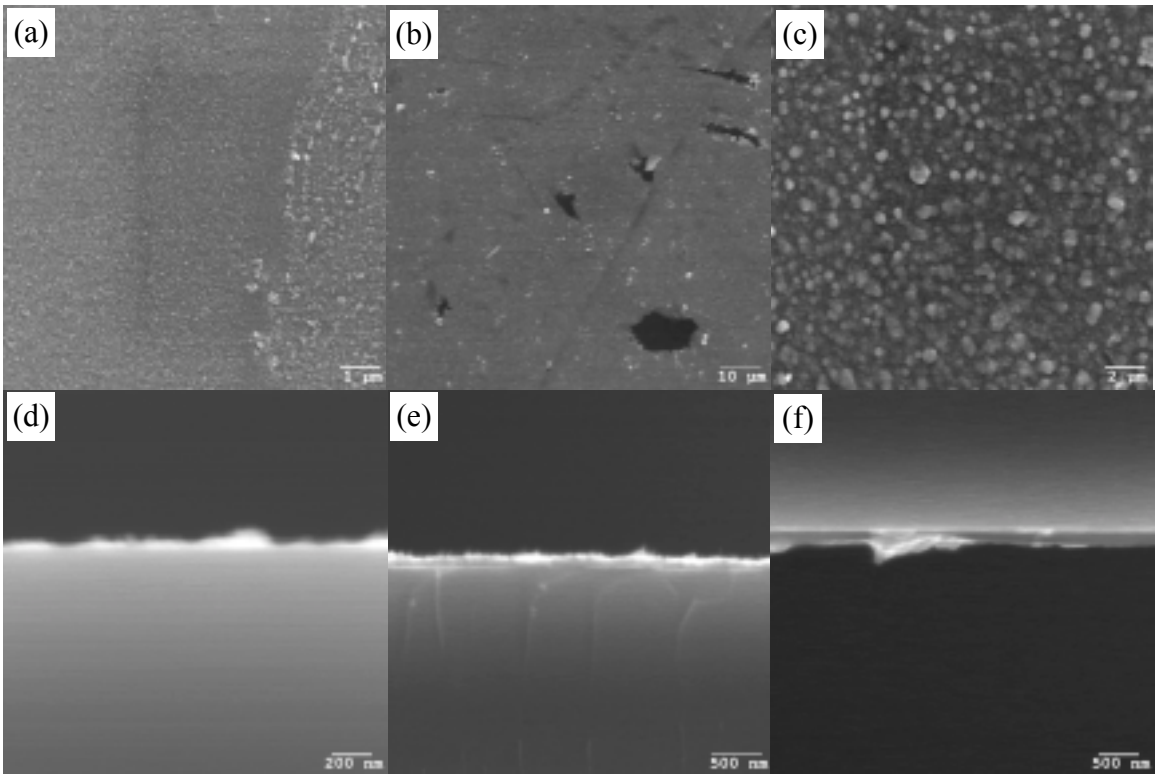

Figure B-1 SEM micrographs of the surface (a, b, c) and cross-section (d, e, f) of the nickel sulfides films prepared on Si wafer. (a) and (d) are for film with 30 sec sputtering, (b) and (e) are for film with 3 min sputtering, (c) and (f) are for film with 9 min sputtering.

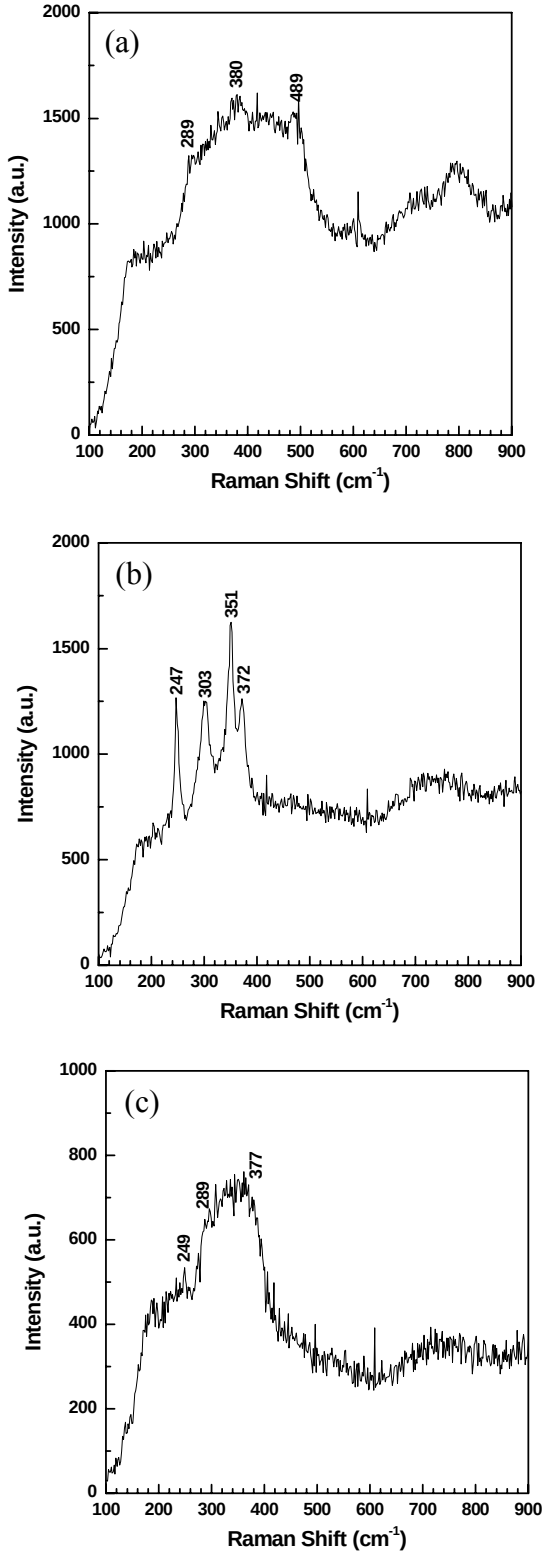

Figure B-2 Raman spectra of the nickel sulfide films prepared on quartz substrate. The time of sputtering was (a) 30 sec, (b) 3 min, and (c) 9 min, respectively.

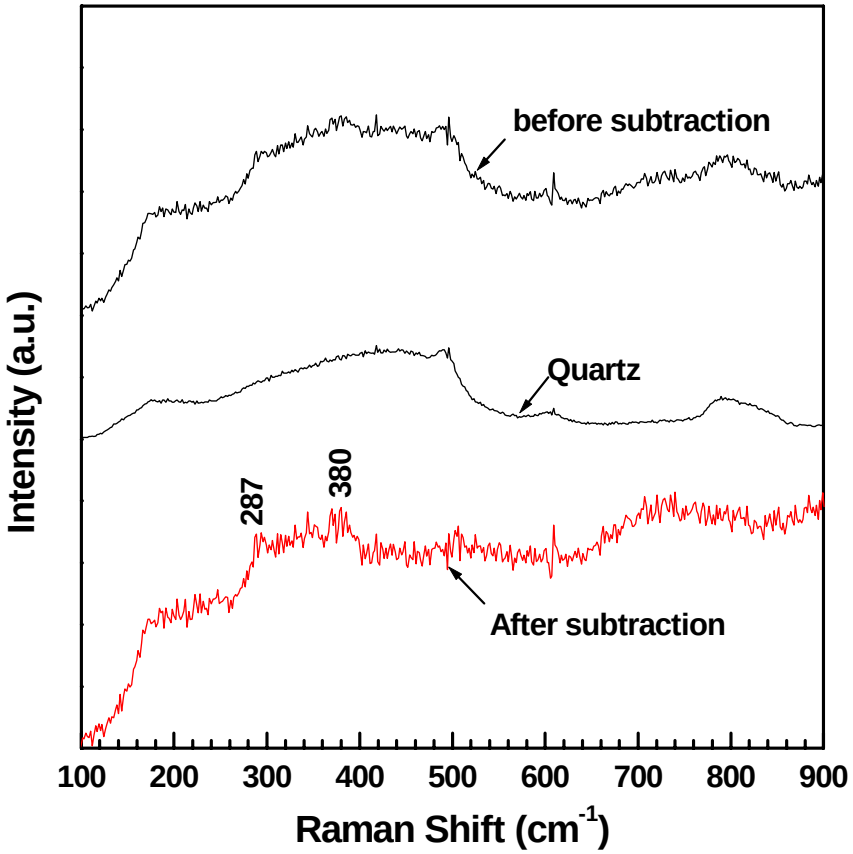

Figure B-3 Raman spectra of the quartz substrate, the nickel sulfide film (30 sec sputtered) before and after subtraction of the contribution from the quartz substrate.

The spectrum after subtraction of the contribution from quartz show close similarity to nickel sulfides with less well defined structure, as shown in Figure B-2. Therefore, the lower detection limit for Raman on nickel sulfide using the configuration in the lab was determined to be ~30 nm.

REFERENCES

1. Aguilar, L., Zha, S., Li, S., Winnick, J., and Liu, M., (2004a), "Sulfur-Tolerant Materials for the Hydrogen Sulfide SOFC," *Electrochemical and Solid-State Letters*, Vol. 7, pp. A324-326.

2. Aguilar, L., Zha, S., Cheng, Z., Winnick, J., and Liu, M., (2004b), "A Solid Oxide Fuel Cell Operating on Hydrogen Sulfide (H_2S) and Sulfur-Containing Fuels," *Journal of Power Sources*, Vol. 135, pp. 17-24.

3. Anderson, H. U., Tietz, F., (2003), "Interconnects," in *High Temperature Solid Oxide Fuel Cells: Fundamentals, Design and Applications*, edited by Singhal, S. C. and Kendall, K., Elsevier Advance Technology, Oxford, UK, pp. 173-195.

4. Anthony, J. W., Bideaux, R. A., Bladh, K. W., and Nichols, M. C., (1990), *Handbook of Mineralogy*, Mineral Data Publishing, Tucson, Arizona.

5. Bard, A. J., Faulkner, L. R., (2001), *Electrochemical Methods: Fundamentals and Applications*, John Wiley & Sons, Inc., USA.

6. Barin, I., (1995), *Thermochemical Data of Pure Substances*, 3rd edition, VCH, Weinheim, Germany.

7. Bartholomew, C. H., Agrawal, P. K. and Katzer, J. R., (1982), "Sulfur Poisoning of Metals," *Advances in Catalysis*, Vol. 31, pp. 135-242.

8. Bartholomew, C. H., (2001), "Mechanism of Catalyst Deactivation," *Applied Catalysis A: General*, Vol. 212, pp. 17-60.

9. Bastow, B. D., Wood, G. C., (1975), "Multilayer Scale Formation During the Sulfidation of Nickel," *Oxidation of Metals*, Vol. 9, pp. 473-496.

10. Batawi, E., Weissen, U., Schuler, A., Keller, M. and Voisard, C., (2001), "Cell Manufacturing Processes at Sulzer Hexis," in *Proceedings of the 7th International Symposium on Solid Oxide Fuel Cells*, edited by Yokokawa, H. and Singhal, S. C., The Electrochemical Society Proceedings Series, Vol. 2001-16, The Electrochemical Society, Pennington, NJ, pp.140-147.

11. Binnewies, M., Milke, E., (1999), *Thermochemical Data of Elements and Compounds*, Wiley-VCH, Weinheim, NY.

12. Bishop, D. W., Thomas, P. S., and Ray, A. S., (1998), "Raman Spectra of Nickel (II) Sulfide," *Materials Research Bulletin*, Vol. 33, pp.1303-1306.

13. Bishop, D. W., Thomas, A. S., and Ray, A. S., (2000), "Micro Raman Characterization of Nickel Sulfide Inclusions in Toughened Glass," *Materials Research Bulletin*, Vol. 35, pp. 1123-1128.

14. Chase, M. W. Jr., Davies, C. A., Downey, J. R. Jr., Frurip, D. J., McDonald, R. A., Syverud, A. N., (1985), *JANAF Thermochemical Tables*, Third Edition, American Chemical Society, Washington DC.

15. Cheng J. and Navrotsky, A., (2003), "Enthalpies of Formation of $LaBO_3$ Perovskites (B = Al, Ga, Sc, and In)," *Journal of Materials Research*, Vol. 18, pp. 2501-2508.

16. Cheng J. and Navrotsky, A., (2004), "Energetics of Magnesium, Strontium, and Barium Doped Lanthanum Gallate Perovskites," *Journal of Solid State Chemistry*, Vol. 177, pp. 126-133.

17. Cheng J., Navrotsky, A., Zhou, X.-D., Anderson, H. U., (2005), "Enthalpies of Formation of $LaBO_3$ Perovskites (B = Cr, Fe, Co, and Ni)," *Journal of Materials Research*, Vol. 20, pp. 191-200.

18. Cheng, Z., Abernathy, H., and Liu, M., (2007), "Raman Spectroscopy of Nickel Sulfide Ni_3S_2," *Journal of Physical Chemistry C*, Vol. 111, pp. 17997-18000.

19. Cheng, Z. and Liu, M. (2007), "Characterization of Sulfur Poisoning of Ni–YSZ Anodes for Solid Oxide Fuel Cells using in situ Raman Microspectroscopy," *Solid State Ionics*, Vol. 178, pp. 925-935.

20. Cheng, Z., Sacks, M. D., Wang, C-A., (2003), "Synthesis of Nanocrystalline Silicon Carbide Powders," *Ceramic Engineering and Science Proceedings*, Vol. 24, pp. 23-32.

21. Cheng, Z., Zha, S., Aguilar, L. and Liu, M., (2005), "Chemical, Electrical, and Thermal Properties of Strontium Doped Lanthanum Vanadate," *Solid State Ionics*, Vol. 176, pp.1921-1928.

22. Cheng, Z., Zha, S. and Liu, M., (2006), "Stability of Materials as Candidate for Sulfur-Resistant Anode of Solid Oxide Fuel Cells," *Journal of the Electrochemical Society*, Vol. 153, pp. A1302-A1309.

23. Cheng, Z., Zha, S., and Liu, M. (2007), "Influence of Cell Voltage and Current on Sulfur Poisoning Behavior of Solid Oxide Fuel Cells," *Journal of Power Sources*, Vol. 172, pp. 688-693.

24. Chick, L. A., Pederson, L. R., Maupin, G. D., Bates, J. L., Thomas, L. E. and Exarhos, G. J., (1990), "Glycine-Nitrate Combustion Synthesis of Oxide Ceramic Powders," *Materials Letters*, Vol. 10, pp. 6-12.

25. Choi, Y. M., Compson, C., Lin, M. C., Liu, M., (2006), "A Mechanistic Study of H_2S Decomposition on Ni- and Cu-Based Anode Surfaces in a Solid Oxide Fuel Cell," *Chemical Physics Letters,* Vol. 421, pp. 179-183.

26. Choi, Y. M., Compson, C., Lin, M. C., Liu, M., (2007), "*Ab initio* Analysis of Sulfur Tolerance of Ni, Cu, and Ni-Cu Alloys for Solid Oxide Fuel Cells," *Journal of Alloys and Compounds,* Vol. 427, pp. 25-29.

27. Choi, S, Wang, J., Cheng, Z., and Liu, M. (2008), "Surface Modification of Ni-YSZ using Niobium Oxide for Sulfur Tolerant Anodes in Solid Oxide Fuel Cells," *Journal of the Electrochemical Society*, accepted.

28. Colpa, J. P., Ketelaar, J. A., (1958), "The Pressure-Induced Rotational Adsorption Spectrum of Hydrogen," *Molecular Physics*, Vol. *1*, pp. 14-22.

29. Dees, D. W., Balachandran, U., Dorris, S. E., Heiberger, J. J., McPheeters, C. C. and Picciolo, J. J., (1989a), "Interfacial Effects in Monolithic Solid Oxide Fuel Cells," in *Proceedings of the First International Symposium on Solid Oxide Fuel Cells*, edited by S. C. Singhal, The Electrochemical Society Proceedings Series, Vol. 89-11, The Electrochemical Society, Pennington, NJ, pp.317-321.

30. Dees, D. W., Balachandran, U., Dorris, S. E., Heiberger, J. J., McPheeters, C. C. and Picciolo, J. J., (1989b), in *Proceedings of the Symposium on Fuel Cells: November 6-7, 1989, San Francisco, CA.*, edited by White, R. E. and Appleby, A. I., The Electrochemical Society Proceedings Series, Vol. 89-14, The Electrochemical Society, Pennington, NJ, pp. 130-137.

31. Dicks, A. L., (1996), "Hydrogen Generation from Natural Gas for the Fuel Cell Systems of Tomorrow," *Journal of Power Sources*, Vol. 61, pp. 113-124.

32. Dietz, R. E., Parisot, G. I., and Meixner, A. E., (1971), "Infrared Absorption and Raman Scattering by Two-Magnon Processes in NiO," *Physical Review B: Solid State*, Vol. 4, pp. 2302-10.

33. Dong, J., Zha, S. and Liu, M. (2005), "Study of Sulfur-Nickel Interaction Using Raman Spectroscopy," in *Proceedings of the 9th International Symposium on Solid Oxide Fuel Cells*, edited by Singhal, S. C. and Mizusaki, J., The Electrochemical Society Proceedings Series, Vol. 2005-07, The Electrochemical Society, Pennington, NJ, pp. 1284-1293.

34. Dong, J., Cheng, Z., Zha, S., and Liu, M., (2006), "Identification of Nickel Sulfides on Ni-YSZ Cermet Exposed to H_2 Fuel Containing H_2S Using Raman Spectroscopy," *Journal of Power Sources*, Vol. 156, pp. 461-465.

35. Eckert, L. J. and Bradt, R. C., (1973), "Thermal Expansion of Corundum Structure Ti_2O_3 and V_2O_3," *Journal of Applied Physics*, Vol. 44, pp. 3470-3472.

36. Feduska, W and Isenberg, A. O., (1983), "High-Temperature Solid Oxide Fuel Cell – Technical Status," *Journal of Power Sources*, Vol. 10, pp. 89-102.

37. Geyer, J., Kohlmüller, H., Landes, H. and Stübner, R., (1997), "Investigation into the Kinetics of the Ni-YSZ-Cermet-Anode of A Solid Oxide Fuel Cell," in

Proceedings of the 5th International Symposium on Solid Oxide Fuel Cells, edited by Stimming, U., Singhal, S. C., Tagawa, H. and Lennert, W., The Electrochemical Society Proceedings Series, Vol. 97-18, The Electrochemical Society, Pennington, NJ, pp.585-594.

38. Goddard W. A. III, Walch, S. P., Rappe, A. K., Upton, T. H., Melius, C. F., (1977), "Methanation of CO over Ni Catalyst: A Theoretical Study," *Journal of Vacuum Science and Technology*, Vol. 14, pp. 416-418.

39. Grasselli, J. G., Snavely, M. K. and Bulkin, B. J., (1981), *Chemical Applications of Raman Spectroscopy*, John Wiley & Sons, NY.

40. He, H., Gorte, R. J. and Vohs, J. M., (2005), "Highly Sulfur Tolerant Cu-Ceria Anodes for SOFCs," *Electrochemical and Solid State Letters*, Vol. 8, pp. A279-A280.

41. He, P., Liu, M., Luo, J. L., Sanger, A. R. and Chuang, K. T., (2002), "Stabilization of Platinum Anode Catalyst in a H_2S-O_2 Solid Oxide Fuel Cell with an Intermediate TiO_2 Layer," *Journal of Electrochemical Society*, Vol. 149, pp. A808-A814.

42. Helean, K. B., Ushakov, S. V., Brown, C. E., Navrotsky, A., Lian, J., Ewing, R. C., Farmer, J. M., and Boatner, L. A., (2004), "Formation Enthalpies of Rare Earth Titanate Pyrochlores," *Journal of Solid State Chemistry*, Vol. 177, pp. 1858-1866.

43. Hepola, J. and Simell, P., (1997), "Sulfur Poisoning of Nickel-Based Hot Gas Clearning Catalyst in Synthetic Gasification Gas: II. Chemisorption of Hydrogen Sulfide," *Applied Catalysis B: Environmental*, Vol. 14, pp. 305-321.

44. Hui, S. and Petric, A., (2001), "Conductivity and Stability of $SrVO_3$ and Mixed Perovskites at Low Oxygen Partial Pressures," *Solid State Ionics*, Vol. 143, pp. 275-283.

45. Iritani, J., Kougami, K., Komiyama, N., Nagata, K., Ikeda, K., Tomida, K., (2001), "Pressurized 10 kW Class Module SOFC," in *Proceedings of the 7th International Symposium on Solid Oxide Fuel Cells*, edited by Yokokawa, H. and Singhal, S. C., The Electrochemical Society Proceedings Series, Vol. 2001-16, The Electrochemical Society, Pennington, NJ, pp. 63-71.

46. Ishihara, T., Sammes, N. M., and Yamamoto, O., (2003), "Electrolytes," in *High Temperature Solid Oxide Fuel Cells: Fundamentals, Design and Applications*, edited by Singhal, S. C. and Kendall, K., Elsevier Advance Technology, Oxford, UK, pp. 83-117.

47. S. P. Jiang, J. G. Love, J. P. Zhang, M. Hoang, Y. Ramprakash, A. E. Hughes, S.P.S. Badwal, (1999), "The Electrochemical Performance of LSM/ Zirconia–Yttria Interface as a Function of A-site Non-stoichiometry and Cathodic Current Treatment," *Solid State Ionics*, Vol. 121, pp. 1-10.

48. Jorgensen, M. J., Mogensen, M., (2001), "Impedance of Solid Oxide Fuel Cell LSM/YSZ Composite Cathodes," *Journal of Electrochemical Society,* Vol. 148, pp. A433-A442.

49. Juretchke, H. J., Landauer, R., Swanson, J. A., (1956), "Hall Effect and Conductivity in Porous Media," *Journal Applied Physics*, Vol. 27 pp. 838-839.

50. Kendall, K., Minh, N. Q., Singhal, S. C., (2003), "Cell and Stack Design," in *High Temperature Solid Oxide Fuel Cells: Fundamentals, Design and Applications*, edited by Singhal, S. C. and Kendall, K., Elsevier Advance Technology, Oxford, UK, pp. 197-228.

51. Kim, H., Vohs, J. M. and Gorte R. J., (2001), "Direct Oxidation of Sulfur-Containing Fuels in a Solid Oxide Fuel Cell," *Chemical Communications*, pp. 2334-2335.

52. Kramer, S. A. and Tuller, H. L., (1995), "A Novel Titanate-based Oxygen Ion Conductor: $Gd_2Ti_2O_7$," *Solid State Ionics*, Vol. 82, pp. 15-23.

53. Krasser, W. and Renouprez, A. J., (1979), "Raman Scattering of Hydrogen Chemisorbed on Silica-Supported Nickel, *Journal of Raman Spectroscopy*, Vol. 8, pp. 92-94.

54. Kurokawa H., Sholklapper T. Z., Jacobson, C. P., De Jonghe L. C., and Visco, S. J., (2007), "Ceria Nanocoating for Sulfur Tolerant Ni-Based Anodes of Solid Oxide Fuel Cells," *Electrochemical and Solid-State Letters*, Vol. 10, pp. B135-B138.

55. LaMont, D. C., Gilligan, A. J., Darujati, A. R. S., Chellappa, A. S., Thomson, W. J., (2003), "The effect of Mo_2C synthesis and pretreatment on catalytic stability in oxidative reforming environments," *Applied Catalysis A: General*, Vol. 255, pp. 239-253.

56. Lee, Y.-K., Kim, J.-Y., Lee, Y.-K., Kim, I., Moon, H.-S., Park, J.-W. Jacobson, C. P., Visco, S. J., (2003), "Conditioning Effects on $La_{1-x}Sr_xMnO_3$-Yttria Stabilized Zirconia Electrodes for Thin-Film Solid Oxide Fuel Cells," *Journal of Power Sources*, Vol. 115, pp. 219-228.

57. Li, C. and Li. M., (2002), "UV Raman Spectroscopic Study on the Phase Transformation of ZrO_2, Y_2O_3-ZrO_2 and SO_4^{2-}/ZrO_2," *Journal of Raman Spectroscopy*, Vol. 33, pp. 301-308.

58. Liu, D. W., Perry, C. H., and Ingel, R. P., (1988), "Infrared Spectra in Nonstoichiometic Yttria-Stabilized Zirconia Mixed Crystals at Elevated Temperatures," *Journal of Applied Physics*, Vol. 64, pp. 1413-1417.

59. Liu, M., He, P., Luo, J. L., Sanger, A. R. and Chuang, K. T., (2001), "Performance of a Solid Oxide Fuel Cell Utilizing Hydrogen Sulfide as Fuel," *Journal of Power Sources*, Vol. 94, pp. 20-25.

60. Liu, M., Wei, G., Luo, J.L., Sanger, A. R. and Chuang, K. T., (2003), "Use of Metal Sulfides as Anode Catalysts in H_2S-Air SOFCs," *Journal of the Electrochemical Society*, Vol. 150, pp. A1025-A1029.

61. Marina, O. A., Canfield, N. L. and Stevenson, J. W., (2002), "Thermal, Electrical, and Electrocatalytical Properties of Lanthanum-doped Strontium Titanate," *Solid State Ionics*, Vol. 149, pp. 21-28.

62. Marina, O., Stevenson, J., (2004), "SOFC Anode Materials Development at PNNL," in *2004 Office of Fossil Energy Fuel Cell Program Annual Report*, Office of Fossil Energy, U.S. Department of Energy, pp. 90-92.

63. Marquez, A. I., Abreu, Y. D., and Botte, G. G., (2006), "Theoretical Investigation of Ni/YSZ in the Presence of H_2S," *Electrochemical and Solid-State Letters*, Vol. 9, pp. A163-166.

64. Matsuzaki, Y. and Yasuda, I., (2000), "The Poisoning Effect of Sulfur-Containing Impurity Gas on a SOFC Anode: Part I. Dependence on Temperature, Time, and Impurity Concentration," *Solid State Ionics*, Vol. 132, pp. 261-269.

65. Matsuzaki, Y. and Yasuda, I., (2001), "Effect of A Sulfur-Containing Impurity on Electrochemical Properties of A Ni-YSZ Cermet Electrode," in *Proceedings of the 7th International Symposium on Solid Oxide Fuel Cells*, edited by Yokokawa, H. and Singhal, S. C., The Electrochemical Society Proceedings Series, Vol. 2001-16, The Electrochemical Society, Pennington, NJ, pp. 769-779.

66. McCarty, J. G., Wise, H., (1980), "Thermodynamics of Sulfur Adsorption on Metals. I. Alumina-Supported Nickel," *Journal of Chemical Physics*, Vol. 72, pp. 6332-6337.

67. Melendres, C. A. and Xu, S., (1984), "In Situ Laser Raman Spectroscopic Study of Anodic Corrosion Films on Nickel and Cobalt," Journal of the Electrochemical Society, Vol. 130, pp. 2239-2243.

68. Minh, N. Q. and Takahashi, T., (1995), *Science and Technology of Ceramic Fuel Cells*, Elsevier Science, Netherlands.

69. Minh, N. Q., Anumakonda, A., Chung, B., Doshi, R., Ferrall, J., Guan, J., Lear, G., Montgomery, K., Ong, E. and J. Yamanis, (1999), "Development of Reduced-Temperature Solid Oxide Fuel Cell Power Systems," in *Proceedings of the 5th International Symposium on Solid Oxide Fuel Cells*, edited by S. C. Singhal and M. Dokiya, The Electrochemical Society Proceedings Series, Vol. 99-19, The Electrochemical Society, Pennington, NJ, pp.68-74.

70. Moon, J., Choi, H., Kim, Y., and Lee, C., (2001), "Cool Rate Effect on Phase Transformation of Plasma Sprayed Partially Stabilized Zirconia," *Journal of Materials Science Letters*, Vol. 20, pp. 1611-1613.

71. Mukundan, R., Brosha, E. L. and Garzon, F. H., (2004), "Sulfur Tolerant Anodes for SOFCs," *Electrochemical and Solid-State Letters*, Vol. 7, pp. A5-A7.

72. Navrotsky, A., (1981), "Energetics of Phase Transition in AX, ABO_3, and AB_2O_4 Compounds," in *Structure and Bonding in Crystals*, edited by M. O.'Keefe and A. Navrotsky, Vol. II, Academic Press, NY, pp. 71-93.

73. Noponen, M., Halinen, M., Kiviaho, J., and Saarinen, J., (2006), "Feasibility of Autothermally Reformed Natural Gas on Anode Supported Solid Oxide Fuel Cells," *Transactions of the ASME*, Vol. 3, pp. 438-444.

74. Porat, O., Heremans, C., Tuller, H. L., (1997), "Stability and Mixed Ionic Electronic Conduction in $Gd_2(Ti_{1-x}Mo_x)_2O_7$ Under Anodic Conditions," *Solid State Ionics*, Vol. 94, pp. 75-83.

75. Primdahl, S. and Mogensen, M., (1999), "Limitations in the Hydrogen Oxidation Rate on Ni/YSZ Anodes," in *Proceedings of the 5th International Symposium on Solid Oxide Fuel Cells*, edited by S. C. Singhal and M. Dokiya, The Electrochemical Society Proceedings Series, Vol. 99-19, The Electrochemical Society, Pennington, NJ, pp.530-540.

76. Pujare, N. U., Semkow, K. W. and Sammells, A. F., (1987), "A Direct H_2S/Air Solid Oxide Fuel Cell," *Journal of the Electrochemical Society*, Vol. 134, pp. 2639-2640.

77. Pujare, N. U., Tsai, K. J. and Sammells, A. F., (1989), "An Electrochemical Claus Process for Sulfur Recovery," *Journal of the Electrochemical Society*, Vol. 136, pp. 3662-3678.

78. Rosenqvist, T., (1954), "A Thermodynamic Study of the Iron, Cobalt, and Nickel Sulphides," *Journal of the Iron and Steel Institute*, 176, pp. 37-57.

79. Rostrup-Nielsen, J. R., (1971), "Some Principles Relating to the Regeneration of Sulfur-Poisoned Nickel Catalyst," *Journal of Catalysis*, Vol. 21, pp. 171-178.

80. Rostrup-Nielsen, J. R., (2001), "Conversion of Hydrocarbons and Alcohols for Fuel Cells," *Physical Chemistry and Chemical Physics*, Vol. 3, pp. 283-288.

81. RRUFF database of Raman spectra, X-ray diffraction and chemistry data for minerals, The university of Arizona, http://rruff.info/index.php.

82. Sasaki, K., Susuki, K., Iyoshi, A., Uchimura, M., Imamura, N., Kusaba, H., Teraoka, Y., Fuchino, H., Tsujimoto, K., Uchida, Y., Jingo, N., (2005), "Sulfur Tolerance of Solid Oxide Fuel Cells," in *Proceedings of the 9th International Symposium on Solid Oxide Fuel Cells*, edited by Singhal, S. C. and Mizusaki, J., The Electrochemical Society Proceedings Series, Vol. 2005-07, The Electrochemical Society, Pennington, NJ, pp.1267-1274.

83. Sekulić, A., Furić, K., Tonejc, A., Tonejc, A. M., Stubičar, M., (1997), "Determination of the Monoclinic, Tetragonal and Cubic Phases in Mechanically Alloyed ZrO_2-Y_2O_3 and ZrO_2-CoO Powder Mixtures by Raman Spectroscopy," *Journal of Materials Science Letters*, Vol. 16, pp. 260-262.

84. Shannon, R. D., (1976), "Revised Effective Ionic Radii and Systematic Studies of Interatomic Distances in Halides and Chalcogenides," Acta Crystallography, Vol. A32, pp. 751-767.

85. Shen, G., Chen, D., Tang, K., An C., Yang, Q., Qian, Y., (2003), "Phase-Controlled Synthesis and Characterization of Nickel Sulfides Nanorods," *Journal of Materials Chemistry*, Vol. 173, pp. 227-231.

86. Simner, S. P.; Anderson, M. D.; Pederson, L. R.; Stevenson, J. W., (2005), "Performance Variability of La(Sr)FeO_3 SOFC Cathode with Pt, Ag, and Au Current Collectors.," *Journal of the Electrochemical Society*, Vol. 152, pp. A1851-1859.

87. Singhal, S. C. and Kendall, K., (2003), *High Temperature Solid Oxide Fuel Cells: Fundamentals, Design and Applications*, Elsevier Advance Technology, Oxford, UK.

88. Singhal, S. C., Ruka, R. J., Bauerle, J. E. and Spengler, C. J., (1986), *Anode Development for Solid Oxide Fuel Cells*, Report No. DOE/MC/22046-2371, U.S. Department of Energy, Washington, DC.

89. Smith, E. and Dent, G., (2005), *Modern Raman Spectroscopy - A Practical Approach*, John Wiley & Sons, England.

90. Smith, M. and McEvoy, A. J., (2005), "Sulfur-Tolerant Cermet Anodes," in *Proceedings of the 9th International Symposium on Solid Oxide Fuel Cells*, edited by Singhal, S. C. and Mizusaki, J., The Electrochemical Society Proceedings Series, Vol. 2005-07, The Electrochemical Society, Pennington, NJ, pp.1437-1444.

91. Sprenkle, V., Kim, J.Y., Meinhardt, K., Lu, C., Chick, L., Canfield, N., Bonnett, J., Mukerjee, S., Shaffer, S., "Sulfur Poisoning Studies on the Delphi-Battelle SECA Program," presented at the 31st International Cocoa Beach Conference & Exposition on Advanced Ceramics and Composites, Daytona Beach, FL 2007.

92. Stencel, J. M., (1990), *Raman Spectroscopy for Catalysis*, Van Norstrand Reinhold, NY.

93. Stoklosa, A., Zajecki, J., (1996), "Phase Diagram and Electrical Properties, Defect Concentration in Oxides and Sulphides of 3d Metals," *Solid State Ionics*, Vol. 91, pp. 315-322.

94. Stolten, D., Späh R. and R. Schamm, (1997), "Status of SOFC Development at Daimler-Benz/Dornier," in *Proceedings of the 5th International Symposium on Solid*

Oxide Fuel Cells, edited by Stimming, U., Singhal, S. C., Tagawa, H. and Lennert, W., The Electrochemical Society Proceedings Series, Vol. 97-18, The Electrochemical Society, Pennington, NJ, pp.88-93.

95. Surdoval, W., (2007), "The U. S. Department of Energy Fossil Energy Fuel Cell Program Solid State Energy Conversion Alliance: Goals and Challenges," DOE Eighth SECA Annual Workshop, August 7 - 9, 2007, San Antonio, Texas, http://www.netl.doe.gov/publications/proceedings/07/SECA_Workshop/index.html.

96. Tao, S. and Irvine, J. T. S., (2004), "Synthesis and Characterization of $(La_{0.75}Sr_{0.25})Cr_{0.5}Mn_{0.5}Mn_{3-\delta}$, A Redox-Stable, Efficient Perovskite Anode for SOFCs," Journal of the Electrochemical Society, Vol. 151, pp. A252-A259.

97. Trembly, J. P., Marquez, A. I., Ohrn, T. R., and Bayless, D. J., (2006), "Effects of Coal Syngas and H_2S on the Performance of Solid Oxide Fuel Cells: Single-Cell Tests," *Journal of Power Sources*, Vol. 158, pp. 263-273.

98. Tuller, H. L., (1991), "Highly Conductive Ceramics," in *Ceramic Materials for Electronics*, edited by Buchanan, R. C., Marcel Dekker, NY.

99. van Gerwen, R. J. F., (2003), "System and Applications," in *High Temperature Solid Oxide Fuel Cells: Fundamentals, Design and Applications*, edited by Singhal, S. C. and Kendall, K., Elsevier Advance Technology, Oxford, UK, pp. 363-392.

100. Voorhoeve, R. J. H., Johnson, D. W. Jr., Remeika, J. P. and Gallagher, P. K., (1977), "Perovskite Oxides: Materials Science in Catalysis," *Science*, Vol. 195, pp. 827-833.

101. Waldbillig, D., Ivey, D. G., and Wood, A., (2005), "The Poisoning Effect of H_2S Fuel Impurities on SOFC Anodes," in *Fuel Cell and Hydrogen Technologies - Proceedings of the International Symposium on Fuel Cell and Hydrogen Technologies*, 1st, p. 237, Canadian Institute of Mining, Metallurgy and Petroleum, Montreal, Canada.

102. Wang, J.-H., Cheng, Z., Brédas, J.-L., and Liu, M., (2007), "Electronic and Vibrational Properties of Nickel Sulfides from First Principles," *Journal of Chemical Physics*, Vol. 127, p. 214705.

103. Wang, J.-H., Liu, M., (2007), "Computational Study of Sulfur–Nickel Interactions: A New S–Ni Phase Diagram," *Electrochemistry Communications*, Vol. 9, pp. 2212-2217.

104. Wang, J.-H., Liu, M., (2008), "Surface Regeneration of Sulfur-Poisoned Ni Surfaces under SOFC Operation Conditions Predicted by First-Principles-Based Thermodynamic Calculations," *Journal of Power Sources*, Vol. 176, pp. 23-30.

105. Wang, S., Liu, M. and Winnick, J., (2001) "Stabilities and Electrical Conductivities of Electrode materials for Use in H_2S-Containing Gases," *Journal Solid State Electrochemistry*, Vol. 5, pp. 188-195.

106. Wei, G. L., Luo, J. L., Sanger, A. R. and Chuang, K. T., (2004), "High-Performance Anode for H_2S-Air SOFCs," *Journal of the Electrochemical Society*, Vol. 151, pp. A232-237.

107. Weimer, A. W., (1997), *Carbide, Nitride and Boride Materials Synthesis and Processing*, Chapman & Hall, London.

108. Xia, C. and Liu, M., (2001a), "A Simple and Cost-Effective Approach to Fabrication of Dense Ceramic Membranes on Porous Substrates," *Journal of American Ceramic Society*, Vol. 84, pp. 1903-1905.

109. Xia, C. and Liu, M., (2001b), "Low-Temperature SOFCs Based on $Gd_{0.1}Ce_{0.9}O_{1.95}$ Fabricated by Dry Pressing," Solid State Ionics, Vol. 144, pp. 249-255.

110. Xia, S. J. and Birss, V. I., (2005), "Deactivation and Recovery of Ni-YSZ Anode in H_2 Fuel Containing H_2S," in *Proceedings of the 9th International Symposium on Solid Oxide Fuel Cells*, edited by Singhal, S. C. and Mizusaki, J., The Electrochemical Society Proceedings Series, Vol. 2005-07, The Electrochemical Society, Pennington, NJ, pp.1275-1283.

111. Yates, C. and Winnick, J., (1999), "Anode Materials for a Hydrogen Sulfide Solid Oxide Fuel Cell," *Journal of the Electrochemical Society*, Vol. 146, pp. 2841-2844.

112. Yokokawa, H. and Horita, T., (2003), "Cathodes," in *High Temperature Solid Oxide Fuel Cells: Fundamentals, Design and Applications*, edited by Singhal, S. C. and Kendall, K., Elsevier Advance Technology, Oxford, UK, pp. 119-147.

113. Yokokawa, H., Kawada, T. and Dokiya, M., (1989), "Thermodynamic Regularities in Perovskite and K_2NiF_4 Compounds," *Journal of the American Ceramic Society*, Vol. 72, pp. 152-153.

114. Yokokawa, H., Sakai, N., Kawada, T., and Dokiya, M., (1990), "Chemical Potential Diagram for Rare Earth-Transition Metal-Oxygen Systems: I, Ln-V-O and Ln-Mn-O Systems," *Journal of the American Ceramic Society*, Vol. 73, pp. 649-658.

115. Yokokawa, H., Sakai, N., Kawada, T., and Dokiya, M., (1991a), "Chemical Thermodynamic Consideration in Sintering of $LaCoO_3$-Based Perovskites," *Journal of the Electrochemical Society*, Vol. 138, pp. 1018-1027.

116. Yokokawa, H., Sakai, N., Kawada, T., and Dokiya, M., (1991b), "Thermodynamic analysis of Reaction Profiles Between $LaMO_3$ (M=Ni, Co, Mn) and ZrO_2," *Journal of the Electrochemical Society*, Vol. 138, pp. 2719-2727.

117. Zha, S., Cheng, Z. and Liu, M., (2005a), "A Sulfur-Tolerant Anode Materials for SOFCs: $Gd_2Ti_{1.4}Mo_{0.6}O_7$," *Electrochemical and Solid-State Letters*, Vol. 8, pp. A406-A408.

118. Zha, S., Cheng, Z. and Liu, M., (2007), "Sulfur Poisoning and Regeneration of Ni-based Anodes," *Journal of the Electrochemical Society*, Vol. 154, pp. B201-B206.

119. Zha, S., Tsang, P., Cheng, Z. and Liu, M., (2005b), "Electrical Properties and Sulfur Tolerance of $La_{0.75}Sr_{0.25}Cr_{1-x}Mn_xO_3$ under Anodic Conditions," *Journal of Solid State Chemistry*, Vol. 178, pp. 1844-1850.